Multi-Scale Engineering of Lead-Free Piezoelectric Pavement Sensing Systems

Von der Fakultät für Bauingenieurwesen der Rheinisch-Westfälischen TechnischenHochschule Aachen zur Erlangung des akademischen Grades einer Doktorin der Ingenieurwissenschaften genehmigte Dissertation

Vorgelegt von

Kai Zheng

Berichter: Jun.-Prof. Dr.-Ing. Pengfei Liu

Univ.-Prof. Dr. Alvaro Garcia Hernandez

Prof. Dr.-Ing. habil. Alexander Zeißler

Tag der mündlichen Prüfung: 19.05.2026

Diese Dissertation ist auf den Internetseiten der Universitätsbibliothek online verfügbar

Publication list of the doctoral dissertation:

1. Kai Zheng, Ning Xie, Yuanbin Deng, Mariano Febbo, Christoph Broeckmann, Pengfei Liu. “A review on lead-free piezoelectric ceramic sensors for sustainable and intelligent applications”. In: Chemical Engineering Journal. 2025: 172363. (Section 1.2 in Chapter 1)

   https://doi.org/10.1016/j.cej.2025.172363

2. Kai Zheng, Ning Xie, Li-Feng Zhu, Pengfei Liu. “Enhanced piezoelectric performance and thermal stability in KNN-BNZ ceramics modified by CaHfO3”. In: Journal of Materials Science: Materials in Electronics.37, 379 (2026). (Chapter 2)

   https://doi.org/10.1007/s10854-026-16793-0

3. Kai Zheng, Ning Xie, Pengfei Liu. “Epoxy-cement composite packaging for KNN piezoelectric sensors”. In: Sensors and Actuators A: Physical. 2025: 117356. (Chapter 3)

   https://doi.org/10.1016/j.sna.2025.117356

4. Kai Zheng, Ning Xie, Jiao Jin, Pengfei Liu. “Environmentally friendly lead-free piezoelectric ceramics as pavement sensing element: A multi-scale finite element perspective”. In: Case Studies in Construction Materials. 2025: e05174. (Chapter 4)

   https://doi.org/10.1016/j.cscm.2025.e05174

5. Kai Zheng, Taowei Gao, Pengfei Liu. “A Sensor Arrangement Evaluation Framework for Lead-Free Potassium Sodium Niobate Pavement Sensors in Vehicle Classification”. In: Measurement. 2026: 120999. (Chapter 5)

   https://doi.org/10.1016/j.measurement.2026.120999

Acknowledgements

As I come to the end of this doctoral dissertation, my journey at RWTH Aachen University also reaches an important milestone. Looking back, these years at ISAC have been filled with challenges, growth, moments of uncertainty, and many rewarding experiences. This work would not have been possible without the support, guidance, and kindness of numerous people, to whom I would like to express my heartfelt gratitude.

First and foremost, I would like to express my deepest gratitude to my supervisor, Junior Professor Pengfei Liu. Throughout my PhD studies, his rigorous scientific attitude, clear research vision, and constant encouragement have provided me with invaluable guidance and confidence. Our discussions have greatly helped shape this dissertation and influenced the way I approach scientific problems. I am truly grateful for his patience, trust, and unwavering support during both the challenging and successful moments of my research journey. I would also like to sincerely thank Prof. Alvaro Garcia Hernandez, the head of ISAC, for his continuous support and encouragement. His open-minded leadership and strong support for experimental research and project coordination created an excellent research environment, from which I benefited greatly.

My sincere gratitude also goes to my former master's supervisor, Prof. Ning Xie, now at Aston University. His guidance during my earlier academic training laid a solid foundation for my research skills and scientific thinking. Even after I started my PhD, his advice and encouragement remained a valuable source of motivation for me.

I would further like to thank my colleagues and friends at ISAC, as well as those from the collaborating institutions in China, for their kind assistance, fruitful discussions, and strong support during different stages of my research. Whether in laboratories in Aachen or during experimental work in China, your professionalism, cooperation, and friendship greatly contributed to the progress of this dissertation. These experiences made my doctoral journey productive, meaningful, and truly memorable.

I am deeply grateful to my family for their unconditional love, understanding, and patience throughout this journey. Even when distance and busy schedules kept us apart, their

encouragement remained my greatest source of strength and comfort.

I am also sincerely grateful to the China Scholarship Council (CSC) for providing the financial support that made it possible for me to pursue my doctoral studies in Germany.

This journey has also taught me to rely on myself, to remain patient in difficult times, and to move forward step by step even when the path is unclear. Completing this dissertation has been one of the most demanding and meaningful experiences of my life, shaping not only my academic abilities but also my resilience and perspective on life.

Finally, I would like to thank everyone who has accompanied me, directly or indirectly, along this path. This dissertation is not only a record of academic work, but also a reflection of the trust, kindness, and support I have received over the years. I will carry these experiences with me into the future with gratitude and humility.

Declaration

The work described in this dissertation was conducted at the Institute of Highway Engineering, RWTH Aachen University. I declare that the work is my own and has not been submitted for another university degree.

Abstract

The development of intelligent road infrastructure requires sensing systems that are reliable, durable, and compatible with long-term pavement service conditions. Piezoelectric sensing technologies are widely used in traffic monitoring because they convert mechanical loading into electrical signals without an external power supply. Most pavement sensing systems are based on lead-containing piezoelectric ceramics, especially lead zirconate titanate (PZT), due to their high intrinsic sensitivity. However, environmental considerations and sustainability requirements motivate the exploration of lead-free alternatives. Potassium sodium niobate (KNN)-based ceramics offer promising thermal stability and are suitable for elevated pavement temperatures, yet their intrinsic piezoelectric response is lower than that of PZT. Therefore, the challenge of applying KNN-based materials in pavement sensing systems lies not only in optimizing the material properties but also in understanding how material behavior interacts with pavement structures and sensing arrangements.

This dissertation adopts a multi-scale engineering perspective for integrating lead-free piezoelectric materials into pavement sensing systems. The study links multiple scales, including material-level piezoelectric behavior, device-level sensor packaging, pavement-scale structural interaction, and system-level sensing performance. At the material level, KNN-based ceramics were designed and evaluated under pavement-relevant thermal conditions to assess their functional stability. The experimental results confirm their suitability for pavement environments while revealing that the relatively limited piezoelectric response requires further structural optimization at higher system levels.

At the device scale, the influence of sensor packaging on sensing behavior is systematically investigated. Because signal generation in pavement sensors strongly depends on mechanical confinement and load transfer, the effects of packaging on sensitivity, linearity, and durability under cyclic loading are analyzed. The results show that mechanical strength or peak voltage alone does not determine sensing reliability. Instead, stable signal evolution and consistent response characteristics are more critical for long-term monitoring applications.

At the structural scale, the sensing response of embedded sensors within pavement

structures is investigated through numerical simulations. Parametric studies are conducted to examine how different traffic conditions and sensor embedding configurations influence the generated piezoelectric signals. The analyses consider factors such as load magnitude, vehicle type, sensor depth, and spatial position. The results provide insight into how pavement structural conditions affect sensor output signals and help clarify the sensitivity of the sensing response to traffic loading and installation parameters.

At the system scale, a simulation-driven framework is developed to evaluate sensor arrangement strategies for pavement monitoring. The framework integrates pavement structural parameters, sensor characteristics, and traffic scenarios to assess signal distinguishability for vehicle classification. Rather than assuming dense sensor placement, the framework identifies configurations that preserve essential sensing information while reducing the number of embedded sensing units, introducing an information-efficiency perspective into pavement sensing design.

The investigation combines laboratory experiments and numerical modeling with emphasis on mechanism clarification and methodological development. Full-scale field validation and long-term in-situ monitoring are beyond the scope of the present study and remain subjects for future work.

This dissertation presents a multi-scale engineering pathway for translating lead-free piezoelectric materials into pavement sensing systems. It contributes a mechanics-based description of signal attenuation in layered pavement structures and proposes a rational framework for sensor arrangement. The findings demonstrate that reliable traffic classification can be achieved through coordinated system design, even when the intrinsic piezoelectric response is limited, thereby providing a foundation for subsequent field implementation and model refinement.

Table of Contents

Acknowledgements ..... **I**

Declaration ..... **III**

Abstract ..... **IV**

Table of Contents ..... **VI**

List of Figures ..... **X**

List of Tables ..... **XIV**

1. Introduction **1**

1.1. Research Background 1

1.2. A Review on Lead-Free Piezoelectric Ceramic Sensors for Sustainable and Intelligent Applications 2

1.2.1. Abstract 2

1.2.2. Introduction 3

1.2.3. Classification of Lead-free Piezoelectric Ceramics and Doping Strategies 6

1.2.4. Multidimensional Performance Assessment Criteria 8

1.2.4.1. Conventional Evaluation Standards 9

1.2.4.2. Multidimensional Assessment Criteria 10

1.2.4.3. Functionalization via Autonomous Intelligence 21

1.2.5. Structural Design 22

1.2.5.1. Conflicts Between Traditional Manufacturing and Updated Requirements 23

1.2.5.2. Progressive Manufacturing Process 24

1.2.5.3. Flexibility 29

1.2.5.4. Heterogeneous Structures 31

1.2.6. Intelligent Integration 34

1.2.6.1. Constraints of Conventional Sensing Systems 34

1.2.6.2. Machine Learning and Neuromorphic Computing 35

1.2.6.3. Multimodal Energy and Sensing Integration 38

1.2.7. Emerging Horizons 44
1.2.7.1. Beyond Classical Theories 44
1.2.7.2. Smart Sensing and Life Sciences Integration 48
1.2.8. Conclusions 50
1.3. Objective and Scope 52
2. Enhanced Piezoelectric Performance and Thermal Stability in KNN-BNZ Ceramics Modified by $CaHfO_3$ 55
2.1. Abstract 55
2.2. Introduction 55
2.3. Experimental 58
2.3.1. Material Preparation 58
2.3.2. Environmental Risk Assessment Methodology 60
2.4. Results and Discussion 62
2.4.1. Comprehensive Evaluation of Functional and Microstructural Characteristics 62
2.4.2. Environmental Risk Assessment Analysis 69
2.5. Conclusions 72
3. Epoxy-Cement Composite Packaging for KNN Piezoelectric Sensors 73
3.1. Abstract 73
3.2. Introduction 73
3.3. Materials and Characterization Methods 76
3.3.1. Materials Preparation 76
3.3.1.1. Synthesis of KNN Ceramics 76
3.3.1.2. Preparation of Packaging Materials 77
3.3.1.3. Fabrication of Embedded Sensors 78
3.3.2. Characterization Methods 79
3.4. Results and Discussion 80
3.4.1. Characterization of Packaging Materials 80
3.4.1.1. Mechanical Properties 80

3.4.1.2. Interactions between the Cement and Epoxy Resins 82
3.4.2. Force-voltage Generation 84
3.4.2.1. Voltage Collection 84
3.4.2.2. Linearity of Force vs. Voltage Signal 89
3.4.3. Evaluation of Sensor Fatigue Behavior 95
3.5. Conclusions and Outlook 97
4. Environmentally Friendly Lead-Free Piezoelectric Ceramics as Pavement Sensing Element: A Multi-Scale Finite Element Perspective 99
4.1. Abstract 99
4.2. Introduction 100
4.3. Methodology 103
4.3.1. Raw Materials 103
4.3.2. Parameters Determination of the Small-Scale Model 105
4.3.3. Development of a Tire Model 106
4.3.4. Development of the Large-Scale Model 108
4.3.5. Verification of Models 110
4.3.6. Setting of Input Variables 112
4.4. Results and Discussion 114
4.4.1. Mechanical Response for the Large-Scale Model 116
4.4.2. Mechanical Response for the Small-Scale Model 120
4.4.3. Piezoelectric Performance for the Small-Scale Model 123
4.4.3.1. Variable Effects for Open-Circuit Voltage 124
4.4.3.2. Correlation Analysis of Variable Effects 128
4.5. Conclusions and Outlook 129
5. A Sensor Arrangement Evaluation Framework for Lead-Free Potassium Sodium Niobate Pavement Sensors in Vehicle Classification 131
5.1. Abstract 131
5.2. Introduction 131

5.3. Objective 133
5.4. Methodology 134
5.4.1. Vehicle Passage Paths 135
5.4.2. Sensor Arrangement Strategies 136
5.4.3. Attenuation Function Derivation 140
5.4.3.1. Simulation of KNN Sensor Models 140
5.4.3.2. Simulation of Pavement Models 142
5.4.3.3. Simulation of Vehicle and Sensor Signal Collection 144
5.4.3.4. Attenuation Function Fitting from Signal Collection 146
5.4.4. Reliability Assessment and Arrangement Evaluation 149
5.4.4.1. Reliability Assessment of the ESAM Framework 150
5.4.4.2. Evaluation for Sensor Arrangement 151
5.5. Results and Discussion 153
5.5.1. Sensor Response under Different Vehicle Types 153
5.5.2. Sensor Arrangement under Random Path 154
5.5.2.1. Uniform Arrangement 154
5.5.2.2. Centrally Weighted Arrangement 157
5.5.2.3. Minimum Coverage Arrangement 158
5.5.3. Sensor Arrangement under Wheel-Tack Constraint 160
5.5.4. Comparison of Sensor Arrangement Strategies 162
5.6. Conclusions and Outlook 165
6. Conclusions and Outlook 166
6.1. Conclusions 166
6.2. Outlook 167
Reference 168
Appendix 198

List of Figures

Fig. 1-1: Bridging fundamental material research and application in lead-free piezoelectric ceramics 6
Fig. 1-2: (a) Diagram of a typical tape casting process, (b) texturing mechanism schematics of the TGG method, and (c) engineered domain structure of <001>-textured ceramics with R phase after poling treatment (Shen et al., 2025)..... 13
Fig. 1-3: (a) Design strategy of the HpeD, (b) Schematic representation of the sensing system (Dinh Trung et al., 2024)..... 14
Fig. 1-4: Schematic representation of the advancement of wearable piezoelectric sensors (Y. Chen et al., 2024; H. Zhou et al., 2020)..... 15
Fig. 1-5: (a) Schematic illustration of the time-dependent in-situ photoreduction reaction and (b) illustration of silver particle doping. Comparison of SEM images of (c) BTO, (d) 1 m-Ag/BTO, and (e) elemental mapping of 1 m-Ag/BTO. (f) TEM image of 1 m-Ag/BTO ceramic, (g) TEM of Ag nanoparticles, and (h) SEAD pattern of Ag nanoparticles (Hamza et al., 2025)..... 25
Fig. 1-6: Extrusion-based 3D printing. (a) presents the fundamental printing mechanism, while (b) demonstrates the fabrication of a 3D construct and (c) displays diverse printed geometries. In (d), the deformation behavior of the printed components is shown under early-stage loading, stretching, bending, and torsional motion (Hamza et al., 2025)..... 26
Fig. 1-7: Schematic diagram of flexible sensor (Taleb et al., 2023) 31
Fig. 1-8: Visual Representation of the Smart Glove-Based Monitoring System for Parkinson's Patients (De Fazio et al., 2025) 37
Fig. 1-9: Vibro-piezoelectric detection system for classifying maize grain and impurity (Y. Li et al., 2024)..... 37
Fig. 1-10: Schematic diagram of generator prepared from PVDF/SM-KNN (Bairagi and Ali, 2020) 40
Fig. 1-11: Schematic diagram of a hybrid energy harvester coupling a thermoelectric generator and a piezoelectric generator (S.-B. Kim et al., 2023) 43
Fig. 2-1: Strategies for preparing KNN-BNZ-*x*CHO with different dosages of $CaHfO_3$ 58
Fig. 2-2: System boundary of the life cycle assessment (LCA) for KNN and PZT piezoelectric ceramics 61
Fig. 2-3: The dielectric constant and *tan δ* for the KNNS-BNZ-*x*CHO ceramics of (a) $x = 0$, (b) $x = 0.01$, (c) $x = 0.03$, and (d) $x = 0.04$ with different temperatures and frequencies about 100 kHz, 300 kHz, and 1000 kHz..... 63
Fig. 2-4: XRD patterns of KNN-BNZ-*x*CHO ceramics as a function of (a) $x = 0$, 0.01, 0.02, 0.03, 0.04 measured at $2\theta = 20\text{-}80°$, (b) magnified XRD patterns at $2\theta = 44\text{-}47°$ 64
Fig. 2-5: Rietveld refinement of XRD patterns in KNN-BNZ-0.03CHO ceramic 65
Fig. 2-6: The micromorphology of KNN-BNZ-*x*CHO ceramics for various x values. (a) $x = 0$, (b) $x = 0.01$, (c) $x = 0.02$, (d) $x = 0.03$, and (e) $x = 0.04$..... 65
Fig. 2-7: P-E curves of KNN-BNZ-xCHO ceramics as a function of (a) $x = 0$, (b) $x = 0.01$, (c) $x = 0.02$, (d) $x = 0.03$, (e) $x = 0.04$, and (f) the comparison of E_c, P_r, and t_G at different $CaHfO_3$ contents..... 66

Fig. 2-8: Evolution of dielectric constant, piezoelectric constant, electromechanical coupling factor, and Curie temperature of KNN-BNZ-*x*CHO ceramics as a function of $CaHfO_3$ content 69
Fig. 2-9: (a) GWP of KNN-series and PZT series in the manufacturing and end-of-life process, (b) Costs of KNN-series and PZT series in the manufacturing and end-of-life process 71
Fig. 3-1: Schematic workflow of sensor encapsulation, characterization, and performance evaluation 79
Fig. 3-2: The compressive strength of packaging materials with varying cement dosage, (a) solvent-based epoxy packaging material, (b) waterborne epoxy packaging material 81
Fig. 3-3: Fracture surfaces SEM morphologies of (a) neat solvent-based epoxy and (b) solvent-based epoxy/cement 82
Fig. 3-4: Fracture surface SEM morphologies of waterborne epoxy/cement, (a) low-magnification image, and high-magnification images of (b) hydration product with flat surface, and (c) and d) other forms of surface of C-S-H hydration products 83
Fig. 3-5: Fracture surface SEM morphologies of waterborne epoxy/cement with (a) low-magnification image, and (b) high-magnification images 84
Fig. 3-6: Schematic illustration of how the radar graphs and ΔR are derived from repeated measurements to assess voltage response repeatability 85
Fig. 3-7: Radar graphs and corresponding voltage-distribution sensitivity of the force-voltage response for waterborne and solvent-based epoxy-cement packaging materials of KNN piezoelectric sensors under a 2 g falling ball: (a) solvent-based epoxy: cement = 100:0; (b) solvent-based epoxy: cement = 100:100; (c) waterborne epoxy: cement = 5:100; (d) waterborne epoxy: cement = 100:100 86
Fig. 3-8: Radar graphs and corresponding voltage-distribution sensitivity of the force-voltage response of KNN piezoelectric sensors packaged with waterborne and solvent-based epoxy-cement composites under a 5 g falling ball: (a) solvent-based epoxy: cement = 100:0, (b) solvent-based epoxy: cement = 100:100, (c) waterborne epoxy: cement = 5:100, and (d) waterborne epoxy: cement = 100:100 87
Fig. 3-9: Radar graphs and the corresponding voltage-distribution sensitivity of the force-voltage response of solvent-based epoxy mixed with cement as packaging materials for KNN piezoelectric sensors under 20 g and 30 g falling balls: (a) solvent-based epoxy: cement = 100:0, (b) solvent-based epoxy: cement = 100:100, (c) solvent-based epoxy: cement = 100:0, and (d) solvent-based epoxy: cement = 100:100 88
Fig. 3-10: The oscillogram of a 2-gram ball in free fall on the surface of the sensor 90
Fig. 3-11: Force-voltage response of the waterborne and solvent-based epoxy mixed with cement as packaging materials for KNN piezoelectric sensors, (a) median voltage, (b) mode voltage, (c) average voltage, (d) peak voltage, (e) solvent-based epoxy: cement = 100:0 under 20 g falling ball, (f) solvent-based epoxy: cement = 100:100 under 30 g falling ball 91
Fig. 3-12: Force-output voltage relationship derived from the momentum conservation theorem, (a) solvent-based epoxy: cement = 100:0, and (b) solvent-based epoxy: cement = 100:100 94
Fig. 3-13: Waveforms of sensors packaged with solvent-based epoxy embedded in roadbed

material with a load of 5 kN, (a) 1 cycle, (b) 10,000 cycles, (c) 20,000 cycles, (d) 30,000 cycles, (e) 40,000 cycles, (f) 60,000 cycles, (g) 80,000 cycles, (h) 100,000 cycles 96
Fig. 4-1: Technical framework of study 103
Fig. 4-2: (a) KNN piezoelectric sensors, (b) open-circuit voltage measurement using the oscilloscope 105
Fig. 4-3: Piezoelectric effect of working mode (d_{33}) 106
Fig. 4-4: Components of tire model 107
Fig. 4-5: Components of numerical models: (a) tire-asphalt pavement-KNN sensor model, (b) tire-concrete pavement-KNN sensor model 109
Fig. 4-6: (a) Contour plots of von Mises stress and equivalent elastic strain distributions in the pavement model, (b) local enlargement of the von Mises stress contour plot 111
Fig. 4-7: Open-circuit voltage results of the experiment and the simulation 112
Fig. 4-8: Input variables used for studies 113
Fig. 4-9: Simulation results of the numerical models: (a) schematic of cross-section view, (b) simulation results for the asphalt pavement model, (c) simulation results for the concrete pavement model 115
Fig. 4-10: Contour plots of von Mises stress distribution for different pavements with various horizontal offsets: (a) 0 cm, (b) 4 cm, (c) 8 cm, (d) 12 cm, (e) 16 cm 116
Fig. 4-11: Contour plots of von Mises stress distribution for different pavements with various cambers: (a) -2°, (b) -1°, (c) 0°, (d) 1°, (e) 2° 117
Fig. 4-12: Contour plots of von Mises stress distribution for different pavements with various axle loads: (a) 1.5 kN, (b) 3 kN, (c) 5 kN, (d) 7 kN, (e) 9 kN 118
Fig. 4-13: Contour plots of von Mises stress distribution for different pavements with various speeds: (a) 30 km/h, (b) 50 km/h, (c) 70 km/h, (d) 90 km/h, (e) 110 km/h 119
Fig. 4-14: Contour plots of von Mises stress distribution for different pavements with various decelerations: (a) 10 m/s^2, (b) 15 m/s^2, (c) 20 m/s^2, (d) 25 m/s^2, (e) 30 m/s^2 120
Fig. 4-15: Contour plots of von Mises stress distribution for different pavements with various friction coefficients: (a) 0.1, (b) 0.3, (c) 0.5, (d) 0.7, (e) 0.9 120
Fig. 4-16: Contour plots of von Mises stress distribution for KNN sensor in different pavements with various buried depths: (a) 0 cm, (b) 2 cm, (c) 4 cm, (d) 6 cm, (e) 8 cm 121
Fig. 4-17: Contour plots of von Mises stress distribution for KNN sensor in different pavements with various phase angles: (a) 0°, (b) 15°, (c) 30°, (d) 45°, (e) 60° 122
Fig. 4-18: Contour plots of von Mises stress distribution for KNN sensor in different pavements with various arrangement spacings: (a) 15 cm, (b) 20 cm, (c) 25 cm, (d) 30 cm, (e) 35 cm 122
Fig. 4-19: Contour plots of open-circuit voltage distribution for KNN sensor in different pavements with various buried depths: (a) 0 cm, (b) 2 cm, (c) 4 cm, (d) 6 cm, (e) 8 cm 124
Fig. 4-20: Open-circuit voltage of KNN sensors under various groups of variables, (a) Horizontal, (b) Camber, (c) Alex load, (d) Speed, (e) Deceleration, (f) Friction coefficient, (g) Buried depth, (h) Phase angle, (i) Arrangement spacing 125
Fig. 5-1: Technical framework 135

Fig. 5-2: "Signal missed" situation illustration diagram 136
Fig. 5-3: Physical dimensions of the KNN sensor model 141
Fig. 5-4: FEM of the pavement-tire-sensor interaction system with embedded sensor arrangement 144
Fig. 5-5: Baseline arrangement of 8 embedded sensors for vehicle attenuation functions 147
Fig. 5-6: The effect of sensors embedded in pavement stress response 147
Fig. 5-7: Flowchart for extracting open-circuit voltage of sensors in FEM models 148
Fig. 5-8: Voltage attenuation curves for different vehicle models in summer and winter (FC: family car, LT: light car, BUS: bus, TR: trailer, HT: heavy truck) 149
Fig. 5-9: Comparison of FEM results and ESAM prediction results for peak voltage in (a) summer and (b) winter 151
Fig. 5-10: Signal overlap caused by improper sensor arrangement 152
Fig. 5-11: ESAM software GUI 152
Fig. 5-12: Contour plot of vertical stress and open-circuit voltages distribution with various vehicles, (a) family car, (b) light truck, (c) bus, (d) trailer, and (e) heavy truck 153
Fig. 5-13: The minimum voltage varies with the number of sensors with Uniform Arrangement in a single-lane road (G1) 155
Fig. 5-14: The vehicle type is bus through 7 (a) and 8 (b) sensors on the roadway 156
Fig. 5-15: The minimum voltage varies with the number of sensors with Uniform Arrangement in a single lane (G7) 157
Fig. 5-16: The minimum voltage varies with the number of sensors with the Centrally Weighted Arrangement in a) single-lane (G2) and b) multi-lane (G8) 158
Fig. 5-17: The missing of the bus model when passing over the pavement surface 159
Fig. 5-18: The minimum voltage varies with the number of sensors with the Minimum Coverage Arrangement in (a) single-lane (G3) and (b) multi-lane (G9) 159
Fig. 5-19: The minimum voltage value varies with the number of sensors in a single-lane with various sensor arrangements: in single-lane, (a) Uniform G4, Centrally Weighted G5, and Minimum Coverage G6; in multi-lane, (b) Uniform G10, Centrally Weighted G11, and Minimum Coverage G12 161
Fig. 5-20: Comparison of AC for three arrangement strategies in single-lane: (a) random path G1, G2, G3, and (b) wheel-track-constraint G4, G5, G6, in multi-lane: (c) random path G7, G8, G9, and (d) wheel-track-constraint G10, G11, G12 163

List of Tables

Table 1-1 Representative evaluation criteria for practical applications of lead-free piezoelectric sensors 20
Table 1-2 Critical differences, advantages, and disadvantages of sputtering deposition, sol-gel method, and Laser lift-off 28
Table 1-3 Comparison of traditional piezoelectric sensors and lead-free flexible sensors 30
Table 2-1 Comparative LCA and economic assessment of lead-free and lead-based piezoelectric ceramics 70
Table 3-1 Mix composition of the packaging materials 78
Table 3-2 The force and time of action corresponding to different balls 90
Table 3-3 Vmax and ΔR/Vmax of different falling balls 92
Table 4-1 Material properties of KNN sensor model 106
Table 4-2 Selected tire specifications 107
Table 4-3 Material properties of the tire 107
Table 4-4 Geometrical data and material properties of the asphalt pavement 109
Table 4-5 Geometrical data and material properties of the concrete pavement 110
Table 4-6 Groups of variables. 114
Table 4-7 Pearson correlation coefficients for asphalt and concrete pavements 129
Table 5-1 Identification of the 12 representative sensor arrangement scenarios 140
Table 5-2 Elastic stiffness and piezoelectric stress constants of the material 142
Table 5-3 Parameter values for multi-layer structures in pavement models in summer and winter 143
Table 5-4 Representative vehicle types and parameters 145
Table 5-5 The specific positions of sensor #3 in the FEM model 147
Table 5-6 The minimum number of sensors is required to distinguish between five vehicle types 163
Table 5-7 Recommendation of sensor arrangement for different traffic conditions 164

1. Introduction

1.1. Research Background

Pavement sensing has become an important topic in modern road engineering. As transportation systems grow more complex, roads are no longer viewed only as load-bearing structures. They are expected to provide information. By embedding sensors into pavement layers, engineers can obtain data on vehicle presence, axle loads, and traffic conditions directly from the structure itself. Such information supports traffic monitoring and infrastructure management (Siddiqui et al., 2016; Song et al., 2019). Among the available sensing technologies, piezoelectric sensors are widely used in road applications. They respond quickly to dynamic loading and can operate without an external power supply under traffic excitation. In practice, piezoelectric sensors have been applied for vehicle detection, weight-in-motion systems, and traffic classification. Their feasibility in pavement environments has already been demonstrated.

Most of these systems are based on lead-containing piezoelectric ceramics, especially lead zirconate titanate (PZT) (Horchidan et al., 2016; Shrout and Zhang, 2007). PZT provides high piezoelectric sensitivity and stable performance. For this reason, it has become the conventional choice in pavement sensing. However, the presence of lead raises environmental concerns. Large-scale and long-term deployment of lead-based materials in road infrastructure is increasingly questioned in the context of sustainability and regulatory control. This situation has driven interest in lead-free alternatives (Fadhlina et al., 2022; Rödel et al., 2015).

Potassium sodium niobate (KNN)-based ceramics are considered one of the most promising lead-free piezoelectric materials (Leng et al., 2024). They exhibit relatively high Curie temperatures and good thermal stability, which is advantageous for pavement sensing applications exposed to high summer temperatures. However, compared with conventional PZT ceramics, KNN materials generally exhibit lower intrinsic piezoelectric responses. When used as embedded pavement sensors, this lower response may directly affect the amplitude and detectability of the electrical signals generated under traffic loading. Therefore, replacing PZT

with KNN cannot be regarded as a simple material substitution, but becomes an engineering problem requiring coordinated consideration of material performance, sensor design, and structural integration.

In addition, pavement sensing performance depends on more than the piezoelectric coefficient. Once a sensor is embedded in a real pavement structure, its behavior is influenced by packaging, embedded depth, load transfer mechanisms, traffic conditions, and spatial arrangement. These factors interact. Improving material properties alone does not guarantee reliable sensing performance. Many studies concentrate on material optimization, but fewer address how materials perform after integration into pavement systems.

In this regard, an important challenge is how lead-free piezoelectric materials can be effectively integrated into pavement sensing systems. This involves not only material performance, but also sensor packaging, load transfer, and sensor arrangement under realistic traffic conditions. These aspects will be further discussed in the following literature review.

1.2. A Review on Lead-Free Piezoelectric Ceramic Sensors for Sustainable and Intelligent Applications

1.2.1. Abstract

Lead zirconate titanate (PZT) has long been regarded as the gold standard material for piezoelectric sensors owing to its outstanding piezoelectric performance (d33 = 500-600 pC/N) and well-established industrial scalability. However, its environmental toxicity, limited mechanical flexibility, and instability under extreme conditions make it less suitable for wearable electronics, biomedical implants, and high-temperature sensing. These limitations have spurred intensive efforts to develop lead-free ceramic piezoelectric materials as more sustainable and versatile alternatives. Recent advancements in this field highlight the increasing potential of lead-free systems to rival or even surpass conventional PZT-based devices. This review systematically explores the latest progress in lead-free piezoelectric materials, focusing on two major directions: the formulation of alternative compositions such as potassium sodium niobate (KNN) and bismuth sodium titanate (BNT) that aim to achieve comparable

performance metrics, and the development of intelligent sensing systems that offer enhanced sensitivity, broader operational temperature ranges, and mechanical adaptability. Rather than focusing solely on replacing toxic components, this review proposes a multidimensional evaluation framework that considers piezoelectric coefficients, dielectric properties, and mechanical compliance as equally critical parameters. Moreover, the integration of artificial intelligence (AI) is discussed as an emerging tool to accelerate the discovery and optimization of high-performance lead-free compounds. Looking ahead, the field is anticipated to move toward the realization of intelligent, flexible, and multifunctional sensing platforms for use in self-powered systems, harsh environments, and advanced energy harvesting technologies, signifying a crucial shift toward sustainable piezoelectric device innovation.

1.2.2. Introduction

Over the past few decades, it seems that the lead zirconate titanate (PZT) ceramics have become the established industry standard for piezoelectric materials with broad applications across diverse fields (Panda and Sahoo, 2015). This is primarily attributed to its high piezoelectric coefficient (ranging from 500 to 600 pC/N), which significantly surpasses that of other piezoelectric materials (Shrout and Zhang, 2007). PZT exhibits a relatively high Curie temperature (approximately 300 °C), making it suitable for most daily life application scenarios (Avanish Babu and Madhuri, 2022; Yoo et al., 2017). As a result of these advantages, a mature fabrication route and a well-established industrial supply chain have gradually formed around PZT-based devices (Singh and Mahato, 2025). However, despite its strong performance profile, the use of PZT has been increasingly restricted in engineering practice due to the presence of lead (Pb), which raises environmental and health concerns (Rödel et al., 2015). They also experience significant performance degradation under extreme conditions, particularly in deep-sea exploration, aerospace applications, or flexible electronics (Mo et al., 2025). These limitations have driven growing interest in alternative, environmentally benign materials that could circumvent the drawbacks of PZT while still offering competitive performance.

Driven by the goal of green manufacturing, exploring lead-free piezoelectric materials is burgeoning due to environmental and human health concerns (Xiang et al., 2023). Current research on lead-free materials is primarily focused on two distinct directions. The first one

involves the development of a direct substitution for PZT. This approach aims to explore lead-free piezoelectrical materials, such as potassium sodium niobate (KNN), bismuth sodium titanate (BNT) (Maria Joseph Raj et al., 2021), and polyvinylidene fluoride (PVDF) (Talbourdet et al., 2018), with comparable piezoelectric properties to PZTs (Xiang et al., 2023). While these materials exhibit performance close to or even surpassing PZT in certain aspects, they still face significant engineering limitations and lack extensive practical application experience (Cao et al., 2016; Chen et al., 2022; Khan et al., 2024). The second direction explores lead-free piezoelectric ceramics based on novel mechanisms, such as polarized glassy materials and relaxor ferroelectric materials (Lang et al., 2024). These efforts aim to develop piezoelectric sensors with higher sensitivity and broader operational temperature ranges. However, this approach substantially increases both engineering application costs and research expenditures. Most importantly, lead-free piezoelectric materials are not only driven by environmental sustainability but also hold the potential to revolutionize the performance of piezoelectric sensors. For instance, self-powered piezoelectric sensors based on piezoelectric nanogenerators can enable battery-free detection (M. He et al., 2021). Sensors fabricated from high-temperature-stable materials, such as bismuth sodium potasium (BNK)/BNT system, are suitable for extreme environments like aerospace and nuclear energy (Ji et al., 2019). Flexible KNN-PVDF thin films are ideal for wearable devices and electronic skin applications (Deng et al., 2025). With the rapid development of piezoelectric ceramics, their functions have expanded from a simple force-electricity conversion (Khanna et al., 2004; Lee and Esashi, 2004) to self-adaptive, self-regulating, and increasingly capable of on-board data processing for real-time decision-making (Kairui Chen et al., 2024; Firoozi et al., 2024; Ma et al., 2023; Zuo et al., 2025). Thus, lead-free piezoelectric ceramics are not merely substitutes for PZT but also represent a new frontier in the era of intelligent globalization.

Although a myriad of reviews have summarized the lead-free piezoelectric ceramics from a material's point of view, it is still imperative to give an intensive analysis of challenges from the application perspective after the materials have been developed. This study compacts the physical mechanisms, fabrication technologies, and optimization strategies of the updated promising lead-free piezoelectric devices in practical applications (Fig. 1-1). Furthermore, insights into the future trends of lead-free ceramic piezoelectric sensors in terms of intelligence,

flexibility, and multifunctionality are presented. By redefining the "high-performance" of piezoelectric materials from a multidimensional perspective, this work not only emphasizes piezoelectric coefficients but also considers dielectric responses, flexibility compatibility, and adaptability with exposure to aggressive environments. This article broadens the evaluation of lead-free piezoelectric ceramics from an engineering application standpoint and deepens the development of their practical application value. Last but not least, this review integrates the contents of AI and materials, summarizing the feasibility of using machine learning to boost the discovery of next-generation lead-free piezoelectric materials. By establishing the inverse design for hierarchically tailored microstructures guided by AI-driven material selection frameworks, a closed-loop optimization strategy integrating targeted defect engineering with performance-driven property modulation can be generalized. This computational-experimental nexus is rigorously applied to decode the untapped potential of lead-free ceramics within intelligent piezoelectric sensor architectures, particularly emphasizing their adaptive response mechanisms under dynamically coupled electromechanical stimuli. Crucially, the research introduces an intelligent manufacturing paradigm enabling AI-embedded lead-free piezoceramic transducers to achieve cognitive sensing functionalities, featuring embedded signal preconditioning algorithms and self-optimizing wireless telemetry modules that fundamentally redefine edge computing capabilities in distributed sensor networks.

The structure of this article is composed of five parts. The first part presents a general overview of the physical mechanisms, manufacturing methods, and performance optimization strategies of lead-free piezoelectric materials, along with their latest advancements as key technologies in intelligent sensing and energy harvesting applications. The second part establishes a multidimensional sustainability-performance matrix evaluating lead-free systems through biocompatibility, environmental stability, flexibility and wearability, intelligence, and self-power. The third part decodes design evolution trajectories via three synergistic lenses-innovative manufacturing techniques, form transformation, and heterogeneous structural engineering. The fourth part strategically maps the convergence frontier between adaptive intelligence platforms and cross-domain energy transduction ecosystems. The discourse culminates in the fifth part with a foresight analysis identifying emergent research vectors spanning the design of tailored lead-free piezoelectric ceramics and advances in the integration

of intelligent sensing systems, charting transformative opportunities beyond conventional piezoelectric design orthodoxy.

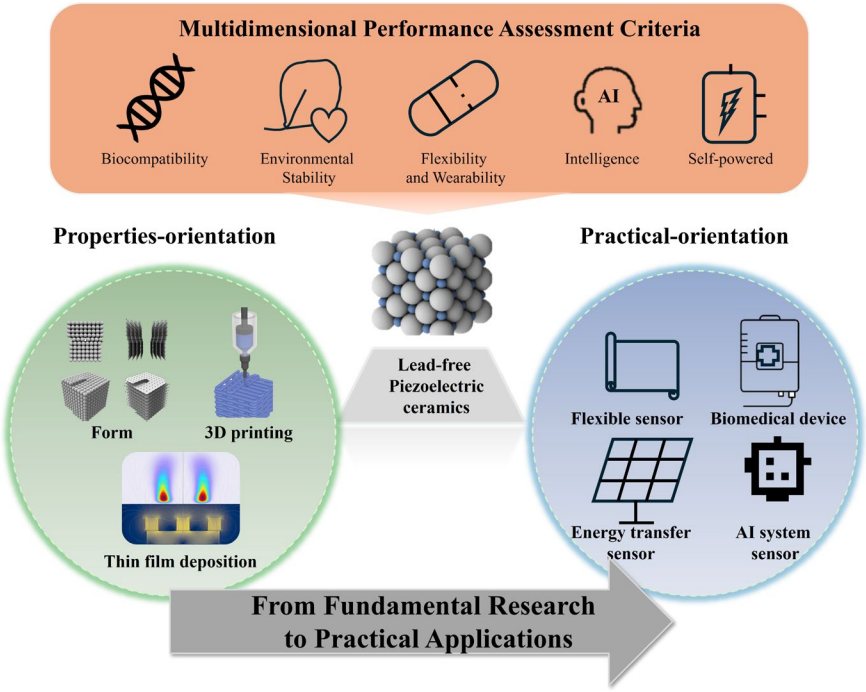


Fig. 1-1: Bridging fundamental material research and application in lead-free piezoelectric ceramics

1.2.3. Classification of Lead-free Piezoelectric Ceramics and Doping Strategies

In recent years, lead-free piezoelectric ceramics have received considerable attention as environmentally benign substitutes for conventional lead-based materials, particularly $Pb(Zr/Ti)O_3$ (PZT) (Takenaka and Nagata, 2005). Intensive experimental studies have led to the establishment of several representative lead-free systems, among which $BaTiO_3$-based, $(K/Na)NbO_3$-based, and $Bi_{0.5}Na_{0.5}TiO_3$-based compositions are the most extensively investigated (Huang et al., 2024; Nie et al., 2025; Panda and Sahoo, 2015; Sayagués et al., 2024). These systems exhibit distinctive crystallographic features, Curie temperatures, and electromechanical responses, reflecting their diverse structural origins (Pinheiro and Deivarajan, 2019). The $BaTiO_3$-based family, characterized by a classical perovskite framework, has been revisited in recent years owing to its simple composition and strong ferroelectric behavior. By tailoring its composition through aliovalent ion substitution, Ca^{2+} at the A-site and Zr^{4+} at the B-site, the $(Ba/Ca)(Zr/Ti)O_3$ (BCZT) solid solution can form a morphotropic or polymorphic phase boundary between tetragonal, orthorhombic, and rhombohedral phases (Rahman et al., 2023). The coexistence of these phases enhances polarization rotation under electric fields,

resulting in large piezoelectric coefficients (typically d_{33} of 500 pC/N). Despite these advantages, the relatively low Curie temperature of $BaTiO_3$-based ceramics (120 °C) remains a major limitation for high-temperature applications (Acosta et al., 2017; Lang et al., 2024). Current laboratory research focuses on compositional engineering and microstructural optimization to extend their operational stability and thermal endurance.

(K/Na)NbO_3-based (KNN) system exhibits a much higher Curie temperature (~400 °C) and strong ferroelectricity, making it one of the most promising candidates for high-temperature and high-power applications (Yang and Hao, 2019). However, the leaching of alkali elements and the narrow sintering window make it challenging to process. Doping plays a key role in addressing these issues. A-site substitutions with Li^+, Ba^{2+}, or Bi^{3+} improve densification and phase stability, while B-site doping with Ta^{5+}, Sb^{5+}, or Mn^{2+} can tune the orthorhombic-tetragonal phase transition and enhance domain mobility (H. Wang et al., 2024). Multi-element co-doping has been shown to induce broad phase boundaries analogous to the MPB in PZT, resulting in enhanced piezoelectric coefficients (d_{33} > 400 pC/N) and good thermal reliability.

The $Bi_{0.5}Na_{0.5}TiO_3$-based (BNT) system represents another important class of lead-free materials. BNT ceramics show high remnant polarization and strong electric-field-induced phase transitions, along with a moderate Curie temperature (~320 °C). However, pure BNT suffers from high coercive fields and dielectric losses (H. Liu et al., 2024; Jinyan Zhao et al., 2025). To overcome these drawbacks, researchers have developed several solid solutions, such as BNT-$BaTiO_3$ (BNT-BT), BNT-(K/Na)NbO_3 (BNT-KNN), and BNT-$Bi_{0.5}Na_{0.5}TiO_3$ (BNT-BKT) (Hu et al., 2020; Singh et al., 2021; Jinyan Zhao et al., 2025). These compositions exhibit large strain responses, reduced dielectric loss, and improved ferroelectric fatigue resistance, making them suitable for actuators and energy-harvesting applications.

Piezoelectric performance enhancement in lead-free ceramics can be broadly attributed to intrinsic and extrinsic mechanisms. Intrinsic mechanisms are associated with changes in the crystal lattice and polarization behavior, including lattice distortion, phase boundary engineering, and polarization rotation. These effects directly modify the fundamental electromechanical coupling and are generally reflected in the small-signal piezoelectric response. Extrinsic mechanisms arise from microstructural contributions such as domain wall motion, defect dipoles, internal stress fields, and grain boundary effects. These mechanisms

contribute to field-dependent responses and play a critical role in large-signal actuation, hysteresis behavior, and fatigue performance. While intrinsic mechanisms determine the upper limit of piezoelectric activity, extrinsic contributions strongly influence stability and reliability under practical operating conditions. Therefore, an effective performance optimization strategy requires a balanced consideration of both intrinsic and extrinsic effects.

Most of the current studies on doping in lead-free piezoelectric ceramics are predominantly laboratory-based and primarily oriented toward enhancing intrinsic electrical properties such as piezoelectric coefficients, dielectric constants, and polarization behavior. While these efforts have significantly advanced the understanding of structure-property relationships and have yielded materials with impressive electromechanical performance at the laboratory scale, their engineering feasibility remains largely unexplored. In many cases, the reported improvements rely on complex or high-cost dopants, narrow compositional windows, or sophisticated sintering conditions that are difficult to replicate in industrial environments. Moreover, only a few studies have systematically evaluated key practical factors such as sintering temperature compatibility, production cost, long-term reliability, or environmental stability under real working conditions. As a result, most laboratory findings, though scientifically valuable, remain distant from large-scale or commercial applications. Bridging this gap requires not only continued efforts in performance optimization but also greater attention to process simplicity, cost-effectiveness, and manufacturability, which are essential for the practical deployment of lead-free piezoelectric ceramics.

1.2.4. Multidimensional Performance Assessment Criteria

The performance evaluation of piezoelectric materials is typically quantified using parameters such as piezoelectric coefficients, dielectric constants, electromechanical coupling factors, dielectric loss factors, and Curie temperature. These metrics are meaningful for comparing the piezoelectric properties of ceramics. However, when piezoelectric ceramics are fabricated into sensors for applications, these indicators often appear limited and insufficient. Therefore, it is imperative to redefine high-performance piezoelectric ceramics in terms of sensors from a multidimensional perspective. Beyond the traditional material performance metrics, additional evaluation criteria such as biocompatibility, environmental stability,

flexibility and wearability, intelligence, and self-powered must be incorporated to align with the advancements in modernized sensing technologies. This comprehensive approach ensures that piezoelectric materials meet the evolving demands of modern applications.

1.2.4.1. Conventional Evaluation Standards

The performance of piezoelectric materials is traditionally evaluated using four key parameters: piezoelectric coefficients, dielectric constants (including dielectric loss), electromechanical coupling coefficients, and operational parameters (Curie temperature) (Fadhlina et al., 2022). Piezoelectric coefficients represent the conversion efficiency between mechanical energy and electrical energy, reflecting the coupling relationship between the elastic (mechanical) and dielectric properties of piezoelectric materials (Zeng et al., 2025). These coefficients are typically expressed as d_{31} (where the polarization direction is perpendicular to the applied force) (Y. Sun et al., 2023) and d_{33} (where the polarization direction aligns with the applied force) (Yang et al., 2024). Higher values indicate stronger piezoelectric effects. For instance, conventional PZT ceramics exhibit a d_{33} value of 500-600 pC/N, while lead-free KNN-based ceramics generally achieve around 300 pC/N (pure KNN ceramic: 80~120 pC/N), highlighting the challenge of achieving high piezoelectric performance in lead-free systems (Panda and Sahoo, 2015).

Dielectric constants characterize the dielectric or polarization properties of materials, often used to evaluate energy storage capabilities in energy harvesting applications. These constants are influenced by material composition, operating frequency, environmental temperature, humidity, load magnitude, and duration (Ji et al., 2025). Dielectric loss is typically considered alongside dielectric constants for a comprehensive assessment (P. Wang et al., 2025).

Electromechanical coupling coefficients quantify the efficiency of mechanical-to-electrical energy conversion. PZT ceramics can achieve values up to 0.7, whereas KNN and BNT ceramics typically range between 0.3 and 0.5 (Zeng et al., 2025). Among operational parameters, the Curie temperature is particularly critical, as it indicates the phase transition temperature of the material. Higher Curie temperatures generally correlate with better stability in high-temperature environments. For example, KNN-based ceramics can reach Curie temperatures of up to 400 °C, and BNT-based ceramics up to 500 °C, both surpassing PZT's Curie temperature of approximately 300 °C (Shi et al., 2020).

While these parameters are essential for evaluating piezoelectric ceramics, they do not fully represent the material's performance in sensor applications. The operational efficacy of piezoelectric sensors is inherently governed by complex environmental synergies, where superior quasi-static electromechanical outputs may become secondary to dynamic stability in extreme multiphysics environments. A paradigmatic example emerges in high-temperature sensing applications: the capacity to detect signals stably at elevated temperatures assumes greater significance in comparison to the sensor's large signal output due to the occurrence of substantial strains (Shen et al., 2025). Therefore, it is necessary to introduce a multidimensional set of criteria to redefine high-performance piezoelectric ceramics, ensuring their evaluation aligns more closely with practical conditions. This framework will enable a physics-informed redesign of piezoceramics, bridging the critical gap between idealized material metrics and in-situ operational demands. This systems-level approach not only redefines "high performance" through application-adaptive criteria but also catalyzes the transition from laboratory-scale property optimization to field-deployable piezoelectric solutions.

1.2.4.2. Multidimensional Assessment Criteria

From the perspective of the piezoelectric ceramic field, a multidimensional evaluation system building upon traditional performance assessment frameworks has been proposed to enhance the applicability of materials. This approach aims to address the limitations of conventional metrics by incorporating additional criteria that reflect real-world operational demands, thereby ensuring that piezoelectric ceramics are better suited for practical applications.

1.2.4.2.1. Biocompatibility

The utilization of environmentally friendly sensing materials with low or even no toxicity is imperative for applications necessitating long-term development. The employment of degradable materials or eco-friendly low-carbon manufacturing processes is strongly recommended for future piezoelectric sensors to minimize the environmental impact of electronic waste.

The cellulose-based sensor fabricated through the integration of conductive polypyrrole (PPy), chitosan (CS), phytic acid (PA), and Lycra textile (LC) exhibits shape-adaptive

electromechanical response, generating an open-circuit voltage of 0.3 V under 2 N compressive loading. This eco-designed system achieves complete biodegradation within 120 days under soil burial conditions, demonstrating an environmentally neutral lifecycle (Yu et al., 2024). Parallel advancements utilize waste-cotton-derived microcrystalline cellulose (MCC) particulates to develop film-type sensors capable of powering low-energy microelectronics through self-sustained operation, establishing a circular materials paradigm for green sensor technologies (Graham et al., 2019).

Biosensors are typically non-toxic and environmentally friendly. Pioneering work by Weber (Weber et al., 2010) demonstrated the cytocompatibility of electrospun P(VDF-TrFE) fibrous scaffolds through comprehensive in vivo/in vitro evaluations, establishing their potential as piezoelectric tissue engineering matrices. Contemporary studies reveal that macromolecular conformational dynamics within cellular matrices can induce dipole realignment in ferroelectric polymers, thereby enhancing therapeutic efficacy through intrinsic electromechanical coupling mechanisms (Badaraev et al., 2020; Venault et al., 2020). Barium titanate (BTO) is a widely used biomedical implantable sensor that can be stabilized in vivo for a long period of time. Li (Y. Li et al., 2017) fabricated electroactive poly(l-lactic acid) (PLLA) fibrous scaffolds via electrospinning, incorporating ferroelectric barium titanate ceramic nanoparticles to engineer a piezoelectrically enhanced microenvironment. Systematic in vitro evaluations revealed that the BTO-induced surface charge polarization significantly promoted osteogenic differentiation of mesenchymal stem cells (MSCs). Gel-cast $BaTiO_3$/P(VDF-TrFE) nanocomposite membranes generate surface potentials approximating physiological ranges (76.8 mV), effectively mimicking native bioelectrical microenvironments (Zhang et al., 2016). These polarized systems promote osteogenic differentiation of bone marrow mesenchymal stem cells (BMSCs) in vitro and enhance critical-sized bone defect regeneration in vivo through sustained electromechanical stimulation. This electromechanical coupling mechanism facilitates extracellular matrix remodeling while maintaining mechanical compliance comparable to host tissues.

1.2.4.2.2. Environmental Stability

High-performance piezoelectric sensors are required not only in general social

environments but also under extreme service conditions such as elevated temperatures (J. Li et al., 2025), cryogenic conditions (Kunimatsu, 2001), and high-pressure scenarios (Tadaki et al., 2020). Conventional PZT ceramics exhibit significant performance degradation due to their inherent limitations in Curie temperature (typically <300 °C) (Xin et al., 2023), making them unsuitable for critical applications in aerospace engineering, deep-sea exploration, and mining operations. This technological gap has driven the development of novel piezoelectric materials with enhanced environmental stability.

The approaches to enhance thermal stability involve compositional engineering of lead-free piezoelectric ceramics. Strategic substitution of Pb with Bi in $BiScO_3$-$PbTiO_3$ systems significantly elevates Curie temperatures while maintaining piezoelectric performance. The optimized ceramic demonstrates stable sensitivity exceeding 4 V/N across wide operational ranges (60-200 °C, 10-40 Hz). It is worth noting that its quasi-linear pressure-voltage response (0.07-0.55 N) under elevated temperatures (160-260 °C) retains sensitivity above 5.4 V/N at 220 °C. These characteristics position this material as a promising candidate for high-temperature pressure/vibration sensing applications (Xin et al., 2023). A similar approach has been taken by replacing Na with Li (Sharma and Kumar, 2024; Yang et al., 2023), which also ensures that the material is stable at high temperatures. $BiFeO_3$-$BaTiO_3$ (BF-BT) piezoceramics have garnered significant research interest for high-temperature piezoelectric accelerometers due to their elevated Curie temperatures (>500 °C) and moderate piezoelectric coefficients (d_{33} ~200-300 pC/N). However, their practical deployment is hindered by temperature-dependent performance degradation caused by depolarization-induced domain wall mobility and oxygen vacancy aggregation under thermal cycling (Xun et al., 2019). To address these stability limitations, a ternary doping strategy incorporating $(Ba_{0.85}Ca_{0.15})(Zr_{0.10}Ti_{0.90})O_3$ (BCZT) as a phase-stabilizing agent has been developed (Xinran Wang et al., 2025). The engineered 0.7BF-0.3BT-1 wt.%BCZT composite exhibits unprecedented thermomechanical stability, with <5% variation in charge sensitivity across 25-450 °C, a critical improvement over baseline BF-BT systems. It is shown that acceleration sensors made from this ceramic exhibit excellent signal sensitivity over a wide temperature range, which is promising for high-temperature and high-speed friction applications such as in the aerospace industry.

The templated grain growth (TGG) technique provides a crystallographic engineering pathway to simultaneously address piezoelectric performance and environmental stability bottlenecks in lead-free ceramics (Moriana and Zhang, 2018). As demonstrated in Fig. 1-2, <001>-textured $0.75BiFeO_3$-$0.25BaTiO_3$ ceramics synthesized via TGG exhibit superior environmental stability, retaining >92% of initial piezoelectricity (d_{33} = 265 pC/N) after repeated thermal cycles (25-300 °C) (Shen et al., 2025). Notably, the material maintains piezoelectric functionality beyond 450 °C, a critical threshold where conventional perovskite ferroelectrics (e.g., PZT, BNT-based systems) undergo irreversible phase decomposition accompanied by >80% piezoelectric loss. This work establishes texture engineering as a universal paradigm to reconcile piezoelectricity-environmental stability trade-offs, particularly for sensors requiring long-term reliability in extreme thermal/chemical operational envelopes. Textured processing can effectively enhance the piezoelectric performance of lead-free ceramics such as KNN (Li et al., 2018) and BNT-BT (Moriana and Zhang, 2018), while maintaining their Curie temperature (T_C) and piezoelectric thermal stability, making them suitable for extreme environment applications.

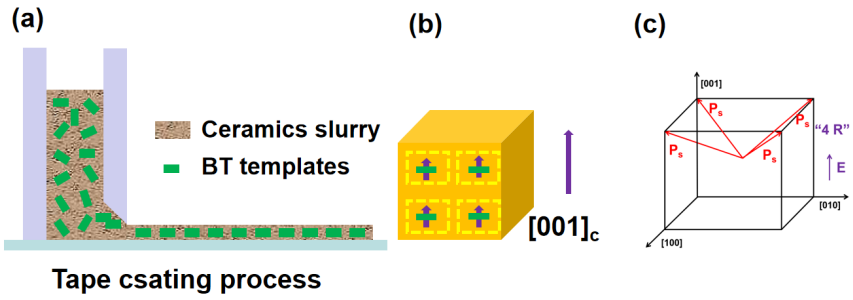


Fig. 1-2: (a) Diagram of a typical tape casting process, (b) texturing mechanism schematics of the TGG method, and (c) engineered domain structure of <001>-textured ceramics with R phase after poling treatment (Shen et al., 2025)

Beyond high-temperature performance degradation, the operational viability of piezoceramics in biomedical implants is critically challenged by low-temperature sterilization-induced functional deterioration. Magnus investigated the performance of various ceramics using low-temperature plasma sterilization and associated cleaning procedures to determine the feasibility of preparing ceramics for implantable sensors after low-temperature sterilization (Rotan et al., 2021). Comparative analysis of PZT, BCZT, and KNN ceramics exposed to cyclic low-temperature hydrogen peroxide gas plasma treatment demonstrates stark divergence in

piezoelectric properties. Post-sterilization crystallographic analysis confirms KNN's superior phase stability (rhombohedral-tetragonal coexistence preserved vs. BCZT's cubic phase transition) and oxygen vacancy suppression capability. These findings validate KNN as a lead-free alternative to PZT for implantable sensors requiring combined biocompatibility and electromechanical reliability under sterilization duress, particularly in deep-brain stimulation electrodes and orthopedic load monitoring systems. The sensor signal output in high-humidity environments (Trung et al., 2024; Wang and Wang, 2019) and the highly sensitive signal variations in low-pressure conditions (H. Zhou et al., 2020) also require careful attention. The barium titanate (BTO)-based piezoelectric sensor, as illustrated in Fig. 1-3, demonstrates exceptional electromechanical transduction efficiency under dynamic liquid-solid interactions (Dinh Trung et al., 2024). When subjected to microfluidic droplet impacts (40 μL water droplet, 5 Hz frequency), the device generates a peak output voltage of 1.86 V within a 60-second operational window, accompanied by a pressure sensitivity of 0.098 kPa^{-1} in the ultralow-pressure regime (0-8.2 kPa).

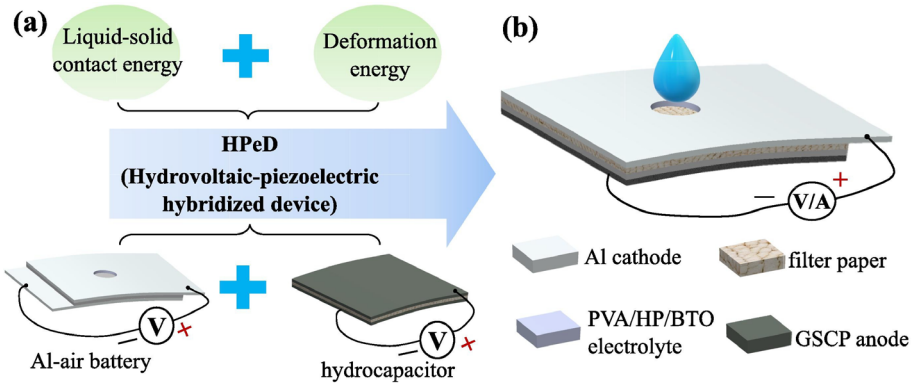


Fig. 1-3: (a) Design strategy of the HpeD, (b) Schematic representation of the sensing system (Dinh Trung et al., 2024)

These synergistic material innovation strategies establish novel design paradigms for developing piezoelectric sensors with enhanced environmental stability and operational adaptability through crystallographically-guided substitution approaches.

1.2.4.2.3. Wearability

While PZT ceramics remain the material of choice for conventional transducer applications due to their superior piezoelectric coefficients, their inherent limitations in mechanical compatibility (Young's modulus >60 GPa) and Pb-containing composition present critical

challenges for emerging flexible/wearable sensor technologies. This technological gap has driven material innovation strategies focused on lead-free piezoelectric thin films (e.g., KNN-based systems) and polymer-based composites (PVDF/$BaTiO_3$), which combine enhanced flexibility (bending radius <5 mm) with eco-compatibility - essential characteristics for epidermal electronics and textile-integrated sensing applications.

The development of high-performance wearable sensing systems necessitates simultaneous optimization of comfort, flexibility, and dynamic response characteristics (see Fig. 1-4) (Y. Chen et al., 2024; H. Zhou et al., 2020). Although P(VDF-TrFE) and $BaTiO_3$ have opposite piezoelectric properties, their composites enable the fabrication of high-performance piezoelectric devices (Kalyani et al., 2014; Zhang et al., 2006). The size, distribution, and crystalline phase of the $BaTiO_3$ fillers play a critical role in enhancing the piezoelectric and mechanical properties of the composite (Yan et al., 2022). Incorporating 10 wt.% of cubic and tetragonal $BaTiO_3$ particles into P(VDF-TrFE) films improves flexibility for wearable applications (Taleb et al., 2023), while significantly increasing the piezoelectric voltage coefficient (from 158 to 205 mV-m/N) and polarization value (from 4.23 to 6.18 $\mu C/cm^2$) compared to pure P(VDF-TrFE). Bending experiments on human fingers under three different conditions further demonstrate that the composite sensor achieves a 2-fold increase in output voltage and a 4.6-fold increase in output power compared to the pure P(VDF-TrFE) sensor. This material, which fulfils the requirements of practicality and higher piezoelectric properties, is a research trend for flexible wearable sensing devices (Guan et al., 2020).

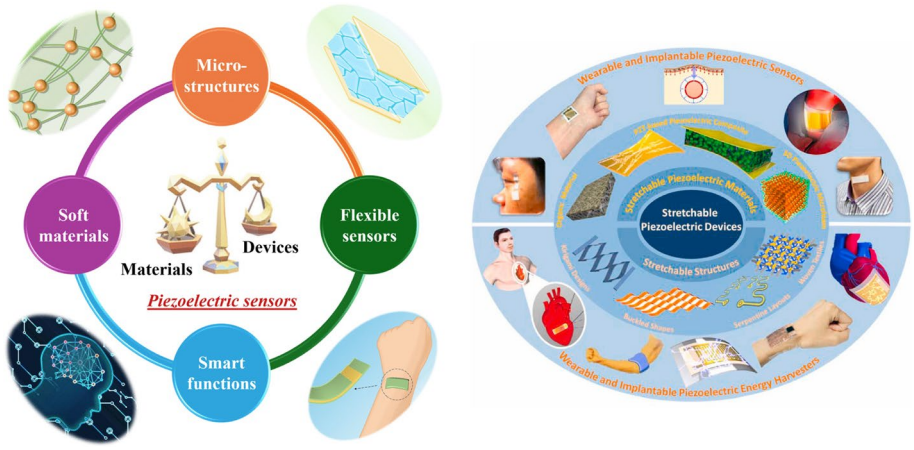


Fig. 1-4: Schematic representation of the advancement of wearable piezoelectric sensors (Y. Chen et al., 2024; H. Zhou et al., 2020)

The fabrication of composite piezoelectric ceramic materials does not necessitate compromised signal output, as demonstrated by rationally designed flexible sensors that maintain high electromechanical conversion efficiency (Jie Zhang et al., 2025). Through optimized structural engineering, including interfacial charge transport enhancement and strain distribution modulation, flexible composites achieve substantial signal generation while fulfilling application-specific mechanical requirements. This dual capability enables precise physiological monitoring and reliable data acquisition, overcoming the traditional limitations of rigid piezoelectric devices in wearable applications, effectively decoupling the sensitivity-durability trade-off inherent in conventional designs.

1.2.4.2.4. Self-power

Externally powered sensing systems are fundamentally constrained by their energy dependency, which manifests as a cascade of technological limitations (Zheng et al., 2022). The necessity for hardwired electrical connections introduces infrastructural complexity, significantly escalating installation costs and spatial constraints. Such architectures exhibit critical vulnerabilities in remote or extreme operational environments due to unreliable power provisioning, while their reliance on finite energy budgets inherently compromises long-term operational autonomy. Furthermore, the recurring maintenance demands for battery replacement and power infrastructure upkeep impose prohibitive lifecycle costs, particularly in large-scale deployments where centralized energy management systems struggle to maintain scalable reconfigurability (Yao et al., 2020). These intrinsic limitations severely diminish their viability in distributed sensing networks, unmanned monitoring platforms, and embedded industrial IoT ecosystems (Bhatta et al., 2024), ultimately failing to meet the rigorous demands of sustainable smart infrastructure (H. He et al., 2025).

Self-powered sensing systems present a transformative alternative to conventional battery-dependent devices by harvesting ambient energy through mechanical, thermal, and photonic transduction mechanisms (M. Zhang et al., 2025). This energy-autonomous operation eliminates reliance on external power sources, significantly enhancing operational longevity and sustainability while reducing maintenance requirements (X. Liang et al., 2024; Qixiang Zhang et al., 2023). The integration of lead-free piezoelectric ceramics with nanogenerator

technologies has emerged as a strategic approach for developing hybrid energy harvesting platforms. These systems synergistically combine the environmental stability of ceramic components with the flexibility of polymeric nanogenerators, enabling efficient energy conversion across diverse mechanical excitation frequencies. Recent advancements in self-powered sensing demonstrate targeted applications through synergistic integration of energy harvesting mechanisms and domain-specific detection requirements. Shu's wireless photometric system (Shu et al., 2025) enables precision agriculture by quantifying residual plant nutrients via piezoelectric microcantilever-based weight analysis, while Zheng's triboelectric nanogenerator (TENG)-machine learning hybrid achieves 81.06% accuracy in vehicle classification through road vibration signature decoding (Zheng et al., 2022). Concurrently, TENG-AlGaN/GaN HEMT configurations exemplify sustainable aquatic monitoring by coupling hydrodynamic energy scavenging with electrochemical pollutant detection, particularly effective in turbulent environments (Sharma et al., 2025).

The integration of self-powered sensors with advanced textile technologies enables biomimetic sensing architectures for medical monitoring applications, including dynamic gesture recognition and joint mobility tracking in patients with neuromuscular disorders such as hand spasticity (Dong et al., 2020; Mi et al., 2024). These textile-based systems also demonstrate capabilities in continuous physiological signal acquisition for personalized healthcare diagnostics (M. He et al., 2021). By combining energy autonomy with textile conformability, such sensor platforms show significant potential for long-term clinical monitoring and adaptive human-machine interaction systems without requiring external power sources (Bhatnagar et al., 2023).

The optimization of energy conversion efficiency in self-powered sensors remains a critical research focus, particularly through advanced structural design. Anwer (Anwer et al., 2024) developed a superstructure triboelectric nanogenerator (TENG) utilizing a multilayer $Ti_3C_2T_x$ MXene/Kapton composite as the tribonegative electrode and MXene-seeded TiO_2 superstructures embedded in a polyvinyl alcohol (PVA) matrix as the tribopositive electrode. This configuration achieves an open-circuit voltage of 120 V and a power density of 5.66 W/m^2, demonstrating significant advancements in energy harvesting efficiency through tailored

material interfaces and hierarchical architecture. The output performance of TENG can also be significantly enhanced through synergistic optimization strategies encompassing physical interface engineering, chemical surface functionalization, and charge density amplification mechanisms (Lone et al., 2022; Pongampai et al., 2021).

1.2.4.2.5. Autonomous Intelligence

For sensor applications in specialized environments, the ability to provide real-time feedback and information transmission is often essential, necessitating the development of autonomous operation and computational capabilities. On one hand, computational materials science can be leveraged to optimize material selection, enhancing performance tailored to specific requirements. On the other hand, integrating machine learning techniques, particularly neural network-based computations, can unlock advanced functionalities such as autonomous decision-making and adaptive sensing. This dual approach not only improves material performance but also enables intelligent, self-regulating systems capable of meeting the demands of complex and dynamic operational conditions.

The application of machine learning (ML) in materials science is gaining increasing attention, particularly for its significant potential in optimizing material parameters to enhance performance. Rocha employed ML techniques to develop a data-driven model, utilizing extensive dielectric measurement datasets of $(1-x)Na_{0.5}Bi_{0.5}TiO_3$-$xCaTiO_3$ to train the ML model for predicting dielectric constants (ε′) and dielectric loss (tan δ). This approach also enabled the analysis of environmental factors, such as temperature and Ca content, on the electrical properties of $(1-x)Na_{0.5}Bi_{0.5}TiO_3$-$xCaTiO_3$ piezoelectric ceramics. Through this methodology, optimal experimental conditions were identified within the dataset, demonstrating the effectiveness of ML in guiding material design and performance optimization (Rocha et al., 2024). Significant progress has also been made in the model-based prediction of piezoelectric properties for ceramics (J. He et al., 2021; Ma et al., 2023; Yuan et al., 2019). However, predicting high-performance compositions using ML models remains challenging, as experimental validation is often required to confirm their accuracy (Gu et al., 2023). In existing research, it has been demonstrated that piezoelectric coefficients can be predicted based on a set of elemental and atomic characteristics. Hu used feature engineering techniques to extract

representative descriptors, including relative molecular mass (W), ionic displacement (D), electronegativity (EN-P), electron affinity (EA), and Curie temperature (Tc). These features were used to statistically describe the d_{33} values of samples within a database. By utilizing the extracted features as inputs and conducting three iterative experiments, the optimal composition for KNN-based lead-free piezoelectric ceramics was successfully identified (Hu et al., 2024). The diversity in piezoelectric mechanisms across different types of ceramics leads to inconsistencies in model generalization, limiting the universal applicability of these predictive frameworks (Ma et al., 2023; Yuan et al., 2019). This highlights the need for further refinement of ML approaches to address the unique characteristics and complexities inherent in various piezoelectric systems.

The integration of piezoelectric ceramic sensors with machine learning-driven time-frequency eigenfeature analysis heralds a paradigm shift toward intelligent detection systems, replacing labor-intensive manual operations. Li et al. developed a system for evaluating the cleanliness of corn kernels based on piezoelectric signals that accurately distinguishes corn kernels from impurities (Y. Li et al., 2024). The study utilized a vibrating piezoelectric detection device to capture the time-domain response signals of grains and impurities, thereby establishing a database of corn collision signals. The absolute error of grain loss rate can be controlled within 0.43% by signal characterization, thus enabling the reliable classification of grain and impurities. The integration of piezoelectric sensing with machine learning algorithms has catalyzed a paradigm shift toward intelligent agricultural sorting systems, extending far beyond traditional signal threshold detection (Dong et al., 2025). By leveraging the intrinsic mechanoelectric coupling properties of piezoceramics, advanced signal processing frameworks now decode crop-specific vibrational fingerprints through multiscale time-frequency analysis. This approach enables precise classification of rice, rapeseed, and other crops without optical or chemical interventions (D. Li et al., 2022; J. Li et al., 2022; Xu et al., 2019).

The transition toward intelligent piezoelectric sensing systems epitomizes an irreversible technological evolution, driven by the convergence of advanced material engineering, adaptive signal processing, and embedded artificial intelligence (AI). By synergizing defect-modulated piezoceramics with machine learning-driven feature extraction frameworks, these systems

transcend conventional threshold-based detection to achieve context-aware mechanoelectronic phenotyping capability critical for applications ranging from extreme-environment industrial monitoring to precision agriculture.

1.2.4.2.6. Performance Criteria for Typical Applications

While the multidimensional criteria discussed above describe the key performance aspects of lead-free piezoelectric sensors, they are often insufficient on their own to judge practical applicability. In real devices, materials are exposed to synergistic thermal, mechanical, and electrical conditions that are not fully captured by single-parameter characterization. Therefore, it is necessary to combine these criteria with application-specific requirements. Representative requirements are introduced for several typical application scenarios. These benchmarks are intended to provide practical reference points rather than strict pass–fail standards. They are used to indicate whether a given material system is likely to meet the basic demands of a specific application, such as high-temperature operation or long-term sensing stability. Table 1-1 summarizes commonly reported benchmark ranges for different application scenarios.

Table 1-1 Representative evaluation criteria for practical applications of lead-free piezoelectric sensors

Application	Key performance aspect	Typical values
High-temperature sensing	Thermal stability	Curie temperature is typically above 300 °C; and d_{33} retention is around 70-90% at elevated temperature (Habib et al., 2022; Shi et al., 2020; Xin et al., 2023; M.-H. Zhang et al., 2017)
Energy harvesting	Electrical output and loss	Eielectric loss generally below 0.03 (Ziyan Gao et al., 2024; Lu et al., 2024; Osinaga et al., 2024; Talbourdet et al., 2018; Xing et al., 2021; Zhang et al., 2015)
Wearable sensing	Mechanical flexibility	Stable signal output under 1-2% tensile strain (Bhatnagar et al., 2023; Dai et al., 2023; Ziyan Gao et al., 2024; Ray et al., 2019; Wu et al., 2021)
Long-term operation	Reproducibility and stability	Stable response under continuous loading (Hu et al., 2020; Ji et al., 2025; Yang et al., 2023)

The values are based on representative literature data and typical device considerations. Although exact requirements may be different with various device designs and operating conditions, these benchmarks help narrow the gap between laboratory-scale material evaluation and real device performance.

1.2.4.3. Functionalization via Autonomous Intelligence

While multidimensional evaluation frameworks spanning biocompatibility, environmental robustness, mechanical flexibility, and self-powering capability have broadened the criteria for assessing piezoelectric devices, they largely remain focused on isolated component-level performance. However, as applications increasingly shift toward distributed, adaptive, and autonomous platforms, evaluation must move beyond traditional property-centric approaches. This shift requires transitioning from performance-driven material optimization to system-level functional integration. In this context, lead-free piezoelectric ceramics are no longer expected only to exhibit strong intrinsic electromechanical responses but also to interact effectively with algorithmic control systems, dynamic environments, and multimodal external stimuli (Siddiqui et al., 2016). This section explores how these materials are evolving toward more comprehensive roles within intelligent and responsive systems, focusing on emerging strategies such as structural programmability, embedded computation, and adaptive behavior (Safaei et al., 2019).

The role of lead-free piezoelectric ceramics is being fundamentally redefined. Rather than serving only as substitutes for lead-based materials like PZT, they are increasingly regarded as integral components within intelligent, self-regulating, and energy-autonomous systems. This shift reflects a broader evolution in material science, where design is no longer centered solely on intrinsic properties such as piezoelectric coefficients or Curie temperature, but instead guided by interdisciplinary integration across materials science, embedded computation, and system-level engineering.

Recent advances emphasize the need for structural programmability across multiple scales, enabling materials to adapt their internal configurations in response to external stimuli (Chafik et al., 2024; Xia et al., 2022). When combined with embedded computational components such as neuromorphic circuits and edge processors, these ceramics extend beyond their traditional

role as passive transducers (Yan et al., 2025). They can function as active decision-making units within distributed sensor and actuator networks, capable of not only sensing but also interpreting context, issuing feedback, and initiating autonomous responses. At the core of this transformation is the integration of mechanically responsive lattice structures, functional heterointerfaces, and embedded logic circuits (Xia et al., 2022). Together, these elements enable real-time electromechanical interactions that support intelligent behaviors such as selective signal amplification, localized energy harvesting, and dynamic impedance modulation based on environmental conditions.

System-integrated lead-free ceramics are becoming increasingly aligned with bioinspired functional integration strategies, where mechanical, electrical, and computational elements are designed in unison to achieve complex emergent functionalities. Their applications span a wide range of fields, from soft robotics with distributed control capabilities to wearable diagnostic systems capable of interpreting physiological signals (Dai et al., 2023; Jie Zhang et al., 2025). These materials are no longer confined to the role of transducers, but instead serve as intelligent modules within holistic, feedback-rich platforms that support next-generation developments in the Internet of Things (IoT), edge AI, and closed-loop biomedical systems.

1.2.5. Structural Design

For multidimensional assessment, property optimization is merely a necessary condition. More importantly, for practical application scenarios, the structural design strategy and criteria are critical factors that determine whether the materials can be practically applied in the field. In other words, improving the intrinsic material properties is important, but it does not guarantee that the material will function well once it is assembled into a sensor.

In lead-free piezoelectric systems, the transition from laboratory results to practical devices depends strongly on structural design. Compositional tuning can improve piezoelectric or dielectric parameters, but factors such as device geometry, electrode arrangement, film thickness, and internal stress distribution determine whether a sensor can operate stably under repeated loading, environmental fluctuations, or long-term service conditions. These aspects often play a more decisive role in real applications than the intrinsic material properties themselves. Structural design is also directly related to manufacturability. The compatibility of

a material with modern fabrication methods, including 3D printing, tape casting, thin-film deposition, and micro/nano processing, influences not only production efficiency but also device consistency and reliability. The ability to integrate piezoelectric materials with flexible substrates or heterogeneous structures further expands their practical use, especially in wearable, lightweight, or miniaturized applications.

Despite its importance, structural design has not yet been systematically assessed from multiple perspectives. This gap makes it necessary to summarize and compare the advantages and limitations of existing structural design strategies, so as to provide guidance for optimizing the practical use of lead-free piezoelectric sensors.

1.2.5.1. Conflicts Between Traditional Manufacturing and Updated Requirements

Conventional solid-state sintering of bulk piezoelectric ceramics (both lead zirconate titanate and lead-free ceramics) imposes fundamental constraints that critically impede their deployment in next-generation intelligent systems (Benabdallah et al., 2015). The inherent mechanical properties of sintered monoliths (characterized by high elastic modulus, negligible ductility, and susceptibility to brittle fracture) render them intrinsically incompatible with applications demanding mechanical compliance. This inflexibility precludes conformal integration with biological tissues for implantable diagnostics, limits stable interfacial contact on dynamic curvilinear surfaces in structural health monitoring, and obstructs seamless incorporation into lightweight, ergonomic wearable platforms (S. Gong et al., 2024; Ray et al., 2019). Material processing challenges compound these limitations. Precision micromachining of dense, brittle ceramics to achieve sub-millimeter features or complex topographies incurs excessive fabrication costs, induces microcrack formation compromising device reliability, and exhibits poor scalability for mass production of miniaturized sensors.

Beyond mechanical and manufacturing challenges, integration and performance bottlenecks persist. The volumetric bulk and geometric inflexibility of sintered ceramics impede direct integration with complementary technologies such as flexible hybrid electronics (Khan et al., 2020). This hinders the realization of compact, multifunctional sensor systems. As for ceramic structures, the isotropic, polycrystalline nature of sintered ceramics intrinsically limits optimization of piezoelectric coefficients (e.g., d_{33}, d_{31}) and electromechanical coupling factors across desired frequency bands, while inhibiting engineered anisotropy for directional

sensitivity or multimodal response.

Taken together, these limitations of mechanical rigidity, fabrication complexity, poor integration compatibility, constrained performance tunability, and resource inefficiency highlight the inadequacy of traditional bulk ceramic processing. These challenges drive the need for transformative manufacturing paradigms that emphasize innovative processes, controlled morphologies, and architected structures to enable the next generation of high-performance, application-tailored piezoelectric transducers.

1.2.5.2. Progressive Manufacturing Process

The continuous advancement of processing techniques has served as a major driving force behind the structural evolution of lead-free ceramic materials for building applications. While conventional solid-state sintering has long been employed in bulk ceramic fabrication, recent developments have enabled the production of nanostructured thin films, offering greater design flexibility. This process-led shift has supported the transition from single-phase systems to multilayer composite configurations, resulting in improved piezoelectric performance and expanded functionality. These improvements are particularly relevant for sensor-integrated building materials, where both material properties and structural integration are critical.

1.2.5.2.1 3D-printed Piezoelectric Composites

Traditional PZT ceramics or other lead-free ceramics are mostly prepared by the solid-phase sintering method, yielding products that typically manifest in the form of blocks (Yang and Hao, 2019). These materials are characterized by their high purity, substantial material density, and cost-effectiveness. However, their elevated stiffness and fragility constrain their applicability in sensors that necessitate flexibility and wearability. The high sintering temperatures employed during traditional solid-phase sintering (usually exceeding 1000 °C) can lead to increased energy consumption and production costs, as well as challenges in achieving compatibility with low-temperature processes. Solid-phase sintering can face difficulties in controlling the microstructure and preparing complex structures. At the same time, due to the internal stress accompanying the sintering, the material is prone to an increased risk of cracking.

3D printing can well compensate for the limitations brought about by solid-phase sintering and can easily realize the printing of complex structures (Wei et al., 2025). However, it should

be noted that 3D printing is selective to materials and has high requirements for the interlayer bonding force of materials during the printing process (Fig. 1-5). Current 3D printing technologies face challenges in cost control and production efficiency, suggesting that there remains considerable room for further optimization. Although fully realizing 3D printing of lead-free piezoelectric ceramic sensors is still difficult at the present stage, the technology demonstrates significant potential for applications that require personalized customization, such as functional sensing devices and medical implants. As printed components continue to evolve toward greater structural diversity and multifunctionality, their mechanical flexibility also warrants close attention. The deformation behavior, as shown in Fig. 1-6, from the initial response to external forces to subsequent stretching, bending, and even torsional distortion, plays an essential role in ensuring the reliability, durability, and adaptability of these printed structures in practical environments.

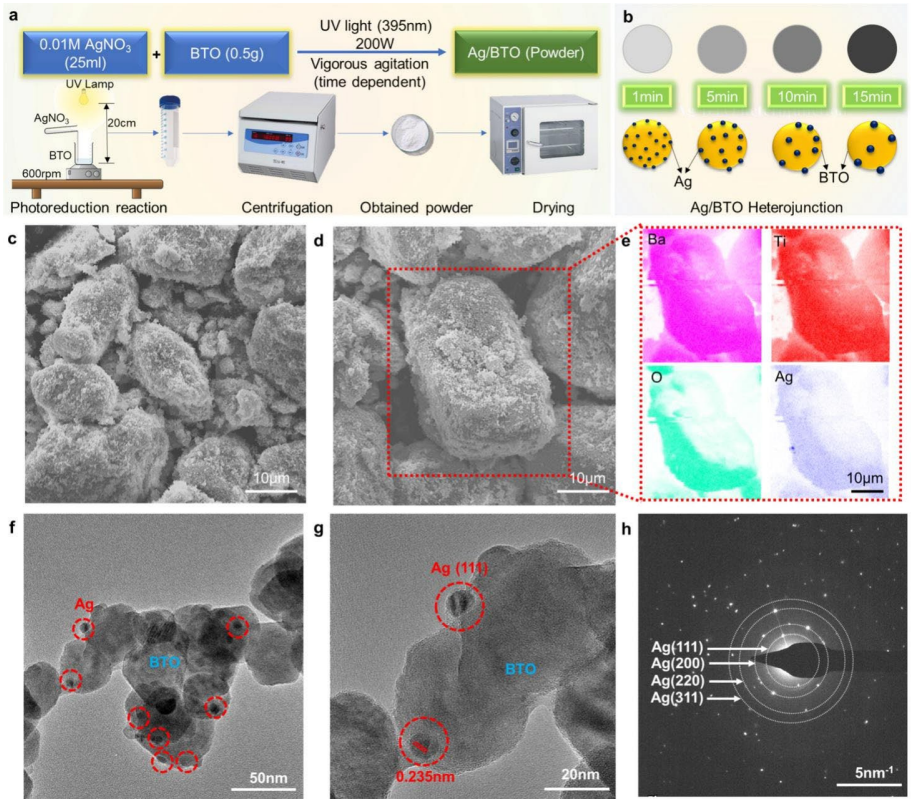


Fig. 1-5: (a) Schematic illustration of the time-dependent in-situ photoreduction reaction and (b) illustration of silver particle doping. Comparison of SEM images of (c) BTO, (d) 1 m-Ag/BTO, and (e) elemental mapping of 1 m-Ag/BTO. (f) TEM image of 1 m-Ag/BTO ceramic, (g) TEM of Ag nanoparticles, and (h) SEAD pattern of Ag nanoparticles (Hamza et al., 2025)

The current state of 3D printing of ceramic sensors primarily utilizes digital light processing (DLP) (Rosental et al., 2021), selective laser sintering (SLS) (Yang et al., 2021), and fused deposition modeling (FDM). These methods enable the precise design and printing of microstructures that meet the structural and mechanical requirements necessary for certain applications, while also allowing for the creation of lightweight, high-strength piezoelectric structures. Furthermore, the slurry, composed of a mixture of ceramic powder and various binders, can be printed with a structural design to produce hollow (L. Zhao et al., 2024), porous (Qingping Wang et al., 2024), prismatic (Kai Chen et al., 2024), and other special-shaped structures, thereby enhancing the energy conversion efficiency. It is noteworthy that the majority of sintered products necessitate decreasing and sintering at elevated temperatures to achieve the desired densification of the ceramic structure. Additive manufacturing of KNN-based ceramics enables the fabrication of architectural geometries with periodic arrays and hemispherical cavities. Post-processed through optimized deboning and sintering protocols, these 3D-printed components exhibit comparable piezoelectric coefficients and ferroelectric polarization hysteresis loops to their conventionally sintered counterparts (Rosental et al., 2024).

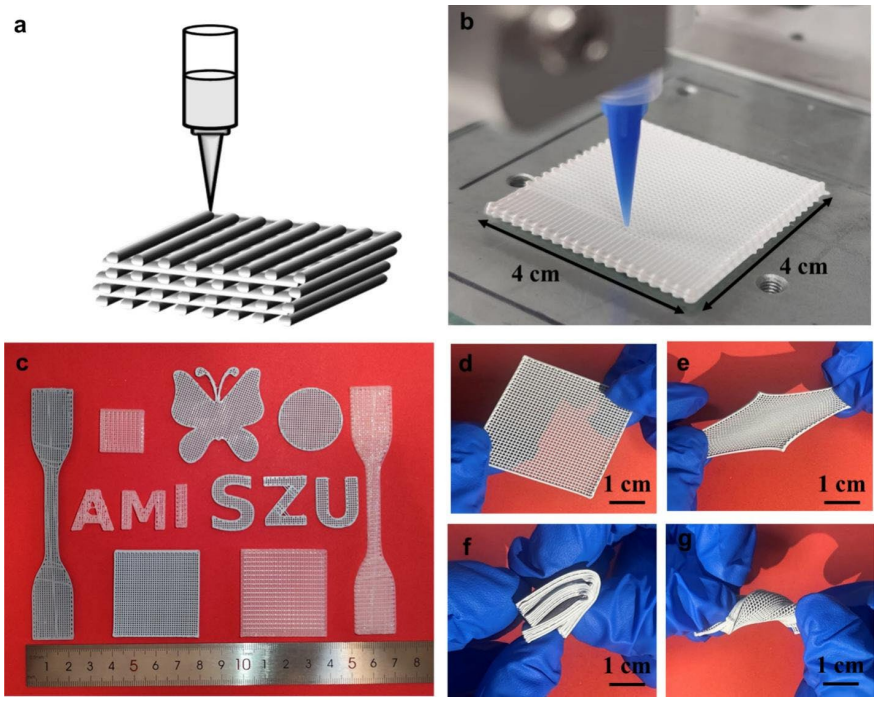


Fig. 1-6: Extrusion-based 3D printing. (a) presents the fundamental printing mechanism, while (b) demonstrates the fabrication of a 3D construct and (c) displays diverse printed geometries. In (d), the deformation behavior of the printed components is shown under early-stage loading, stretching, bending, and torsional motion (Hamza et al., 2025)

However, recent studies have demonstrated that flexible sensing units can be fabricated without sintering, provided they possess the appropriate structural design and proportions (Chen et al., 2019; D. Sun et al., 2023). Conventional PVDF/$BaTiO_3$ 2D piezoelectric harvesters exhibit limited open-circuit voltage output. In contrast, FDM-printed 3D prismatic architectures enable nanocomposite energy harvesters to achieve 30.8 V open-circuit voltage, capable of charging commercial 1 μF capacitors to 25 V within 260 s, thereby enabling the operation of a self-powered "smart mouse" device while maintaining mechanical flexibility (bending radius <5 mm) and piezoelectric responsiveness (Megdich et al., 2024). Structural engineering strategies, particularly those applied in the additive manufacturing of ceramics, have shown substantial potential in enhancing piezoelectric properties beyond those of conventional bulk materials. Zhao (L. Zhao et al., 2025) reported that a 3D-printed BCZT-based ceramic featuring a honeycomb-inspired sandwich structure exhibited significant improvements in functional performance. The optimized porous architecture led to an increase of approximately 16% in the piezoelectric charge coefficient and 111% in the voltage coefficient compared to its dense ceramic counterpart. These findings underscore the pivotal role of engineered porosity in tuning electromechanical performance in printed ceramic systems.

The transition from the initial requirement of sintering dense 3D-printed lead-free ceramics to the development of high-performance, sinter-free 3D-printed ceramics, along with the shift from planar structures to complex geometries, demonstrates the practical viability of fabricating flexible lead-free ceramic architectures via 3D printing. The printed structures achieve exceptional compliance and mechanical stability while retaining robust piezoelectric response, making them strong candidates for stretchable sensors, e-skin systems, and smart biomedical devices that demand both flexibility and effective electromechanical conversion (Wu et al., 2021).

1.2.5.2.2 Micro- and Nano-thin Films

The development of microelectronics technology has promoted the rise of nano-thin film devices. Sputtering deposition, sol-gel method, and laser lift-off (LLO) are the technical means for advanced thin film preparation. Their advantages, disadvantages, and differences are listed in Table 1-2.

Table 1-2 Critical differences, advantages, and disadvantages of sputtering deposition, sol-gel method, and Laser lift-off

Technology	Principle	Key Features	Advantages	Disadvantages
Sputtering Deposition (Kuo and Yin, 2025)	Plasma bombards the target material, ejecting atoms that deposit on the substrate to form a thin film.	A Physical Vapor Deposition (PVD) technique that produces high-density films	Uniform coating, strong adhesion, suitable for metals, oxides, and nitrides	Expensive equipment, slow deposition rate, suitable for small-area films
Sol-Gel Method (Budinská et al., 2025)	The chemical solution forms a sol, which transitions into a gel, then deposits and sinters into a ceramic or oxide film.	A low-temperature chemical deposition method capable of nanoscale film formation	Low cost, suitable for large-area coatings, controllable composition, enables porous or composite films	Requires high-temperature sintering, lower film density, and mechanical strength
Laser Lift-Off (LLO) (Chowdhury et al., 2024; Kim et al., 2021)	Laser pulses irradiate the release layer, which absorbs energy and decomposes, separating the thin film from the substrate	Used for transferring thin films in flexible electronics, Micro-LEDs, and semiconductor applications	Enables high-quality thin film transfer to flexible substrates, supports large-area production	Requires specific release layer materials, precise laser parameter control, and a complex process

Thin-film technology (Bhattacharyya et al., 2024) provides a critical breakthrough for performance optimization and application expansion of lead-free piezoelectric ceramic sensors, addressing the inherent limitations of conventional bulk materials through unique morphological regulation mechanisms. By leveraging strain engineering and interfacial charge modulation, the thin-film structure significantly enhances the piezoelectric response (d_{33} reaching 150-300 pm/V) of lead-free systems (KNN- and BNT-based ceramics) while effectively suppressing polarization switching hysteresis and dielectric loss (Herrera-Pérez et al., 2023; Leal-Perez et al., 2023; Mugheri et al., 2024). This enables the material to maintain stability under high temperatures (>300 °C) and cyclic mechanical loading conditions, substantially improving environmental adaptability. Miniaturization stands as another core advantage of thin-film technology, where submicron-level thickness endows devices with MHz-range high-frequency response capability and μW-level ultralow power consumption.

Integrated with microelectromechanical systems (MEMS) processes, microsensor units with feature sizes <100 μm can be fabricated, laying the hardware foundation for implantable medical devices (e.g., real-time intracranial pressure monitoring) and flexible wearable electronics (e.g., self-powered tactile sensing) (Y. Chen et al., 2024; Mahanty et al., 2024; Zhang et al., 2015).

Technical feasibility is anchored in dual innovations in material design and system integration. On one hand, two/three-dimensional heterojunctions (for example, graphene/piezoelectric films) optimize charge transport efficiency through interfacial band engineering, while gradient compositional designs balance piezoelectricity and thermal stability (M. Liang et al., 2024). On the other hand, the heterogeneous integration of thin-film sensors with edge AI chips achieves in situ signal feature extraction and dynamic calibration (Beigh et al., 2023). Driven by these advancements, thin-film technology is propelling lead-free piezoelectric sensors toward environmental adaptability, promising to unlock novel application scenarios in industrial IoT (e.g., high-temperature equipment condition monitoring) and smart healthcare (e.g., biodegradable biosensors). This progress is reshaping the performance boundaries and deployment paradigms of sensing technologies, heralding a new era of intelligent, sustainable sensing solutions (Mugheri et al., 2024; Peng et al., 2022).

1.2.5.3. Flexibility

With the rapid advancement of wearable devices, smart healthcare systems, and flexible electronics, the design and structural form of piezoelectric sensors are undergoing a significant transformation. Conventional piezoelectric materials-typically rigid and brittle-are increasingly being supplanted by alternatives that are flexible, stretchable, and biocompatible, to meet the mechanical and physiological demands of next-generation electronic environments. This evolution not only enhances user comfort and device adaptability but also expands the potential applications of piezoelectric sensors in real-time health monitoring, human-machine interfaces, and soft robotics. As a result, the development of high-performance, lead-free, and mechanically robust piezoelectric materials has become a critical research focus in the field of advanced functional materials and flexible sensing technologies.

Traditional PZT-based piezoelectric ceramics offer high performance but suffer from brittleness, toxicity, and limited compatibility with flexible systems. In contrast, lead-free

flexible ceramic sensors provide excellent mechanical adaptability, enhanced biocompatibility, and improved integration with emerging technologies such as wearable devices, soft robotics, and bioelectronic systems. The following Table 1-3 compares their key characteristics.

Conventional biomedical implant materials, including stainless steel, titanium alloys, silicone rubber, and hydroxyapatite ceramics, face limitations due to their lack of inherent biodegradability and biocompatibility, coupled with operational dependencies on external power sources (Ziyan Gao et al., 2024). In contrast, flexible lead-free piezoelectric sensors have garnered significant attention in bioelectronic applications owing to their non-toxic composition and skin-like mechanical properties, such as softness (<1 MPa elastic modulus), stretchability (>100% strain), self-healing capability, and tunable biodegradation rates (J. Park et al., 2014). These attributes enable the development of epidermal-conformable devices capable of high-fidelity health monitoring and electrophysiological signal modulation with minimal tissue irritation (Wu et al., 2021). Fig. 1-7 shows a flexible composite piezoelectric sensor made of P(VDF-TrFE) and $BaTiO_3$ for the detection and energy harvesting of hand joint movements (Taleb et al., 2023).

Table 1-3 Comparison of traditional piezoelectric sensors and lead-free flexible sensors

Characteristic	**Traditional PZT Piezoelectric Sensors** (Horchidan et al., 2016; Lee and Esashi, 2004; Panda and Sahoo, 2015; Qian Wang et al., 2024; R. Wang et al., 2020)	**Lead-Free Flexible Ceramic Sensors** (Y. Chen et al., 2024; De Fazio et al., 2025; Gu et al., 2020; M. He et al., 2021; Taleb et al., 2023; Yang et al., 2025)
Material Form	Rigid bulk, brittle	Ultra-thin, flexible, and bendable
Manufacturing Process	High-temperature sintering	Low-temperature sputtering, 3D printing
Application Fields	Structural monitoring, ultrasound imaging	Wearable health monitoring, flexible robotics
Biocompatibility	Contains toxic lead	Eco-friendly, lead-free
Mechanical Properties	Fragile, prone to cracking under stress	Highly flexible, stretchable, and durable
Integration with Electronics	Difficult to integrate with flexible substrates	Easily integrates with soft and wearable electronics
Energy Efficiency	High output but limited adaptability	Lower energy loss, adaptable to dynamic environments

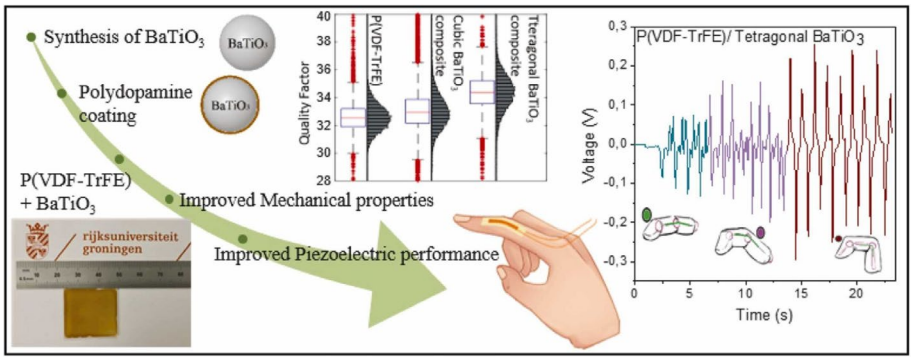


Fig. 1-7: Schematic diagram of flexible sensor (Taleb et al., 2023)

Recent advancements demonstrate their implantable potential for seamless organ-tissue integration (C. Zhao et al., 2024). Hydrogel-based piezoelectric sensors incorporating $BaTiO_3$ nanoparticles with gelatin extracellular matrix components exhibit conformal adhesion to the human epidermis, functioning as flexible motion detectors. When integrated with microelectronic systems, these devices enable real-time signal feedback and preliminary diagnostics, effectively streamlining data analysis processes (Fu et al., 2023). Concurrently, a $Ti_3C_2T_x$-embedded bio-patch fabricated from flexible lead-free piezoelectric composites demonstrates therapeutic efficacy in managing bacterially infected diabetic wounds (Kong et al., 2025). Wang (Wang et al., 2009) engineered porous $(Li_{0.06}Na_{0.5}K_{0.44})NbO_3$ ceramics via cold isostatic pressing, revealing piezoelectric coefficients comparable to natural bone alongside favorable cytocompatibility. In vitro assessments confirmed enhanced osteoblast adhesion and differentiation, suggesting potential as bone replacement materials. The advancement of environmentally sustainable lead-free piezoceramics meeting practical durability requirements (fatigue resistance $>10^6$ cycles, stable d_{33} retention >80% after 6-month implantation) is critical for replacing toxic lead-based systems, thereby mitigating ecological hazards throughout material lifecycles. Heavy metal-free compositions further position these materials as promising candidates for high-impact biomedical applications, including tissue regeneration therapies and advanced implantable devices such as self-powered cardiac pacemakers and neural interfaces, underscoring the strategic significance of performance-optimized piezoelectric ceramics in next-generation medical technologies (Rosso et al., 2022).

1.2.5.4. Heterogeneous Structures

Current lead-free piezoceramic systems, including $(K, Na)NbO_3$ (KNN) (J. He et al., 2025), $(Bi_{0.5}Na_{0.5})TiO_3$ (BNT) (Nie et al., 2025), and $(Ba, Ca)TiO_3$-$Ba(Ti, Zr)O_3$ (BCZT) (Sayagués et

al., 2024), exhibit performance limitations that hinder practical implementation. KNN-based ceramics require complex multi-element doping (e.g., Li/Sb/Ta co-doping) to enhance piezoelectric coefficients (d_{33} ~ 300-450 pC/N) and Curie temperatures (T_C ~ 250-420 °C), yet suffer from compositional heterogeneity and batch-to-batch variability (Wang and Li, 2010). BNT ceramics achieve ultrahigh strain responses (d_{33}* ~ 916 pm/V) but are constrained by low depolarization temperatures (T_d ~ 100-150 °C) and strong temperature-dependent piezoelectric degradation (Δd_{33} >40% from 25-80 °C) (T. Li et al., 2017). BCZT systems demonstrate moderate d_{33} values (~ 620 pC/N) with critically low T_C (~ 90 °C), resulting in thermal instability under operational conditions (>60 °C ambient temperature) (Habib et al., 2022). These intrinsic limitations underscore the scientific challenge in developing minimally doped lead-free piezoceramics.

Constructing localized structural heterogeneity has emerged as an effective strategy for achieving comprehensive performance in piezoceramics. Habib developed $0.67Bi_{1.03}FeO_3$-$0.33Ba_{1-x}Sm_xTiO_3$ ceramics via quenching-induced morphotropic phase boundary (MPB) engineering and tetragonality maximization (c_t/a_t = 1.02), yielding enhanced piezoelectricity (d_{33} = 334 pC/N, d_{33}* = 552 pm/V) with temperature-insensitive strain response (<10% variation from 25-125 °C) (Habib et al., 2022). For $BiFeO_3$-$BaTiO_3$ systems, analogous compositional modifications as $NaTaO_3$ (Xie et al., 2022) and $La(Mg_{2/3}Nb_{1/3})O_3$ (Qingtong Zhang et al., 2023) incorporation enhance relaxor characteristics through localized nanodomain formation. Sb doping in $0.93(Na_{0.52}K_{0.48})(Nb_{1-x}Sb_x)O_3$-$0.05BaZrO_3$-$0.02(Bi_{0.5}Na_{0.5})HfO_3$ ceramics induces compositionally heterogeneous regions, triggering diffuse phase transitions and enhanced piezoelectric strain coefficients (Q. Liu et al., 2018).

In addition to doping to form a heterogeneous structure to improve the properties of the ceramic, multilayer structure engineering has emerged as an effective strategy for enhancing piezoelectric performance through interfacial stress modulation. Two distinct approaches have been developed: homogeneous-phase and heterogeneous-phase sandwich-type configurations. Huang (Huang et al., 2025) engineered a BFO-BT/BT composite ceramic, where chemical heterogeneity between bismuth ferrite-barium titanate (BFO-BT) and barium titanate (BT) phases generated abundant heterointerfaces, inducing localized stress gradients and internal bias fields. This structural optimization yielded a giant electric strain of 1.06% via domain wall

mobility enhancement. Similarly, a laminated BNT1/BNT2 system combining high-T_d $0.89(Bi_{0.5}Na_{0.5})TiO_3$-$0.11BaTiO_3$ and high-d_{33} $0.87(Bi_{0.5}Na_{0.5})TiO_3$-$0.11BaTiO_3$-$0.02(Sm_{0.5}K_{0.5})TiO_3$ achieved concurrent piezoelectric enhancement (d_{33} = 140 pC/N) and thermal stability (T_d = 232 °C) through diffusion-controlled ferroelectric-relaxor (FE-RE) phase transitions. The alternating internal bias fields in such homogeneous multilayers mimic defect-dipole engineering principles, synergistically boosting strain response (H. Liu et al., 2024). To address temperature sensitivity, Fang developed a $BaTi_{0.93}Sn_{0.07}O_3$/$0.75BiFeO_3$-$0.25BaTiO_3$-0.1 wt.%MnO_2/$BaTi_{0.93}Sn_{0.07}O_3$ (SWS-BFBT) sandwich architecture. The graded interfaces promoted reduced domain sizes and increased polar nanoregion density, broadening phase transition temperature windows through polar pinning effects. This structural heterogeneity elevated both piezoelectric coefficients and depolarization temperature in BFBT-based systems (Fang et al., 2025).

Recent studies have expanded the design paradigm of heterogeneous composite architectures across distinct material systems. Zhang (Jitao Zhang et al., 2025) demonstrated a segmented composite of impedance-tailored piezoceramics and spinel ferrites, achieving multichannel power distribution via controlled impedance gradients. This approach enables asymmetric power splitting in solid-state magnetoelectric devices, extending operational frequency ranges to sub-kHz regimes. In parallel efforts, Elkelany engineered BCZT/glass composites through tricritical triple phase point modulation, where glass-phase incorporation suppressed tetragonal (T) and rhombohedral (R) phase fractions. Optimal performance was achieved at x = 0.025 glass content, yielding enhanced thermal stability, alongside peak dielectric permittivity (ε = 4,102 at 1 kHz) and peak converse piezoelectric response d_{33}^* = 1,150 pm/V (Elkelany et al., 2023).

Two different lead-free piezoelectric ceramics form a sandwich structure to show good performance. In the BNT-BT-*x*KNN system, optimal dielectric properties with minimal loss were achieved at 0.02 mol% KNN content. Composite membranes incorporating this composition with polyvinylidene difluoride (PDMS) can make the output voltage reach 30 V and the current density reach 0.28 μA/cm^2 (Panpho et al., 2024). Alternatively, sol-gel-derived BNT-BT-0.05KNN thin films without polymer matrices showed ultra-large strain (>1.6%) and reduced hysteresis, attributed to reversible phase transitions and polarization order-disorder

transformations (Jinyan Zhao et al., 2025). < 001 >-textured BCZT-KNN composites were obtained by Liu through template grain growth, yielding enhanced ferroelectric ($2P_r$ = 43.5 μC/cm^2) and piezoelectric properties (d_{33} = 190 pC/N, d_{33}* = 137 pm/V, k_p = 0.54) compared to randomly oriented counterparts. The textured ceramics also exhibited lowered phase transition temperatures (T_{O-T} = 170.2 °C, T_C = 388.3 °C), indicating reduced thermal-driven property degradation (Liu et al., 2023).

Through structural heterogeneity, sandwich structure, and other methods, the performance of lead-free ceramic sensors can be further improved, and a wider range of applications can be achieved.

1.2.6. Intelligent Integration

When the sensing task involves noisy signals, multiple stimuli or changing conditions, traditional evaluation methods that focus on a few separate parameters, are not suitable for describing sensor behavior in practical applications. As a result, a multidimensional assessment framework has become necessary to meet the requirements of real applications. However, building such a framework remains difficult, partly because of the lack of systematic tools that can handle complex data and capture the interactions between different sensing factors.

In recent years, with the rapid progress of artificial intelligence, new methods have become available to address these challenges. Machine learning has been widely used in materials research, for example, in composition screening and property prediction, but its value is not limited to the materials domain. For sensing systems, AI and machine-learning techniques provide flexible ways to extract useful features from complicated signals and to adjust the processing strategy when external conditions change. This adaptive capability is one of the key advantages that distinguishes AI-based approaches from conventional sensing systems, which rely on fixed and often rigid processing schemes.

1.2.6.1. Constraints of Conventional Sensing Systems

Lead-free piezoelectric technologies, while environmentally compliant and mechanically robust, remain anchored to passive operating frameworks. Most devices execute fixed-response protocols under invariant structural and computational assumptions. Their design lacks mechanisms for behavioral adaptation, structural reconfiguration, or performance feedback,

limiting applicability in dynamic or data-intensive environments.

Signal transduction typically follows static interpretation schemes. Preset thresholds, unchanging spectral filters, and uniform feature extraction workflows dominate sensing logic. These rigid signal pipelines cannot discriminate between relevant mechanical signatures and environmental noise in fluctuating or multi-field conditions (Rathod, 2019). Cross-axis coupling, thermal shifts, and nonlinear stimulus overlap frequently degrade output fidelity, especially in mobile or biologically interfaced scenarios (Izadi, 2011). At the system level, energy conversion and signal acquisition remain operationally decoupled. Strain-derived energy is rarely shared or redirected across functions. The absence of coordinated strain-energy partitioning constrains energy efficiency and limits operational autonomy, particularly in untethered or resource-constrained platforms.

These characteristics expose a deeper issue: sensing systems that neither evolve nor learn. They do respond, but do *NOT* adapt; they do sense, but do *NOT* interpret. As demands increase for integrated, autonomous, and multimodal sensing platforms, static material logic proves insufficient. The next section examines pathways toward intelligent reconfiguration, guided signal recognition, and co-designed transduction-energy frameworks.

1.2.6.2. Machine Learning and Neuromorphic Computing

The evolution of piezoelectric sensing technology has undergone a paradigm shift from material-centric optimization to intelligent system integration. Conventional piezoelectric sensors primarily function as passive transduction units, requiring external computational modules for post-acquisition signal processing. This period sensor inherently suffers from limited sensitivity, stemming from the mismatch between the material and the analysis method. The inability to implement real-time noise cancellation (SNR <40 dB in the 1-100 Hz range) further exacerbates performance degradation. As the demand for these sensors increases, there is an increasing demand for sensors to provide feedback, thus marking the beginning of the first stage of evolution: data pre-processing, with typical methods such as denoising. The signal processing technique of wavelet decomposition and reconstruction involves the division of the signal into disparate scale and frequency components. Subsequently, specific features are selectively emphasized or noise is eliminated through the reconstruction of the signal (Shi et al., 2024).

During the preprocessing stage, it was determined that, in addition to denoising, there was also data loss during acquisition and anomalous signal generation, rendering conventional preprocessing techniques inadequate (Azad et al., 2024). This limitation has driven the increasing integration of machine learning frameworks implementing interpolation, data imputation, and anomaly detection algorithms to enhance data fidelity (SNR improvement >12 dB) and sensing accuracy (error reduction >35%), thereby enabling autonomous learning capabilities in sensor systems (Di Lorenzo et al., 2023; S. Kim et al., 2023; Malekloo et al., 2022). A representative advancement by Lee (Jung et al., 2022) demonstrated a noise-resistant piezoelectric microphone employing multi-resonant band positioning outside dominant noise spectra (50-200 Hz range). Coupled with a convolutional neural network (CNN) architecture incorporating optimized attention blocks, the system achieved 96% speaker identification accuracy with 62% error rate reduction compared to commercial microphones, validating machine learning-enhanced piezoelectric sensing paradigms. Langat (Langat et al., 2025) studied a novel structure health monitoring methodology for the aeronautical industry, which integrates embedded piezoelectric sensor arrays with streamlined machine learning. This approach employs simplified ML models (e.g., decision tree ensembles with $<10^4$ parameters) to achieve real-time diagnosis of individual and composite defects-including scratches, voids, notches, and delaminations, while maintaining computational efficiency. It achieves a 100% accuracy rate in the diagnosis of fault combinations, such as holes and scratches. For scratch damage, the model demonstrates an accuracy of 88.89%. This enhances the overall efficiency of on-site sensing by reducing the computational cost.

While data-driven machine learning approaches gain prominence across piezoelectric applications due to their adaptability to diverse signal patterns (Cross et al., 2022), persistent limitations of single-modality data augmentation underscore the necessity for sensor-level decision autonomy through multimodal fusion. De Fazio (De Fazio et al., 2025) developed a Parkinson's assessment smart glove integrating a multi-sensor fusion framework, two piezoelectric sensors and an inertial sensor, as shown in Fig. 1-8. Three neural network (NN)-based embedded ML algorithms were implemented on the microcontroller unit (MCU) to classify composite piezoelectric-inertial signatures, achieving 95.12%, 98.39%, and 96.62% accuracy in detecting finger tapping, fist closure, and resting tremor, respectively. These

intelligent electromechanical sensing systems integrate real-time data preprocessing, adaptive learning, and autonomous decision-making, enabling them to filter noise, extract critical features, and analyze signals locally without relying on external computing resources (Dai et al., 2023). Key data preprocessing techniques, including data cleaning, transformation, fusion, augmentation, and computational optimization, significantly enhance data accuracy, model stability, and system reliability (Fig. 1-9 illustrates the process of determining the precise classification of the input source by the signal) (Y. Li et al., 2024). By embedding machine learning and edge AI, these sensors can autonomously adjust their response based on environmental changes, making them highly efficient for dynamic applications.

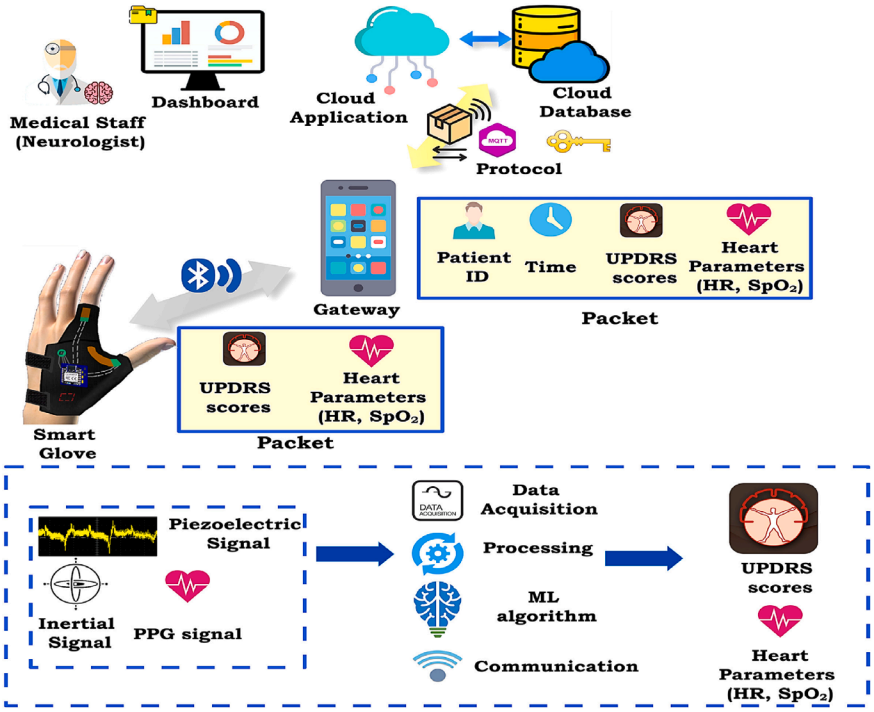


Fig. 1-8: Visual Representation of the Smart Glove-Based Monitoring System for Parkinson's Patients (De Fazio et al., 2025)

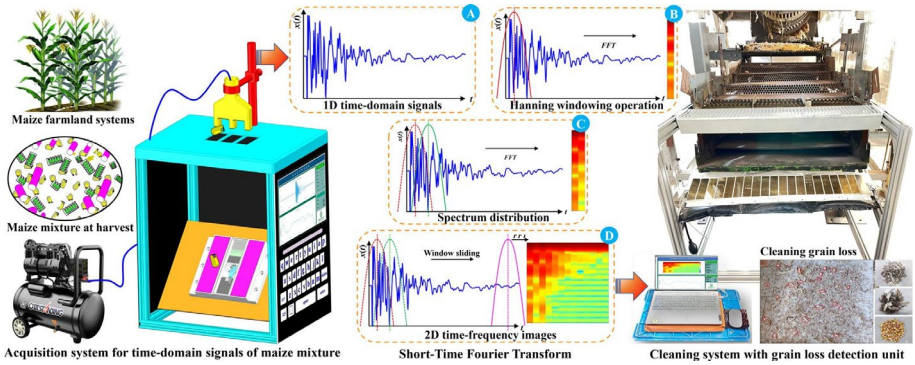


Fig. 1-9: Vibro-piezoelectric detection system for classifying maize grain and impurity (Y. Li et al., 2024)

Recent advancements in sign language translation systems reveal a paradigm shift from limited-character recognition to intelligent multimodal communication architectures. Single-module sensor translators typically achieve restricted performance (e.g., 5-letter alphabet recognition with 70-85% accuracy) (Maharjan et al., 2020), whereas next-generation systems integrate a sensing glove, a deep learning module, and a virtual reality interface, and can recognize 50 words and 20 sentences (Wen et al., 2021). The optimized system demonstrates unprecedented generalization capability, recognizing novel sentence combinations through phoneme-grapheme recombination with 86.67% mean accuracy. Furthermore, the sign language recognition results are projected into the virtual space and translated into text and audio, effectively bridging communication gaps between signing and non-signing populations. This technological leap underscores the transformative potential of intelligent lead-free piezoelectric systems in developing socially inclusive, environmentally conscious human-machine interfaces (Z. Zhou et al., 2020).

The urgent need for intelligent piezoelectric sensors is apparent in areas such as wearable health monitoring, structural integrity assessment, human-machine interaction, and soft robots, where real-time responsiveness, energy efficiency, and adaptive sensing play a critical role (Sajal et al., 2020). Future developments will prioritize the integration of multifunctional materials, AI-powered signal processing, and energy-efficient computing, laying the foundation for the next generation of smart, autonomous, and highly reliable piezoelectric sensing technologies. The innovation in lead-free piezoelectric ceramics and the advancement of their sensor applications are key drivers in achieving this vision.

1.2.6.3. Multimodal Energy and Sensing Integration

1.2.6.3.1 Energy Harvesting

Sustainable power autonomy has emerged as a critical frontier in next-generation sensor development (Y. Wang et al., 2022; H. Zhao et al., 2025). Conventional battery-dependent architectures face dual challenges of ecological burden (e.g., toxic disposal of 2.8 million metric tons/year of lithium-ion batteries globally) and operational limitations in maintenance-sensitive deployments, particularly in structural health monitoring (Yang et al., 2018), smart city grids (Song et al., 2019), and implantable biomedical devices (Xue et al., 2023), where frequent battery replacement proves impractical (Safaei et al., 2019). These constraints fundamentally

restrict sensor network scalability and long-term reliability. Lead-free piezoceramics offer a paradigm-shifting solution through intrinsic energy harvesting capabilities, converting ambient mechanical vibrations (0.5-200 Hz) and biomechanical motions into usable electrical energy. This self-powered mechanism aligns with circular economy principles by eliminating disposable battery dependence while enabling perpetual operation in remote or embedded installations, thereby enabling self-powered sensing across five primary domains: 1) structural health monitoring, 2) wearable physiological tracking, 3) environmental sensing, 4) biomedical implants, and 5) industrial automation.

Piezoelectric nanogenerators (PENG) are a particular type of energy harvesting device that utilizes the piezoelectric effect to transform mechanical energy at the nanoscale into electrical energy (Anbalagan et al., 2024). The converted electrical energy can be stored in storage devices such as batteries and capacitors, which can be utilized as a power source for various portable, wireless, and wearable electronic devices (which can operate efficiently with minimal power). A novel flexible energy harvesting system was developed through the strategic integration of KNN nanostructures into electrospun polyvinylidene fluoride (PVDF) fiber networks (Teka et al., 2018). Systematic modulation of KNN nanofiller geometry revealed that anisotropic particles with elevated aspect ratios function as β-phase nucleating agents, inducing preferential crystallization of PVDF's electroactive β-phase. This phase evolution generated aligned molecular dipoles that enhanced piezoelectric outputs by 40-fold, yielding 1.9 V under cyclic mechanical stimulation compared to 0.047 V for pure PVDF. The optimized nanocomposite demonstrated practical viability by directly powering commercial LEDs (1.8 V threshold) without energy storage components. Complementary studies on hydrothermally synthesized KNN/PVDF composites (Bairagi and Ali, 2019) and silane-functionalized-KNN/PVDF (Bairagi and Ali, 2020), corroborated the universal enhancement principle-lead-free ceramic incorporation increased output voltages by 300-500% across architectures. These consistent demonstrations of LED illumination validate electrospun piezoelectric nanogenerators as scalable solutions for self-powered wearable microsystems requiring mechanical flexibility and sustainable energy autonomy (see Fig. 1-10). KNN can also be used to prepare energy-harvesting devices without polymer composites, such as those employed in the harvesting of sound energy. An ultrasonic energy harvester composed of KNN and $BiFeO_3$,

fabricated through compounding, has been shown to generate an instantaneous power density of 52.07 mW/cm^2 when subjected to an incident ultrasonic pressure of 1.90 MPa and an optimized load resistance of 900 Ω (Xing et al., 2021).

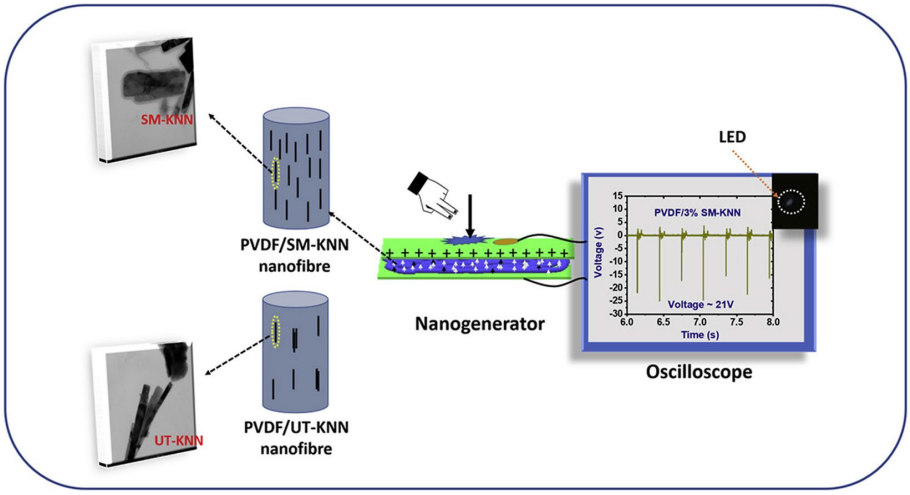


Fig. 1-10: Schematic diagram of generator prepared from PVDF/SM-KNN (Bairagi and Ali, 2020)

Barium titanate (BT) nanoparticles have emerged as an effective alternative to PZT for enhancing piezoelectric energy harvesting performance in polymer composites. Siddiqui (Siddiqui et al., 2016) engineered PVDF/BT nanocomposites (15% BT loading) into flexible PENGs integrated within footwear insoles. Under biomechanical excitation simulating human walking (0.6 Hz frequency, 600 N dynamic load), the optimized device generated a 25 V output voltage through coordinated stress-induced dipole alignment. Another study (Athira et al., 2022) further revealed that BT nanoparticles function as β-phase nucleating agents analogous to KNN, elevating PVDF's β-phase content via interfacial confinement effects. This crystalline reorganization yielded enhanced electromechanical conversion, with the BT-PVDF PENG demonstrating superior performance metrics: open-circuit voltage = 50 V ± 3 V, short-circuit current density = 0.312 mA/m^2, and power density = 4.07 mW/representing a 10 times improvement over pure PVDF counterparts. The achieved power density exceeds operational thresholds for wearable microelectronics (≥1 mW/m^2). Innovative textile-integrated piezoelectric energy harvesters were developed using barium titanate (BT)-reinforced polyvinyl chloride (PVC) composite yarns. Zhang's research (Zhang et al., 2015) yielded a two-dimensional fabric-like nanogenerator, which was developed based on three types of fibers: $BaTiO_3$ nanowire-PVC hybrid piezoelectric fibers, conventional cotton fibers, and copper wires,

and the BT fineness of the nanogenerator was measured to be 60-70 μm. The d_{33}-mode piezoelectric response was activated under dynamic mechanical deformation. When integrated into elbow-mounted textile substrates during flexion-extension cycles, the devices produced quantifiable electrical outputs (V_{oc} 1.9 ± 0.2 V, I_{sc} = 24 ± 3 nA), sufficient to power low-consumption LCD interfaces (operational threshold: 1.5 V, 20 nA). Comparative analysis revealed the PVC-BT system's reduced voltage output relative to PVDF-based counterparts (2.3 V) stems from PVC's intrinsically lower piezoelectric coefficients ($|d_{33}|$ = 2-3 pC/N vs. PVDF's 20-30 pC/N). This performance gap underscores the critical role of polymer selection in textile-based energy harvesting systems. The output power of BNT-BT-based energy harvesting devices under vibrational excitation has been demonstrated to depend significantly on geometric shape (Difeo et al., 2021). The correlation between their crystal structure, piezoelectric properties, and electrical performance serves as the basis for evaluating energy harvesting potential (Camargo et al., 2021).

Substantial research efforts over recent decades have focused on enhancing the performance and applicability of piezoelectric nanogenerators through five primary strategies: optimization of piezoelectric material selection, structural modifications, hybrid material design, substrate engineering, and advanced fabrication methodologies (Hu et al., 2019; Soin et al., 2014; Talbourdet et al., 2018). While significant progress has been achieved in textile-integrated piezoelectric nanogenerators, a critical gap persists between laboratory-scale demonstrations and commercial viability. Addressing this disparity requires intensified research on scalable manufacturing processes, long-term durability validation, and cost-effective production pathways to bridge technological innovation with real-world applications (Bairagi et al., 2022).

1.2.6.3.2 Synergistic Sensing of Multiple Energy Fields

Energy harvesting systems have garnered considerable scientific interest, yet their practical implementation faces inherent limitations due to the stochastic nature of ambient energy availability and operational instability under variable harvesting conditions. Monolithic energy harvesters employing singular transduction mechanisms (e.g., piezoelectric, triboelectric, or thermoelectric) often prove insufficient to sustain the continuous operation of wireless sensor networks and microelectronic platforms under fluctuating ambient conditions. This fundamental constraint has driven the emergence of hybrid energy harvesting architectures that

synergistically integrate complementary transduction principles (piezoelectric-triboelectric-thermoelectric coupling) to exploit multi-physical domain energy sources (J. Wang et al., 2021).

In industrial applications, vibration and heat sources frequently coexist. Many researchers have previously employed hybrid energy harvesting methods that utilize both thermal and mechanical energy flows (Guo and Lu, 2017; Oh et al., 2019). There is an inverse relationship between the thermoelectric performance coefficient and the dielectric constant of piezoelectric ceramics. This limitation restricts the application of high-dielectric materials like KNN (Yang and Hao, 2019) in thermal detection systems. To address this, researchers (Huang et al., 2024) have developed composite ceramics by incorporating low-dielectric BNT as a secondary phase into KNN matrices, leveraging KNN's high Curie temperature and piezoelectricity (Srikanth et al., 2018, 2017). These composites exhibit improved pyroelectric properties, enabling self-powered thermal detectors with enhanced responsiveness to environmental temperature fluctuations for ultraviolet/infrared radiation detection. Moreover, there have been documented instances of thermoelectric and piezoelectric energy harvesters being utilized in conjunction with industrial applications. One example involves the integration of large cooling fins with thermoelectric harvesters to ensure the maintenance of a temperature gradient (Du et al., 2015; Lin et al., 2019). Additionally, the implementation of large-deformation piezoelectric cantilever beams facilitates the dissipation of heat from the module.

However, such configurations typically lack synergistic interactions between energy conversion mechanisms. A breakthrough was achieved by Kim in 2023 (S.-B. Kim et al., 2023), who integrated thermoelectric and piezoelectric generators on a resonant cantilever. Under concurrent vibrational excitation (0.5 g acceleration), the hybrid system demonstrated synergistic effects, achieving a 50% increase in power output compared to standalone operation. This advancement validates the potential of multimodal energy harvesting strategies and establishes a foundation for efficiency-optimized hybrid systems. A novel dynamic piezoelectric-thermoelectric generator (dPTEG) was engineered through synergistic integration of a Brayton cycle-inspired non-turbine configuration and coordinated piezoelectric-thermoelectric coupling mechanisms (Fig. 1-11). This system enables concurrent harvesting of low-grade mechanical and thermal energies via mechano-thermal-electric hybridization. Zhou (Y. Zhou et al., 2020) architectured radial PVDF piezoelectric modules concentrically arranged

with annular Bi_2Te_3 thermoelectric units, evaluating both series and parallel configurations under steady-state flow conditions (volumetric flow rate: 473 cm^3/s). The series-connected configuration demonstrated superior length-specific power density (55 μW/cm) compared to the parallel arrangement (19 μW/cm), representing 35% and 158% enhancements in electrical output relative to conventional thermoelectric generators under analogous operational parameters. This innovation establishes a scalable framework for harvesting previously untapped low-grade mechanical/thermal energy from heated fluids and industrial waste heat streams. Ongoing progress in materials engineering, especially the development of high-performance thermoelectric materials, is expected to further improve the efficiency of waste heat recovery systems.

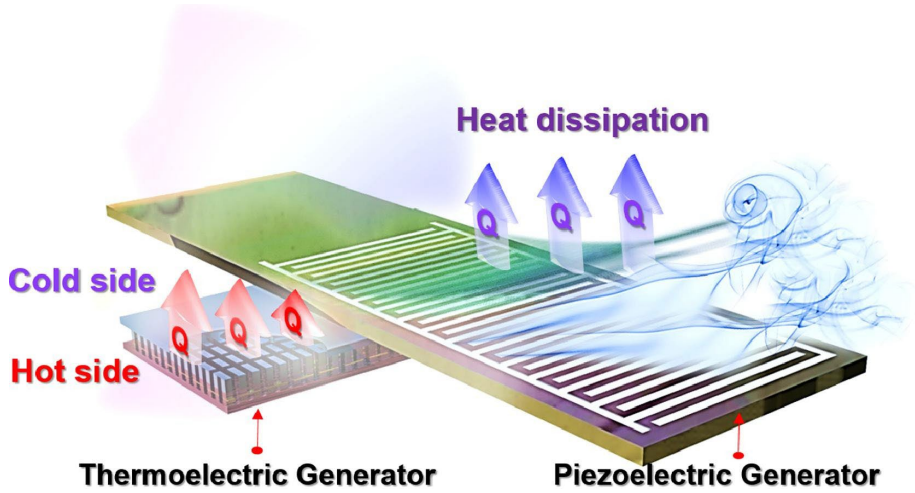


Fig. 1-11: Schematic diagram of a hybrid energy harvester coupling a thermoelectric generator and a piezoelectric generator (S.-B. Kim et al., 2023)

Solar energy harvesting has emerged as a critical pathway for sustainable power generation, with recent innovations demonstrating multifunctional energy conversion capabilities (Van De Loo et al., 2025). Qian (Qian et al., 2024) engineered a self-powered interface circuit synergistically integrating piezoelectric and photovoltaic energy harvesting, achieving 189 μW power output under dual excitation conditions (3.3 V piezoelectric open-circuit voltage and 0.6 V photovoltaic input). This architecture eliminates external power requirements through intelligent energy management algorithms. In parallel efforts, Xu designed bismuth titanate ($Bi_4Ti_3O_{12}$, BTO)-polydimethylsiloxane (PDMS) nanocomposite nanosheets leveraging coupled piezoelectric, pyroelectric, and photocatalytic properties (Xu et al., 2023). The multifunctional platform demonstrated tri-modal energy conversion from solar irradiation,

mechanical vibrations, and thermal fluctuations, achieving 99.37% organic dye degradation within 30 minutes under concurrent stimuli, significantly surpassing single-mode efficiencies (photocatalysis: 59.65%; thermocatalysis: 25.84%; mechanocatalysis: 31.99%). This breakthrough enables 24/7 wastewater treatment through coordinated energy-material interactions, establishing new paradigms for environmental remediation technologies.

Integrated piezoelectric-photovoltaic-thermoelectric tri-modal coupling technology enables synergistic harnessing of ambient mechanical, optical, and thermal energies through coordinated energy-material interactions, achieving unprecedented stability in both power generation and sensing functionalities. This multi-physical field coupling architecture fundamentally addresses the energy source dependency limitations inherent to unimodal systems by enhancing energy conversion efficiency across diverse environmental conditions (temperature: -20-80 °C; humidity: 20-90% RH). The multimodal fusion mechanism ensures data reliability for precision-demanding applications, including adaptive smart sensing networks, autonomous environmental monitoring systems, and biocompatible wearable electronics. When interfaced with AI-optimized IoT frameworks, the system demonstrates self-adaptive energy management through reinforcement learning algorithms. These advancements position tri-modal energy-material systems as transformative platforms for next-generation intelligent electronics, sustainable energy infrastructures, and minimally invasive biomedical diagnostics.

1.2.7. Emerging Horizons

The leap in performance of lead-free piezoelectric ceramic sensors is based on a deep deconstruction and reconstruction of the intrinsic physical mechanisms of the material. The core challenge is to break through the classical framework of traditional piezoelectric theory and move toward the limits of micro-design and multimodal energy conversion.

1.2.7.1. Beyond Classical Theories

1.2.7.1.1 Microstructural Manipulation via Phase Tailoring

Ion doping is a prevalent performance optimization strategy for lead-free piezoelectric ceramics due to its ability to meticulously adjust the intrinsic material properties (Nallagatla et al., 2024). Conventional doping research has centered on the isovalent substitution mechanism,

which entails the introduction of ions of isovalent valence into the lattice sites (e.g., Ca^{2+}/Sr^{2+} substituting for Ba^{2+}, Zr^{4+}/Hf^{4+} substituting for Ti^{4+} in the $BaTiO_3$ system, or Li^{+} substituting for Na^{+} and Sb^{5+} substituting for Nb^{5+} in the KNN system) (Khan et al., 2022; Lam et al., 2025; Osinaga et al., 2024; H. Wang et al., 2024; W. Wang et al., 2022). This type of isovalent doping has been shown to cause only limited lattice distortion (change in lattice constant $\Delta a/a <$ 0.3%), because the substitutional ions have similar ionic radii (Δr <5%) and electronic configurations (e.g., Ca^{2+} and Ba^{2+} both have a closed-shell structure), thus maintaining the stability of the crystal structure (Sudha and Karunagaran, 2024). Extensive research has thus established a mature theoretical framework for isovalent doping (Sethuraman et al., 2025; Subohi et al., 2016; Jiyu Zhao et al., 2025). In recent years, as researchers have gained a more profound understanding of the defect-property correlation mechanism, the focus of research has undergone a gradual shift toward the aliovalent doping strategy (Htet et al., 2024; Z.-H. Zhao et al., 2019). In contrast to isovalent substitution, the introduction of aliovalent ions. (e.g., La^{3+} replacing Ba^{2+}, Ti^{4+} replacing Fe^{3+}) disrupts the local charge balance, inducing the formation of oxygen vacancies or electronic defects to maintain electrical neutrality (Das et al., 2016; M. Ma et al., 2022; Jiao Wang et al., 2021). The effects of such defects can be multifaceted (Cao et al., 2016; Khan et al., 2024; D.-X. Li et al., 2025): 1) defect dipoles may align with spontaneous polarization, enhancing piezoelectric response; 2) charged defects can trap mobile charges and suppress dielectric loss. However, it is imperative to note that excessive aliovalent doping can trigger random local fields, thereby destroying the long-range order of the ferroelectric material and leading to increased relaxation or even the loss of ferroelectricity (Feng et al., 2020; Rinke et al., 2009). For instance, excessive Fe^{3+} doping in BNT has been observed to reduce the remanent polarization by more than 10% (Wu et al., 2018).

Most of these studies, however, have been conducted at the laboratory scale, focusing mainly on optimizing electrical and piezoelectric performance rather than evaluating the feasibility of large-scale synthesis or device integration. Laboratory work often employs idealized sintering conditions, high-purity precursors, and precise compositional control that are difficult to replicate in industrial environments. Engineering research must account for manufacturability, cost, and process tolerance factors rarely addressed in current experimental reports.

Aliovalent doping is regarded as a research and exploratory approach that remains essential in the present and will continue to be in the future. In lead-based ceramics, controlled aliovalent substitutions, such as K^+ doping Pb^{2+}, Fe^{3+} doping Ti^{4+} or Zr^{4+}, enable tailored properties, yielding the "hard" PZT-4 and PZT-8 ceramic materials, which enhance mechanical quality factor (Q_m >1000) and reduce dielectric permittivity (ε_r <1300) (Horchidan et al., 2016; Krupska-Klimczak et al., 2023; R. Wang et al., 2020). La^{3+} can substitute for Pb^{2+}, and Ta^{5+} can substitute for Ti^{4+} or Zr^{4+} in the formation of the "soft" PZT-5H/A, which improves polarization reversibility, achieving high d_{33} (>600 pC/N) and dielectric constant (ε_r >3000) (Liu et al., 2015; H. Wang et al., 2025). For lead-free systems like KNN-based ceramics, aliovalent doping addresses multi-parameter optimization. $Mn^{2+/3+}$ doping mitigates thermal sensitivity by pinning domain walls. Wu demonstrated that 1.5 wt.% MnO_2-doped $0.92(Na_{0.5}K_{0.5})NbO_3$-$0.02(Bi_{0.5}Li_{0.5})TiO_3$-$0.06BaZrO_3$ ceramics achieve d_{33}^* = 470 pm/V with <8% degradation at 100 °C, rivaling soft PZT (M.-H. Zhang et al., 2017). This research on the improvement of properties by aliovalent doping has also been confirmed in other studies (Habib et al., 2022; Liu et al., 2015; H. Wang et al., 2025). The introduction of Ba^{2+} and Zr^{4+} into the KNN system has been shown to spontaneously distort the Nb-O octahedron, thereby optimizing the elastic properties of KNN (Chen et al., 2022; Z. Li et al., 2024), but the associated processing complexity and reproducibility challenges are seldom discussed.

This divergence between laboratory discovery and engineering realization has become a major bottleneck. In the lab, researchers pursue high piezoelectric coefficients (d_{33}, d_{33}*), while engineers prioritize thermal stability, cost efficiency, and device reliability. Bridging these objectives requires not only defect-level design but also scalable processing routes, sintering optimization, and long-term performance validation under practical conditions. Future studies should thus combine atomic-scale insights with engineering-level considerations to enable real-world deployment of lead-free piezoelectric ceramics.

1.2.7.1.2 Energy Conversion Modes

Most of the existing research on lead-free piezoelectric sensors has concentrated on laboratory demonstrations of single-mode signal generation, such as uniaxial pressure sensing or simple combinations of piezoelectric, thermoelectric, and acoustic transduction. These studies have successfully verified the feasibility of multimodal or multi-channel energy

conversion at the material level, yet their evaluations are generally limited to idealized laboratory conditions, emphasizing the improvement of sensitivity or output voltage rather than device reliability, integration, or large-scale manufacturability.

The development of wearable lead-free piezoelectric sensors has demonstrated significant potential in biomechanical monitoring applications, including gesture recognition (Y. Chen et al., 2024) and blood pressure measurement (J. Qiu et al., 2025). However, most reported experiments employ simplified loading modes (uniaxial compression, bending, or tension) under controlled test setups, which do not fully represent the complex, multidirectional, and dynamic forces encountered in real-world environments. Engineering-oriented research that addresses packaging durability, cyclic fatigue, environmental stability, and sensor calibration remains limited. To address this limitation, Prashanth (Maria Joseph Raj et al., 2021) built a self-powered $0.8(Bi_{0.5}Na_{0.5}TiO_3)$-$0.2(Bi_{0.5}K_{0.5}TiO_3)$ piezoelectric sensor capable of concurrent compression, bending, and tensile force harvesting. The ceramic exhibited a piezoelectric coefficient d_{33} = 110 pC/N and remnant polarization P_r = 37.14 μC/cm^2. A sensor fabricated from this ceramic material has demonstrated an output voltage of 8.1 V and a current of 80 nA under tensile stress, 12.5 V and 110 nA under bending deformation, and 22.5 V and 210 nA under compressive loading. This innovation bridges the gap between complex mechanical environments and simplified electrical signal acquisition (Mahanty et al., 2024). The study did not explore process reproducibility, power conditioning circuitry, or long-term signal stability, critical factors for translating such devices into practical engineering applications.

Parallel advancements in the broad dynamic frequency range sensing systems further overcome energy conversion bottlenecks. Pirim (Pirim et al., 2024) developed a bioinspired cochlear sensor array integrating four multi-modal piezoelectric units, which collaboratively capture and filter environmental acoustics across eight frequency bands (300 Hz-6 kHz). Compared to single-mode detectors, this architecture demonstrated a 105% increase in signal-to-noise ratio through phase-synchronized multi-resonant energy harvesting. Such systems exemplify the transformative potential of lead-free piezoelectric in replicating biological sensory paradigms while addressing spectral limitations of conventional devices. These systems rely on precise micro-assembly, clean-room fabrication, and controlled acoustic environments, all of which pose significant challenges to scalable manufacturing and cost-effective

deployment.

The ferro-photovoltaic (FPV) effect has emerged as a critical mechanism for enhancing optoelectronic performance in lead-free piezoelectric systems (Ait Bassou et al., 2024). In KNN/PVDF-TrFE heterostructures, ferroelectric polarization-induced band bending significantly improves carrier separation efficiency, yielding a 13.9% increase in photovoltaic current density under standardized illumination (AM 1.5G) (Lee et al., 2011). The integration of BTO nanoparticles into PVDF matrices leverages strain-gradient-driven flexoelectricity, where mechanical deformation generates spatially modulated internal electric fields (Zhang et al., 2022). These studies highlight the potential for multi-physics energy conversion, combining mechanical, electrical, and optical domains. However, current investigations mainly remain at the proof-of-concept stage, focusing on the enhancement of photoelectric response or strain sensitivity under controlled illumination and deformation conditions. The transition from laboratory-scale prototypes to integrated, robust, and reproducible sensor systems suitable for industrial or biomedical use is still underexplored.

Current research continues to push the boundaries of energy conversion mechanisms in lead-free piezoelectric ceramics; engineering-oriented studies are shortened. Bridging this gap requires cross-disciplinary efforts that integrate materials science, device engineering, and systems design. Future work should emphasize device reliability, packaging, signal conditioning, and cost-performance optimization to translate laboratory innovations into scalable, commercially viable technologies.

1.2.7.2. Smart Sensing and Life Sciences Integration

The proliferation of high-resolution sensor networks has precipitated an era of data deluge, where heterogeneous multimodal data streams from distributed nodes create overwhelming computational demands (Wan et al., 2022; Zhou and Chai, 2020). To address these challenges, laboratory research has primarily focused on the proof-of-concept development of bioinspired sensing systems, which integrate perception, data storage, and local signal processing at the material or device level. These prototypes have demonstrated remarkable sensitivity and multi-modal responsiveness under controlled experimental environments. However, most of these demonstrations remain confined to laboratory conditions, relying on well-controlled stimuli, precise alignment, and short-term measurements. The transition from laboratory prototypes to

deployable engineering systems capable of stable long-term operation in complex real-world environments remains limited.

The realization of bioinspired interactive networks necessitates the integration of multimodal sensing technologies capable of perceiving and processing diverse external stimuli with high fidelity. Bioinspired mechanical sensors detect pressure, tensile forces, and vibrational signals by leveraging advanced piezoelectric, triboelectric, or strain-sensitive materials (Mangi et al., 2025), while thermal sensors utilize thermoelectric and pyroelectric effects to capture dynamic temperature variations (Y. Wang et al., 2022). Similarly, acoustic sensors mimic biological auditory systems by converting vibrational energy into electrical signals through piezoelectric or optomechanical transduction (Pirim et al., 2024), and bioinspired visual sensors employ photodetectors based on the photoelectric and optoelectronic effects to process optical stimuli with high spatial and temporal resolution (Gu et al., 2020). However, current experimental studies often emphasize material sensitivity and signal amplitude improvements, while overlooking system-level integration issues such as data fusion, signal calibration, packaging reliability, and communication interfaces (Beigh et al., 2023; Zhu et al., 2024). This imbalance highlights a critical gap between materials innovation and practical deployment. Neuromorphic computing paradigms inspired by biological neural circuits offer a promising avenue for real-time learning, event-driven processing, and energy-efficient computation (Firoozi et al., 2024; Y. Wang et al., 2022). These studies have shown how memristive and synaptic devices can emulate spatiotemporal signal processing, offering a pathway toward artificial tactile and auditory systems. However, such neuromorphic sensor networks are still tested under simplified laboratory conditions, without addressing thermal drift, noise interference, or power management in realistic scenarios.

From an engineering perspective, large-scale implementation of such intelligent sensor systems requires substantial progress beyond material-level performance. Future research must incorporate robust packaging, standardized testing, long-term reliability evaluation, and the integration of hardware and algorithm co-design to handle data complexity. Unlike laboratory studies that prioritize achieving record-level sensitivity or short-term signal amplification, engineering applications demand reproducibility, scalability, and energy efficiency under uncontrolled and variable operating conditions.

Bridging this divide will require interdisciplinary collaboration between materials scientists, electrical engineers, and data scientists. Laboratory breakthroughs in lead-free piezoelectric materials and neuromorphic architectures must be translated into system-level innovations through scalable fabrication, real-time signal processing algorithms, and adaptive hardware integration. By combining laboratory precision with engineering pragmatism, next-generation intelligent sensing networks could achieve both high-performance functionality and long-term operational reliability, thus driving real-world applications in soft robotics, healthcare, and human–machine interfaces.

1.2.8. Conclusions

The transition toward lead-free piezoelectric sensors represents not only an environmentally responsible shift away from toxic lead-based systems but also a profound transformation in the design philosophy of modern sensing technologies. Over the past decade, laboratory research has achieved remarkable progress in composition design, domain engineering, and defect modulation, yielding materials with electromechanical performance comparable to, or exceeding, that of traditional PZT. Systems such as KNN and BNT have demonstrated outstanding piezoelectric coefficients, tunable Curie temperatures, and strong ferroelectric stability, offering a sustainable foundation for next-generation sensors.

However, most current studies remain confined to the laboratory scale, emphasizing intrinsic property enhancement while neglecting engineering feasibility, process scalability, and cost-effectiveness. Many reported breakthroughs rely on idealized sintering conditions, high-purity precursors, or complex dopant schemes that are difficult to replicate in industrial production. Bridging this gap between laboratory innovation and engineering implementation will be the decisive step in realizing the full practical potential of lead-free piezoelectric technologies. Future research should focus on scalable synthesis, low-temperature sintering, and robust packaging solutions compatible with integrated system architectures.

The synergy between lead-free piezoelectric sensors and artificial intelligence marks a pivotal advancement in sensing technology. Traditional sensors primarily collect data for external processing, but future designs are moving toward intelligent, self-learning systems capable of real-time data interpretation and adaptive responses. Piezoelectric materials exhibit

nonlinear and hysteretic behaviors that were once regarded as limitations but are now being repurposed to facilitate neuromorphic computing. These characteristics enable event-driven sensing, where sensors dynamically adjust their operation in response to changing stimuli rather than continuously acquiring redundant data. This paradigm shift could lead to energy-efficient and highly responsive systems that redefine real-time monitoring and predictive analytics across diverse industrial and biomedical sectors.

Another transformative direction for lead-free piezoelectric sensors is self-powered operation, addressing a longstanding limitation in traditional electronic sensing-reliance on external power sources. By harnessing the mechanical energy present in the environment, these materials can convert motion, vibrations, or pressure into electrical energy, enabling long-term, maintenance-free operation. When combined with complementary energy conversion mechanisms (triboelectric, thermoelectric, and photovoltaic technologies), these sensors have the potential to function autonomously, eliminating the need for batteries. This development is particularly valuable in applications such as remote environmental monitoring, continuous health tracking, and large-scale IoT networks, where power constraints have historically limited deployment and longevity. The prospect of a fully self-sustaining, AI-enhanced sensor network could redefine industrial automation, healthcare, and smart infrastructure.

The breakthroughs required to fully realize the potential of lead-free piezoelectric sensors will require breakthroughs that extend beyond material innovation alone. Progress in this field will depend on a deep integration of multiple disciplines, including materials science, electrical engineering, computational modeling, and bioelectronics. High-throughput computational tools and machine learning algorithms are already accelerating the discovery of optimized material formulations, while advancements in micro/nanofabrication, such as atomic layer deposition (ALD) and additive manufacturing, are enabling unprecedented precision in device structuring. Meanwhile, AI-driven signal processing is enhancing sensor intelligence, allowing for real-time pattern recognition and autonomous decision-making. The convergence of these fields is moving sensor technology beyond incremental improvements, laying the foundation for the next generation of adaptive, multifunctional, and highly efficient sensor systems.

The future of lead-free piezoelectric sensors lies in the integration of laboratory science with engineering practice. Achieving this will require a coordinated effort across materials

science, electronics, data processing, and system design. By coupling atomic-level design strategies with manufacturable device architectures, the field can transition from isolated laboratory demonstrations to scalable, intelligent, and self-sustaining sensor platforms. Lead-free piezoelectric ceramics are not merely substitutes for PZT, they are the foundation for a new generation of smart, adaptive, and sustainable sensing technologies that bridge the gap between environmental responsibility and technological innovation.

1.3. Objective and Scope

From the above discussion, it can be concluded that although lead-free piezoelectric ceramics have demonstrated significant potential for sensing applications in intelligent transportation infrastructure, several critical challenges remain. First, the lack of a systematic and unified evaluation framework hinders the effective comparison of different lead-free piezoelectric systems and limits the translation of laboratory-scale performance into engineering-oriented material selection and design. Second, achieving a balanced optimization of piezoelectric performance and thermal stability in KNN-based ceramics remains a major technical obstacle, which directly affects their long-term reliability under practical service conditions. Third, the electromechanical response of piezoelectric sensors is not only governed by the ceramic material itself but is also strongly influenced by the packaging materials and pavement-sensor interaction, which have not yet been sufficiently quantified. Finally, the arrangement strategy of piezoelectric sensors in pavements lacks a comprehensive modeling framework to ensure accurate vehicle identification with a minimal number of sensors.

Therefore, the objective of this dissertation is to develop high-performance lead-free piezoelectric ceramic materials and compatible packaging systems for pavement sensing applications, to establish a systematic multi-scale evaluation and modeling framework bridging fundamental material research and engineering implementation. Furthermore, the study aims to optimize sensor arrangement strategies for reliable vehicle type identification under realistic traffic conditions. The scope of this research is structured as follows:

Chapter 1 presents a comprehensive review of lead-free piezoelectric ceramics for sensing applications, with particular emphasis on their material systems, processing methods,

piezoelectric performance, thermal stability, and durability. A systematic evaluation framework is established to quantitatively compare different material systems and to assess their suitability for engineering applications. By integrating material performance metrics with application-oriented requirements, this chapter aims to narrow the gap between laboratory-scale research and practical deployment in pavement-based sensing systems.

Chapter 2 focuses on the modification of KNN-based ceramics using $CaHfO_3$ to achieve simultaneous enhancement of piezoelectric properties and thermal stability. The effects of composition, microstructure evolution, phase structure, and dopant distribution on the electromechanical performance are systematically investigated. The optimized ceramic system demonstrates superior piezoelectric coefficients and improved temperature stability, providing a promising candidate material for long-term pavement sensing applications.

Chapter 3 investigates the influence of packaging materials on the piezoelectric response and sensitivity of KNN-based ceramic sensors. Two material systems, epoxy resin-cement composites and waterborne epoxy resin-cement composites, are systematically compared in terms of mechanical compatibility, piezoelectric output characteristics, signal stability, and sensitivity after packaging. The results provide quantitative guidelines for selecting and designing packaging materials that can effectively protect piezoelectric sensors while preserving their electromechanical performance in pavement environments.

Chapter 4 evaluates the feasibility of KNN ceramics as embedded pavement sensors by developing a multiscale dynamic finite element framework based on experimentally measured material properties. Traffic-related factors and sensor configuration parameters are systematically considered to analyze the electromechanical responses of KNN sensors in asphalt and concrete pavements. The results demonstrate the superior applicability of KNN sensors in asphalt pavements and identify optimal installation schemes for different pavement types, providing quantitative guidance for the design and deployment of lead-free piezoelectric sensors in pavement sensing systems.

Chapter 5 is based on the basis of Chapters 2 to 4, which aim to establish an optimization framework for efficient sensor arrangement in intelligent pavement systems using lead-free piezoelectric sensors. An empirical attenuation function between voltage output and tire-sensor

distance is established to enable rapid prediction of sensor responses without repetitive finite element simulations. By integrating different sensor arrangement strategies, vehicle passage paths, and representative vehicle types, the framework identifies optimal deployment schemes under various road and traffic conditions. The results demonstrate that accurate vehicle classification can be achieved with substantially reduced sensor density, providing a scalable and environmentally sustainable solution for practical pavement sensing applications.

Charter 6 summarizes the main conclusions of this dissertation and discusses the key findings obtained from the previous chapters. In addition, it outlines several recommendations and potential directions for future research related to lead-free piezoelectric pavement sensing systems.

2. Enhanced Piezoelectric Performance and Thermal Stability in KNN-BNZ Ceramics Modified by $CaHfO_3$

2.1. Abstract

(K, Na)NbO_3 (KNN) is regarded as a promising lead-free piezoelectric candidate due to its high Curie temperature and environmental compatibility. However, its piezoelectric performance remains inferior to Pb-based ceramics, mainly due to the rigid lattice and high coercive field that restrict domain switching. In this study, $CaHfO_3$ was introduced to modify the perovskite structure of KNN through a homologous co-doping mechanism. The simultaneous substitution of Ca^{2+} and Hf^{4+} modifies the local bonding environment and induces lattice softening, which effectively reduces the coercive field and facilitates polarization switching. At the optimal composition of $0.95(K_{0.5}Na_{0.5})NbO_3$-$0.02(Bi_{0.5}Na_{0.5})ZrO_3$-$0.03CaHfO_3$ (0.95KNN-0.02BNZ-0.03CHO), the ceramics exhibit significant improvements in both ferroelectric and piezoelectric properties, while maintaining a balanced Curie temperature. This work provides clear evidence that structural softening induced by Ca-Hf incorporation provides an effective materials design strategy for enhancing the performance of lead-free KNN-based ceramics, while the compositional limits and long-term device-level behavior require further investigation.

2.2. Introduction

$PbTiO_3$-$PbZrO_3$ (PZT) is one of the typical sensor materials that has been extensively investigated and utilized due to its outstanding piezoelectric performance (Jiang et al., 2024; Liu et al., 2019; Panda and Sahoo, 2015). However, the high lead content in PZT has been identified as a significant environmental and human health hazard (Maizal Hairi et al., 2024; Mourya et al., 2021). To eliminate the risk of using toxic elements, a series of regulations, such as WEEE (Ardolino et al., 2021), RoHS (Fasquelle et al., 2015), and ELV (Rao et al., 2024) have therefore accelerated the search for sustainable and lead-free alternatives. Perovskite ceramics, including barium titanate (G. Li et al., 2025), sodium bismuth titanate (BNT) (Zhou

et al., 2021), and potassium-sodium niobate (KNN) (Difeo et al., 2025), have emerged as promising candidates, with KNN particularly attractive owing to its relatively high Curie temperature (Mondal et al., 2023; Shi et al., 2020). Although the exploration of these piezoelectric materials is growing at an astonishing pace, and several perovskite materials have shown their great potential as lead-free piezoelectric materials, so far, none of them can meet the application requirements either from the piezoelectric properties or the thermal stability perspectives compared with those of PZT (Jin et al., 2025; X. Wang et al., 2025; W. Yang et al., 2020).

To tackle the challenges of relatively low dielectric properties and thermal instability, manufacturing dual-phase KNN/PVDF(Polyvinylidene Fluoride) composites has been proven as an effective method (Rahsepar et al., 2024; Sharma et al., 2024). However, this approach shows a promising way in manufacturing piezoelectric films, its application in bulk ceramics remains difficult due to the large mismatch in mechanical and thermal properties between KNN and PVDF (Zheng et al., 2026a). Apart from the dual-phase piezoelectric composites, selective ion doping is another promising strategy to enhance the dielectric performance of KNN. Unlike the KNN/PVDF composites, which are largely designed for piezoelectric films, selective ion doping is a feasible method for manufacturing bulk piezoelectric materials because the doping process will not confront the property disparity of the main components (Dubernet et al., 2022). The doping elements can be divided into several types, including metal dopants (Mn, Fe, Zn, Cu, Co, Bi) (Qi et al., 2024; Xing et al., 2021; Y. Zheng et al., 2025), rare earth dopants (La, Ce, Sm, Nd, Pr, Y) (Batra et al., 2022; Emmanuel, 2023; Qi et al., 2024; Xianzhao Zhang et al., 2024), alkali metal dopants (Li, Rb, Cs) (Peng et al., 2024), alkaline earth metal dopants (Ca, Ba, Sr) (Chang and Qi, 2022; Dahiya and Hooda, 2024), and tetravalent dopants (Zr, Ti, Sn, Hf) (Tao and Wu, 2016; Tian et al., 2023; Xianzhao Zhang et al., 2024). The Mn/Sb were successfully doped in KNN by a supersonic plasma spraying strategy. It was found that the mechanical and dielectric properties were both enhanced without the formation of a secondary phase (H. Wang et al., 2024). Similarly, Li doping shows the same piezoelectric property boosting effect (Sharma and Kumar, 2024). Na doping has proven a high hardness and outstanding frequency stability (T. Gao et al., 2024).

Previous methods infer that the selective ion doping is a mature and successful method to reach the goal of manufacturing bulk high-performance piezoelectric ceramics. However, two persistent challenges limit the development of high-performance, eco-compliant bulk KNN ceramics. Although chemical doping can enhance domain mobility through lattice distortion and defect engineering, excessive substitution often causes local structural inhomogeneity, defect accumulation, or secondary phases, which offset the expected electrical improvements (Beltrán-Mir et al., 2023; Huo et al., 2023). Achieving effective modification without degrading crystalline quality remains a key challenge (Batra et al., 2022). The strong covalent character of the Nb-O bonds and the limited flexibility of the NbO_6 octahedra hinder polarization rotation, and domain-wall motion, restricting the attainable ferroelectric and piezoelectric response in many KNN-based systems (Xu Zhang et al., 2024). Even compositions with optimized chemistry frequently exhibit only moderate electrical performance due to insufficient domain activation (Q. Qiu et al., 2025; F. Wang et al., 2022). This inverse relationship has emerged as a common bottleneck, limiting the simultaneous optimization of both properties for demanding applications (Nanda et al., 2025b).

Considering these persistent challenges, co-doping strategies (Mn/Sn, Li/Ta) have been explored (Tian et al., 2023; B. Wang et al., 2025; Yao et al., 2013). However, most existing studies focus on heterologous dopants with large differences in ionic radius or valence, whereas the behavior of homologous ions with similar chemistry and ionic size remains largely unexplored. Conventional solid-solution models assume strict competition due to site equivalence and mutual solubility suppression at high concentrations. Recent studies have shown that homologous ions can also relax the lattice cooperatively, which may benefit domain motion (Spurling et al., 2024; Tong et al., 2024).

Motivated by these considerations, $CaHfO_3$ was incorporated into a KNN-based ceramic system to investigate how homologous co-doping affects structural evolution and electrical behavior. Ca^{2+} (r = 134 pm) and Hf^{4+} (r = 78 pm) were selected due to their chemical compatibility with the KNN perovskite framework and their potential to modify the local bonding environment. A comprehensive set of characterizations, including phase analysis, microstructure observation, ferroelectric hysteresis, and piezoelectric measurements, was

conducted to clarify the correlation between lattice characteristics, domain switching behavior, and macroscopic electrical properties. Through this approach, the role of Ca-Hf incorporation in improving functional performance can be systematically evaluated. Furthermore, a comprehensive life cycle assessment (LCA) (Mir et al., 2022; Zygmuntowicz et al., 2024) framework was employed to compare pure KNN, KNN-based composites, conventional PZT, and PZT-based materials, providing a quantitative evaluation of their environmental sustainability.

2.3. Experimental

2.3.1. Material Preparation

The $0.95(K_{0.5}Na_{0.5})NbO_3$-$(0.05-x)$ $(Bi_{0.5}Na_{0.5})ZrO_3$-xCaHfO$_3$ (KNN-BNZ-xCHO, x = 0, 0.01, 0.02, 0.03, 0.04) ceramic systems were fabricated by the solid-state method. K_2CO_3 (99 %), Na_2CO_3 (99.8 %), Nb_2O_5 (99.5 %), Bi_2O_3 (99.999 %), $CaCO_3$ (99.9 %), ZrO_2 (99.5 %), and HfO_2 (99.5 %) (Sinopharm Chemical Reagent Co., Ltd, China, and Aladdin Industrial Corporation) were selected as raw materials. The flow chart of the KNN preparation process is shown in Fig. 2-1.

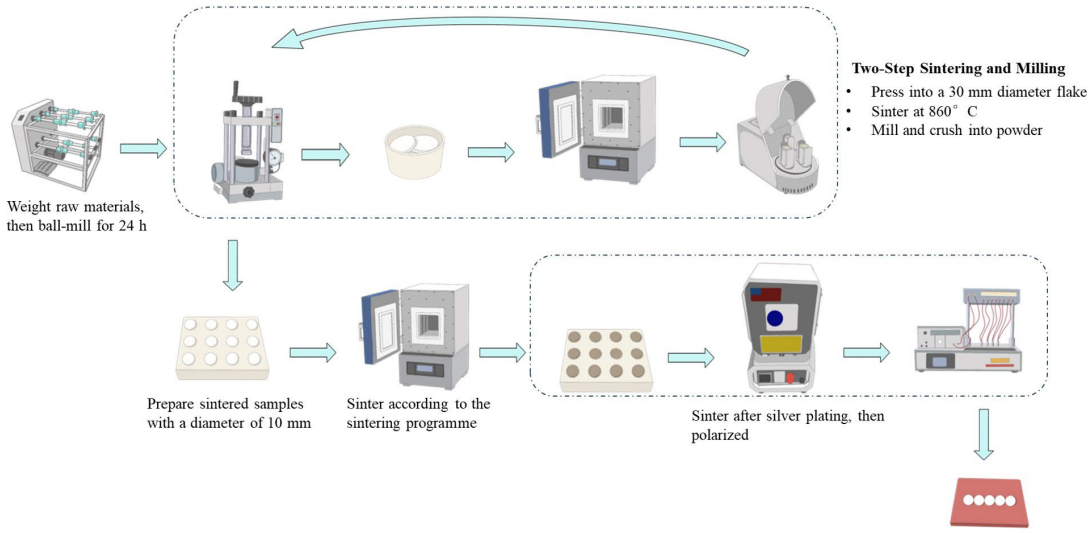


Fig. 2-1: Strategies for preparing KNN-BNZ-xCHO with different dosages of CaHfO$_3$

All raw materials were dried before weighing according to the stoichiometric ratio. These raw materials were mixed by ball mill for 24 h with anhydrous ethanol as the medium. The

mixed powder was pressed into flakes for pre-firing in a corundum crucible at 860 °C for the first time for 5 h. The pre-sintered flakes were crushed in a mortar and placed in a planetary ball mill jar with anhydrous ethanol as the milling medium for 4 hours. Then, the samples were dried and compressed into flakes, followed by a second pre-sintering process at 860 °C for 2 hours. Ball milling was repeated using anhydrous ethanol as the medium. The resulting calcined powder was passed through a 60-mesh sieve and then shaped into 10 mm diameter discs, utilizing 8 wt.% polyvinyl alcohol (PVA) as the binder. The temperature was initially raised from 50 to 1090 °C at a heating rate of 4.5 °C/min, followed by cooling to 1060 °C at a rate of 3.0 °C/min and holding for 2 hours. The temperature was then reduced to 800 °C at a cooling rate of 3.5 °C/min, followed by controlled cooling to room temperature. All ceramic samples were processed under identical conditions to minimize variability from the preparation process. To assess the electrical properties of the ceramics, silver paste was applied to both sides of the sintered disks to form electrodes, which were subsequently baked at 600 °C for 30 minutes. Poling was carried out by applying a DC electric field of 3 kV/mm at 80 °C for 0.5 hours, which was chosen to enhance domain-wall mobility while maintaining structural stability (Q. Li et al., 2017; Zheng and Wu, 2016).

A comprehensive investigation was conducted into the macroscopic properties and microscopic mechanisms of the prepared KNN ceramics. The quasi-static piezoelectric-d_{33} meter (ZJ-3A, Chinese Academy of Sciences, China) was utilized to measure the d_{33} values. Crystal structure information for the sintered ceramics was gathered using an X-ray diffractometer (Bruker D8 Advance). The relative permittivity (ϵ_{33}) as a function of temperature at low temperatures was evaluated with a precision impedance analyzer (Agilent 4990A) equipped with a liquid nitrogen cooling system. The surface morphology of the polished ceramic samples was examined using a scanning electron microscope (Zeiss, Gemini 500, Germany). The high-temperature behavior, including the Curie temperature and dielectric constant, was analyzed using dielectric temperature spectroscopy (Partulob, DMS-500). Polarization (P-E) hysteresis loops were recorded using a ferroelectric test system (Radiant, Premier II, USA). The electromechanical coupling factor k_p (San Emeterio et al., 2003) was calculated from the parameters (f_r: resonance frequency, f_a: antiresonance frequency) obtained

using an impedance analyzer (Agilent E4990A, Hewlett-Packard, Palo Alto, CA) according to Eq. (2-1). The tolerance factor (t_G) (Sato et al., 2016) was calculated according to Eq. (2-2) (where r_A, r_B, and r_O denote the ionic radii of A-site cations, B-site cations, and oxygen anions, respectively).

$$k_p = \frac{1}{\sqrt{0.395\frac{f_r}{f_a - f_r} + 0.574}} \quad \textbf{(2-1)}$$

$$t_G = \frac{r_A + r_O}{\sqrt{2}(r_B + r_O)} \quad \textbf{(2-2)}$$

2.3.2. Environmental Risk Assessment Methodology

Life cycle assessment (LCA) was employed to evaluate the environmental footprint profiles of lead-free KNN ceramic and conventional PZT ceramics (lead-free KNN-BNZ-0.03CHO, undoped $K_{0.5}Na_{0.5}NbO_3$ (Malič et al., 2015), modified $0.3Pb(Zn_{1/3}Nb_{2/3})O_3$-$0.7Pb(Zr_{0.5}Ti_{0.5})O_3$ (Vittayakorn et al., 2006), and conventional $Pb(Zr_{0.45}Ti_{0.55})O_3$ (Bian et al., 2016; Kaur et al., 2017)) across their product systems. The LCA framework comprised four phases: (1) goal and scope definition, (2) life cycle inventory (LCI) analysis, (3) life cycle impact assessment (LCIA), and (4) interpretation.

In this assessment, the functional unit was established as equivalent to piezoelectric ceramic components, adhering to a cradle-to-grave life cycle perspective. The system boundaries encompass all major stages, including raw material extraction, component fabrication, operational use, and end-of-life treatment (see Fig. 2-2).

During the LCI phase, data related to material and energy flows across the entire product system were systematically collected and quantified using a process-based methodology. It is recognized that the KNN ceramics evaluated in this work incorporate certain rare elements, which tend to be associated with elevated energy demands during production. Although prior studies have highlighted the feasibility of recovering elements such as Nb and Bi through optimized recycling techniques (Huang et al., 2023; Lv et al., 2023; Shi et al., 2025), potentially reducing initial resource input and environmental burden. These methods have not yet been effectively extended to ceramic systems, and publicly available databases remain insufficient

in this context. As a result, this study did not incorporate reductions in energy consumption or carbon emissions related to elemental recovery, but instead considered post-use management from a harmless disposal perspective. In contrast, PZT ceramics, characterized by a high Pb content, present additional environmental challenges at the end-of-life stage, which are accounted for in the downstream impact analysis.

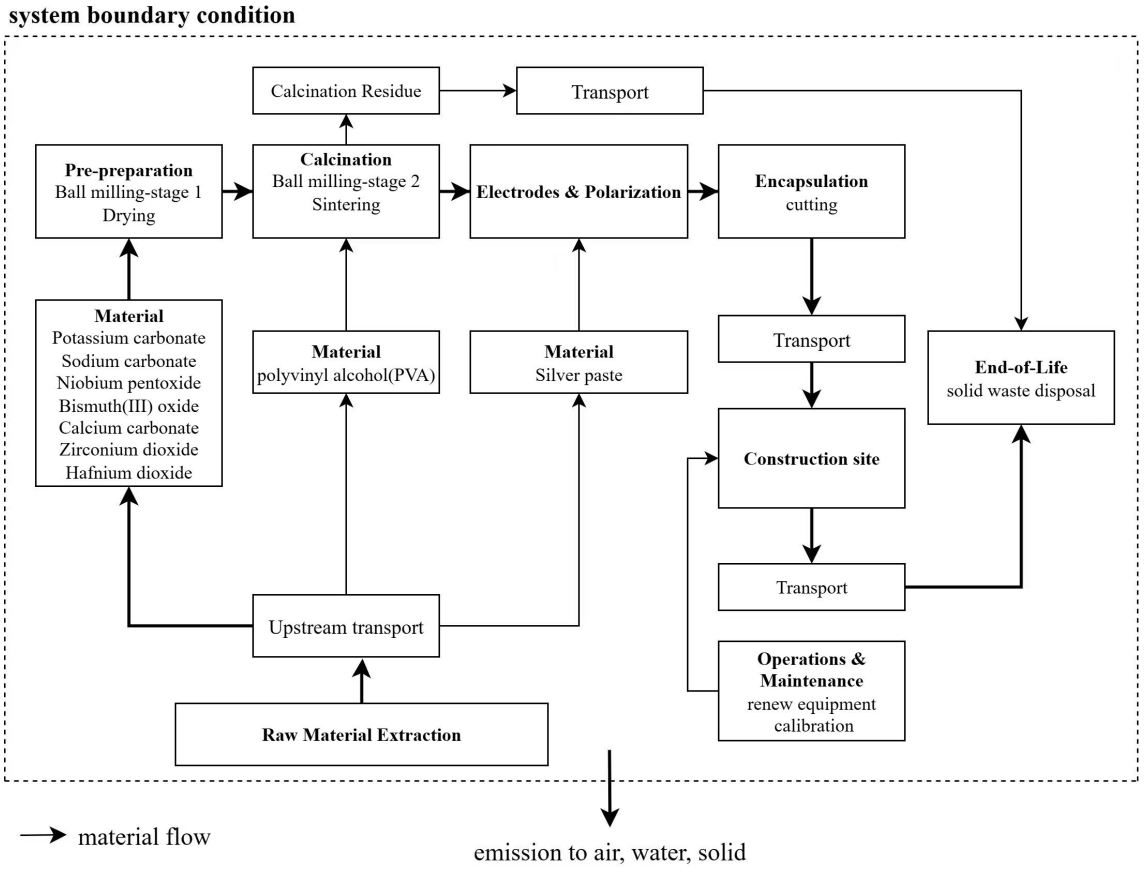


Fig. 2-2: System boundary of LCA for KNN and PZT piezoelectric ceramics

Within the life cycle impact assessment framework, the evaluation focused on two primary environmental indicators: cumulative energy demand (measured in MJ) and global warming potential (GWP, expressed in kg CO_2-equivalent). The GWP metric quantifies the climate impact of greenhouse gas emissions by converting CH_4 and N_2O into carbon dioxide equivalents based on their respective radiative forcing values over a 100-year time horizon. Specifically, the characterization factors applied in this study were 1 for CO_2, 28 for CH_4, and 265 for N_2O, consistent with the IPCC 2013 assessment report (GWP100a). Material procurement costs were calculated using chemical pricing from Sinopharm Chemical Reagent

Co., Ltd. and Aladdin Industrial Corporation. Material procurement costs were calculated using chemical pricing from Sinopharm Chemical Reagent Co., Ltd. and Aladdin Industrial Corporation. Energy consumption parameters were derived from industry electricity tariffs (0.13 €/kWh) by the North Rhine-Westphalia Federal Energy Agency ("North Rhine-Westphalia Federal Energy Agency," n.d.). Hazardous solid waste disposal expenses (solid treatment fee) were sourced from representative quotations of three licensed treatment facilities within the same region, with transportation costs explicitly excluded from the analysis. This geographical boundary limitation ensures methodological consistency by eliminating variables associated with cross-border or inter-state logistics.

2.4. Results and Discussion

2.4.1. Comprehensive Evaluation of Functional and Microstructural Characteristics

The dielectric constant of the KNN-BNZ-*x*CHO composite as a function of temperature (ranging from 25 °C to 425 °C) is shown in Fig. 2-3. A distinct orthorhombic-tetragonal (O-T) phase transition appears near 100 °C and shifts to higher temperatures with increasing CHO content. At $x = 0$ and 0.01, $T_{O\text{-}T}$ are essentially identical, both around 72 °C (71.2 and 71.9 °C, respectively). With further CHO addition, the temperature increased slightly. The Curie temperature (T_c) remains predominantly within 300-320 °C, indicating a good potential for high-temperature applications (Li et al., 2015). The dielectric peak position remains nearly unchanged across 100-1000 kHz, confirming a typical normal ferroelectric (non-relaxor) transition. Dielectric properties were evaluated at 100 kHz, where the influence of electrode polarization and space-charge effects is reduced. The dielectric loss (tan δ) remains relatively low across the temperature range, with a slight increase at higher doping levels, which could be attributed to defect-induced dipolar relaxation. The dielectric constant reaches its maximum at a $CaHfO_3$ doping level of 0.03, rather than at the highest level of 0.04. This observation strongly suggests that the moderate $CaHfO_3$ leads to an optimal synergistic effect within the KNN system, enhancing the dielectric response. Further doping beyond this level degrades the dielectric performance due to microstructural distortion and reduced lattice cooperation caused by competitive cation substitution.

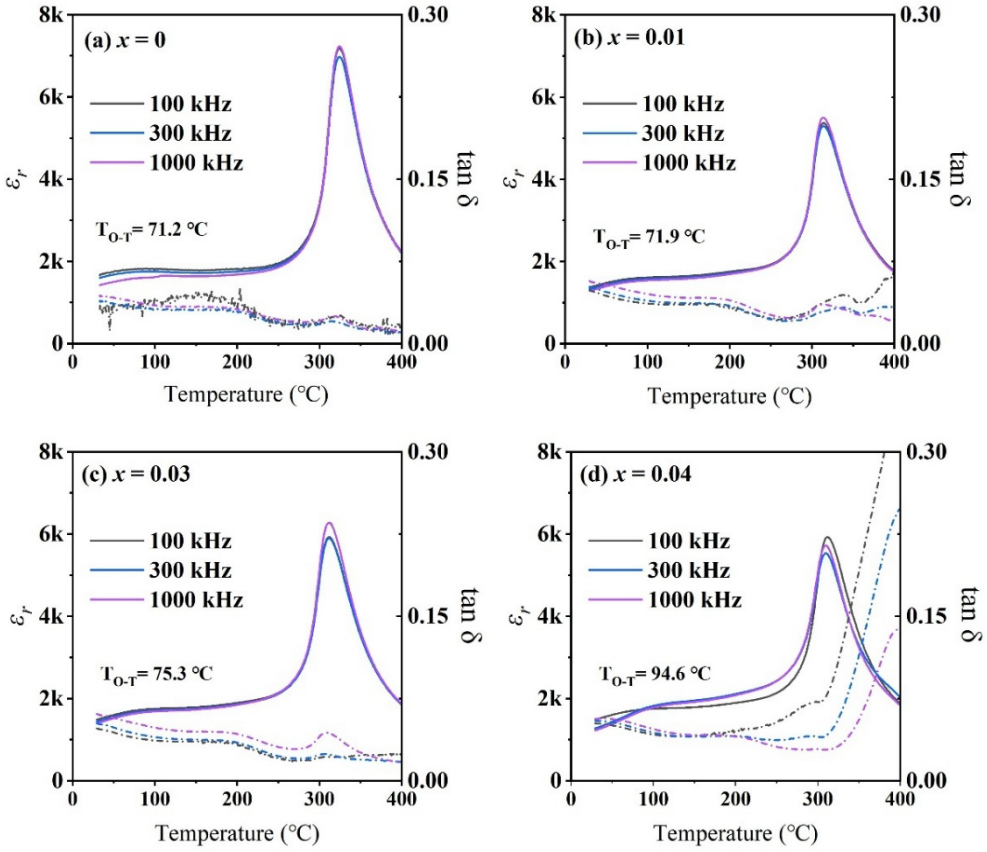


Fig. 2-3: The dielectric constant and tan δ for the KNNS-BNZ-*x*CHO ceramics of (a) x = 0, (b) x = 0.01, (c) x = 0.03, and (d) x = 0.04 with different temperatures and frequencies about 100 kHz, 300 kHz, and 1000 kHz

To further investigate the phase change mechanism of the doping of $CaHfO_3$ in KNN with sintering temperature lower than 1100 °C, especially to explain the impact of the crystal structure on the piezoelectric properties, XRD was implemented to analyze the crystal structure evolution (shown in Fig. 2-4). All samples exhibit a single perovskite phase without detectable secondary phases, indicating that $CaHfO_3$ is successfully incorporated into the KNN-BNZ lattice. As shown in the magnified region around 2θ = 44-47°, the (002) and (200) gradually evolve with increasing $CaHfO_3$ content. The intensity ratio (002): (200) changes from less than 1:2 for low doping levels to approximately 1:2 at x = 0.04, suggesting that the structure gradually changes from an O-T coexistence to an orthorhombic-dominant phase at x = 0.04 (Dwivedi et al., 2018). Rietveld refinement was performed for the best-performing composition (x = 0.03), as shown in Fig. 2-5. The pattern was refined using a two-phase model with orthorhombic (Bmm2) and tetragonal (P4mm) symmetries (Dwivedi et al., 2018; Eklund and

Karttunen, 2025), resulting in a P4mm: Bmm2 phase fraction of 0.22:0.78. For the orthorhombic phase, the refined lattice parameters are a = 5.640 Å, b = 3.974 Å, and c = 5.668 Å, while the tetragonal phase shows lattice parameters of a = 3.985 Å and c = 4.028 Å. This quantitative result supports the structural interpretation derived from the peak-splitting behavior observed in Fig. 2-4. Meanwhile, all diffraction peaks shift slightly toward lower angles with increasing x, indicating a slight lattice expansion due to the substitution of larger Hf^{4+} ions for Nb^{5+} at the B-site. Although XRD reflects only the average crystal structure, these observations imply that $CaHfO_3$ co-doping effectively modifies the lattice configuration and phase balance.

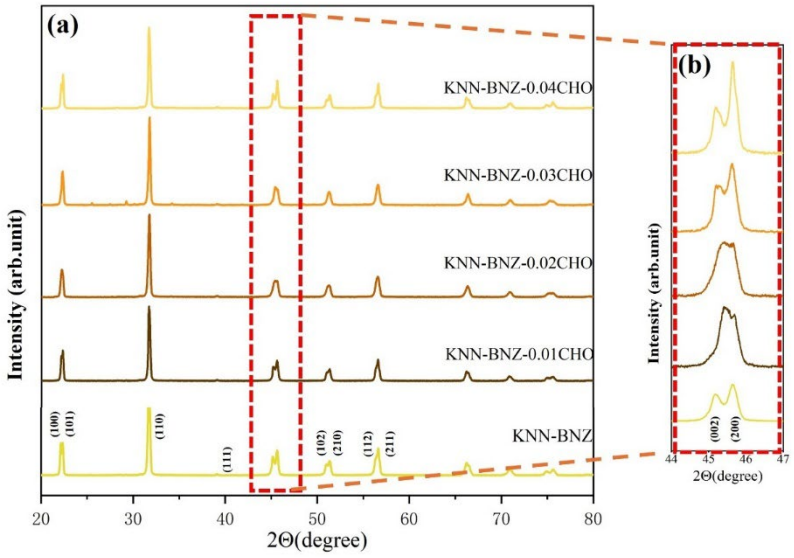


Fig. 2-4: XRD patterns of KNN-BNZ-*x*CHO ceramics as a function of (a) *x* = 0, 0.01, 0.02, 0.03, 0.04 measured at 2θ = 20-80°, (b) magnified XRD patterns at 2θ = 44-47°

The evolution of the microstructure was analyzed by measuring the SEM images of ceramics with varying compositions, as illustrated in Fig. 2-6. The images reveal that all compositions exhibit dense microstructures with well-defined polyhedral grains. $CaHfO_3$ doping does not induce significant changes in grain morphology, suggesting that the performance enhancement is primarily associated with lattice distortion rather than microstructural modification. Across all samples, the grain sizes exhibit a typical bimodal distribution with both large and small grains.

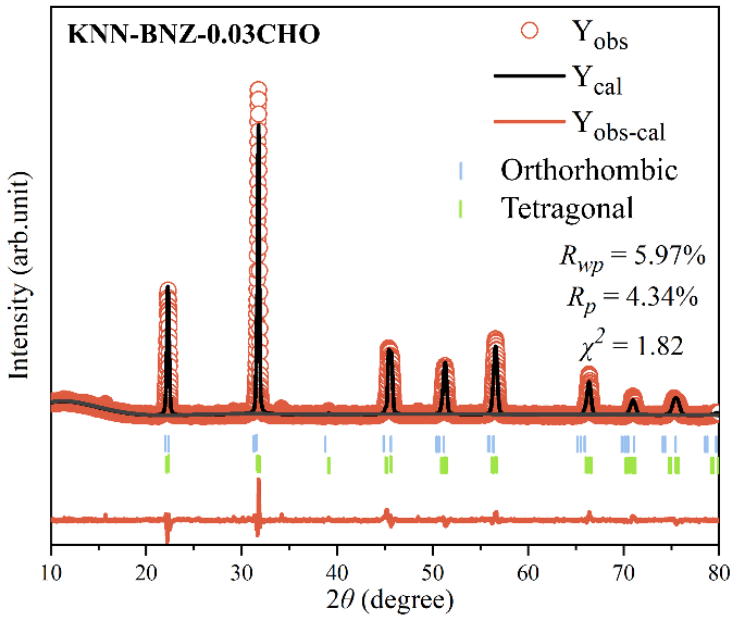


Fig. 2-5: Rietveld refinement of XRD patterns in KNN-BNZ-0.03CHO ceramic

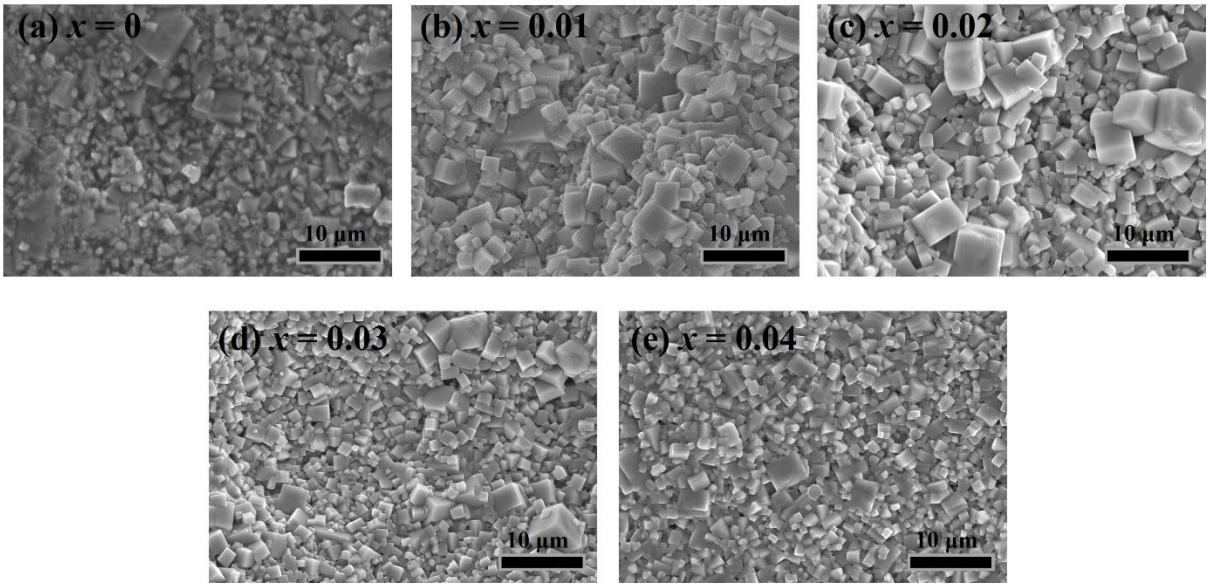


Fig. 2-6: The micromorphology of KNN-BNZ-*x*CHO ceramics for various x values. (a) *x* = 0, (b) *x* = 0.01, (c) *x* = 0.02, (d) *x* = 0.03, and (e) *x* = 0.04

Apart from the dielectric constant, the polarization-electric field (P-E) hysteresis loop is another important indicator for evaluating the ferroelectrically driven piezoelectric response in KNN ceramics. The shape and area of the P-E hysteresis loop can provide insights into their

piezoelectric behavior (Huan et al., 2022). A well-defined loop with high remnant polarization (P_r) and low coercive field (E_c) is generally desirable for practical applications, as it indicates efficient electromechanical energy conversion (R. Li et al., 2024), which is beneficial for piezoelectric energy harvesting and sensing devices. Notably, the interpretation of P-E loops in relation to piezoelectric performance (d_{33}) demands a multifaceted analysis that accounts for both intrinsic and extrinsic mechanisms, including lattice polarization and domain wall dynamics. Fig. 2-7 presents the polarization-electric field hysteresis loops of KNN-BNZ-*x*CHO ceramics under various electric fields and $CaHfO_3$ doping levels.

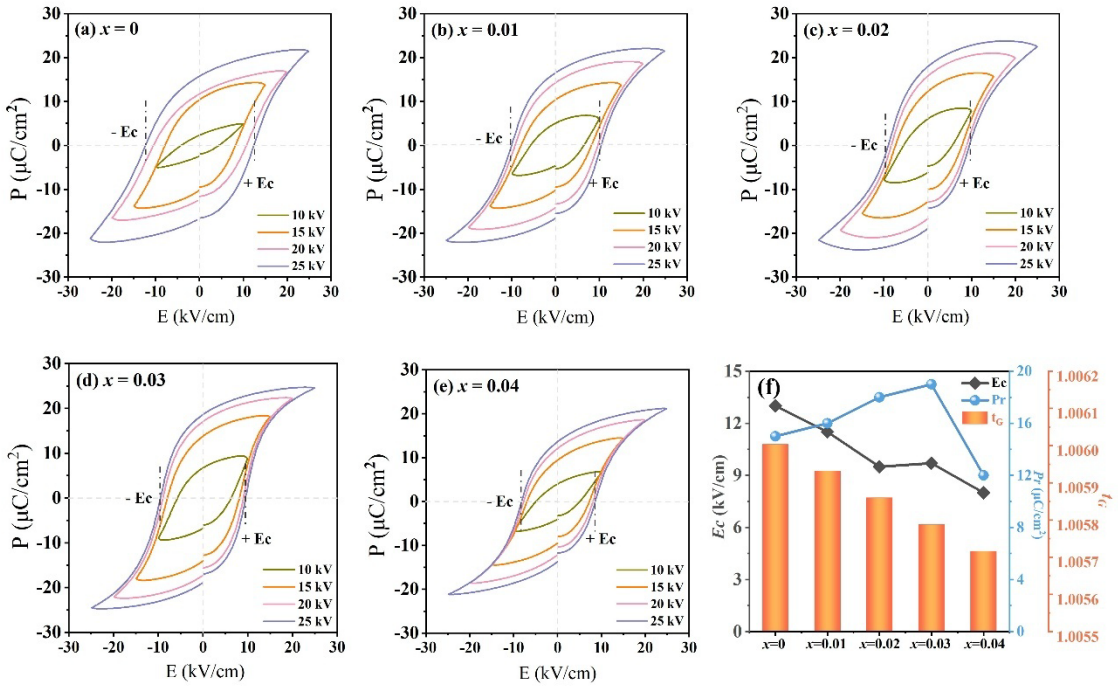


Fig. 2-7: P-E curves of KNN-BNZ-xCHO ceramics as a function of (a) x = 0, (b) x = 0.01, (c) x = 0.02, (d) x = 0.03, (e) x = 0.04, and (f) the comparison of E_c, P_r, and t_G at different $CaHfO_3$ contents

Fig. 2-7 (a)-(e) depicts the P-E loops of samples with $CaHfO_3$ doping levels of 0, 0.01, 0.02, 0.03, and 0.04, which were measured at the electric field (E_c) intensities of 10 kV/cm, 15 kV/cm, 20 kV/cm, and 25 kV/cm, respectively. All compositions exhibit saturated ferroelectric loops under high fields, while the shape and P_r evolve with doping, the undoped specimens (x = 0) exhibit well-saturated hysteresis loops under high electric fields (25 kV/cm), achieving a remanent polarization of 20 μC/cm^2. While P_r increases gradually from 15 μC/cm^2 to 19 μC/cm^2

as the x doping level increases from 0 to 0.03, and then decreases to 12 μC/cm^2 when the doping level reaches 0.04. A similar non-monotonic trend is observed for Pmax, with the highest value also appearing at x = 0.03. This phenomenon indicates that $CaHfO_3$ promotes ferroelectric domain alignment in the low-to-moderate doping range, whereas excessive addition weakens polarization due to over-doping effects (Kumar et al., 2025).

This enhancement is closely related to the structural modification caused by $CaHfO_3$. Ca^{2+} incorporation at the A-site introduces local charge compensation that mitigates defect-induced domain pinning, while Hf^{4+} for Nb^{5+} slightly relaxes the [BO_6] octahedral environment. These factors collectively enhance domain-wall mobility and improve the long-range ferroelectric ordering, resulting in higher P_r. Beyond x = 0.03, defect accumulation and local lattice stiffening suppress domain mobility, leading to weakened switching behavior.

As summarized in Fig. 2-7 (f), the E_c, P_r, and t_G exhibit clear correlations with the doping concentration of $CaHfO_3$. E_c was determined from the P-E hysteresis loop measured at 25 kV/cm, as indicated by the dashed line. With increasing x, E_c exhibits a consistent decline, indicating a reduced energy barrier for polarization reversal and thus facilitating domain switching. The P_r rises significantly within the low doping range (x = 0.01-0.02), attains a maximum value at x = 0.03, and undergoes a noticeable reduction at x = 0.04. The nonmonotonic variation of P_r is consistent with the structural evolution from O-T coexistence to O-phase dominance. The variation of t_G demonstrates a gradual decrease across the doping series, signaling a structural evolution from initial tetragonal distortion toward higher cubic symmetry, confirming a progressive lattice relaxation. The concurrent reduction in E_c and enhancement in P_r suggest that $CaHfO_3$ incorporation induces a softened lattice environment, in which the decreased domain-wall pinning enables more accessible polarization switching. Therefore, compositions within x = 0.02-0.03 achieve an optimal balance between lattice flexibility and ferroelectric stability, providing the structural framework for superior piezoelectric performance, as shown in Fig. 2-7.

The variation of ε_r, d_{33}, k_p, and T_c as a function of $CaHfO_3$ content is presented in Fig. 2-8. The dielectric constant demonstrates a general downward slope with the incorporation of $CaHfO_3$, attaining a local maximum (~1492) at x = 0.03. This variation is mainly related to the

structural evolution. As the orthorhombic phase becomes dominant at higher doping levels, the polarization rotation becomes constrained, leading to a reduction in ε_r. The piezoelectric coefficient remains nearly constant but reaches a maximum of 332 pC/N at x = 0.03, representing a 7% enhancement compared to the undoped system. This slight improvement results from enhanced domain-wall mobility under the balanced structural state. Further increase in $CaHfO_3$ content strengthens the orthorhombic phase, increasing lattice rigidity and reducing d_{33}. k_p shows a similar trend, both reaching their maxima at x = 0.03 and decreasing thereafter. This correlation indicates that both parameters are governed by the same domain-wall motion mechanism. Tc remains stable at 300-320 °C for all compositions, confirming the excellent thermal reliability of the system (Nanda et al., 2025a). Therefore, x = 0.03 represents the optimal composition, achieving a balanced relationship among lattice distortion, phase structure, and domain mobility.

Previous studies have demonstrated that the incorporation of moderate amounts of Hf or Zr ions can significantly enhance d_{33}, but this improvement is usually accompanied by a substantial reduction in the T_c, with the decrease reaching as high as 30-50% (see Fig. S1) (Batra et al., 2022; Kumar et al., 2025; B. Wang et al., 2025; F. Wang et al., 2022). But this work shows that $CaHfO_3$ modification enhances d_{33} while maintaining T_c above 300 °C, ensuring stable performance under elevated operating temperatures.

The non-monotonic enhancement in electromechanical properties (peak d_{33} = 332 pC/N, k_p = 0.457 at x = 0.03) reveals a cooperative co-doping effect between Ca^{2+} and Hf^{4+} in the KNN–BNZ system. $CaHfO_3$ incorporation modifies both A- and B-site sublattices, inducing moderate lattice distortion and increasing octahedral flexibility while maintaining structural integrity during sintering. The synergistic substitution of Zr^{4+}, Hf^{4+}, and Nbf^{5+} in the $[BO_6]$ octahedra provides a more switchable lattice environment, facilitating polarization rotation and enhancing domain-wall mobility. At x = 0.03, this structural configuration yields simultaneous improvement in ferroelectric and piezoelectric properties, while maintaining a balanced Curie temperature. Excessive $CaHfO_3$ addition leads to defect clustering and lattice stiffening, while insufficient doping fails to generate the critical lattice strain required for domain activation. These findings confirm that controlled $CaHfO_3$ co-doping provides an efficient route for

enhancing ferroelectric-piezoelectric performance without compromising thermal stability in lead-free KNN-based ceramics.

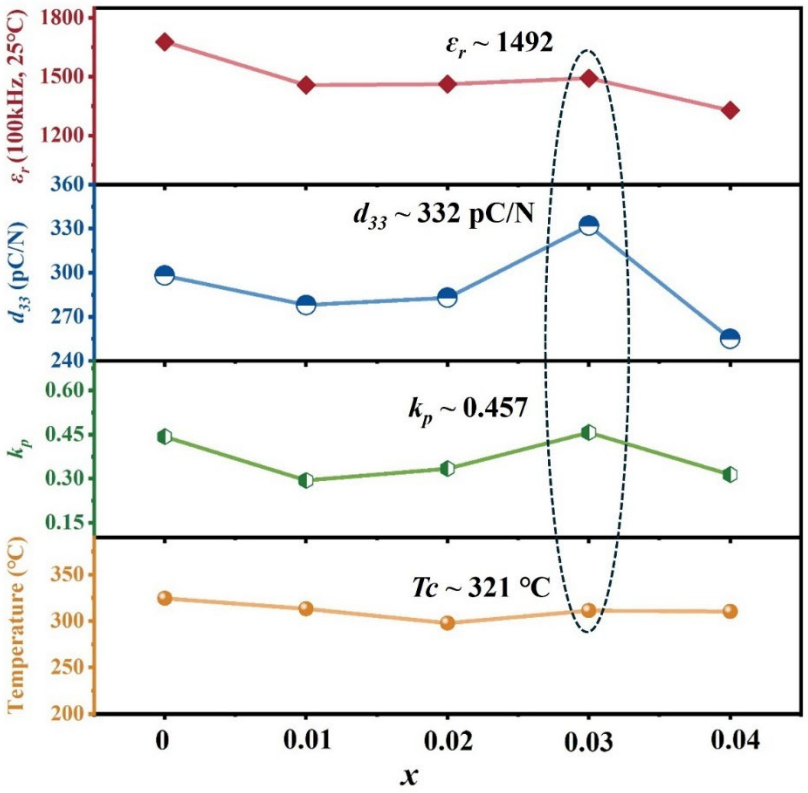


Fig. 2-8: Evolution of dielectric constant, piezoelectric constant, electromechanical coupling factor, and Curie temperature of KNN-BNZ-*x*CHO ceramics as a function of $CaHfO_3$ content

2.4.2. Environmental Risk Assessment Analysis

To evaluate the environmental and economic viability of KNN-BNZ-0.03CHO ceramics compared to conventional lead-based alternatives, a cradle-to-grave life cycle assessment (LCA) was conducted using SimaPro 9.5, according to the ISO 14040 standard. The functional unit was defined as 1 cm^3 of sintered piezoelectric ceramic, encompassing raw material acquisition, ceramic synthesis, energy consumption, and end-of-life waste management.

Table 2-1 presents a comparative analysis of piezoelectric characteristics, life-cycle economic costs, and GWP for four ceramic systems: lead-free KNN-BNZ-0.03CHO (KNN), undoped $K_{0.5}Na_{0.5}NbO_3$ (pure-KNN), modified $0.3Pb(Zn_{1/3}Nb_{2/3})O_3$-$0.7Pb(Zr_{0.5}Ti_{0.5})O_3$ (PZT), and conventional $Pb(Zr_{0.45}Ti_{0.55})O_3$ (pure-PZT). Data reveal that while KNN-based ceramics exhibit suboptimal piezoelectric performance (d_{33} = 160-332 pC/N) compared to PZT systems (d_{33} = 200-690 pC/N), they demonstrate superior environmental and economic sustainability.

The lead-free KNN series achieves a 13-28% reduction in GWP and a remarkable 600% decrease in solid waste disposal costs relative to lead-containing ceramics. Notably, the raw material expenditure shows a strong correlation with dopant ion selection, where strategic optimization could potentially reduce expenses by 18-25% through optimized synthesis protocols. Furthermore, the absence of standardized industrial production processes for KNN ceramics suggests substantial potential for cost reduction through scalable manufacturing implementation.

Table 2-1 Comparative LCA and economic assessment of lead-free and lead-based piezoelectric ceramics

	d_{33} pC/N	Raw materials cost €/t	Energy consumption €/t	Solid waste disposal costs €/t	GWP
KNN	332	228365.1	221.0	300	6.6
pure-KNN	160	88065.4	198.9	130	5.3
PZT	690	202329.5	145.6	1300	7.6
pure-PZT	200	164900.7	249.6	950	7.4

An LCA of four representative piezoelectric ceramics (KNN, pure-KNN, PZT, and pure-PZT) demonstrates significant differences in their GWP, as illustrated in Fig. 2-9a. The lead-free KNN-based systems (GWP, 5.3-5.6 kg CO_2 eq) exhibit markedly lower environmental impact compared to the lead-based PZT counterparts (GWP, 7.4-7.6 kg CO_2 eq). PZT and pure-PZT show a substantial contribution from solid waste disposal, owing to their high lead content. However, such emissions are negligible in KNN and pure-KNN, highlighting the end-of-life environmental safety of lead-free systems. Although the raw material burden is slightly higher in KNN due to the use of Nb_2O_5, this is offset by the absence of toxic by-products and the overall reduction in CO_2-equivalent emissions. Moreover, the electricity-related GWP in KNN can be further mitigated with increased adoption of renewable energy. These findings underscore the environmental compatibility and sustainability of KNN ceramics, validating their potential as a viable and eco-friendly alternative to conventional PZT in lead-restricted applications. This eco-friendly profile strongly aligns with increasingly strict regulations in Europe and other regions that aim to phase out hazardous substances in electronic components.

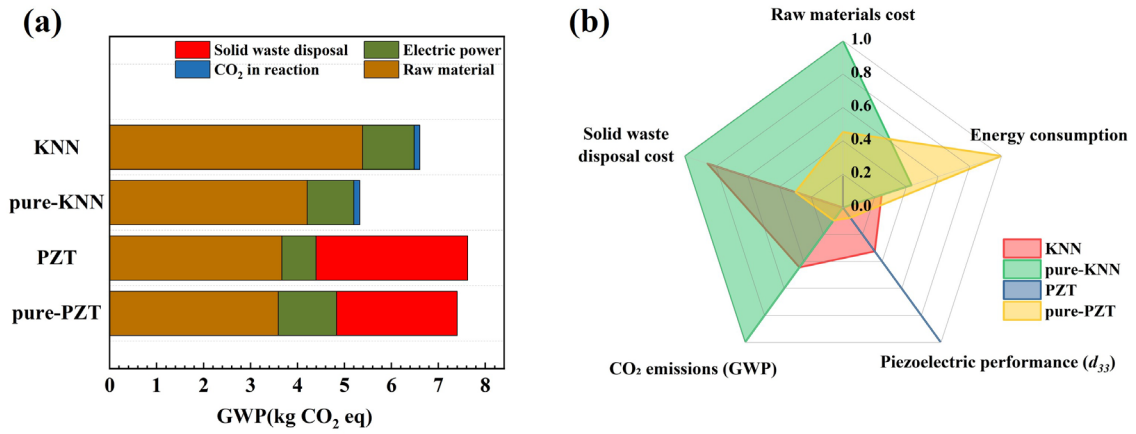


Fig. 2-9: (a) GWP of KNN-series and PZT series in the manufacturing and end-of-life process, (b) Costs of KNN-series and PZT series in the manufacturing and end-of-life process

Beyond environmental advantages, the economic viability of KNN-based ceramics emerges as a critical factor in their industrial adoption. As evidenced by the multicriteria radar analysis (Fig. 2-9b), KNN systems achieve a balanced optimization across material procurement, energy consumption, waste management, piezoelectric functionality, and carbon footprint (scores range from 0 to 1, where 1 represents the most advantageous and 0 the least advantageous). While raw material costs for KNN ceramics remain marginally elevated compared to lead-based alternatives, primarily due to niobium compound utilization, the total life-cycle economics demonstrate parity when incorporating long-term regulatory liabilities associated with lead waste disposal. The piezoelectric coefficient of the optimized KNN composition bridges the performance gap between conventional KNN and PZT ceramics, meeting operational requirements for mid-tier electromechanical applications such as industrial sensors and energy harvesting devices. This functional adequacy is attained without compromising environmental compliance.

Methodological limitations should be considered when interpreting these results. First, converting laboratory energy data to industrial production introduces ± 12% variability in GWP calculations. Second, the current energy demand for KNN fabrication is relatively high, partly because large-scale production facilities and process optimization are still developing. However, reports on continuous sintering equipment suggest that the overall energy requirement can be reduced substantially once industrial manufacturing is established. The economic model accounts for direct material and waste treatment costs, but indirect liabilities associated with Pb-based systems were not included. Although these factors may influence absolute values, the relative advantage of KNN remains unchanged. Improvements in raw-material utilization, Nb

recovery, and waste-handling efficiency are likely to reduce overall cost as industrial production expands (Shi et al., 2025). Therefore, KNN-BNZ-0.03CHO ceramics show practical potential for applications where environmental compliance is required.

2.5. Conclusions

This work demonstrates that the introduction of $CaHfO_3$ into KNN-based ceramics is an effective way to improve piezoelectric performance without increasing the sintering temperature. An appropriate $CaHfO_3$ content promotes the formation of a more complete solid solution, which is reflected in the improved functional properties observed in this work. The ceramic with composition $0.95(K_{0.5}Na_{0.5})NbO_3$-$0.02(Bi_{0.5}Na_{0.5})ZrO_3$-$0.03CaHfO_3$ exhibits a balanced combination of piezoelectric coefficient (d_{33} ~ 332 pC/N), electromechanical coupling factor (k_p ~ 45.7%), and Curie temperature (Tc ~ 321 °C). A life-cycle assessment carried out under the processing assumptions adopted in this study indicates that $CaHfO_3$-modified KNN ceramics can reduce energy consumption and CO_2 emissions compared with conventional PZT-based systems, while avoiding lead-related environmental concerns. It should be noted that these results depend on the selected system boundaries and the specific processing routes considered here.

Although the saturation limit of $CaHfO_3$ doping and long-term performance at the device level have not yet been fully established, and the reproducibility of the piezoelectric properties under large-scale processing conditions was not addressed in this study, the present results suggest that $CaHfO_3$ modification provides a practical and experimentally accessible approach to improving the performance of lead-free KNN-based piezoelectric ceramics. The materials design strategy is particularly relevant for applications subject to increasingly strict environmental regulations.

3. Epoxy-Cement Composite Packaging for KNN Piezoelectric Sensors

3.1. Abstract

Durable and high-performance piezoelectric sensors are critical for long-term infrastructure monitoring, especially under harsh mechanical and environmental conditions. The choice of encapsulation materials plays a decisive role in determining their stability, sensitivity, and service life. This study evaluates solvent-based and waterborne epoxy resins, with/without cement, for potassium sodium niobate (KNN)-based sensors. Cement addition in solvent-based epoxy reduced compressive strength and signal stability, yet maintained high sensitivity and good linearity under loading. Waterborne epoxy-cement composites achieved higher strength (≤57.8 MPa) and 2-4 times greater voltage output. However, these composites failed structurally at loads exceeding 600 N, limiting their use in environments with heavy loads. Fatigue tests showed that solvent-based epoxy encapsulation had excellent durability, with only a 4.4% voltage drop after 100,000 loading cycles. This indicates superior robustness for long-term deployment. The results reveal a trade-off between sensitivity and robustness in packaging strategies. Waterborne systems are suitable for low-to-moderate load conditions where sensitivity is prioritized, while solvent-based epoxies offer long-term reliability under repetitive and higher mechanical stresses. These findings provide important material selection guidelines for the development of reliable, lead-free piezoelectric sensors tailored to the specific demands of infrastructure health monitoring applications.

3.2. Introduction

The development and sustainability of urban infrastructure are intrinsically linked to the quality and longevity of road networks (Berglund et al., 2020). Ensuring the safety and structural integrity of pavements requires continuous monitoring, for which embedded sensor technology has emerged as a promising solution (Deng et al., 2023). Among the various sensing technologies, piezoelectric sensors have been widely applied due to their high sensitivity, fast

response, and robustness. In particular, embedded piezoelectric sensors allow for real-time monitoring of internal stress evolution and damage progression in cementitious materials, offering critical data to guide maintenance and extend service life (Dumoulin et al., 2014; Yu et al., 2022).

Indeed, lead zirconate titanate (PZT) piezoelectric ceramics have become the de facto standard for embedded sensors in structural health monitoring of infrastructure (Kee and Zhu, 2013). Extensive research demonstrates their successful deployment within various cement-based and cement-polymer composite packaging systems, including cement-epoxy "smart aggregates" for hydration monitoring, grooved-interface sensors for enhanced coupling (Liu and Wei, 2022; Y. Ma et al., 2022), and dedicated packages for impact damage detection and non-destructive stress/strain evaluation (Pan and Guan, 2022; Zhang et al., 2021). These PZT-based sensors, embedded within the concrete matrix, exhibit proven capabilities such as high sensitivity to internal damage, effective filtering of external noise, and stable signal acquisition during critical processes like curing, establishing their functional efficacy for in-situ monitoring applications. However, a significant and growing concern overshadows this technological maturity: the high lead content intrinsic to PZT ceramics presents substantial environmental and toxicity risks, particularly concerning leaching during end-of-life disposal or structural demolition (Ibn-Mohammed et al., 2016). This critical drawback fundamentally contradicts the principles of sustainable infrastructure development. This has created a pressing demand for high-performance, lead-free piezoelectric alternatives (Panda and Sahoo, 2015).

Potassium sodium niobate (KNN)-based ceramics present a highly promising, environmentally benign alternative to lead-based PZT. Typical piezoelectric charge constants (d_{33}) of 80-160 pC/N, and Curie temperatures of 380-420 °C make KNN competitive with certain PZT formulations, particularly where high-temperature operation and lead-free compliance are required (Huan et al., 2022; Jin et al., 2025; R. Li et al., 2024). However, compared with PZT, KNN’s lower relative permittivity, distinct electromechanical coupling behavior, and differences in mechanical stiffness can reduce charge accumulation and dielectric displacement under identical loading. This often results in lower voltage output and narrower signal bandwidth in embedded applications. Furthermore, the multiphase interphase zone (PZT/KNN sensor/packaging material/pavement matrix) governs the system's efficacy and

longevity (Saber and Hosseini-Toudeshky, 2024). The adhesion between the sensor and the surrounding road surface can significantly impact the sensor's ability to accurately detect and transmit data, potentially leading to signal delays or disruptions and making it challenging to comprehensively understand the real-time situation (Ye et al., 2024; Zhang et al., 2021). The direct substitution of PZT with KNN ceramics in embedded sensors is fundamentally impeded by mismatches in dielectric coupling efficiency and interfacial compatibility, which critically govern electromechanical energy transfer and stress wave propagation within matrices. Thus, research focusing predominantly on bulk KNN properties (Kumari et al., 2019) or employing packaging paradigms optimized for PZT (Pan et al., 2024; Soman and O'Neal, 2011) overlooks these KNN-specific interfacial complexities. A critical knowledge gap persists in understanding the evolution of interfacial bonding under cyclic loading, associated stress transfer mechanisms, and their effects on electromechanical response and cohesive/adhesive failure within the KNN-package-pavement system. Therefore, merely substituting PZT elements with KNN ceramics within existing packaging architectures represents an inadequate strategy, likely leading to suboptimal performance and premature failure. Fundamental investigation into tailoring interface engineering and packaging design specifically for KNN's material characteristics is imperative to achieve robust interfacial bonding, maximize electromechanical coupling efficiency, ensure signal stability, and guarantee compatibility over decades of service.

To address the dual requirements of environmental compatibility and mechanical durability in embedded pavement sensors, this study adopts potassium sodium niobate (KNN) ceramics as the piezoelectric sensing unit, combined with cement/solvent-based epoxy and cement/waterborne epoxy composites as encapsulation materials. These systems were selected to represent a balance between long-term bonding stability and reduced environmental impact, both being representative in pavement sensor integration. Appropriate packaging is critical for maintaining measurement accuracy and extending service life, as mechanical mismatches at the sensor–matrix interface can induce stress concentrations and lead to premature failure (Julphunthong et al., 2025; Zhou et al., 2016).

Previous studies have shown that PZT-based sensors can be effectively packaged using either solvent-based epoxy or cement-based materials (Tiantong et al., 2022; Wittinanon et al., 2024, 2023). Solvent-based epoxy offers strong bonding and stable output in concrete, while

cement-based encapsulation may improve strain transmission and measurement accuracy (Y. Ma et al., 2022; Xu et al., 2014). In addition, several studies have demonstrated that the combination of solvent-based epoxy and cement is also an option to enhance the durability of the sensors by reducing the aging of the epoxy when exposed to UV light (Souza et al., 2025). While these findings confirm that both epoxy and cementitious materials are feasible for packaging PZT piezoelectric devices (Y. Ma et al., 2022; Savakus et al., 1981; Ye et al., 2025), two main knowledge gaps need to be bridged for exploring environmentally friendly piezoelectric sensors. First, while waterborne epoxy is a more sustainable alternative, its compatibility with cementitious matrices has not been fully explored. Second, most existing studies focus on PZT-based systems; the interaction between lead-free ceramics such as KNN and epoxy/cement packaging remains unclear.

In response to these gaps, this work develops a KNN-based piezoelectric sensor encapsulated with waterborne epoxy and cement composites, aiming to evaluate their mechanical compatibility and sensing performance. The mechanical behavior of the packaging layers was characterized at both macro and micro scales, while the sensitivity, stability, and repeatability of the KNN-based sensor were evaluated in a similar testing environment. This work provides a fundamental basis for the development of low-cost, lead-free, high-performance embedded sensors tailored for structural health monitoring in concrete pavements. By targeting both the lack of systematic application of KNN in cementitious environments and the insufficient understanding of sensor-matrix mechanisms, the findings contribute to the advancement of smart, sustainable, and resilient infrastructure systems.

3.3. Materials and Characterization Methods

3.3.1. Materials Preparation

In this study, lead-free piezoelectric ceramics, epoxy-based packaging composites, and embedded sensor prototypes were prepared for experimental evaluation. The preparation procedures for each component are described below.

3.3.1.1. Synthesis of KNN Ceramics

Potassium sodium niobate-based ceramics with the nominal composition 0.95 $0.95(K_{0.5}Na_{0.5})$ NbO_3-$0.02(Bi_{0.5}Na_{0.5})$ ZrO_3-$0.03CaHfO_3$ (KNN-BNZ-0.03CHO) ceramics

were synthesized via the solid-state reaction method. The starting materials included K_2CO_3 (99 %), Na_2CO_3 (99.8 %), Nb_2O_5 (99.5 %), Bi_2O_3 (99.999 %), $CaCO_3$ (99.9 %), ZrO_2 (99.5 %), and HfO_2 (99.5 %), which were supplied by Sinopharm Chemical Reagent Co., Ltd, China. All starting powders were oven-dried and weighed according to the designed stoichiometric composition, then wet-milled in absolute ethanol for 24 h. The dried slurry was pressed into thin compacts and calcined in a corundum crucible at 860 °C for 5 h. The pre-sintered bodies were crushed in an agate mortar, re-milled in a planetary ball mill with ethanol for 4 h, dried, and pressed again into compacts for a second calcination at 860 °C for 2 h. A final milling step in ethanol was performed, and the calcined powder was sieved through a 60-mesh screen to ensure uniform particle size. The powder was then mixed with 8 wt.% polyvinyl alcohol (PVA) binder and uniaxially pressed into 15 mm diameter discs.

Sintering was conducted under a controlled schedule: the temperature was ramped from 50 °C to 1090 °C over 240 min, lowered to 1060 °C within 10 min, and held for 2 h, then reduced to 800 °C over 80 min before furnace cooling to room temperature. All samples were processed under identical conditions to minimize preparation-induced variability (K. Zheng et al., 2025).

3.3.1.2. Preparation of Packaging Materials

Packaging materials: The study selected solvent-based epoxy and waterborne epoxy as matrix materials, which were compounded with cement (Portland cement P·O 42.5 with a density of 3200 kg/m^3) in varying ratios to prepare composite slurries (see Table 3-1). The solvent-based epoxy employed in this study is diglycidyl ether of bisphenol A, with a molecular formula of $C_{21}H_{24}O_4$ and a density of 1.17 g/cm^3. The curing agent used has a molecular formula of $C_5H_{12}FNO$, a density of 0.957 g/cm^3, and a viscosity of 6 Pa·s. A commercially available waterborne epoxy resin (60% solids by weight) was procured from Shandong Jiazihu Lakeside New Materials Science & Technology Co., Ltd., and utilized as the base resin in the formulation.

Epoxy resin and curing agent were premixed at a mass ratio of 100:10 for 3 min, followed by the gradual addition of cement powder under mechanical stirring (800 rpm) to prevent local agglomeration and ensure uniform dispersion. For the waterborne epoxy-cement system, waterborne epoxy resin emulsion, curing agent, and a defoamer (added at 1 wt.% of the total mass of the premixed waterborne epoxy resin) were first premixed for 3 min. Cement powder was then added gradually under mechanical stirring at 800 rpm to ensure uniform dispersion. The effective water-to-cement ratio (w/c = 0.43) was maintained for all mixtures, where the total water content included both the intrinsic water in the waterborne epoxy resin and the

externally added water, which was adjusted accordingly. After mixing, the slurry was gently vibrated to remove air and cast into 20 × 20 × 20 mm cube molds for curing.

Table 3-1 Mix composition of the packaging materials

		Matrix materials/g	Cement/g	Additional solvents (deionized water and defoamer)/g
Solvent-based epoxy	100:0	100	0	0
	100:50	67	33	0
	100:100	50	50	0
	0:100	0	100	0
Waterborne epoxy	100:0	100	0	1
	1:100	1	100	42.61
	5:100	5	100	41.05
	10:100	10	100	39.1
	50:100	50	100	23.5
	100:100	100	100	4
	0:100	0	100	43

3.3.1.3. Fabrication of Embedded Sensors

The resultant ceramic disc was then polished to a thickness of 0.8-1 mm, with silver electrodes printed on the surface, and subsequently sintered at 600 °C for 30 min. The samples were then polarized in an electric field of 3 kV/mm at 80 °C for 0.5 hours.

To construct the piezoelectric sensor unit, five silver-electrode-coated ceramic discs were stacked and bonded to form a cylindrical element with dimensions of approximately 15 mm × 5 mm (see Fig. 3-1). Copper wires were soldered onto the top and bottom surfaces as electrical leads. Finally, the assembled structures were packaged using different packaging materials, resulting in a rectangular sensor with an average length and width of 19 ± 1 mm and 9 ± 1 mm in height (with slight dimensional variations due to the fabrication process).

The piezoelectric coefficient (d_{33}) of the unpackaged KNN ceramic element was measured to be 321 pC/N. After packaging, the d_{33} values decreased slightly to 317 pC/N for the solvent-based epoxy and 309 pC/N for the waterborne epoxy, indicating that the poling state of the ceramic element was well preserved and that the packaging layer caused negligible degradation in the intrinsic piezoelectric properties.

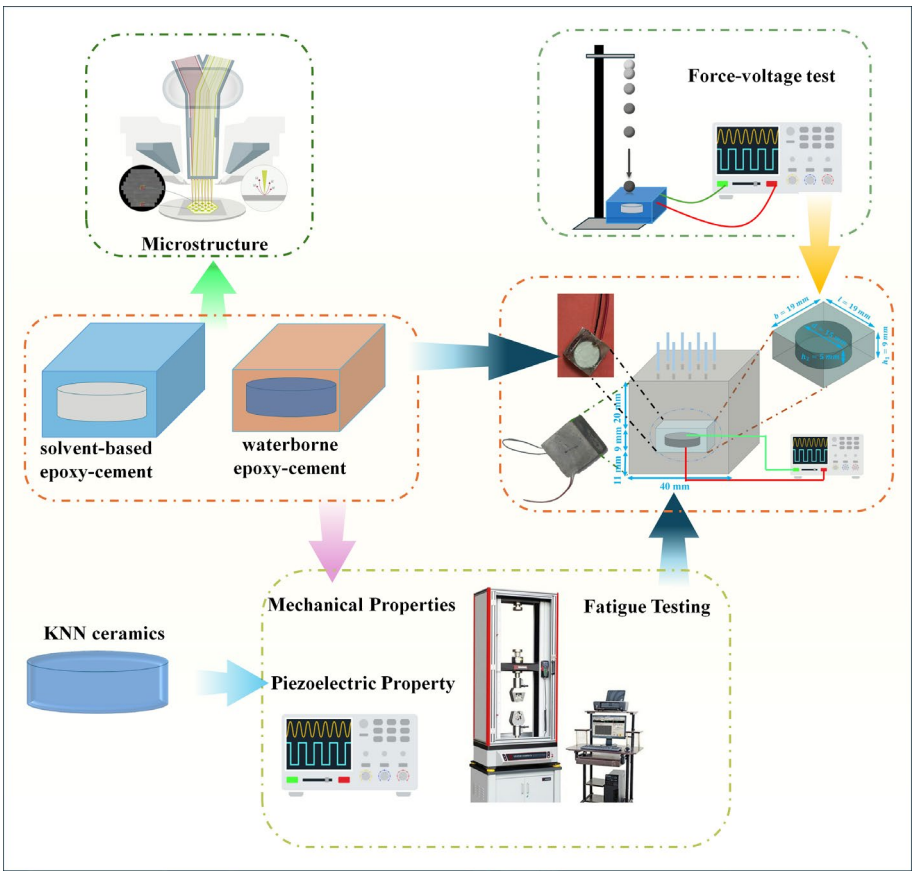


Fig. 3-1: Schematic workflow of sensor encapsulation, characterization, and performance evaluation

3.3.2. Characterization Methods

The slurry was prepared by mixing epoxy resin and cement in different ratios and cast into 20 mm × 20 mm × 20 mm standard cube specimens. The specimens were cured in a constant temperature environment at 60 °C for 24 hours, after which compressive strength tests were conducted following ASTM C109/C109M standards using a universal testing machine (Instron 5967, USA). The compressive load was applied under displacement control at 0.5 mm/min until failure. Given the chemical reaction between waterborne epoxy and cement, a series of specimens with varying ratios was prepared in this study. These specimens were cured in a standard curing chamber (temperature 20 ± 2 °C, relative humidity ≥ 95%) for 3 days, 7 days, and 28 days, respectively. Following this, compressive strength tests were performed to investigate the influence of material ratios and curing ages on the mechanical properties of the composite materials.

For scanning electron microscopy (SEM) analysis, specimens were extracted from the crushed mortar samples obtained from the compressive strength tests. The fragmented specimens were cut into cubes with dimensions of less than 5 mm. These cubes were immersed in isopropanol for 24 hours and subsequently dried in a vacuum oven at 42 °C for an additional

24 hours. The SEM analyses were conducted using a JSM-IT800 field emission scanning electron microscope (FE-SEM) system manufactured by JEOL Ltd., Japan, at an accelerating voltage of 15.0 kV.

Sensitivity testing of the packaged sensing unit was performed based on the principle of momentum conservation. The sensor leads were connected to an oscilloscope (Tek MSO-3014), and small spheres of varying masses were dropped from a fixed height of 30 cm through a guiding frame to ensure consistent alignment and minimize human error during manual release, as illustrated in Fig. 3-1. Each impact test was repeated ten times for every specimen, and the average voltage responses were used for analysis. In total, ten independent specimens were tested for each packaging material, resulting in 1,000 voltage measurements per group. The coefficient of variation of the output voltage was below 5%, demonstrating satisfactory repeatability. The corresponding force-voltage relationship was then derived to evaluate the sensor's force-to-electric conversion characteristics and sensitivity. All voltage data were processed using identical filtering, normalization, and statistical methods to ensure consistent comparison among different material systems.

To evaluate the long-term durability of the piezoelectric sensor, a fatigue test was conducted by embedding the sensor within a 40 mm × 40 mm cement paste specimen. To simulate realistic compressive load transfer, the sensor was embedded at a depth of 20 mm from the specimen surface, as illustrated in Fig. 3-1. The fatigue test was carried out using a hydraulic-servo universal testing machine (COOPER HYD25). The specimens were subjected to a constant axial load of 5 kN at a loading frequency of 10 Hz, with the ambient temperature maintained at 20 ± 5 °C, and relative humidity 40-50%. Three independent specimens were used for this test. A total of 100,000 loading cycles was applied. The open-circuit voltage output of the sensor was continuously monitored using an oscilloscope. Peak voltage values were recorded at intervals of every 10,000 cycles to assess signal variation over time. Additionally, full waveform snapshots were captured after the first loading cycle and upon completion of 100,000 cycles to evaluate waveform consistency and quantify any signal attenuation by the oscilloscope.

3.4. Results and Discussion

3.4.1. Characterization of Packaging Materials

3.4.1.1. Mechanical Properties

Before evaluating the compatibility between the KNN and the epoxy/cement packaging

materials, the essential factor is to explore the mechanical properties of the packaging materials. As a result, we tested the compressive strengths of the solvent-based epoxy and the waterborne epoxy, along with cement with various cement/epoxy ratios. The results are plotted in Fig. 3-2. As can be seen from Fig. 3-2a, the compressive strength of the traditional solvent-based epoxy decreases with increasing cement content from zero to 100%. The neat solvent-based epoxy resin demonstrates a compressive strength of approximately 110 MPa, and remains relatively constant at around 90 MPa for epoxy: cement = 100: 50 and epoxy: cement = 100: 100 by mass. This phenomenon can be ascribed to the fact that the addition of cement primarily serves as a filler material embedded in the solvent-based epoxy matrix. Without the hydration process, the reinforcement effect of the cement in the solvent-based epoxy is quite limited because the addition of the cement particles brings more cement/epoxy interfaces, leading to extra defects that weaken the mechanical properties.

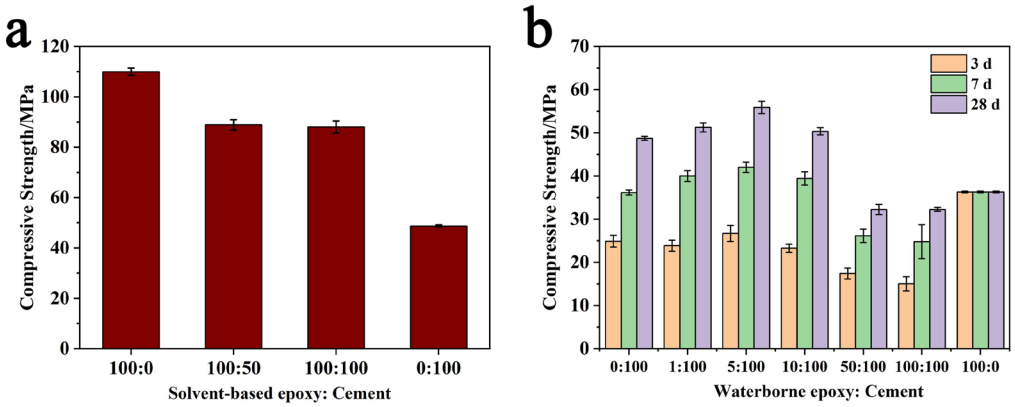


Fig. 3-2: The compressive strength of packaging materials with varying cement dosage, (a) solvent-based epoxy packaging material, (b) waterborne epoxy packaging material

Meanwhile, as demonstrated in Fig. 3-2b, the compressive strength as a function of the cement/epoxy ratio of the waterborne epoxy shows a "*bell*" trend. The maximum 28-day compressive strength (55 MPa) appears at the waterborne epoxy: cement = 5:100. Although the compressive strength is not as high as that of the solvent-based epoxy, the merits of using the neat waterborne epoxy are acceptable. First, the manufacturing cost will be significantly reduced by using the waterborne epoxy because the solid content of the epoxy has been considerably reduced. Second, as can be observed in Fig. 3-2b, with the increasing cement content, the compressive strength boosts from 35 MPa to over 55 MPa, due to the hydration of the cement particles. In addition, for the health monitoring application of the cement concrete structures, provided with cement packaging, the compatibility between the sensing device and the cement structure can be significantly improved, which is beneficial to enhance the accuracy of the output data (Zhang et al., 2021; Zhou et al., 2016).

3.4.1.2. Interactions between the Cement and Epoxy Resins

To understand the interaction mechanism between the epoxy and the cement fillers, the fracture surfaces of the solvent-based epoxy and waterborne epoxy mixed with cement particles are compared through SEM images. As can be observed from Fig. 3-4a, the fracture surface of the neat solvent-based epoxy resin is smooth without any apparent microcracks. However, with the addition of cement particles, the fracture surfaces have become typical brittle fracture modes (Fig. 3-3b). The cracks are propagated along the interfaces between the cement particles and the solvent-based epoxy matrix. Most importantly, barely any hydration products can be observed even with mixing high-weight content of cement. It is in agreement with the results of the compressive strength testing, shown in Fig. 3-2a.

Unlike the solvent-based epoxy, the fracture surfaces of the waterborne epoxy are more complicated. As depicted in Fig. 3-4a, with the addition of cement particles, the hydration production of the cement is observable. In contrast to the unreacted cement particles in the solvent-based epoxy matrix, which cause the interfacial defects (Fig. 3-3b), typical C-S-H hydration products can be identified. In addition, the fracture surface of the waterborne epoxy is not as smooth as the solvent-based epoxy. A distinctive texture of densely packed protrusions can be observed. These nano-sized protrusions are the waterborne epoxy emulsion particles, which are stuck on the surface of the hydration products. It can be detected on the flat surfaces (Fig. 3-4b) and other forms (Fig. 3-4c and d) of the cement hydration products.

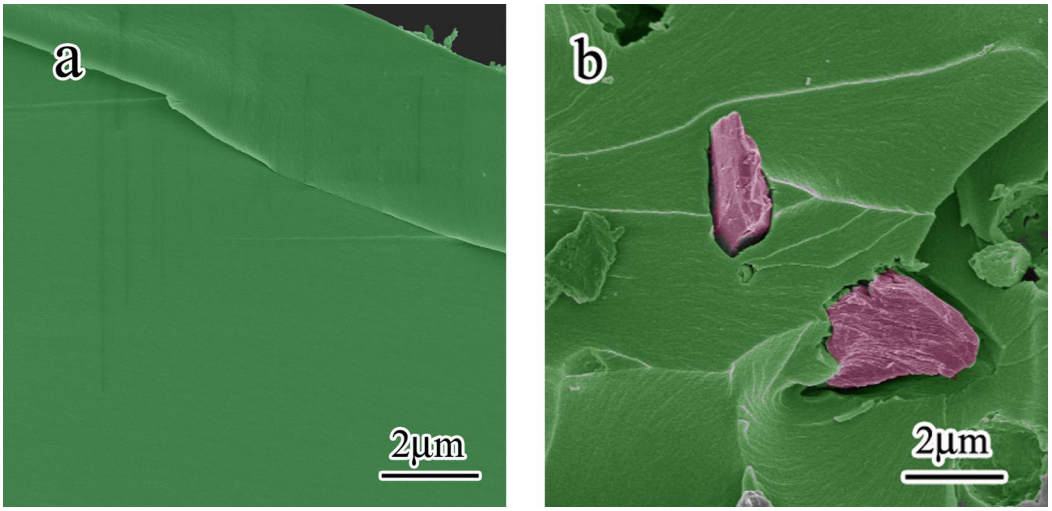


Fig. 3-3: Fracture surfaces SEM morphologies of (a) neat solvent-based epoxy and (b) solvent-based epoxy/cement

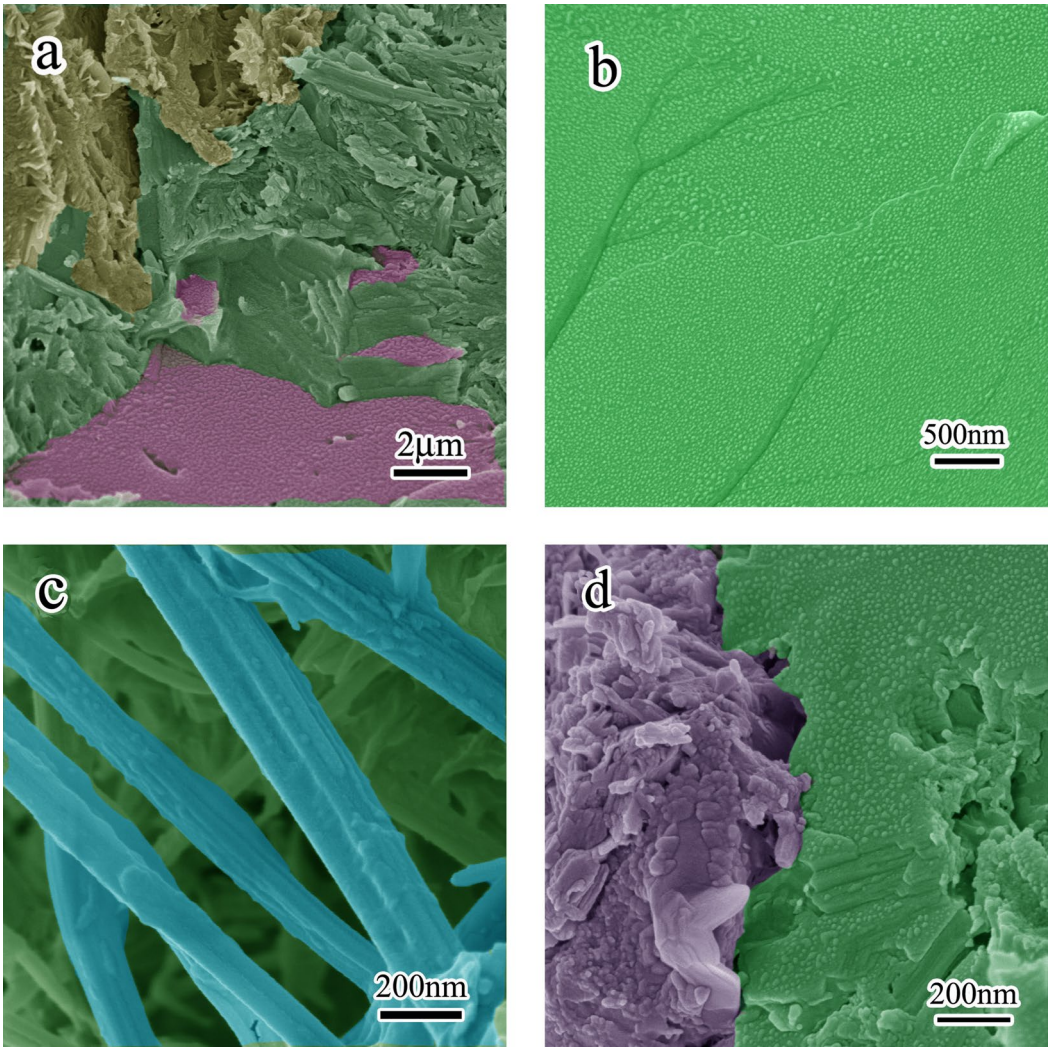


Fig. 3-4: Fracture surface SEM morphologies of waterborne epoxy/cement, (a) low-magnification image, and high-magnification images of (b) hydration product with flat surface, and (c) and d) other forms of surface of C-S-H hydration products

However, with the increase of cement content in the waterborne epoxy, due to the boost of the hydration degree of the cement, the rising pH value will break the emulsion of the waterborne epoxy, and form large-sized epoxy spheres, which weaken the mechanical properties of the waterborne epoxy/cement system due to the new formed weak interfaces. As can be seen from Fig. 3-5a, numerous epoxy spheres of various sizes can be observed, and the cracks propagate along the interfaces of these spheres. Meanwhile, the amount of the nano-sized protrusions stuck on the flat surfaces of the hydration products is significantly reduced due to the breaking of the epoxy emulsions and forming the large-sized epoxy spheres, as demonstrated in Fig. 3-5b (the purple area). These underlying mechanisms confirm the “bell” structure alteration trend of the mechanical properties, as shown in Fig. 3-2.

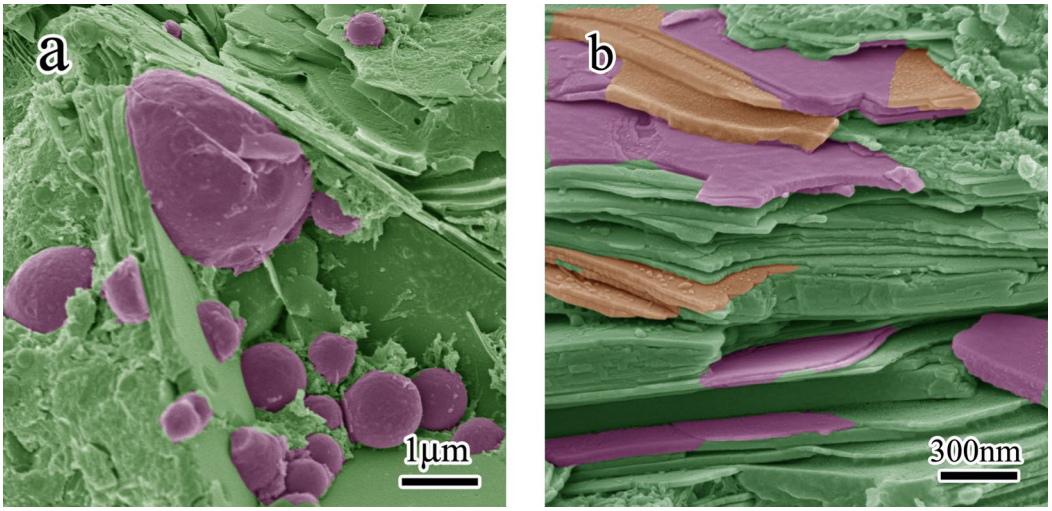


Fig. 3-5: Fracture surface SEM morphologies of waterborne epoxy/cement with (a) low-magnification image, and (b) high-magnification images

3.4.2. Force-voltage Generation

3.4.2.1. Voltage Collection

Since the mechanical properties and the compatibility between the epoxy and the cement have been investigated, the following challenge is to find out the feasibility of using them as the packaging materials for the KNN-based piezoelectric ceramics. To evaluate the force-voltage responsive sensitivity of the KNN/epoxy/cement systems, we compared the voltage signal output of the KNN plates embedded in the waterborne-based epoxy/cement and solvent-based epoxy/cement materials, by using the strategy of free-falling ball test with different masses (2 g, 5 g, 20 g, and 30 g) and a falling height of 30 cm. To ensure statistical reliability and minimize experimental errors, the free-fall impact tests for each ball mass were repeated 1000 times under identical conditions. The corresponding time-voltage signals generated by the sensor were subsequently captured and analyzed using a digital oscilloscope, enabling precise characterization of the sensor's dynamic response to impact forces. This rigorous experimental protocol enhances the validity and reproducibility of the obtained results.

The sensitivity of force-voltage response of the solvent-based and waterborne epoxy mixed with cement as packaging materials for KNN piezoelectric sensors is evaluated through a radar graph (Fig. 3-7, Fig. 3-8, and Fig. 3-9) and their corresponding voltage distribution. Each radar plot consists of 100 equally spaced radial lines, where the radii do not correspond to physical directions but to individual groups of 10 repeated measurements. For each group, the plotted point represents the logarithm of the average output voltage, which was applied to normalize the large dynamic range and to ensure consistent scaling among different samples. Therefore, the radial scaling is log-transformed and normalized rather than arbitrary. Because all radii are

equivalent, the overall circularity of the graph reflects the uniformity of the voltage responses across repeated experiments. A smoother, more symmetric shape indicates better repeatability, while irregularities suggest greater variation between tests. In the distribution graph, ΔR is the difference between the highest and the lowest electric voltage located in the corresponding proportion of the tested sample numbers. For instance, "80±2%: ΔR = 0.558 V" indicates that 80% of the test data fall within a voltage window of 0.558 V. A schematic of this calculation is provided in Fig. 3-6.

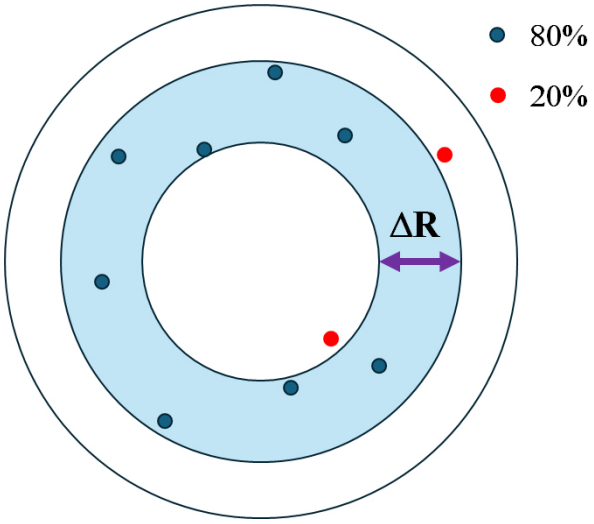


Fig. 3-6: Schematic illustration of how the radar graphs and ΔR are derived from repeated measurements to assess voltage response repeatability

As illustrated in Fig. 3-7, given that the weight of the free-falling ball of 2 g, from the stability perspective, the performance of the solvent-based epoxy/cement packaging materials with the solvent-based epoxy: cement = 5:100 is the best. Compared with the other three, the values of the ΔR corresponding to the 60%, 70%, and 80% are all the lowest, with values of 0.096 V, 0.192 V, and 0.288 V, respectively. However, from a sensitivity perspective, the highest voltages can reach 4.41 V and 6.93 V, corresponding to the waterborne epoxy/cement system with the waterborne/cement ratio of 5:100 and 100:100, respectively. In addition, the average force-responsive voltage of the waterborne epoxy/cement system is higher than that of the solvent-based epoxy/cement system.

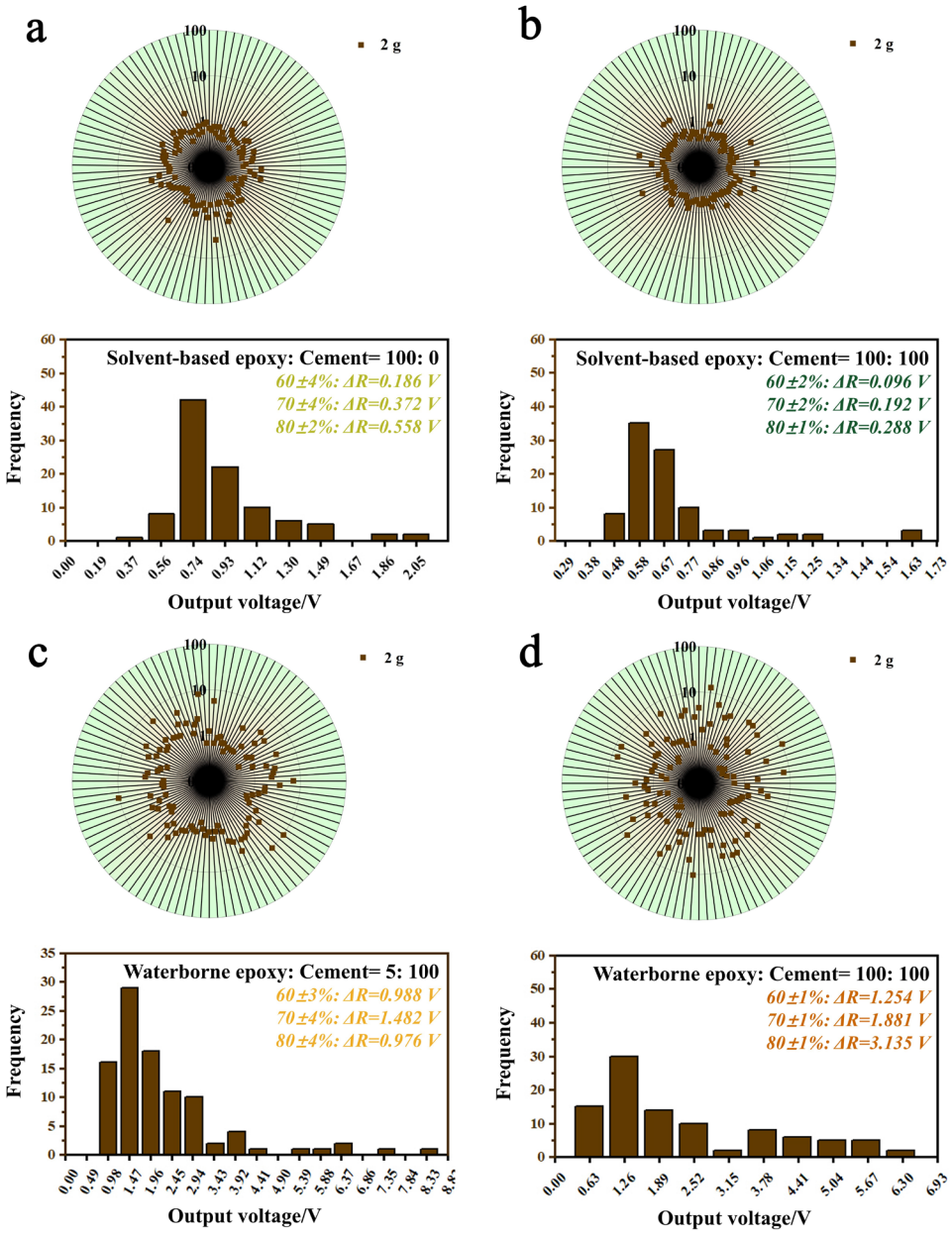


Fig. 3-7: Radar graphs and corresponding voltage-distribution sensitivity of the force-voltage response for waterborne and solvent-based epoxy-cement packaging materials of KNN piezoelectric sensors under a 2 g falling ball: (a) solvent-based epoxy: cement = 100:0; (b) solvent-based epoxy: cement = 100:100; (c) waterborne epoxy: cement = 5:100; (d) waterborne epoxy: cement = 100:100

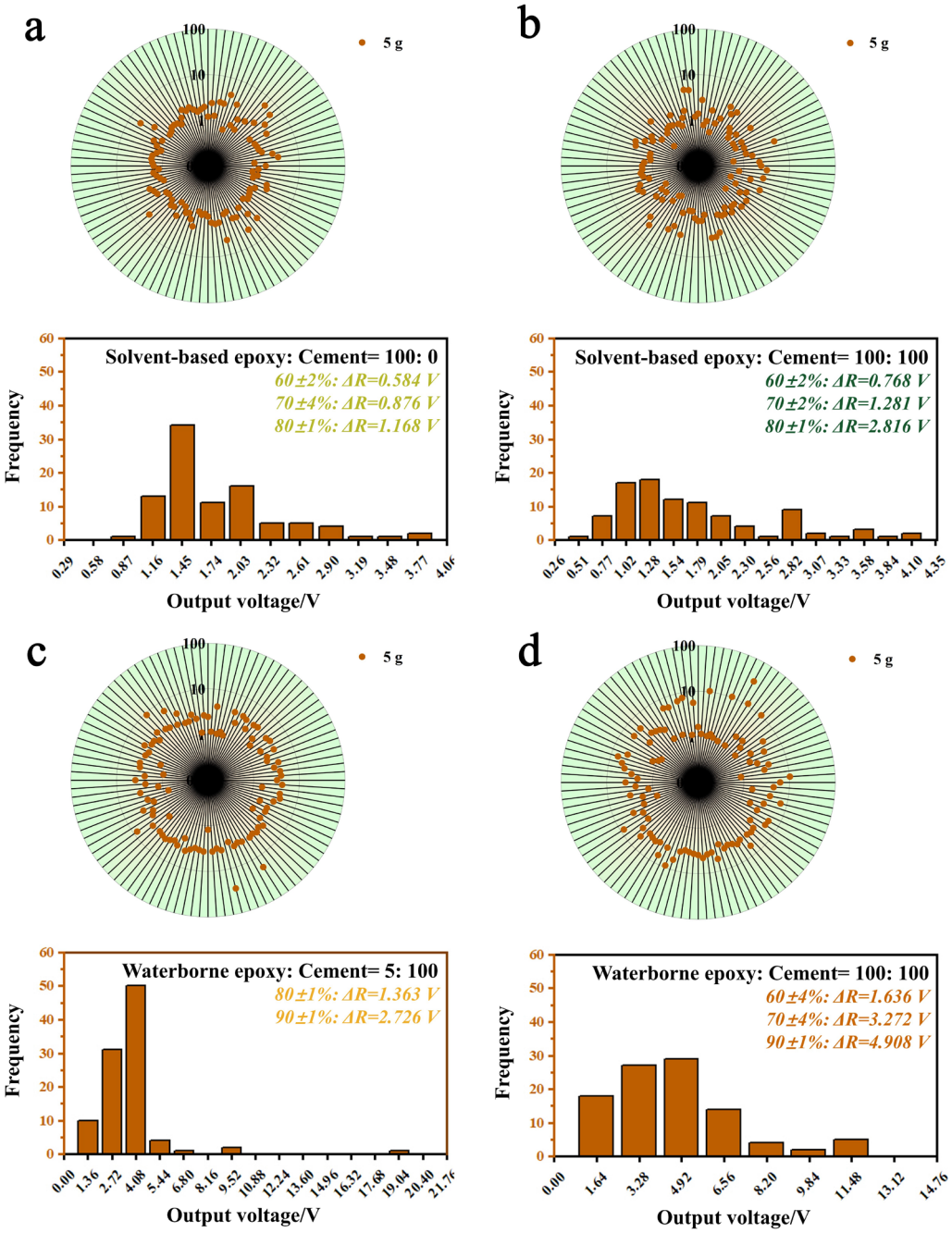


Fig. 3-8: Radar graphs and corresponding voltage-distribution sensitivity of the force-voltage response of KNN piezoelectric sensors packaged with waterborne and solvent-based epoxy-cement composites under a 5 g falling ball: (a) solvent-based epoxy: cement = 100:0, (b) solvent-based epoxy: cement = 100:100, (c) waterborne epoxy: cement = 5:100, and (d) waterborne epoxy: cement = 100:100

According to the 2 g and 5 g free-falling ball testing results, it seems that the waterborne epoxy/cement packaging materials have a better performance compared with the solvent-based epoxy/cement system. However, provided with the weight of the falling ball rising to 20 g and 30 g (as shown in Fig. 3-9), the waterborne epoxy/cement system does not work very well in

contrast to the solvent-based epoxy/cement system. All waterborne epoxy/cement samples have broken, and thus, no data can be obtained. For the solvent-based epoxy/cement system, from both stability and sensitivity perspectives, the neat solvent-based epoxy demonstrates a better performance than the solvent-based epoxy/cement composites.

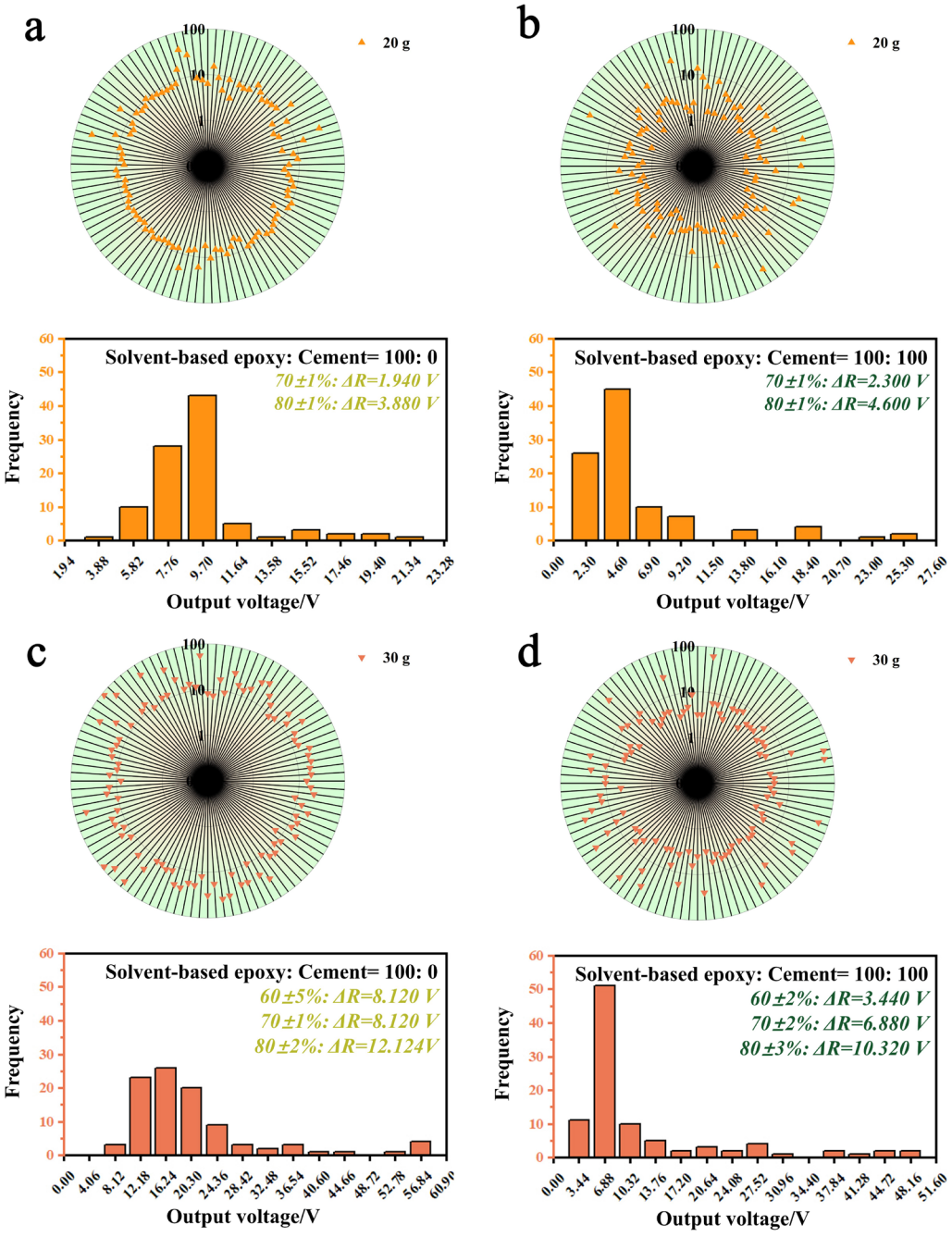


Fig. 3-9: Radar graphs and the corresponding voltage-distribution sensitivity of the force-voltage response of solvent-based epoxy mixed with cement as packaging materials for KNN piezoelectric sensors under 20 g and 30 g falling balls: (a) solvent-based epoxy: cement = 100:0, (b) solvent-based epoxy: cement = 100:100, (c) solvent-based epoxy: cement = 100:0, and (d) solvent-based epoxy: cement = 100:100

3.4.2.2. Linearity of Force vs. Voltage Signal

The impact forces generated by balls of different masses were calculated based on the principle of momentum conservation, expressed as:

$$mgh = E_k = \frac{1}{2}mv^2 \quad \textbf{(3-1)}$$

$$m\,v = F\,\Delta t \quad \textbf{(3-2)}$$

where m is the mass of the ball, g is the gravitational acceleration, h is the drop height, v is the impact velocity, F is the peak impact force, and Δt is the impact duration extracted from the recorded waveform.

The impact duration and maximum output voltage corresponding to each impactor acting on the KNN sensor surface were determined from the waveform diagrams obtained using an oscilloscope. As a representative example, Fig. 3-10 illustrates the waveform generated by a 2 g ball impact on the surface of a sensor packaged with solvent-based epoxy (solvent-based epoxy: cement = 100:0). The analysis reveals a total impact duration of 0.0202 s and a corresponding voltage output of 0.88 V. For higher impact masses (5 g, 20 g, and 30 g), the recorded voltage signals showed similar temporal shapes with proportionally increased peak amplitudes. Using the measured values of Δt and calculated v, the corresponding peak dynamic impact forces were derived from Eq. (3-2). The resulting forces and durations for each impactor mass are summarized in Table 3-2. The short contact durations on the order of tens of milliseconds lead to transient high peak forces even for small impact masses, consistent with typical dynamic impact behavior.

The radar plots (Fig. 3-7, Fig. 3-8, and Fig. 3-9) revealed significant data dispersion for certain materials, indicating inconsistencies in sensor response. Additionally, the sensor encapsulated with waterborne epoxy resin experienced structural failure after 1,000 impact cycles with 20 g spheres, suggesting limited durability under high-load conditions. To enhance the reliability of the comparative analysis, data points exhibiting a coefficient of variation exceeding 10% were excluded, and the remaining voltage data (the voltage responses under 2 g and 5 g impact conditions) were analyzed to determine the median, mode, average, and peak values (from normal distribution statistics), as illustrated in Fig. 3-11. Under the impact of 2 g and 5 g falling balls (corresponding to approximately 240 N and 647 N, respectively), the sensor packaged with waterborne epoxy resin generated output voltages that were 2 to 4 times higher than those packaged with solvent-based epoxy. Under identical impact conditions, the sensor packaged with a waterborne epoxy: cement = 5:100 yielded higher voltage outputs compared

to the 100:100 formulation, suggesting that a moderate incorporation of cement can enhance the piezoelectric sensitivity of the composite. The sensor packaged with solvent-based epoxy resin combined with cement exhibited a significantly reduced voltage response, approximately half compared to the pure solvent-based epoxy, indicating a detrimental effect of cement addition on sensitivity in this particular matrix. These observations are illustrated in Fig. 3-11(a, b, c, d). For the pure solvent-based epoxy resin (Fig. 3-11e and f), a notable increase in output voltage was observed under 20 g and 30 g impacts, highlighting its superior performance under higher loading conditions. Furthermore, the four voltage parameters exhibited considerable variation under identical impact forces, consistent with the findings in Fig. 3-9, which indicates increased signal output dispersion due to potential inhomogeneity introduced by cement incorporation.

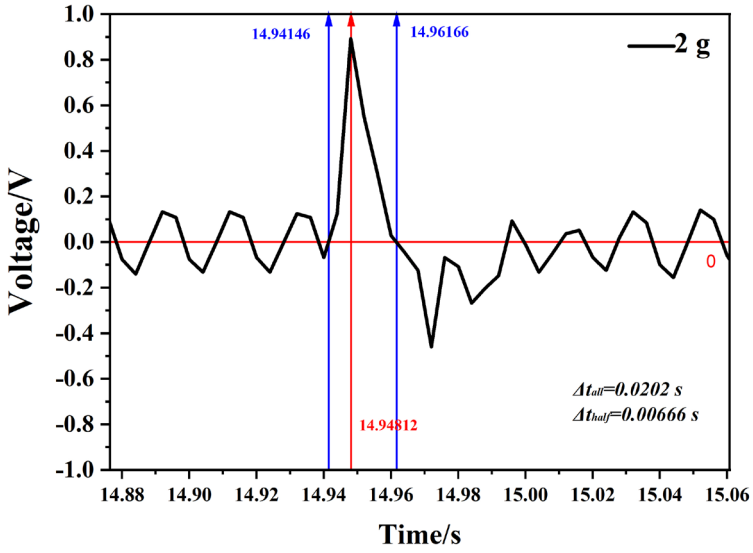


Fig. 3-10: The oscillogram of a 2-gram ball in free fall on the surface of the sensor

Table 3-2 The force and time of action corresponding to different balls

	2 g	5 g	20 g	30 g
F/N	240	647	3491	6367
Δt/s	0.0202	0.0187	0.0139	0.0114

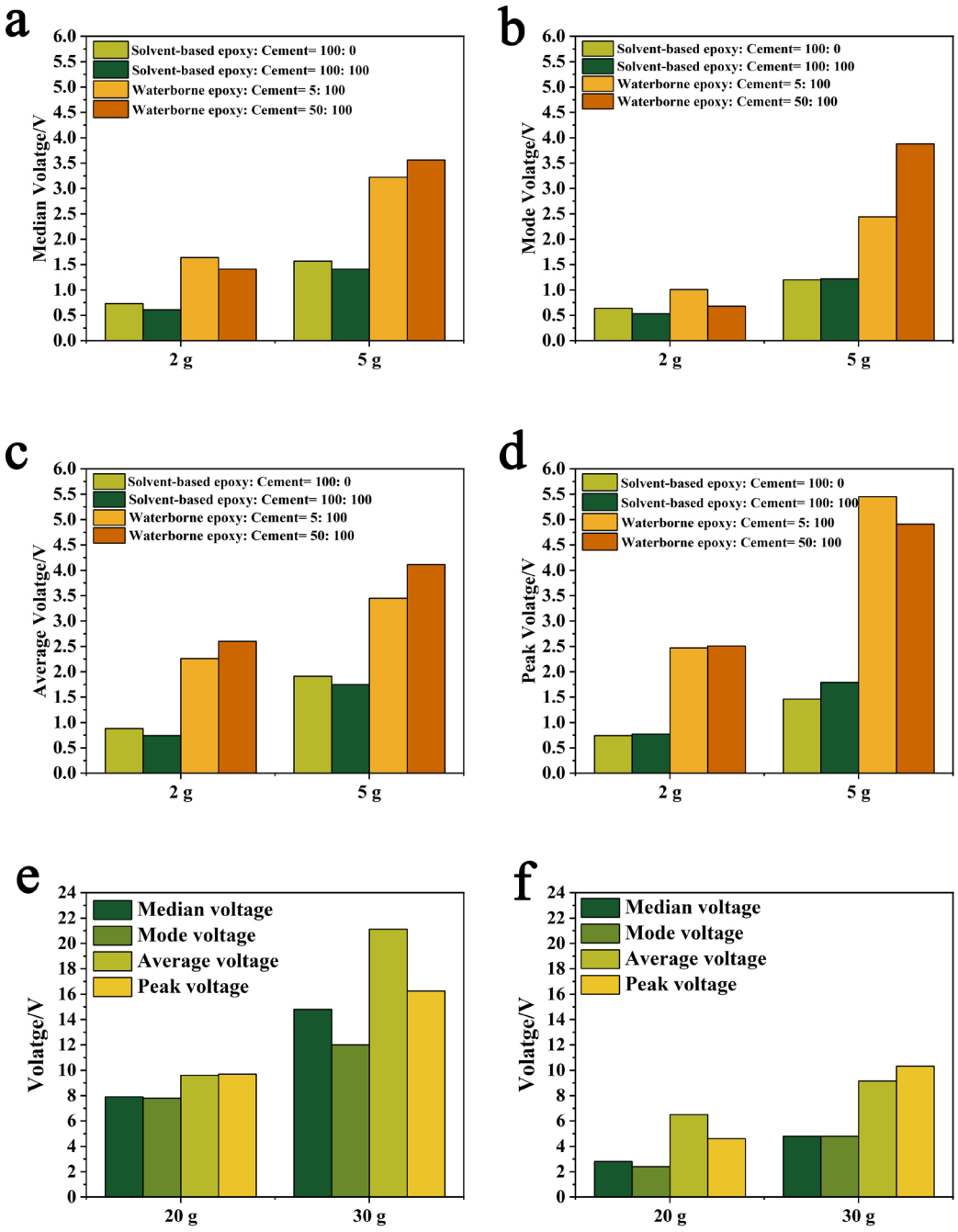


Fig. 3-11: Force-voltage response of the waterborne and solvent-based epoxy mixed with cement as packaging materials for KNN piezoelectric sensors, (a) median voltage, (b) mode voltage, (c) average voltage, (d) peak voltage, (e) solvent-based epoxy: cement = 100:0 under 20 g falling ball, (f) solvent-based epoxy: cement = 100:100 under 30 g falling ball

Apart from the absolute values of the force-generated voltage, the relative voltage values, which were calculated according to $\Delta R/V_{max}$, where V_{max} is the maximum voltage, are also another important criterion to evaluate the overall performance of the packaged sensors. The relative voltage values are listed in Table 3-3. As can be detected from this table, for the 2 g

free-falling ball group, the highest absolute voltage was obtained in the waterborne epoxy/cement system with the W/C ratio of 5:100. However, the lowest relative voltage is observed in the $S/C_{100/100\text{-}2\ g}$ group with a value of 0.17, which is far less than the other three. For the 5 g free-falling ball group, the $W/C_{100/100\text{-}5\ g}$ group reaches the highest absolute voltage with a value of 4.92, while the $W/C_{5/100\text{-}5\ g}$ group has the lowest relative voltage of 0.50. In this group, the waterborne epoxy/cement system performs better than the solvent-based epoxy/cement system. Finally, when the weight of the free-falling ball increased to over 20 g, due to the breakage of the waterborne epoxy/cement samples, the results had to be compared between the neat solvent-based epoxy and the solvent-based epoxy/cement composites. As illustrated by the results, the neat solvent-based epoxy shows a better general performance than the solvent-based epoxy: cement = 100:100.

Table 3-3 Vmax and ΔR/Vmax of different falling balls

	$S/C_{100/0\text{-}2g}$	$S/C_{100/100\text{-}2g}$	$W/C_{5/100\text{-}2g}$	$W/C_{100/100\text{-}2g}$
$V_{max/V}$	0.74	0.58	1.47	1.26
$\Delta R_{80\%}$	0.558	0.288	0.976	3.135
$\Delta R_{70\%}$	0.372	0.192	1.482	1.881
$\Delta R_{60\%}$	0.186	0.096	0.988	1.254
$\Delta R_{80\%}/V_{max}$	0.75	0.50	0.66	2.49
$\Delta R_{70\%}/V_{max}$	0.50	0.33	1.00	1.49
$\Delta R_{60\%}/V_{max}$	0.25	0.17	0.67	1.00
	$S/C_{100/0\text{-}5g}$	$S/C_{100/100\text{-}5g}$	$W/C_{5/100\text{-}5g}$	$W/C_{100/100\text{-}5g}$
$V_{max/V}$	1.45	1.28	4.08	4.92
$\Delta R_{90\%}$	/	/	2.726	4.908
$\Delta R_{80\%}$	1.168	2.816	1.363	/
$\Delta R_{70\%}$	0.876	1.281	/	3.272
$\Delta R_{60\%}$	0.584	0.768	/	1.636
$\Delta R_{90\%}/V_{max}$	/	/	0.67	1.00
$\Delta R_{80\%}/V_{max}$	0.81	2.20	0.50	/
$\Delta R_{70\%}/V_{max}$	0.60	1.00	/	0.67
$\Delta R_{60\%}/V_{max}$	0.40	0.60	/	/
	$S/C_{100/0\text{-}20g}$	$S/C_{100/100\text{-}20g}$	$S/C_{100/0\text{-}30g}$	$S/C_{100/100\text{-}30g}$
$V_{max/V}$	9.70	4.60	16.24	6.88
$\Delta R_{80\%}$	3.880	4.600	12.124	10.320
$\Delta R_{70\%}$	1.940	2.300	8.120	6.880
$\Delta R_{60\%}$	/	/	8.120	3.440
$\Delta R_{80\%}/V_{max}$	0.40	1.00	0.75	1.50
$\Delta R_{70\%}/V_{max}$	0.20	0.50	0.50	1.00
$\Delta R_{60\%}/V_{max}$	/	/	0.50	0.50

Sensors fabricated with waterborne epoxy resin exhibited substantially lower voltage outputs across all impact forces compared to those with solvent-based epoxy (Fig. 3-11). Despite the significant difference in compressive strength between the waterborne epoxy: cement = 5:100 and waterborne epoxy: cement = 50:100, their output voltages were remarkably similar. The gradual increase in peak and median voltage values suggests limited sensor sensitivity, rendering these materials unsuitable for high-load applications. These findings provide critical insights into the relationship between packaging material composition and sensor performance under varying mechanical loads.

Through data processing, four typical voltage parameters were obtained to investigate the influence of different packaging materials on sensor performance. This study particularly focused on the relationship between force and voltage output for two material formulations: solvent-based epoxy to cement ratios of 100:0 and 100:100. The forces and corresponding voltages listed in Table 3-3 were analyzed, and linear fitting methods were applied to examine the trends of median voltage, mode voltage, average voltage, and peak voltage. For sensors packaged with the solvent-based epoxy: cement = 100:0, as shown in Fig. 3-12a, the experimental results demonstrate a highly linear response under varying force conditions. The linear fitting correlation coefficients for median voltage, mode voltage, average voltage, and peak voltage are 0.99932, 0.98278, 0.98498, and 0.99511, respectively. This strong linear relationship indicates that sensors packaged with pure epoxy resin exhibit highly stable voltage output and are exceptionally sensitive to changes in applied force. Notably, under higher force conditions, the voltage output increases significantly, further validating the superior performance of this material in high-load environments. These findings underscore the potential of pure epoxy resin as an effective packaging material for sensors requiring precise and reliable force detection capabilities. Fig. 3-12b shows that the solvent-based epoxy with a cement ratio of 100:100 exhibits inferior performance in terms of voltage output. Experimental data revealed that the voltage output of this material was significantly lower than that of pure epoxy resin, particularly under higher force conditions. The linear fitting correlation coefficients were as follows: median voltage (r^2 = 0.9765), mode voltage (r^2 = 0.9578), average voltage (r^2 = 0.97489), and peak voltage (r^2 = 0.96269). The relatively low correlation coefficient for peak voltage suggests that the incorporation of cement substantially reduced the material's sensitivity, resulting in unstable voltage output under high force conditions. This instability may be attributed to the inhomogeneity introduced by the cement, which increased the dispersion of signal output. These findings highlight the detrimental effects of cement addition on the material's performance, particularly in applications requiring high sensitivity and stability under

varying force conditions.

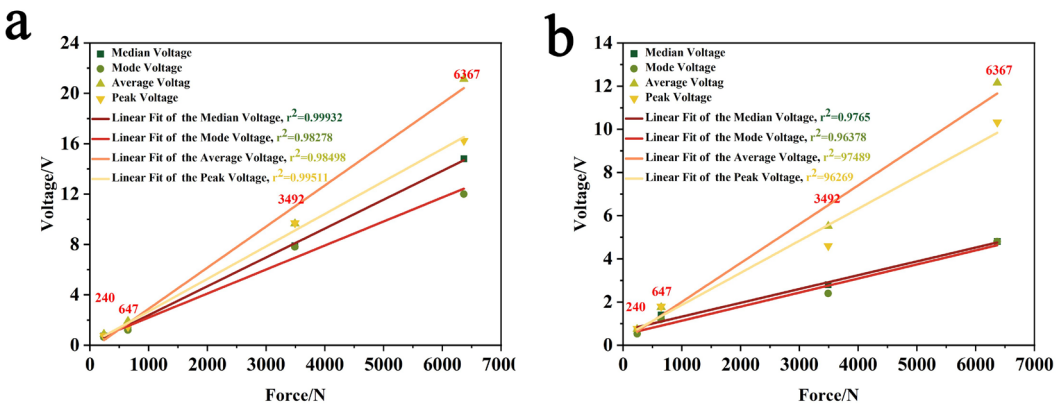


Fig. 3-12: Force-output voltage relationship derived from the momentum conservation theorem, (a) solvent-based epoxy: cement = 100:0, and (b) solvent-based epoxy: cement = 100:100

The comparative analysis of different epoxy-cement formulations revealed crucial insights into how packaging materials affect sensor sensitivity and signal stability under mechanical loading. Notably, sensors encapsulated with pure solvent-based epoxy demonstrated outstanding linearity and high voltage outputs across varying force levels. In contrast, the significant reduction in output voltage and correlation coefficients observed in the solvent-based epoxy: cement = 100:100 configuration indicates that the addition of cement compromises the homogeneity of the matrix. Cement particles introduce interfacial defects and microvoids, which can act as charge traps or scattering centers, thereby reducing piezoelectric efficiency and overall signal stability (Ding et al., 2021; Qiao et al., 2024). These findings align with previous studies on composite-based sensors, where increased filler content often leads to performance trade-offs between mechanical robustness and signal fidelity (Wang et al., 2016).

Interestingly, waterborne epoxy systems exhibited different trends: the inclusion of cement enhanced voltage output, despite the formulation's inherently lower performance compared to solvent-based systems. This suggests a fundamentally different interaction mechanism between waterborne epoxy and cement. One possibility is that the cement particles in the waterborne matrix promote a more conductive or stress-sensitive microenvironment, potentially improving stress transfer or local polarization effects. However, the overall sensitivity remained low, indicating limitations in load-bearing applications.

These contrasting behaviors underscore the importance of matrix-filler compatibility and interfacial interactions in sensor packaging materials. While pure solvent-based epoxy offers superior sensitivity and linearity, its brittleness and environmental concerns limit its broader application. On the other hand, waterborne systems are eco-friendlier and more compatible with

cement, but currently lack sufficient sensitivity. Future research should focus on exploring hybrid formulations, such as incorporating conductive nanoparticles or using modified resins, to enhance both mechanical resilience and signal performance without sacrificing sensitivity (Díez-Pascual, 2019; Poompiew et al., 2023).

The porosity of the encapsulation layer also plays an important role in determining the sensor's output characteristics. Increased porosity within the epoxy-cement composites can reduce the effective stiffness and mechanical impedance of the encapsulating matrix, leading to partial attenuation of the transmitted stress and consequently lower voltage amplitudes. The presence of pores and interfacial voids may also induce local stress scattering and time delays, slightly broaden the response waveform and reduce high-frequency components. On the other hand, moderate porosity can improve strain accommodation and relieve local stress concentrations, which contribute to the stable and repeatable signal generation observed in highly porous waterborne epoxy systems. This balance between stress transfer efficiency and damping explains the observed trade-off between sensitivity and stability across different formulations.

3.4.3. Evaluation of Sensor Fatigue Behavior

To evaluate the long-term electrical stability of sensors under cyclic loading conditions, solvent-based epoxy packaged sensors were embedded within silicate cementitious matrix specimens at a depth of 2 cm from the surface for fatigue testing. A comparative analysis of the open-circuit voltage response was conducted during 100,000 loading cycles, as depicted in Fig. 3-13. Oscilloscope measurements revealed an initial 10,000-cycle peak output voltage of approximately 4.50 V. Following high-cycle fatigue, this peak value exhibited a slight reduction to 4.30 V. Although the oscilloscope exported the voltage waveforms as processed image data rather than uniformly sampled raw signals, the time-domain waveforms exhibited highly stable amplitudes and oscillation periods throughout the fatigue cycles. This consistency strongly indicates that no resonance drift or waveform distortion occurred during testing. This represents a marginal 4.4% reduction in peak voltage amplitude, indicating sustained stability and reproducible electrical signal generation. The observed performance demonstrates exceptional fatigue tolerance, with minimal attenuation of the piezoelectric response, thereby satisfying the reliability requirements for high-durability sensors in practical applications.

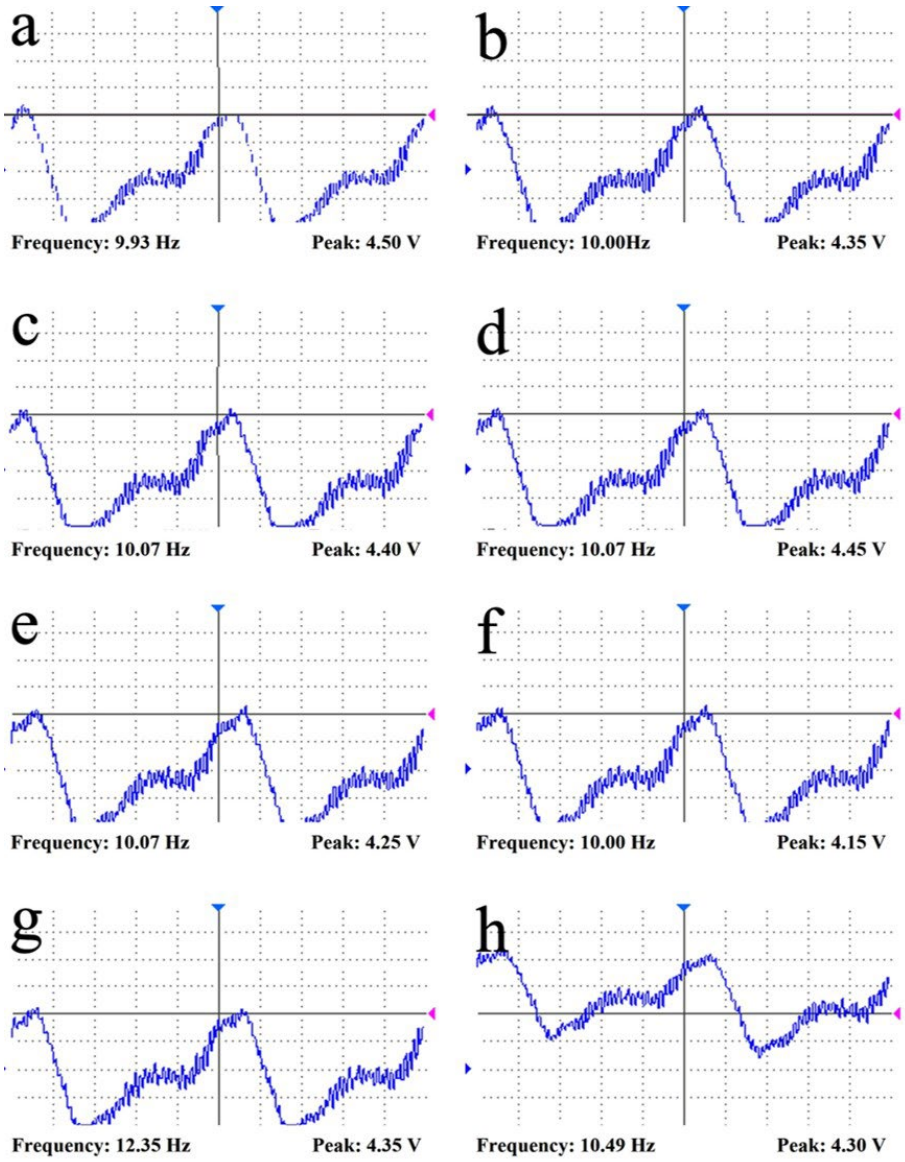


Fig. 3-13: Waveforms of sensors packaged with solvent-based epoxy embedded in roadbed material with a load of 5 kN, (a) 1 cycle, (b) 10,000 cycles, (c) 20,000 cycles, (d) 30,000 cycles, (e) 40,000 cycles, (f) 60,000 cycles, (g) 80,000 cycles, (h) 100,000 cycles

Furthermore, the fundamental waveform morphology remained consistent before and after cyclic loading, with no discernible waveform distortion or significant increase in electrical signal noise. This observation further corroborates the structural integrity of the sensor and the stability of its electrode connections under prolonged operational conditions. This robust performance is essential for real-world applications, such as pavements or bridge decks, where sensors are exposed to millions of repetitive stress events over time. A packaging system that maintains signal fidelity under fatigue not only enhances monitoring accuracy but also reduces maintenance frequency, thus lowering lifecycle costs in structural health monitoring systems.

In contrast, although waterborne epoxy resins demonstrated structural vulnerability under

high-load conditions, their voltage output was 2-4 times higher than that of solvent-based epoxy formulations. This significant signal enhancement suggests that waterborne systems have great potential in low-to-moderate load environments where sensitivity is prioritized over mechanical robustness. However, their long-term durability under cyclic loading remains underexplored. As such, targeted fatigue studies under appropriate loading conditions are critical to unlocking their full application potential, particularly in smart pavement surfaces or wearable sensing platforms where high sensitivity and environmental compatibility are essential.

The contrasting behaviors of these two resin systems underscore the importance of tailoring sensor encapsulation materials not only for their mechanical resistance but also for electrical performance within specific operational contexts. Future work should expand fatigue testing to include variable load amplitudes, environmental stressors, and multi-material hybridization strategies, such as combining waterborne epoxy with nanofillers or flexible reinforcement phases, to achieve a balanced performance profile.

3.5. Conclusions and Outlook

This study bridges a critical research gap by conducting the first systematic investigation into the packaging of KNN piezoelectric sensors for pavement monitoring applications. Comprehensive evaluation of solvent-based epoxy and waterborne epoxy resin composites incorporating cement revealed fundamentally divergent behaviors. The incorporation of cement into solvent-based epoxy significantly reduces compressive strength, and due to particle agglomeration, the packaged sensors exhibit poor signal reproducibility, with output voltages approximately half those of pure resin under the same applied forces. However, sensitivity and linearity remain unaffected. When waterborne epoxy resin is mixed with cement, the compressive strength exceeds that of both pure cement and pure waterborne epoxy resin at ratios of 1:100, 5:100, and 10:100, reaching a maximum value of 57.8 MPa at a ratio of 5:100. This enhancement is attributed to the waterborne epoxy resin promoting hydration and filling voids. Despite this material system demonstrating high signal output voltage responsiveness, generating 2-4 times higher output voltages than solvent-based epoxy systems, there is a risk of rupture after direct action above 600 N, which limits applications.

In the next stage of research, more attention could be given to adjusting the material composition to better balance mechanical properties and electrical output. For example, adding small amounts of nanomaterials like carbon nanotubes or graphene oxide might help improve particle distribution and make the signal more stable. Since the waterborne epoxy systems

responded well at lower loads, it would be worthwhile to test how they perform under repeated stress or long-term loading. At the same time, it's important to observe how the materials behave in outdoor conditions, including temperature changes, moisture, and freezing cycles. These steps could help determine whether the sensors are reliable for long-term use in practical environments.

4. Environmentally Friendly Lead-Free Piezoelectric Ceramics as Pavement Sensing Element: A Multi-Scale Finite Element Perspective

4.1. Abstract

Potassium sodium niobate (KNN), a lead-free piezoelectric ceramic, demonstrates its significant potential as an environmentally friendly element for energy harvesting and sensing due to its relatively high piezoelectricity and cost-effectiveness. Although the properties of KNN have been proven promising as a piezoelectric element in some electronic devices, the application in pavement engineering as a sensing element remains challenging due to the knowledge gap of static mechanical-piezoelectric correlations along with dynamic multi-axial loads and cross-scale coupling effects. Most importantly, due to the shortage of basic information about the properties of bulk KNN ceramics, it is even infeasible to implement numerical simulations. To tackle this challenge, we developed a KNN-based multi-scale dynamic evaluation finite element framework by using real properties obtained from lab-prepared KNN ceramics as pivotal parameters. To assess the feasibility of KNN as a sensing element in pavements, traffic flow-related factors (horizontal offset, camber, axle load, speed, deceleration, and friction coefficient) and sensor position factors (buried depth, phase angle, and arrangement spacing) were involved in this model. The simulation results indicate that KNN sensors exhibit superior applicability in asphalt pavement compared with concrete pavement under dynamic traffic conditions. The optimal open-circuit voltage output for asphalt pavements occurs at a depth of 2 cm, a phase angle of 15°, and an arrangement spacing of 15 cm, whereas in concrete pavements, the optimal configuration is a depth of 2 cm, a phase angle of 0°, and an arrangement spacing of 15 cm. This work establishes a multi-scale coupling theory and scalable optimization framework for dynamically adaptive lead-free piezoelectric sensors in smart transportation systems.

4.2. Introduction

Piezoelectric sensors have been widely applied in various practical fields by converting mechanical deformation into electrical signals (Hirose et al., 2025; Y. Liu et al., 2024; Sharafi et al., 2024). In the past decade, implementing piezoelectric devices under pavements to realize sensing or energy harvesting purposes has been burgeoning (Ziyang Gao et al., 2024; Monazami et al., 2022; Wang et al., 2019). Currently, the most widely used piezoelectric material is lead zirconate titanate (PZT) perovskite ceramics due to its high dielectric and piezoelectric constants (Duddi et al., 2023; Narayanan et al., 2024; Tsai et al., 2009). To improve the sensing accuracy or enhance the energy harvesting efficiency, a myriad of efforts were made to optimize the piezoelectric performance of the PZT ceramics. However, for the aims of sensing or energy harvesting in pavement engineering, merely performance improvement is inadequate. Laboratory measurements found that the piezoelectric signal under load is extremely sensitive to the embedded depth and position of the sensors (Sol-Sánchez et al., 2021). In addition, the sensor also exhibits non-uniform output signals depending on the size of the testing devices (M. Liang et al., 2024). Most importantly, it was found that even when exploiting the same testing conditions, the experimental results may vary due to the multiple coupling impact factors (Dong et al., 2024). Therefore, it is hard to reflect the real situation by merely relying on experimental results due to the uncontrollable multiple variables, even accompanied by time-consuming and laborious work (Liu et al., 2019).

The advent of computing technologies has precipitated a paradigm shift in the utilization of numerical simulations as a means to elucidate the operational characteristics of piezoelectric devices. The finite element method (FEM) can be used to predict the mechanical and piezoelectric behavior of PZT sensors embedded in pavements. By combining experimental and numerical methods, more reliable results can be obtained. For instance, the development of a tire-pavement model can provide the correlation between the mechanical response and signal output of the sensors when subjected to the traffic road (Liu et al., 2019). This methodology can evaluate the impact of force transmission by taking into account the installation locations (Du et al., 2022). Apart from the interaction between the tire and the road surface, the analysis of input and output signals, based on the configuration of the sensors, including their shape,

arrangement, and number, can be undertaken in great detail (C. Wang et al., 2020). Although previous results, from both numerical and experimental perspectives have demonstrated the high predictability of the piezoelectric response of PZT-based sensors, they are facing an innate dilemma, torn between the piezoelectric performance and the toxicity of the lead (Panda and Sahoo, 2015). As a result, exploring high-performance lead-free piezoelectric materials is always the top challenge to obtain environmentally friendly piezoelectric sensors.

In the past decade, potassium sodium niobate ($K_{0.5}Na_{0.5}NbO_3$, KNN) has emerged as a promising lead-free piezoelectric material due to its particular electromechanical properties. As a member of the perovskite family, KNN ceramic possesses a high Curie temperature, high piezoelectric coefficients, and notable dielectric properties, making it suitable as a sensing material. Recently, KNN-based sensor applications have been reported to serve as the replacement of the traditional PZT-based sensors in various fields (Wekalao et al., 2025; Wu et al., 2025; W. L. Zhang et al., 2017). The application potential of KNN ceramics as a flexible and miniature sensor has been well documented. A polyvinylidene fluoride-co-trifluoroethylene [P(VDF-TrFE)] film doped with nano-sized KNN particles was prepared using the hydrothermal method. Due to its high mechanical stability and durability, it can not only be used to monitor human joint movement (Deng et al., 2025) but also as an early warning system for natural disasters (Deng et al., 2024). Moreover, it has been demonstrated that the conjunction of KNN ceramics with other perovskite materials, such as $Bi_xNa_{1-x}TiO_3$ (BNT), is beneficial to prepare self-powered thermal detectors due to the strong response to temperature and ultraviolet and infrared energy (Huang et al., 2024).

Great efforts have been devoted to attempting to implement KNN materials as a replacement for PZT materials in other fields. While the upfront synthesis cost of KNN ceramics is currently higher than that of PZT ceramics, the sustainable development of KNN materials is justified via a comprehensive analysis spanning environmental compliance, lifecycle economics, and system-level efficiency. For environmental compliance cost avoidance, lead-free KNN ceramics inherently avoid costs associated with hazardous material regulations (e.g., EU RoHS, WEEE), PZT materials require specialized waste management (≈ 1200–2000/ton), whereas KNN materials disposal costs are negligible. Meanwhile, the closed-loop recycling process can realize 70-80% reuse of niobium resources, and the cost of KNN raw

materials is reduced by about 30%, improving competitiveness with PZT materials (Huang et al., 2023). However, its utilization in pavement engineering remains underexplored. A critical challenge stems from the inherent mismatch between laboratory-scale evaluations (primarily confined to static or uniaxial loading conditions) and the multi-axial dynamic stress fields (e.g., traffic-induced cyclic loading) encountered in real-world pavement environments. This discrepancy manifests as unpredictable scale-dependent electromechanical coupling behavior, severely limiting the reliability of KNN sensors in infrastructure applications.

To systematically resolve the electromechanical coupling mechanisms of KNN piezoelectric sensors embedded in pavement structures, this study developed a multi-scale tire-pavement coupled numerical model (Fig. 4-1) based on laboratory-fabricated sensor performance data. The model comprises two subsystems: tire-asphalt pavement-KNN and tire-concrete pavement-KNN, representing service scenarios for flexible and rigid substrates, respectively. The pavement structure was modeled at a large scale to characterize mechanical field distributions, while the sensor units were modeled at a small scale to quantify piezoelectric responses, with cross-scale coupling achieved via dynamic load transfer. The model incorporates rolling tire motion (including velocity and deceleration parameters) and defines nine control variables: horizontal offset, camber, axle load, speed, deceleration, friction coefficient, buried depth, phase angle, and arrangement spacing, to rigorously reconstruct the factors influencing KNN sensor deployment in pavements. Employing multi-scale synchronized simulations, correlations between pavement Mises stress fields and sensor open-circuit voltage outputs were analyzed, elucidating the applicability of KNN sensors under diverse pavement types and installation conditions. The deterministic relationship between dynamic loading profiles and piezoelectric voltage signatures enables precise vehicular classification (e.g., passenger vehicles vs. freight trucks) and traffic flow characterization. This work establishes a transferable theoretical paradigm for the reliability-driven design of lead-free piezoelectric sensors in smart pavement infrastructure.

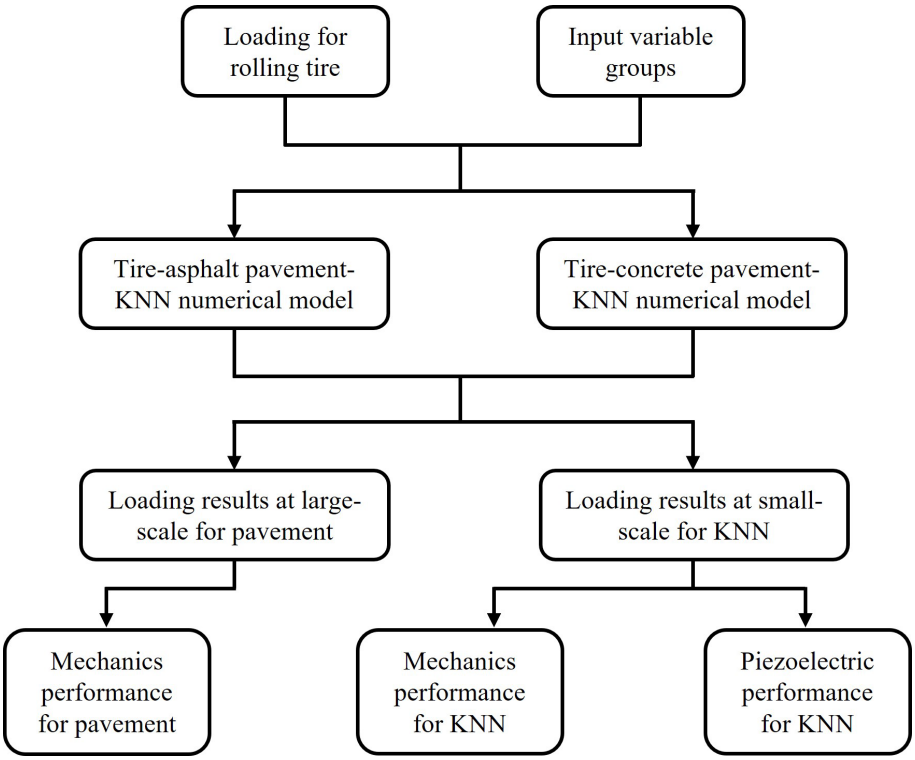


Fig. 4-1: Technical framework of study

4.3. Methodology

4.3.1. Raw Materials

In this study, $0.95(K_{0.5}Na_{0.5})\ NbO_3$-$0.02(Bi_{0.5}Na_{0.5})\ ZrO_3$-$0.03CaHfO_3$ (KNN) lead-free piezoceramic was synthesized using an optimized solid-state reaction route. High-purity oxide/carbonate precursors-K_2CO_3 (99%), Na_2CO_5 (99.8%), Nb_2O_5 (99.5%), Bi_2O_3 (99.999%), $CaCO_3$ (99.9%), ZrO_2 (99.5%), and HfO_2 (99.5%)-were received from Sinopharm Chemical Reagent Co. (China) and thermally dehydrated before stoichiometric blending. The mixed powders were first ball-milled using a planetary ball mill at 200 rpm for 24 hours with anhydrous ethanol as the medium. The ball size ratio was 3 mm: 5 mm: 10 mm = 4: 2: 1, and the ball-to-powder-to-liquid ratio was 2: 1: 0.6. After milling, the slurry was dried at 100 °C and passed through a 60-mesh sieve. The dried powders were pressed into flakes (diameter of 30 mm) and calcined at 860 °C for 5 hours at a heating rate of 5 °C/min in an alumina crucible in a muffle furnace. After calcination, the mixture was first ground using an agate mortar, followed by a second planetary ball milling at 400 rpm for 4 hours to further reduce the particle size distribution. The powders were again dried at 100 °C and sieved through a 60-mesh screen,

then pressed into 20 mm diameter pellets and pre-calcined at 860 °C for 2 hours (5 °C/min). A third ball milling step was then performed under the same conditions (400 rpm, 4 hours). After this, 8 wt.% PVA binder was added for graduation. The powders were pressed into disc-shaped specimens with a diameter of 10 mm and a thickness of 1 mm to ensure uniform sintering. Sintering was carried out at 1090 °C with a heating rate of 4 °C/min, then slowly cooled to 1060 °C at 3 °C/min and held for 2 hours. The furnace was further cooled to 800 °C at 3 °C/min, followed by furnace cooling. This method ensures uniform grain growth and minimizes thermal gradients (<5 °C). To minimize the volatilization of Bi, Na, and K during sintering, the disks were embedded in their corresponding powders. For piezoelectric testing, silver paste was screen-printed on both sides of the sintered ceramic specimens and fired at 600 °C for 30 minutes to form electrodes.

Poling was performed by applying a direct current electric field of 3 kV/mm across the ceramic specimens in a silicone oil bath (Dow Corning 200 Fluid, 100 cSt) at 80 °C for 30 minutes. After poling, the specimens were rested for 24 hours before piezoelectric measurements to ensure stabilization of domain orientation. To ensure batch-to-batch reproducibility, the stoichiometric composition was controlled within ± 0.5%, and sintering parameters were regulated within ± 2 °C using a programmable furnace (SXL-1700C). All experiments were conducted under controlled laboratory conditions (ambient temperature 25 ± 1 °C, relative humidity 50 ± 5%). The relative permittivities ε_{11} and ε_{33} were measured using an LCR meter (Keysight E4980A) at 1 kHz and room temperature (25 °C), with a signal amplitude of 1 V, under unpoled conditions along in-plane and out-of-plane directions, respectively. Quasi-static piezoelectric coefficient (d_{33}) was obtained using a piezometer (ZJ-3A, Chinese Academy of Sciences, China) at room temperature, with a testing frequency of 1 Hz and an applied force of 0.25 N. The d_{31} *and* d_{15} were derived from resonance spectra measured by an impedance analyzer (Keysight E4990A) in the frequency range of 100 kHz–1 MHz, following IEEE Standard 176. Elastic properties, including Young's modulus and Poisson's ratio (ν), were determined using a Universal Testing Machine (UTM, Instron 5944), with the corresponding stiffness constants derived from these measured parameters ambient conditions (25 ± 1 °C, 50 ± 5% RH). The bulk density of KNN specimens was quantified by Archimedes' principle employing distilled water as the immersion medium.

4.3.2. Parameters Determination of the Small-Scale Model

The microscale modeling framework primarily focuses on investigating the mechanical and piezoelectric responses of KNN, necessitating a precise definition of material properties. The KNN sensor architecture comprises a composite structure of KNN ceramics packaged within a resin matrix, as shown in Fig. 4-2, which was prepared in the previous work. To characterize mechanical behavior, laboratory-based testing was conducted to experimentally determine Poisson's ratio, elastic modulus, and density for both KNN ceramics and resin components.

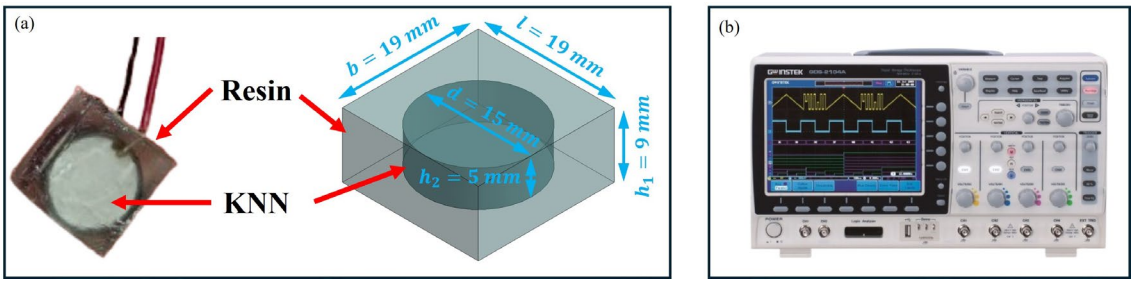


Fig. 4-2: (a) KNN piezoelectric sensors, (b) open-circuit voltage measurement using the oscilloscope

As the functional core of the sensor, KNN ceramics facilitates energy conversion from pavement vibration to electrical output via the piezoelectric effect. As illustrated in Fig. 4-3, the d_{33} operational mode (mechanical stress applied in 3-direction, charge response in 3-direction) demonstrates superior energy harvesting efficiency compared to the d_{31} mode (mechanical stress applied in 1-direction, charge response in 3-direction) in pavement applications (Platt et al., 2005; Wang et al., 2019). Given the non-piezoelectric nature of the resin matrix, material characterization focused solely on KNN ceramics. All values of critical piezoelectric parameters were averaged from five independent measurements, and the error was controlled within 5%. Complete material specifications are compiled in Table 4-1. The sensor depicted in Fig. 4-2 a) was subjected to testing for random forces (240 N, 647 N, 3491 N, and 6367 N), and the open-circuit voltage was subsequently measured using an oscilloscope.

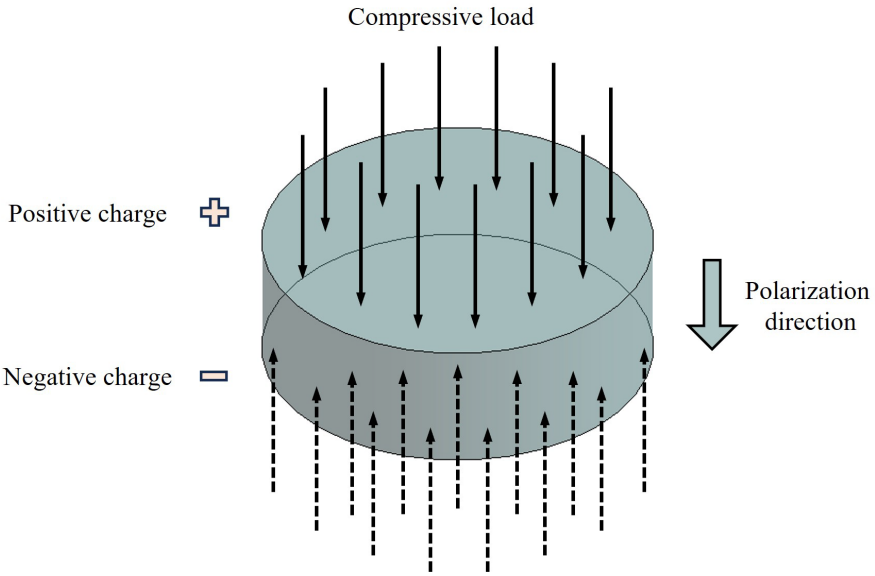


Fig. 4-3: Piezoelectric effect of working mode (d_{33})

Table 4-1 Material properties of KNN sensor model

KNN					
Relative permittivity	ε_{11}	2178	**Density (kg/m^3)**	ρ	4.60
	ε_{33}	2496	**Poison's ratio**	v	0.25
Charge constants ($10^{-12}C/N$)	d_{31}	-159	**Stiffness constants ($10^{10}N/m^2$)**	C_{11}	15.58
	d_{33}	321		C_{12}	9.77
	d_{15}	602		C_{13}	10.76
Young's modulus (MPa)	Y_{11}	78,190		C_{33}	17.29
	Y_{33}	81,500		C_{44}	2.44
	Y_{55}	29,050		C_{66}	2.91

Epoxy Resin		
Density ρ (kg/m^3)	**Young's modulus (MPa)**	**Poison's ratio ν**
0.98	1,000	0.38

4.3.3. Development of a Tire Model

Fig. 4-4 illustrates the tire model for numerical simulations. A common passenger car tire type 185/60 R15 was selected to study the mechanical response of the pavement and the piezoelectric behavior of the KNN sensors under traffic loading. The specifications of the selected 185/60 R15 tire are shown in Table 4-2.

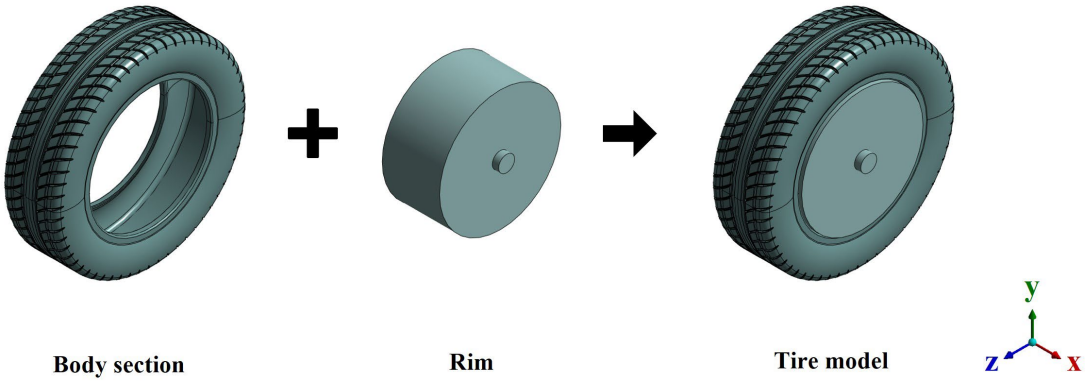


Fig. 4-4: Components of tire model

Table 4-2 Selected tire specifications

Feature	Value
Diameter (mm)	603.0
Width (mm)	185.0
Circumference (mm)	1894.4
Sidewall height (mm)	111.0
Revolutions per mile (km)	527.8

The primary objective of this study is to examine the behavior of the pavement and the KNN sensors. Previous studies (Ge et al., 2023; Lu et al., 2025) have also demonstrated that tire simplification does not significantly affect the response of the pavement and the sensor. The body section is regarded as an elastic body, while the rim is considered a rigid body. The freedom degrees of these two objects are fixed by setting the coupled contact law so that the body section and rim parts can stick together and prevent sliding (Ge et al., 2022). The friction behavior is defined between the tire and the pavement. According to the authors' previous study (P. Liu et al., 2018), the tire material properties used for simulation are specified (as shown in Table 4-3).

Table 4-3 Material properties of the tire

Material parameter	Body section	Rim
Density (kg/m^3)	719	8000
Poisson's ratio	0.3	0.3
Young's modulus (MPa)	80	200,000

The longitudinal behavior of the tire (including rolling and braking) is investigated. The longitudinal behavior of the tire is assigned to simulate the traffic loads on the pavement. For the rolling tire without turning, the longitudinal velocity v can be calculated as follows:

$$v = \omega r \quad \textbf{(4-1)}$$

where ω is the angular velocity with rad/s; r is the radius of the tire with m.

4.3.4. Development of the Large-Scale Model

Aims to examine the adaptability of KNN sensors applied in asphalt and concrete pavements, various types and sizes of FE pavement models were developed in FE software Ansys for different simulation scenarios (as shown in Fig. 4-5). The first model (8.00 m × 1.80 m × 2.92 m) is used for the study of the tire-asphalt pavement-KNN sensor system. The second model (8.00 m × 1.80 m × 5.64 m) is used for the study of the tire-concrete pavement-KNN sensor system on a large scale. KNN sensors are embedded in the pavement and subjected to traffic loads. The model is discretized using quadratic tetrahedral elements, and adaptive sizing is used to enhance local mesh accuracy in the tire-pavement contact interval. This mesh setting is utilized to balance the accuracy and time of the simulation. As boundary conditions, the bottom and sides of the pavement are set to be fixed. The interaction between different layers is defined as surface-to-surface contact, including tangential and normal behavior of the contact properties. The motion of these layers in the vertical direction is correlated with each other, while the motion in the horizontal direction allows for frictionless sliding. The friction behavior of the tire is determined by assigning friction coefficients to the tire surface and between the surface courses.

Table 4-4 and Table 4-5 show the geometrical data and material properties of the numerical models for asphalt and concrete pavements. The geometrical data and material properties of the asphalt pavement are determined according to our previous study (P. Liu et al., 2018). The geometrical and material properties of the numerical model for the concrete pavement are determined comprehensively based on previous studies accordingly (Li et al., 2023).

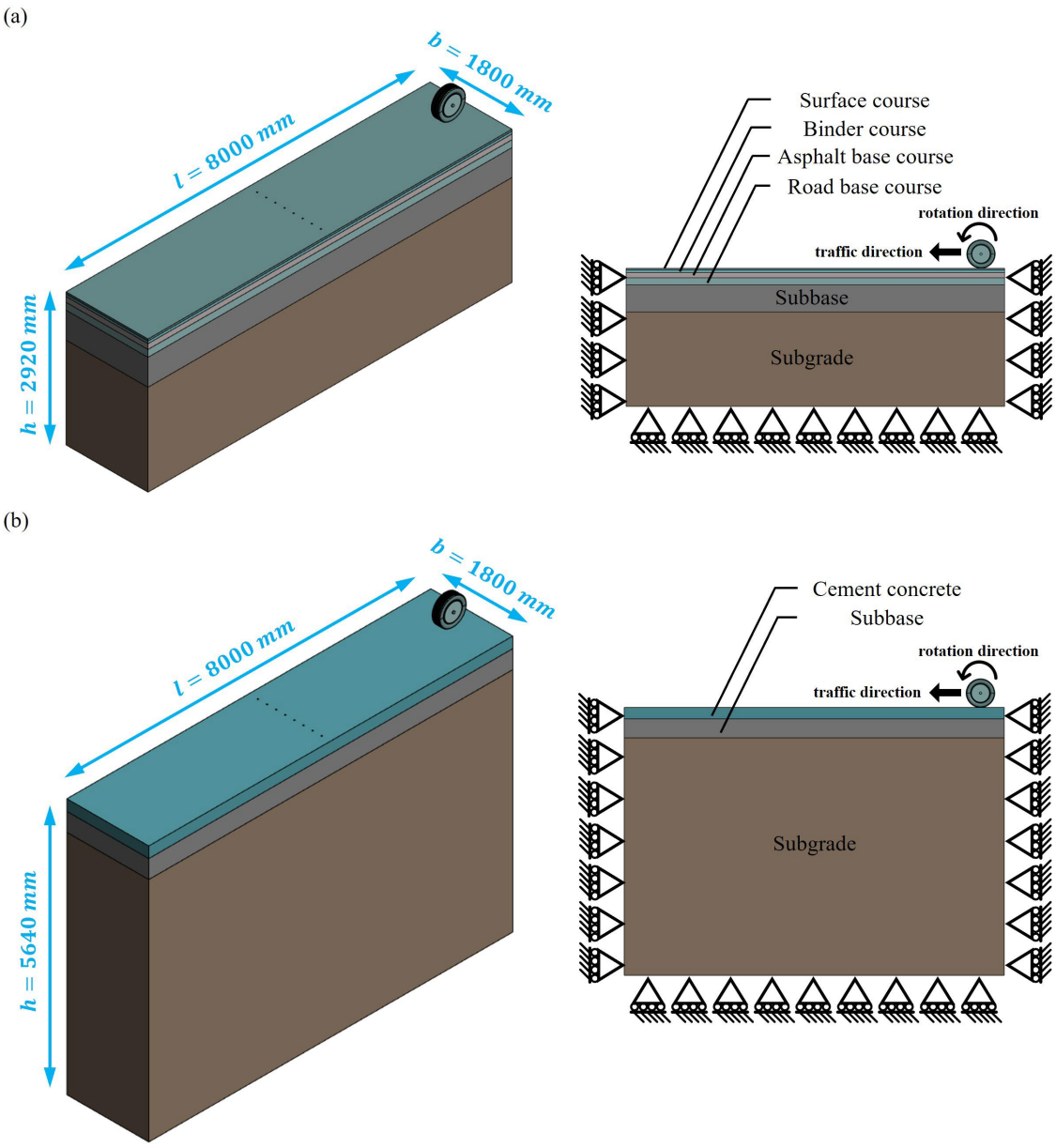


Fig. 4-5: Components of numerical models: (a) tire-asphalt pavement-KNN sensor model, (b) tire-concrete pavement-KNN sensor model

Table 4-4 Geometrical data and material properties of the asphalt pavement

Layer	Thickness (mm)	Young's modulus (MPa)	Poison's ratio	Density (kg/m^3)
Surface course	40	11,150.0	0.35	2.377
Binder course	50	10,435.0	0.35	2.448
Asphalt base course	110	6893.0	0.35	2.301
Road base course	150	157.8	0.49	2.400
Subbase	570	125.7	0.49	2.400
Subgrade	2000	98.9	0.49	2.400

Table 4-5 Geometrical data and material properties of the concrete pavement

Layer	Thickness (mm)	Young's modulus (MPa)	Poison's ratio	Density (kg/m^3)
Cement concrete	240	32,500.0	0.20	2.390
Subbase	400	1,000.0	0.25	2.300
Subgrade	5000	50.0	0.35	1.920

4.3.5. Verification of Models

To verify the large-scale model, it was divided into two parts. The initial segment of the simulation is focused on the model of interaction between the tire and the pavement, employing an asphalt road surface as a case in point. In this scenario, the tire exerts an initial force on the road surface in the normal direction, with a displacement of 0.001 m. Fig. 4-6 (a) illustrates the contour plots of von Mises stress σ_v and equivalent elastic strain ε_e at the end of the simulation for the pavement model. Fig. 4-6 (b) shows the local enlargement of the contour plot of the von Mises stress distribution. The von Mises stresses are mainly distributed in the top two layers of the pavements, where stress concentrations occur at the bottom of each layer. The stress concentration is attributed to the different moduli of each layer. The equivalent elastic strain decreases radially in all directions due to strain transmission. This phenomenon is not observed for von Mises stress because stresses in different directions cancel each other out to present lower von Mises stresses at these locations. The above distribution patterns of von Mises stresses and equivalent elastic strains are consistent with the actual situation. Similar distribution patterns have been observed in previous literature (Buonsanti and Leonardi, 2012; K. Zhao et al., 2024).

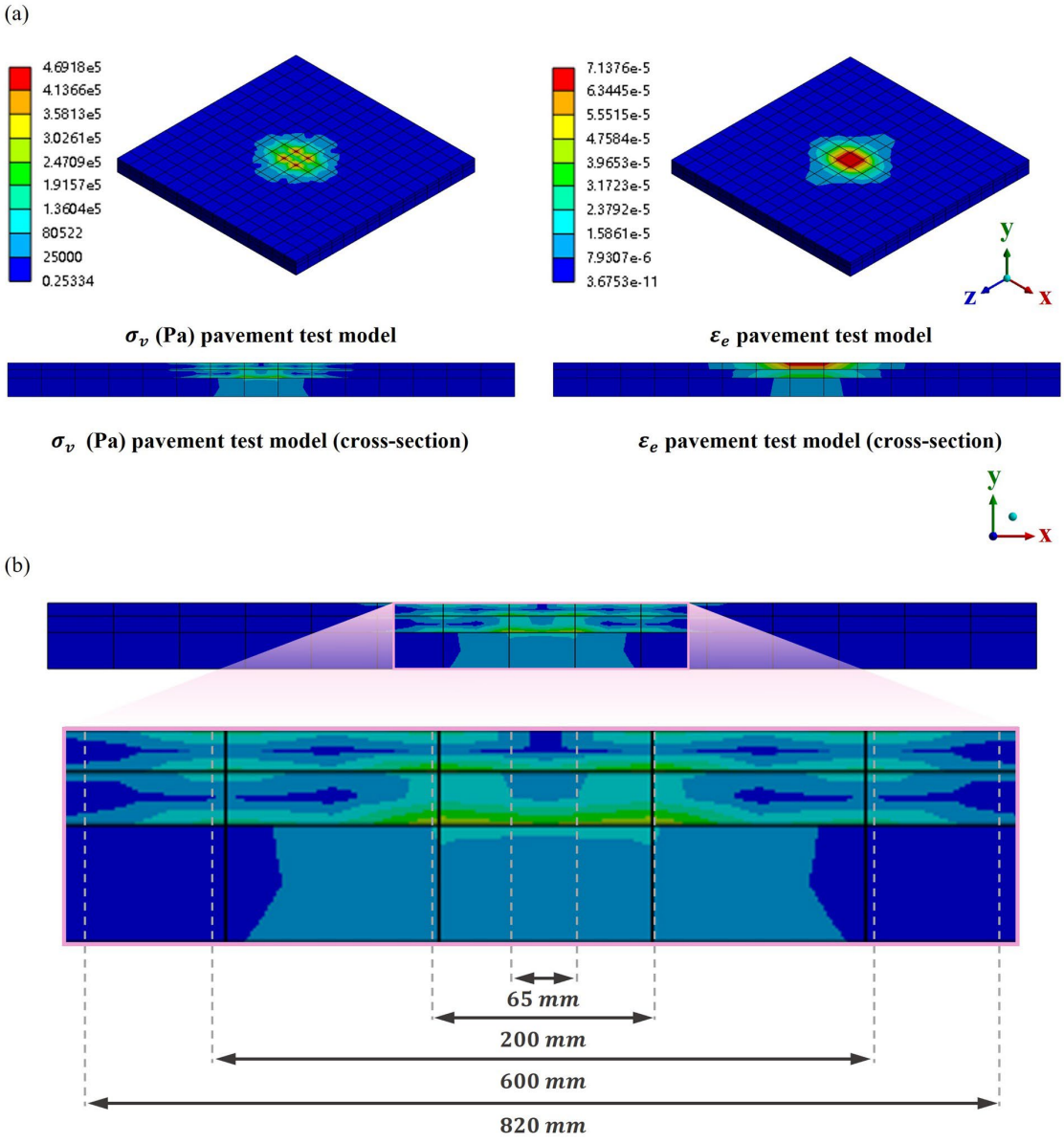


Fig. 4-6: (a) Contour plots of von Mises stress and equivalent elastic strain distributions in the pavement model, (b) local enlargement of the von Mises stress contour plot

Following the verification of the tire-road model, the force and signal output of the small model of the KNN sensor also required verification. Based on real experimental data, the Ansys software was employed to construct a finite element model of the KNN materials. The piezoelectric performance was characterized by calculating the open-circuit voltage of each KNN sensor unit. According to the previous study (Yang et al., 2017), the open-circuit voltage induced by the KNN sensor is calculated as:

$$U = \frac{d_{33}\sigma_{33}h_p}{\varepsilon_0\varepsilon_r} \quad \textbf{(4-2)}$$

where d_{33} is the piezoelectric coefficient; σ_{33} is the stress component in the vertical direction;

h_p is the thickness of the piezoelectric unit; ε_0 is the permittivity of vacuum, $8.9 \times 10^{-12}\ F/m$; ε_r is the relative permittivity.

Experimental and simulated open-circuit voltage characteristics exhibit strong agreement, as quantified in Fig. 4-7. Utilizing the experimental data as a benchmark, the error exhibited a gradual decrease with increasing stress, with the overall error remaining within a defined acceptable range of ± 10%. Although the relative errors at the first two low-force data points were higher (-16.7% and 13.6%), this divergence stems from the small absolute voltage values at minimal stress levels. The error is only 0.2% under a force of 6367 kN. These errors are within an acceptable range for practical applications. This demonstrates that the KNN sensor model effectively captures the mechanical and piezoelectric responses under realistic operating conditions.

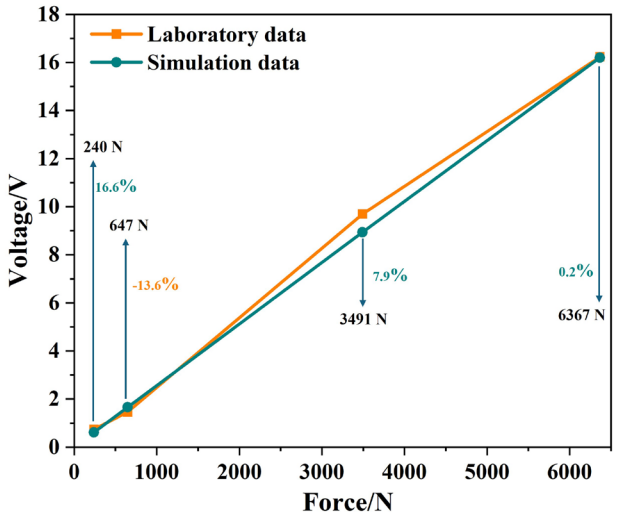


Fig. 4-7: Open-circuit voltage results of the experiment and the simulation

4.3.6. Setting of Input Variables

The validity of the modeling process was confirmed by comparing the simulation results with experimental measurements. The relative errors ranged from a minimum of 0.2% to a maximum of -16.7%, with larger deviations occurring at low voltage levels due to small absolute values. Nine factors were adjusted to analyze the effect on the open-circuit voltage after the KNN sensor was installed and to study the different pavement adaptability. Fig. 4-8 illustrates the nine groups of input variables used for the study. The piezoelectric properties of KNN materials are significantly affected by various traffic flow conditions, which can be

considered via the use of horizontal offset, camber, axial load, speed, deceleration, and friction coefficient (Guo et al., 2022; H. He et al., 2021; Tang et al., 2022; Zhang et al., 2020). The output voltage of KNN piezoelectric sensors exhibits significant sensitivity to embedment depth, phase angle orientation, and inter-sensor spacing (Du et al., 2022; H. Yang et al., 2020). To quantify these parametric dependencies, a systematic investigation was conducted by embedding sensor prototypes at varying positions within pavement structures.

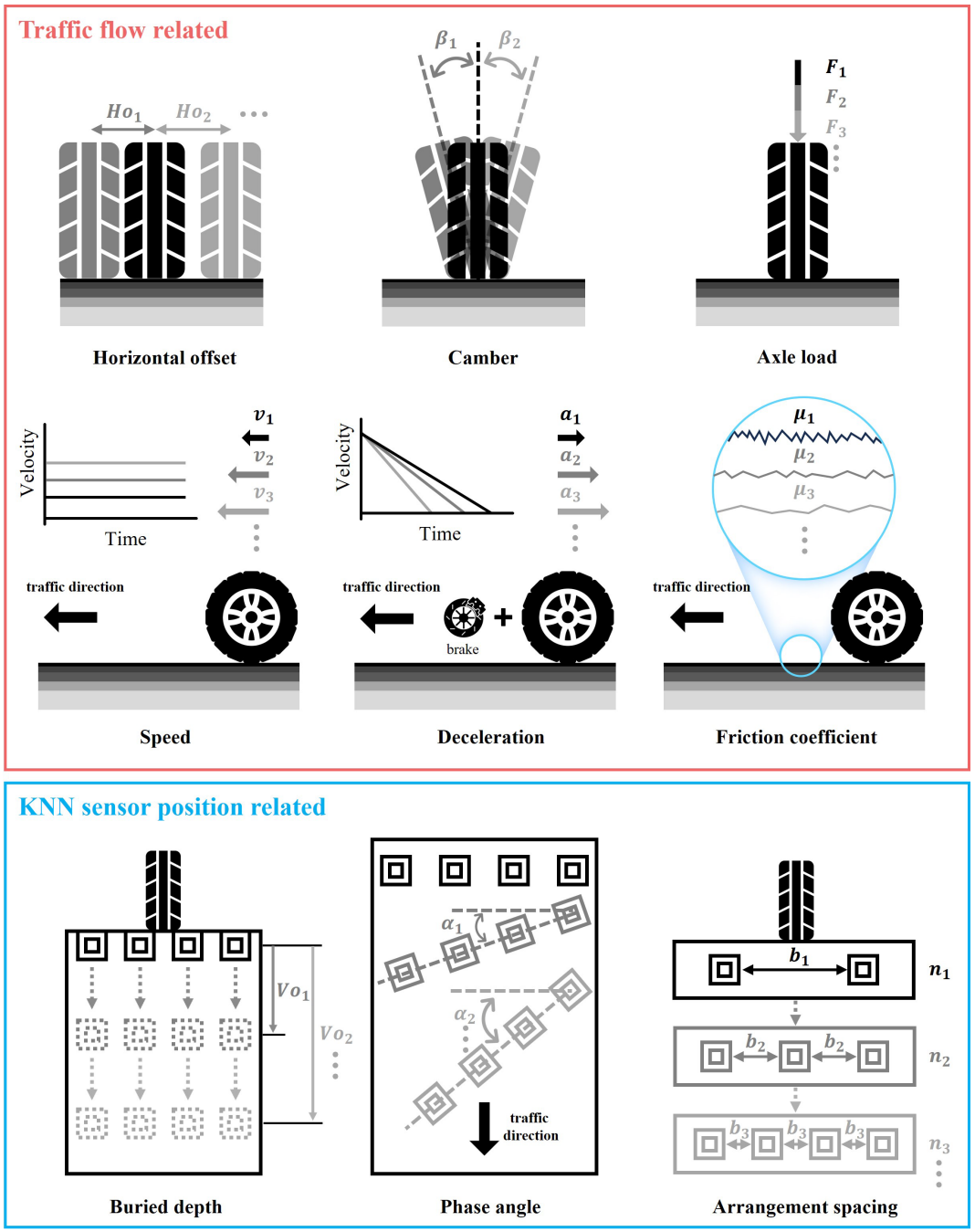


Fig. 4-8: Input variables used for studies

Table 4-6 Groups of variables

Parameters	Reference Value	Variation Range
Horizontal offset	0 cm	0-16 cm (interval 4 cm)
Camber	0°	-2° to 2° (interval 1°)
Axle load	3 kN	1.5, 3, 5, 7, 9 kN
Speed	50 km/h	30–110 km/h (interval 20 km/h)
Deceleration	0 m/s^2	10–30 m/s^2 (interval 5 m/s^2)
Friction coefficient	0.7	0.1–0.9 (interval 0.2)
Buried depth	2 cm	0–8 cm (interval 2 cm)
Phase angle	0°	0°–60° (interval 15°)
Arrangement spacing	20 cm	15–35 cm (interval 5 cm)

4.4. Results and Discussion

A specific cross-section was selected to illustrate the results. The initial tire position is located in the center of the pavement to ensure that it can pass between two neighboring sensors after driving. As shown in Fig. 4-9 (a), the cross-section results of the mechanical response of the tire when it exactly drives over the KNN sensors are selected as benchmarks. The cross-section results are used for the large-scale study related to the pavement. For the small-scale study related to the KNN sensors, the first KNN sensor on the right side of the tire is selected as the benchmark. Fig. 4-9 (a) and Fig. 4-9 (b) show the simulation results of buried depth (see Table 4-6) for asphalt pavement and concrete pavement at a buried depth of 2 cm, respectively. For the asphalt pavement, the stresses are mainly transferred in the surface course, binder course, and asphalt base course; the stress concentration mainly occurs at the connections between layers. The strains are transferred radially along the normal and tangential directions, with periodic patterns of contour plots in each layer; peaks of strain occur at the connections between layers. Compared to the asphalt pavement, the concrete pavement exhibits a different stress and strain transmission pattern. For the cement pavement, the stresses are mainly transferred in cement concrete; the stress distribution exhibits an I-beam shape; and the stress concentrations occur at the top and bottom of the cement concrete. In cement concrete, the strains and stresses exhibit a similar distribution pattern; for the remaining layers, the strains are mainly transferred along the normal direction. The above different distribution patterns of stresses (strains) are attributed to different load transmission modes, which are essentially due to differences in the

elastic modulus of the different layers (Plati, 2019; Qingtao Zhang et al., 2023). Therefore, only the part where the stress changes significantly is considered.

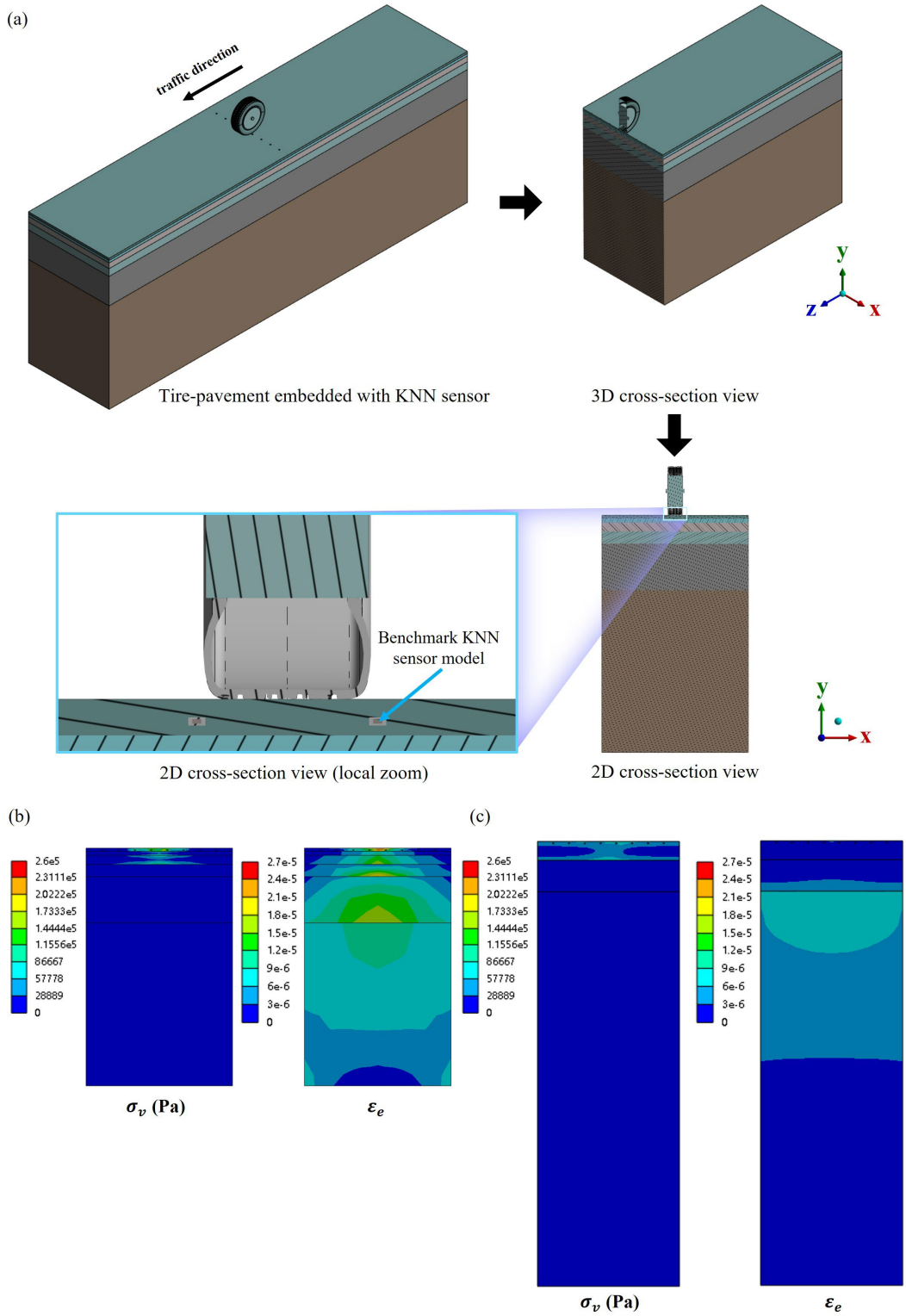


Fig. 4-9: Simulation results of the numerical models: (a) schematic of cross-section view, (b) simulation results for the asphalt pavement model, (c) simulation results for the concrete pavement model

4.4.1. Mechanical Response for the Large-Scale Model

As mentioned above, for asphalt pavement and concrete pavement, stress transmission mainly occurs in the first three layers and the first layer, respectively. Therefore, the contour plots of the above layers are selected for the von Mises stress distribution used to illustrate the results. Fig. 4-10 illustrates the von Mises stress distribution for different pavements with various horizontal offsets. As the tire shifts horizontally, the distribution of stresses also shifts horizontally overall. For the asphalt pavement, the maximum stress occurs in the middle of the surface course under the normal of the tire. For the concrete pavement, the maximum stress occurs at the top of the concrete under the normal of the tire. This is caused by the different elastic modulus of each road layer (Ragni et al., 2020). Asphalt and concrete pavements have different stress concentration regions. This means that for asphalt pavements, KNN sensors buried near the middle of the surface course are more susceptible to failure due to mechanical stress. For concrete pavements, the KNN sensors buried near the top of the concrete are more susceptible to failure due to mechanical stress.

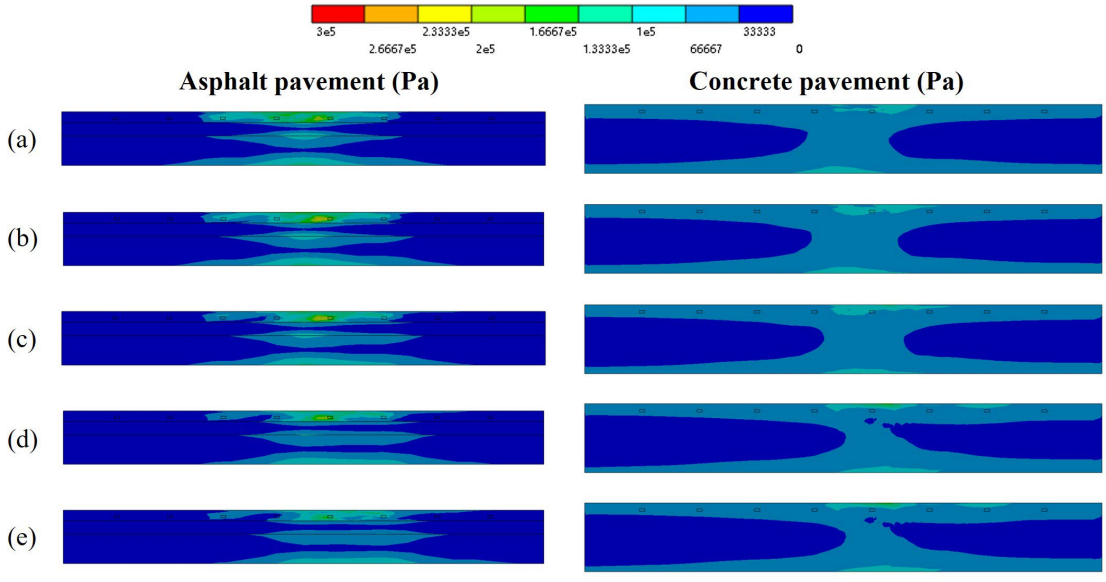


Fig. 4-10: Contour plots of von Mises stress distribution for different pavements with various horizontal offsets: (a) 0 cm, (b) 4 cm, (c) 8 cm, (d) 12 cm, (e) 16 cm

The change in the angle of inclination of the vehicle's tires will result in a change to the contact area of the tires of the same size as the ground. From this, the von Mises stress distribution for different pavements with various cambers has been studied (as shown in Fig. 4-11). As the absolute value of the camber increases, the stress concentration phenomenon

becomes distinctive along with the enhancement of maximum stress in the contour plots and the stress concentration region. In this study, a tilt to the right in the normal direction was defined as a positive angle, and a tilt to the left in the normal direction was defined as a negative angle. At -2° and 2°, the highest stress levels are observed in the respective tilt directions. The change in the camber causes the reduction of the contact patch between the tire and the pavement, leading to an asymmetry in the stress distribution. Therefore, for the same load, the pressure on the pavement rises due to the decrease in contact patch. The results are consistent with the findings in the previous study (Shupei Zhang et al., 2024). This implies that the change in the camber of the tire increases the wear of the KNN sensors. This poses challenges to the load-bearing capacity of the packaging materials, especially the resin.

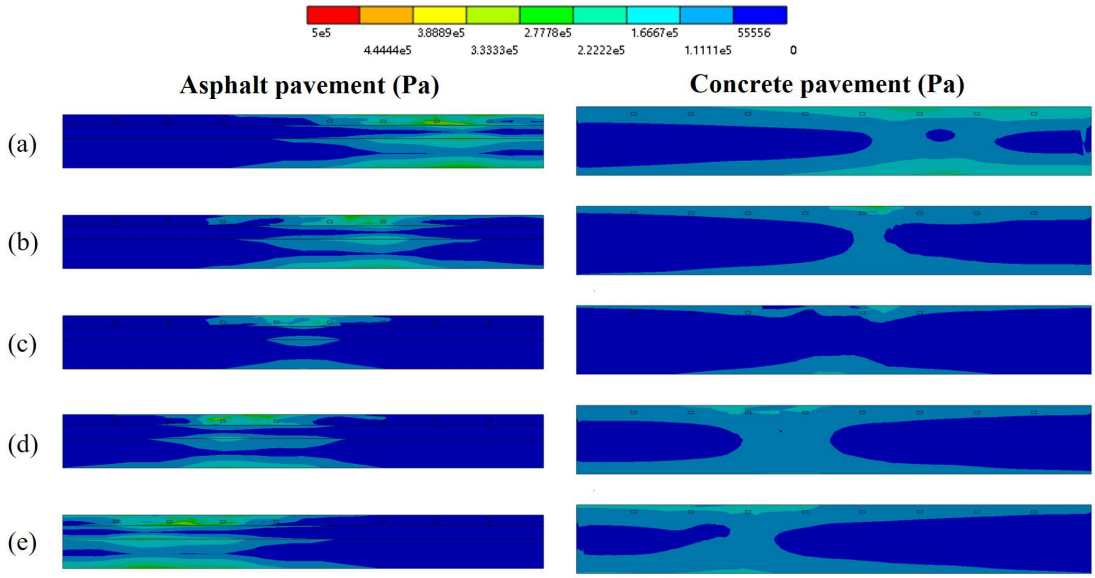


Fig. 4-11: Contour plots of von Mises stress distribution for different pavements with various cambers: (a) -2°, (b) -1°, (c) 0°, (d) 1°, (e) 2°

Fig. 4-12 illustrates the von Mises stress distribution for different pavements with various axle loads. From the change pattern, the effect of axle load on the stress distribution is obvious. As the axle load increases, the stresses within the pavements and the contact region between the tire and the pavement rise correspondingly. The climbing of the axial load further accelerates the stress transmission, which is reflected in the larger stress regions occurring in the horizontal and vertical directions. In addition, with the increasing axle load, the stress distribution near the KNN sensors is distinctly expanded, suggesting that a heavily loaded vehicle can significantly damage the packaging material of the KNN sensors.

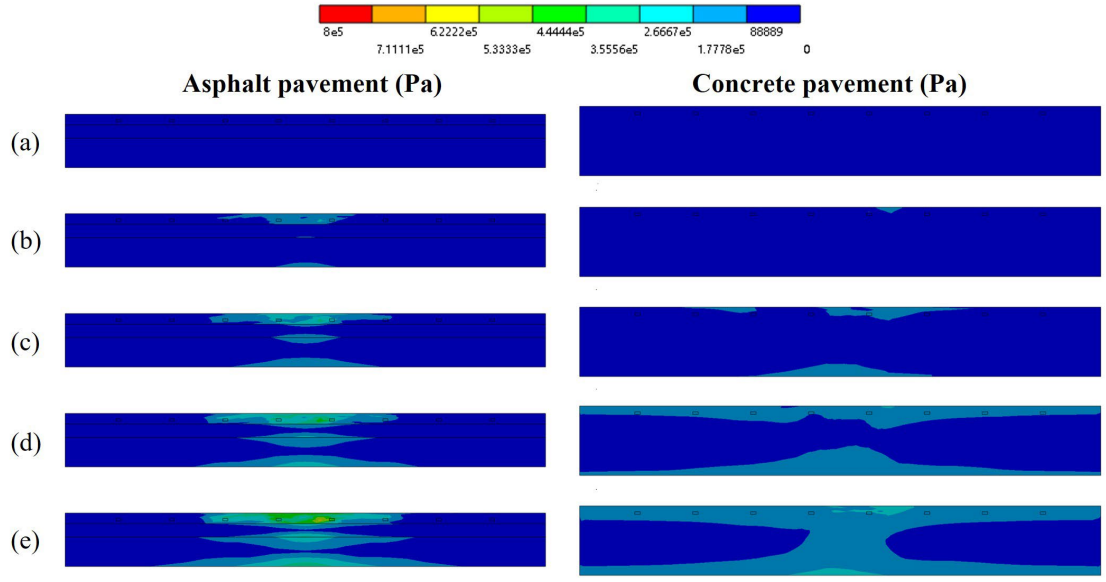


Fig. 4-12: Contour plots of von Mises stress distribution for different pavements with various axle loads: (a) 1.5 kN, (b) 3 kN, (c) 5 kN, (d) 7 kN, (e) 9 kN

In the case of a vehicle, the distribution of stress on the road is affected not only by the vehicle's weight but also by its speed (Fig. 4-13) and deceleration (Fig. 4-14). As the velocity of the vehicle increases, the maximum stress within the pavement gradually rises. Concurrently, the stress concentration region expands, as illustrated in Fig. 4-13. The effect of speed on the stresses within pavements is relatively small. Comparing Fig. 4-12, it can be seen that the effect of axle load on the stresses within pavements is larger than the effect of speed on the stresses within pavements. Previous studies claim that the variation of stress distribution with speed is attributed more to the variation of tangential stress than normal stress (Z. Gong et al., 2024a; Tielking and Roberts, 1987). Furthermore, elevated tangential stresses induced by vehicular speed acceleration may initiate pavement cracking (Hugo and Kennedy, 1985), potentially compromising KNN sensor operational integrity via mechanical vibration interference.

The von Mises stress distribution for different pavements with various decelerations is illustrated in Fig. 4-14. The results demonstrate that as deceleration intensifies, the maximum stress within the pavement increases correspondingly, leading to an expansion of the stress concentration region. Previous studies have attributed this rise in von Mises stress primarily to an increase in shear stress (Oubahdou et al., 2021). Moreover, a combination of the results presented in Fig. 4-12 and Fig. 4-13 indicates that overloading, high-speed driving and emergency braking have a detrimental effect on the shear stress experienced by the pavement.

Therefore, a rational approach to road design, incorporating effective measures to regulate vehicle overloading and speed, is essential to mitigate shear-induced pavement damage.

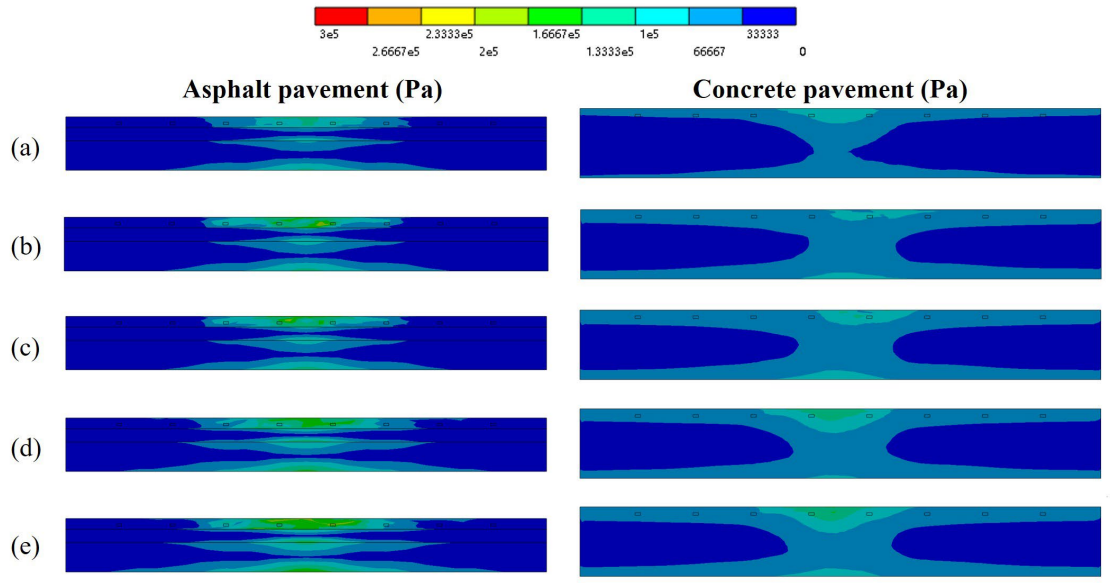


Fig. 4-13: Contour plots of von Mises stress distribution for different pavements with various speeds: (a) 30 km/h, (b) 50 km/h, (c) 70 km/h, (d) 90 km/h, (e) 110 km/h

The interaction between vehicles and the road surface is a complex phenomenon that involves the transmission of force from the vehicle to the road surface, and vice versa. Consequently, the road surface is calibrated and simulated using different friction forces. Fig. 4-15 displays the von Mises stress distribution for different pavements with various friction coefficients. As the friction coefficient of the pavement increases, the maximum stress within the pavement correspondingly rises, accompanied by an expansion of the stress concentration region. This is mainly attributed to the contribution of greater shear stress. A higher friction coefficient leads to an increase in frictional forces, which subsequently intensify shear stress within the pavement structure. The von Mises stress also exhibits a proportional increase due to the enhanced contribution of shear stress. While dry pavement conditions enhance tire grip and skid resistance, the elevated stress levels also accelerate the wear of KNN sensors compared to wet pavement conditions.

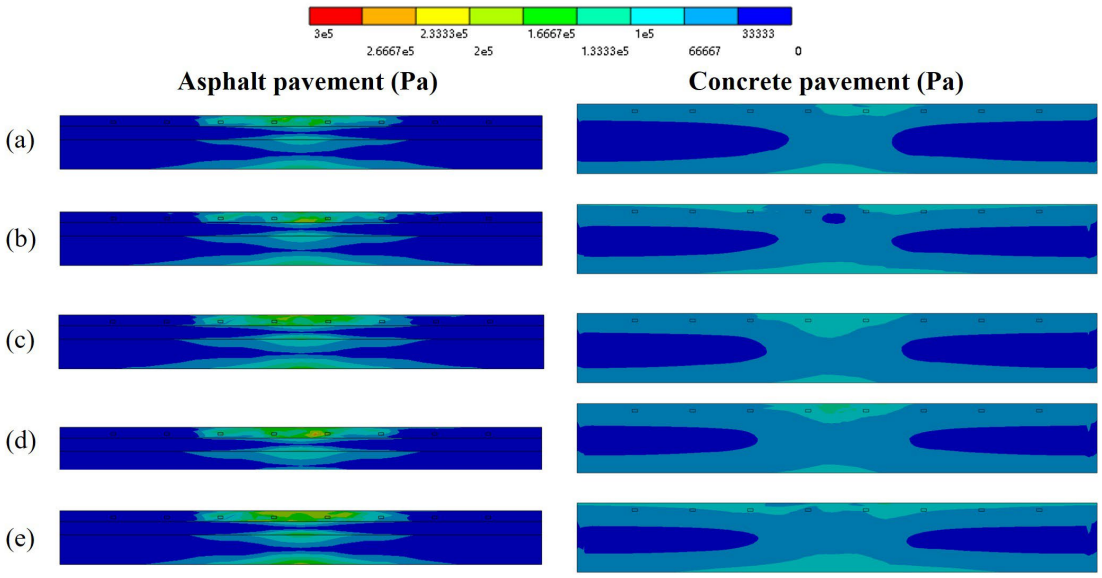


Fig. 4-14: Contour plots of von Mises stress distribution for different pavements with various decelerations: (a) 10 m/s^2, (b) 15 m/s^2, (c) 20 m/s^2, (d) 25 m/s^2, (e) 30 m/s^2

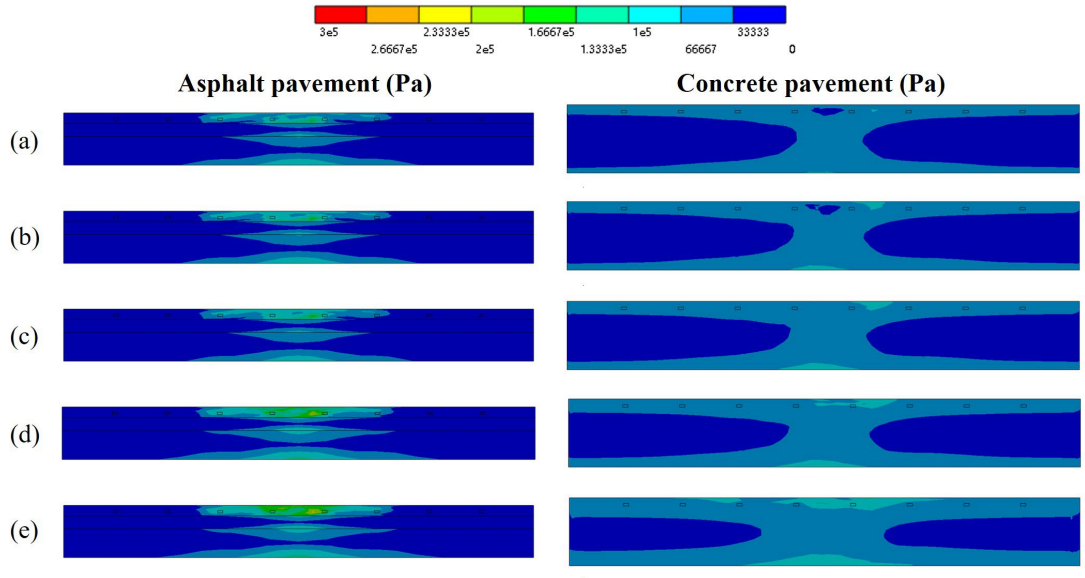


Fig. 4-15: Contour plots of von Mises stress distribution for different pavements with various friction coefficients: (a) 0.1, (b) 0.3, (c) 0.5, (d) 0.7, (e) 0.9

4.4.2. Mechanical Response for the Small-Scale Model

The stress distribution on the road surface is not equivalent to that on the sensor. Consequently, further consideration must be given to the stress distribution acting on the sensor under identical load conditions, following a thorough examination of the tire track model. Fig. 4-16 illustrates the von Mises stress distribution for the benchmark KNN sensors in different pavements with various buried depths. The stresses of KNN sensors in different pavements

show different distributions. The distribution of KNN sensor stresses in the asphalt pavement is more homogeneous, which is attributed to the different load transmission modes. Due to the different modulus of the KNN sensor and the layer, there is a significant stress concentration in the KNN sensor. Stress concentrations occur at the top edge of the KNN sensor, which could potentially damage the packaging material of the KNN sensor. In addition, the stress concentration could also cause damage to the pavement layer. Therefore, the pavement layer above the KNN sensor should be protected to avoid damage to the pavement caused by the KNN sensor. The stress values in KNN decrease significantly with increasing buried depth. Although the increase in buried depth reduces the damage degree of the KNN sensors, the piezoelectric properties of the KNN sensors also need to be taken into account. This will be analyzed in the subsequent section. Moreover, the KNN sensor in the asphalt pavement is subjected to higher stresses than the KNN sensor in the concrete pavement.

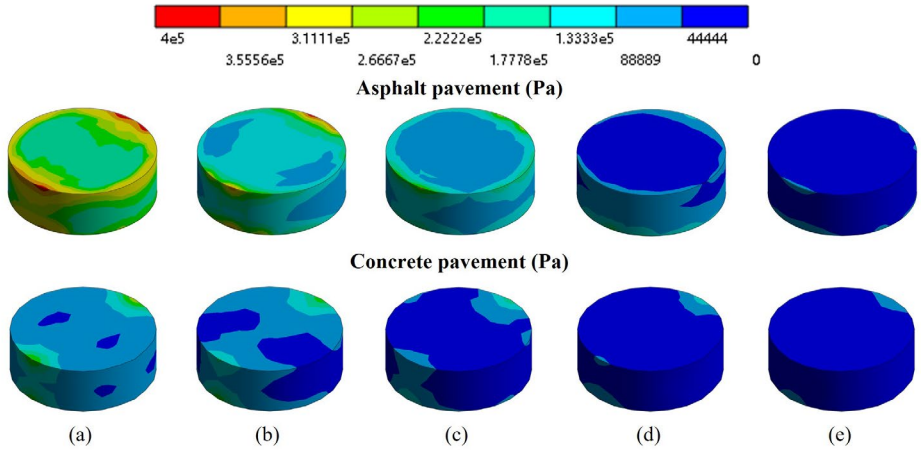


Fig. 4-16: Contour plots of von Mises stress distribution for KNN sensor in different pavements with various buried depths: (a) 0 cm, (b) 2 cm, (c) 4 cm, (d) 6 cm, (e) 8 cm

The effect of varying phase angles on the pressure exerted on the sensor was investigated, as illustrated in Fig. 4-17. The stress values on the KNN sensor are higher at phase angles of 0° and 15°; the stress values on the KNN sensor decrease with further increase in phase angle. However, the effect of phase angle on KNN sensor stress values is less than the effect of buried depth on KNN sensor stress values. Moreover, an increase in the phase angle mitigates the stress concentration phenomenon on the KNN sensor. The phase angle serves as a critical parameter for analyzing the mechanical and piezoelectric responses of the KNN sensor, particularly under conditions where the vehicle is navigating along a nonlinear trajectory. Therefore, it also means

that the stress on the KNN sensor is reduced when the tire offset along the direction of travel is greater than 15°.

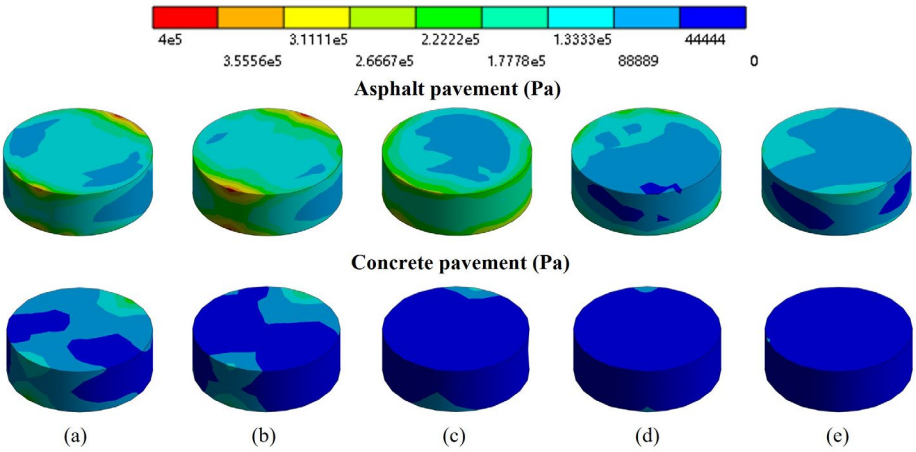


Fig. 4-17: Contour plots of von Mises stress distribution for KNN sensor in different pavements with various phase angles: (a) 0°, (b) 15°, (c) 30°, (d) 45°, (e) 60°

The sensors utilized in this study are of the single-row variety; therefore, it is imperative to undertake a comprehensive investigation into the distribution of stress associated with the internal configuration of the sensors. It is evident from Fig. 4-18 that the stress values in the KNN sensor decrease slowly with an increase in arrangement spacing, which is essentially due to the decay of load transmission. However, the effect of arrangement spacing on KNN sensor stress values is less than the effect of buried depth on KNN sensor stress values. While larger arrangement spacing may offer economic advantages and reduce stress concentration, it does not guarantee optimal piezoelectric performance. This will be analyzed in the next section.

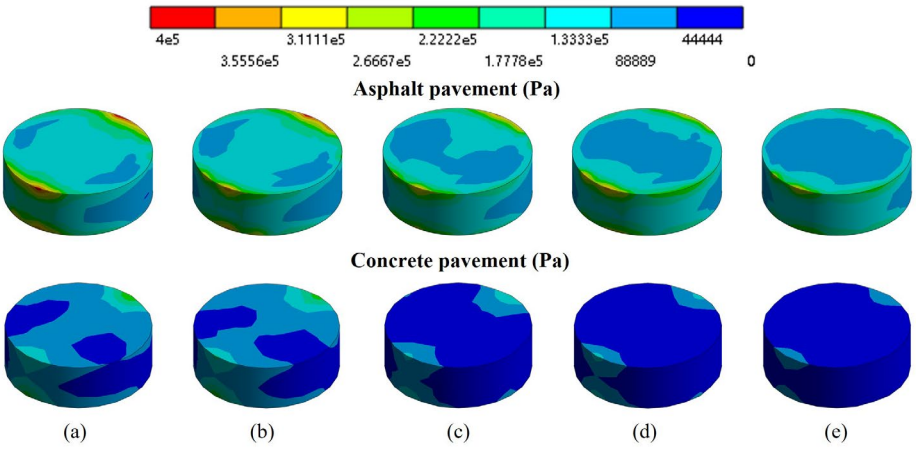


Fig. 4-18: Contour plots of von Mises stress distribution for KNN sensor in different pavements with various arrangement spacings: (a) 15 cm, (b) 20 cm, (c) 25 cm, (d) 30 cm, (e) 35 cm

4.4.3. Piezoelectric Performance for the Small-Scale Model

This section is used to describe the piezoelectric properties of KNN. The open-circuit voltage of the KNN sensor is calculated according to Eq. (4-2). To facilitate the processing of the data, the normal stress component corresponds to the maximum value located directly above the sensor. Because of the substantial volume of data, a single set of open-circuit voltage distribution plots is presented here as an example. Fig. 4-19 illustrates the open-circuit voltage distribution for the benchmark KNN sensor in different pavements with various buried depths. From the results, it can be seen that the voltage generated by the KNN gradually decreases with the buried depth. The KNN sensor buried near the surface of the pavement (0 cm and 2 cm) generates higher voltages, which can be attributed to the weaker stress transmission dissipation in the pavement. When the buried depth is greater than 2 cm, the generated voltage decreases significantly. Near the pavement surface, traffic tire loads can be easily transferred to the embedded KNN sensor model, resulting in a larger voltage generated by the KNN sensor. If only based on numerical values, the KNN sensor has the highest piezoelectric performance when embedded in the road surface (0 cm). However, this probably does not correspond to the actual situation. This is attributed to the higher mechanical stress and environmental exposure (e.g., rainfall, tire friction) experienced by KNN sensors embedded in the road surface (see Fig. 4-16 (a)). This can significantly accelerate the wear of the KNN sensor. Therefore, it is suggested to embed the KNN sensor to a depth of 2 cm, which achieves a balance between piezoelectric performance and the durability of the KNN sensor. Additionally, the piezoelectric voltage output of the KNN sensor embedded in asphalt pavement is on average twice as high as that of the voltage output of the KNN sensor embedded in concrete pavement, same scenario for different buried depths. This is attributable to the higher elastic modulus of the concrete surface, which results in lower normal stresses in the same location. Furthermore, this results in a smaller voltage generated by the KNN sensor embedded in the concrete pavement (Eq. (4-2)).

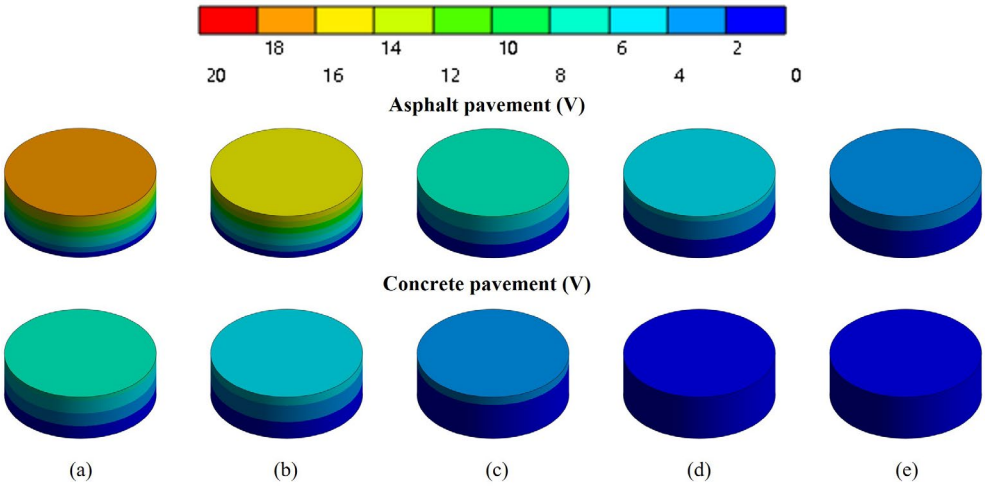


Fig. 4-19: Contour plots of open-circuit voltage distribution for KNN sensor in different pavements with various buried depths: (a) 0 cm, (b) 2 cm, (c) 4 cm, (d) 6 cm, (e) 8 cm

4.4.3.1. Variable Effects for Open-Circuit Voltage

As shown in Fig. 4-20, all the simulated groups of data are summarized, and the results of the open-circuit voltages of the KNN sensor for different cases are plotted into one graph.

Taking an overall view of the results, the KNN sensor embedded in the asphalt pavement generates approximately two to three times the voltage generated by the KNN sensor embedded in the concrete pavement for the same situation. Therefore, to maximize the piezoelectric performance of KNN sensors, it is recommended that they be embedded in asphalt pavements. When KNN sensors are applied to concrete pavements, the higher stiffness of concrete results in smaller deformation and normal stress. Therefore, the signal output is relatively weak.

The influence of horizontal offset on open-circuit voltage is not significant. For both road surfaces, the maximum voltage is generated when the tire is positioned directly above the KNN sensor (see Fig. 4-9 (a)). The difference between the maximum (asphalt: 18 V, concrete: 5.88 V) and minimum (asphalt: 14.2 V, concrete: 5.04 V) open-circuit voltage is not significant, as demonstrated in Fig. 4-20 (a). This is likely attributable to the relatively negligible normal stress attenuation in the horizontal direction, which consequently exerts a minimal influence on the open-circuit voltage. For asphalt pavement, the open-circuit voltage reaches its maximum when the horizontal offset is 8 cm. For concrete pavement, the open-circuit voltage reaches its maximum when the horizontal offset is 12 cm. Due to the elastic modulus of asphalt pavement is lower than concrete pavement, the stress is concentrated below the tire region and decays

more quickly in the horizontal direction. In contrast, the elastic modulus of concrete pavement is higher, the stress is more evenly distributed, and decays more slowly in the horizontal direction.

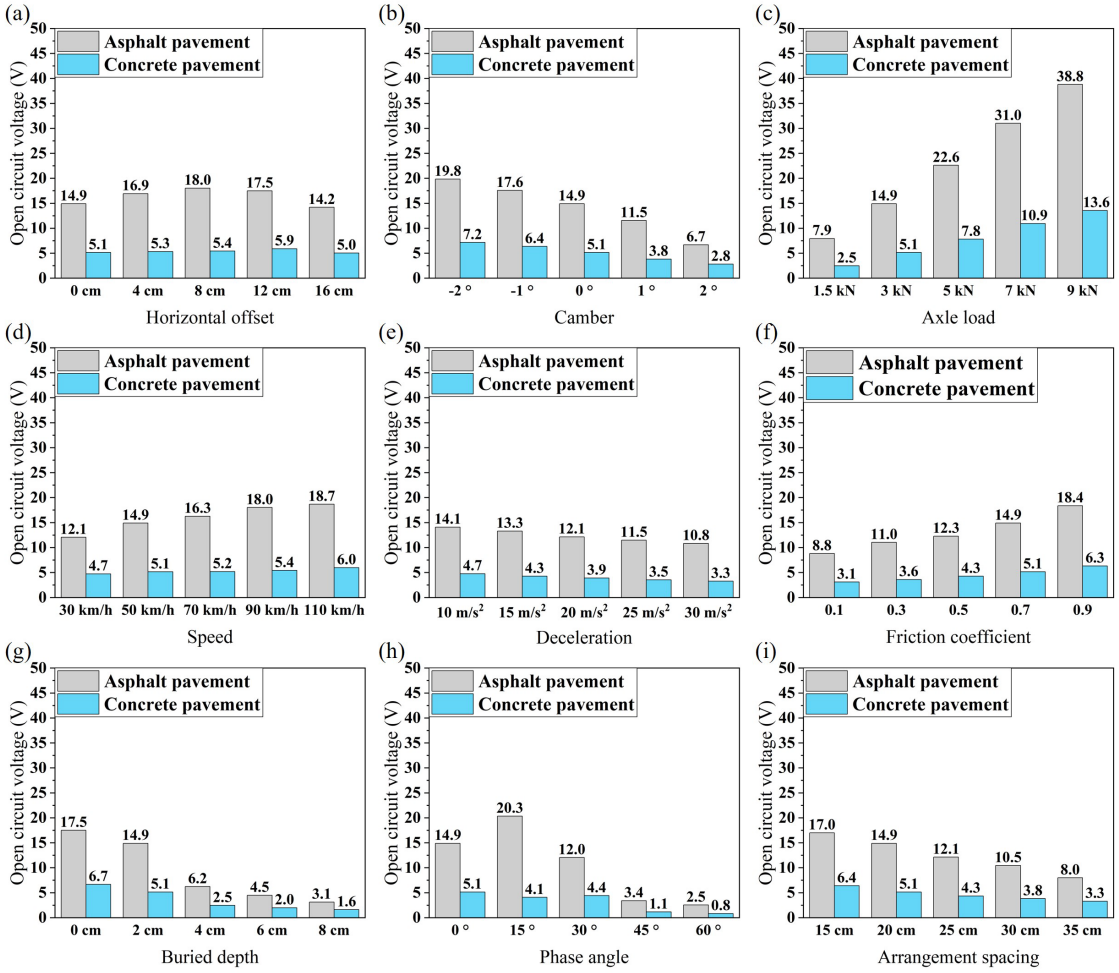


Fig. 4-20: Open-circuit voltage of KNN sensors under various groups of variables, (a) Horizontal, (b) Camber, (c) Alex load, (d) Speed, (e) Deceleration, (f) Friction coefficient, (g) Buried depth, (h) Phase angle, (i) Arrangement spacing

The camber has been shown to exert a greater effect on the open-circuit voltage than the horizontal offset. For both types of pavements, the open-circuit voltage decreases with camber change, as demonstrated in Fig. 4-20 (b). This phenomenon is attributed to the alteration in normal stresses caused by changes in the contact patch between the tire and the pavement. When the camber is set at -2°, it means that the tilt direction of the tire is closest to the sensor, and the open-circuit voltages for both pavements are recorded as 19.8 V and 7.15 V, respectively. When the camber is set at 2°, it means that the tilt direction of the tire is farthest away from the sensor, and the open-circuit voltages are recorded as 6.68 V and 2.81 V for both pavements, respectively.

The camber setting modifies the mode of stress transmission, resulting in the transfer of stresses in the normal direction being directed along the tire slope. While the piezoelectric performance of the KNN sensor can be enhanced by camber adjustment, the wear problem of the tire and the stress concentration of the KNN sensor remain salient concerns.

An investigation was conducted into the effects of axial load, speed, and deceleration on open-circuit voltage (see Fig. 4-20 (c), (d) and (e)). Fig. 4-20 (c) demonstrates that axial load has a significant effect on open-circuit voltage, which increases with increasing axial load. This is undoubtedly due to the heavier load transferring greater normal stress. The effects of speed (Fig. 4-20 (d)) and deceleration (Fig. 4-20 (e)) on the open-circuit voltage were relatively minor. When the vehicle speed elevated from 30 km/h to 110 km/h, the change in the open-circuit voltage was 6.6 V and 1.25 V, respectively. Compared with the other variables, this change was not significant. It can be deduced that vehicle speed does not act as the primary factor in determining the open-circuit voltage. This outcome is in alignment with the findings of the previous study (Sun et al., 2015). In contrast to the positive correlation between speed and open-circuit voltage, a negative correlation has been observed between deceleration and open-circuit voltage. Increases in deceleration, from 10 m/s^2 to 30 m/s^2, result in a decline in open-circuit voltage on asphalt road surfaces from 14.1 V to 10.8 V, and from 4.75 V to 3.27 V on concrete road surfaces. There is a positive correlation between the friction coefficient and the open-circuit voltage, and the friction coefficient has a relatively large effect on the open-circuit voltage, as shown in Fig. 4-20 (f). When the friction coefficient is 0.1, for both pavements, the open-circuit voltages are 8.79 V and 3.09 V, respectively. When the friction coefficient is 0.9, for both pavements, the open-circuit voltages are 18.4 V and 6.31 V, respectively. For the rolling tire, a rise in the friction coefficient induces a greater maximum normal stress at the tire-pavement interface (Yu et al., 2020), thus increasing the open-circuit voltage. The friction coefficient is affected by the skid resistance of the pavement. This means that KNN sensors embedded into pavements have significantly different piezoelectric effects when testing during dry weather versus wet weather. Therefore, it is suggested to embed KNN sensors into pavements in dry regions for higher economic efficiency.

The effect of buried depth on the piezoelectric properties of the KNN sensor has been analyzed and will not be repeated here (see Fig. 4-19 and Fig. 4-20 (g)). The impact of the phase

angle on asphalt is significantly more pronounced than its effect on concrete. As illustrated in Fig. 4-20 (h), the phase angle exerts a significant influence on the open-circuit voltage. For asphalt, the piezoelectric properties of the KNN sensor are optimal at a phase angle of 15°, with an open-circuit voltage of 20.3 V. The maximum open-circuit voltage at a phase angle of 15° can be attributed to the stress transfer mode of the tire. Due to the presence of the tire tread pattern, the maximum stress in the contact between the tire and the pavement is not directly below the tire, but at the tire tread pattern (see Fig. 4-6). Therefore, when the sensors are arranged orthogonally (phase angle 0°), it does not mean the maximum open-circuit voltage. When the sensors are not arranged orthogonally (phase angle 15°), they are subjected to greater stress, and therefore, the open-circuit voltage is greater. When the phase angle exceeds 15°, the open-circuit voltage decreases with increasing phase angle. For concrete, the open-circuit voltage generally decreases with increasing phase angle. The differing sensitivity to phase angle exhibited by distinct road surface types is attributed to disparate stress transfer modes (Fig. 4-9 (b)). For concrete pavements, the phenomenon of maximum open-circuit voltage at 0° was observed. This is because concrete pavements have greater material stiffness and higher uniformity, resulting in smaller stress propagation phase lag and smaller deviation of the stress wave direction from the polarization direction. Therefore, when the sensors are arranged orthogonally, the maximum d_{33} response can be accurately captured. For both road surfaces, a significant decrease in open-circuit voltage is observed as the phase angle increases from 30° to 60°. This finding suggests that the KNN sensor demonstrates superior piezoelectric properties when the vehicle steering angle is less than 30°.

Fig. 4-20 (i) illustrates the influence of arrangement spacing on the open-circuit voltage. For both pavements, the open-circuit voltage decreases as the arrangement spacing widens. The effect of arrangement spacing on open-circuit voltage is less than the effect of buried depth on open-circuit voltage. For the asphalt pavement, the maximum and minimum open-circuit voltages are 17 V and 7.99 V, respectively. For the concrete pavement, the maximum and minimum open-circuit voltages are 6.4 V and 3.29 V, respectively. The arrangement spacing is directly related to the economic cost. A larger arrangement spacing reduces the number of KNN sensors required, thereby lowering the economic cost. For the arrangement of KNN sensors, there is a conflict between piezoelectric performance and economic cost. Therefore, there is a

challenge to balance the relationship between both. A possible solution is to use Life-cycle assessment (LCA) (Baumann and Arvidsson, 2015) to balance the economics and utility of KNN sensors.

4.4.3.2. Correlation Analysis of Variable Effects

The effect of different variables on the piezoelectric performance of KNN sensors has been studied above. However, the effect of different variables on the piezoelectric properties of the KNN sensor is different. It is necessary to investigate the effect degree of the variables. Pearson correlation coefficient (Pearson, 1895) is used to study the degree of effect of different variables on the open-circuit voltage. The Pearson correlation coefficient is widely used to measure the degree of correlation between two variables and has a value between -1 and 1. A negative value is a negative correlation, and a positive value is a positive correlation. In this paper, the Pearson coefficient is used to investigate the correlation degree of different variables. The Pearson coefficient is defined as:

$$r_{xy} = \frac{\sum_{i=1}^{n}(x_i - \bar{x})(y_i - \bar{y})}{\sqrt{\sum_{i=1}^{n}(x_i - \bar{x})^2}\sqrt{\sum_{i=1}^{n}(y_i - \bar{y})^2}} \quad \textbf{(4-3)}$$

where n is the specimen size; x_i and y_i are the individual specimen points indexed with i; $\bar{x}$ and $\bar{y}$ are the mean values of the specimen.

In the case of this paper, the nine groups of variables are independent of each other, and only the open-circuit voltage is the dependent variable. The Pearson correlation coefficients between the nine groups of variables have no practical meaning. Therefore, it is only necessary to list the specimen Pearson correlation coefficients between the independent variables and the open-circuit voltage. Table 4-7 illustrates the specimen Pearson correlation coefficients of variables for open-circuit voltage using different tire-pavement-KNN sensor models.

There are positive and negative values for the specimen's Pearson correlation coefficient. For the convenience of analysis, the absolute value of the value is used in all cases. When the value is closer to 1, it means that the variable is more correlated with the open-circuit voltage. For the asphalt pavement, the effect degree of the variables on the open-circuit voltage is ranked in the following order: axle load, buried depth, phase angle, camber, speed, arrangement spacing, deceleration, friction coefficient, and horizontal offset. For the concrete pavement, the

effect degree of the variables on the open-circuit voltage is ranked in the following order: axle load, phase angle, buried depth, camber, deceleration, friction coefficient, speed, arrangement spacing, and horizontal offset. The axial load is the most important factor that affects the piezoelectric effect of the KNN sensor. Then, the buried depth, phase angle, and camber also significantly impact the piezoelectric effect of the KNN sensor. Other factors have relatively little effect on the piezoelectric effect of KNN sensors. The above provides qualitative results for the effect of different factors on the piezoelectric effect of the KNN sensor, which will provide constructive suggestions for the application of KNN sensors in practical engineering.

Table 4-7 Pearson correlation coefficients for asphalt and concrete pavements

	Open-circuit voltage (asphalt)	Open-circuit voltage (concrete)
Open-circuit voltage	1	1
Horizontal offset	0.0900	0.0740
Camber	-0.2334	-0.2390
Axle load	0.7383	0.7772
Speed	0.1534	0.0903
Deceleration	0.1112	0.1587
Friction coefficient	0.1063	0.1107
Buried depth	-0.3823	-0.3452
Phase angle	-0.3317	-0.3642
Arrangement spacing	-0.1319	-0.0804

4.5. Conclusions and Outlook

This study develops tire-pavement-KNN sensor models to assess KNN's mechano-electrical behavior in pavements. A validated baseline tire-pavement model was established, followed by parameterization of nine variables (horizontal offset, camber angle, axle load, speed, deceleration, friction coefficient, buried depth, phase angle, and arrangement spacing) to quantify their impacts. Comparative analyses differentiated KNN sensor responses in flexible (asphalt) and rigid (concrete) pavements. Pavement mechanical performance was evaluated under variable combinations, while factors in the hierarchy of piezoelectric output were analyzed. The findings support optimized KNN sensor deployment and mitigation of embedded device-induced damage risks. Key contributions include:

(1) Under the same conditions, the asphalt pavement is subjected to higher stresses than the

concrete pavement, which is attributed to the different stress transmission modes. For different pavements, the region of maximum stress distribution is different. The maximum stress in the asphalt pavement has been shown to occur in the middle of the surface layer in the direction normal to the tire. For the concrete pavement, the maximum stress occurs at the top of the concrete.

(2) Speed and deceleration have a relatively minor impact on stress variations within the pavements. An elevation in the friction coefficient raises stresses and expands the stress concentration region within the pavement. As the burial depth increases, the stress in the KNN sensor decreases, and the stress concentration phenomenon diminishes. In contrast, the phase angle and arrangement spacing have a comparatively small influence on the stress in KNN, exhibiting negative correlations with the stress. Changes in the camber reduce the contact patch between the tire and the pavement, which can intensify the stress concentration.

(3) KNN sensors embedded in asphalt generate a voltage that is approximately 200-300% higher than that of a KNN sensor in concrete under equivalent loading configurations. The asphalt sensor demonstrates enhanced sensitivity to diverse signals under load. Consequently, KNN sensors are more appropriate for asphalt pavement.

The current numerical model adopts a homogeneity assumption for pavement media to ensure computational tractability, which underestimates localized stress concentration at sensor-pavement interfaces and reduces the prediction accuracy of electromechanical coupling responses. Future research will develop anisotropic pavement microstructure models incorporating aggregate gradation parameters and viscoelastic phase distribution. This multi-scale computational framework aims to represent real pavement environments while investigating micromechanical coupling at heterogeneous interfaces, particularly stress redistribution under dynamic contact pressures. Furthermore, the service reliability of embedded KNN sensor arrays requires investigation. In-situ monitoring experiments should be conducted to clarify dynamic impedance matching and signal attenuation mechanisms in sensor–pavement systems under traffic-induced multiphysics coupling conditions.

5. A Sensor Arrangement Evaluation Framework for Lead-Free Potassium Sodium Niobate Pavement Sensors in Vehicle Classification

5.1. Abstract

An efficient sensor arrangement is critical for intelligent pavement monitoring, as dense sensor arrangements increase construction complexity and pavement disturbance. Finite element modeling (FEM) can accurately represent vehicle-pavement-sensor interactions, but repeated simulations limit its efficiency for large-scale layout evaluation. This study proposes a simulation-based method (ESAM) for evaluating pavement sensor arrangements using lead-free potassium sodium niobate (KNN) piezoelectric sensors with low piezoelectric response. Finite element outputs are used to describe sensor voltage responses under vehicle loading, and a voltage-distance relationship is used to estimate responses without repeated FEM simulations. Multiple sensor arrangements are examined under representative vehicle passage scenarios and lane configurations. Sensor arrangements are evaluated using a rule-based confusion matrix, from which a classification accuracy (AC) is derived as an indicator of signal separability. The results show that, under the modeled conditions, several layouts can reduce sensor numbers compared with dense deployments while maintaining high AC under the simulated conditions. Uniform Arrangement demonstrated high performance across the single-lane scenarios. Centrally Weighted Arrangement had more advantages in handling the classification of large vehicles. Minimum Coverage Arrangement significantly reduced the number of sensors required when high accuracy was not essential. The results clarify how sensor number and spatial arrangement influence classification performance in the simulated cases. The proposed method enables rapid and consistent comparison of sensor arrangement strategies in KNN-based pavement sensing systems.

5.2. Introduction

The advancement of intelligent transportation and infrastructure management has placed

higher demands on the precision and timeliness of pavement condition monitoring and traffic load identification (D. Chen et al., 2025; Guan et al., 2024; Ye et al., 2022). Continuous observation of stress evolution inside pavement layers enables the assessment of temperature variation, moisture content, cracking, and settlement, all of which influence structural safety and service life (Liu et al., 2022). At the same time, obtaining real-world data (such as dynamic loads, speed, distance, geometry, and weight) supports traffic flow optimization, overload control, and the improvement of intelligent signal management and processing systems (X. Chen et al., 2025; Y. Li et al., 2025). Piezoelectric sensing technologies have gained increasing attention for these purposes because they can operate without external power, remain concealed within the structure, and respond sensitively to transient loads (Bafna et al., 2025).

However, in a practical scenario, without sustainable optimized sensor arrangement strategies, the obtained monitoring data will be either misleading or inefficient (Pascale et al., 2023). An optimized sensor arrangement is required to capture informative load responses using a limited number of sensors. Reducing the number of embedded sensors directly decreases the number of pavement cuts required during deployment, thereby mitigating structural disturbance associated with sensor installation. Conventional approaches often relied on dense arrays comprising numerous sensing units per lane section (Chang et al., 2025). In asphalt pavements, incisions that often extend several centimeters in depth disrupt the material continuity, modify the stiffness distribution, and create interfacial zones to moisture infiltration and freeze-thaw cycling damage (Wei et al., 2019). Under repeated traffic loading, these discontinuities may develop into stress concentration regions (Aduwenye et al., 2024). Dense sensor networks also increase economic and operational demands (Di Graziano et al., 2020). Each additional sensing unit adds to material costs and extends construction time (Ho et al., 2005). The higher the sensor count, the greater the likelihood of partial system failure over time; the malfunction of individual units can progressively degrade overall monitoring fidelity and data continuity, compromising the system's functions (Abdulkarem et al., 2020). Therefore, pavement sensing systems face a complex tripartite challenge: embedded sensors are required to withstand high temperatures (Chantima et al., 2025) and stresses during construction and service (Swett et al., 2008), minimize structural disruption to preserve pavement longevity through appropriate

installation strategies (Chapeleau et al., 2017), and meet environmental sustainability requirements (Boada-Parra et al., 2023). Existing solutions address only one or two of these requirements, which limits their long-term applicability in pavement sensing systems. This limitation motivates the development of sensor arrangement strategies that address all three requirements.

Previous studies have employed the finite element method (FEM) to simulate the deployment of piezoelectric sensors in pavements (Wang et al., 2023). Different types of piezoelectric elements embedded in asphalt and concrete layers have been simulated using FEM to predict stress and voltage responses under moving vehicle loads (Du et al., 2022). Dynamic vehicle-pavement interaction simulations have shown that FEM can accurately reproduce the time-dependent transfer of stress from the tire-pavement contact area to the sensor layer (Bafna et al., 2025; D.-W. Park et al., 2014). Some researchers investigate the open-circuit voltage response of piezoelectric sensors under bidirectional cyclic loading through FEM modeling. FEM-based predictions of open-circuit voltage responses under cyclic loading have been reported to exhibit consistent trends with experimental observations, supporting the validity of the electromechanical modeling approach (Du et al., 2022; Ye et al., 2023).

FEM enables detailed analysis of vehicle-pavement-sensor interactions under specific traffic conditions, such as pavement structure (Chen et al., 2023), vehicle types, driving conditions (Lee and Jang, 2024), and sensor arrangements (P. Wang et al., 2022), thereby enabling vehicle classification (X. Ma et al., 2022). However, extending FEM-based analysis to diverse pavement structures and traffic scenarios requires constructing a large number of models, resulting in high computational cost and limited efficiency (Gonçalves and Ambrósio, 2005). Each change in pavement or traffic parameters necessitates re-modeling, which restricts its applicability for systematic assessment of sensor layouts. FEM provides limited capability for consistent comparison of different sensor arrangement strategies or for examining the influence of sensor quantity under unified evaluation criteria (Nath et al., 2024).

5.3. Objective

This study aims to develop a simulation-based framework for evaluating pavement sensor

arrangement strategies under modeled traffic conditions. The proposed framework, referred to as the Evaluation of Sensor Arrangement Methods (ESAM), is designed to improve the efficiency of sensor layout assessment compared with conventional FEM-based approaches. Based on finite element simulations, ESAM characterizes the relationship between sensor voltage response and tire-sensor distance for representative vehicle types. These relationships are used to estimate voltage responses for different sensor layouts without repeated full-scale simulations. By inputting pavement and traffic parameters (such as pavement width, planned sensor quantity and arrangement, vehicle types, and traffic conditions), it rapidly predicts voltage responses for different arrangements within the same modeling assumptions, supporting the identification of effective sensor layouts. The framework enables direct comparison of different arrangement strategies and sensor counts within modeled conditions. To meet the low-carbon and toxic-free development requirements, the KNN piezoelectric ceramics are adopted in this study as a representative low-response, lead-free sensor material (K. Zheng et al., 2025). The proposed framework itself is material-agnostic and can be extended to other piezoelectric sensors by updating the corresponding material parameters.

5.4. Methodology

The framework of ESAM is established to address the complexity of real-world pavement conditions and the diversity of vehicles. It primarily encompasses three parts (see Fig. 5-1), with the first section covering input parameters such as road width and the intended sensor numbers. The second section focuses on processing, including vehicle passage paths, sensor arrangement strategies, and vehicle attenuation functions. The output results provide the voltage range of vehicle signal outputs under the corresponding sensor arrangements and classification accuracy, enabling reliable evaluation of sensor arrangement performance and supporting the recommendation of optimal, site-specific sensor arrangements.

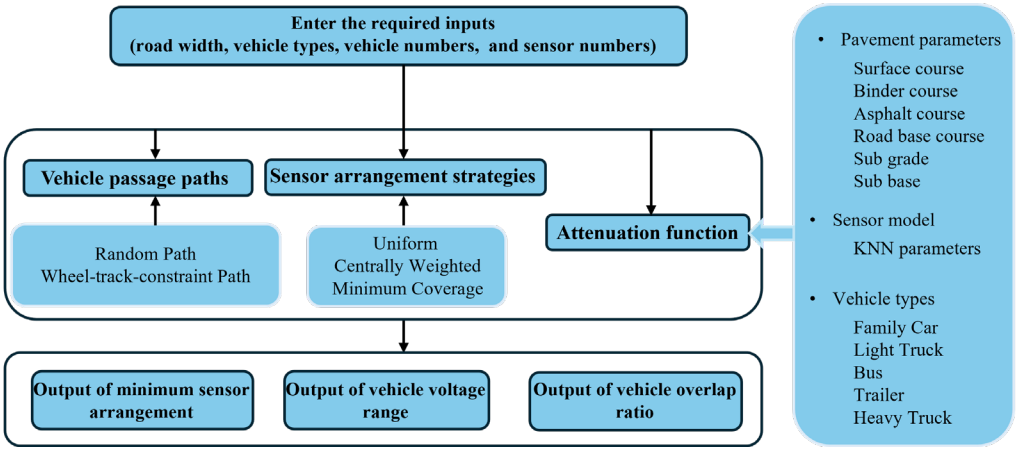


Fig. 5-1: Technical framework

5.4.1. Vehicle Passage Paths

To accurately evaluate the performance of embedded sensors under varied traffic conditions, it is essential to account for the diverse passage paths of vehicles. Vehicle trajectories directly influence the tire-pavement stress distribution, thereby determining the stress characteristics detected by the sensors. Given that real-world traffic environments rarely exhibit a single pattern, this study selected three representative vehicle passage paths.

The Random Path model is designed to simulate the lateral random distribution of vehicles within a lane, capturing the variability in driving behavior, such as lane keeping, edge driving, and lane changing. It assumes that each vehicle travels along the longitudinal x-axis, while its lateral center position is randomly distributed within the lane boundaries. For a given vehicle i, its lateral position can be expressed in Eq. (5-1):

$$y_i(x) = y_i = y_{left} + (y_{right} - y_{left})r_i \quad \textbf{(5-1)}$$

where y_{left} and y_{right} denote the left and right boundaries of the road or lane, respectively, and $r_i \sim U(0,1)$ is a random variable representing the vehicle's lateral position within this range.

When the path generation interval $[y_{left}, y_{right}]$ of a vehicle is set to the road width, it constitutes a Random Path. Because the vehicle's path is randomly generated within the road width, this method accounts for scenarios where vehicles pass close to the edge and change lanes.

The Wheel-track constraint Path reflects ± 0.2 m lateral vehicle deviations typical of

highway conditions. The random generation interval $[y_{left}, y_{right}]$ for the path is set to the road center with ± 0.2 m. Because the randomly generated road paths are strictly confined within the wheel track belts, they can reflect the regular driving patterns of vehicles in real-world scenarios.

5.4.2. Sensor Arrangement Strategies

The inherent noise characteristics of the embedded sensors were examined through a laboratory calibration test. Under static, unloaded conditions, the sensors exhibited small random voltage fluctuations around 0.6-0.7 V, reflecting the intrinsic noise of the system. Based on these results, 0.668 V was identified as the minimum stable threshold above which the sensor response could be reliably distinguished from noise. This threshold was adopted in the study (K. Zheng et al., 2025). To ensure that the arrangement captured detectable responses for all vehicle types, the family car (the lightest vehicle) was used as the reference load to obtain the minimum required number of KNN sensors.

A schematic diagram was prepared to show the sensing coverage. The red region represents the effective sensing zone where the output voltage exceeds 0.668 V. The gray area represents the zone where the output is below the threshold. As shown in Fig. 5-2, two primary types of potential "signal missed" zones were identified. The first type is the far-field attenuation zone, where sensors placed far from the tire experience stress attenuation and produce a low output. The second type is the center line zone, where low tire loads limit lateral stress propagation and reduce the voltage near the vehicle center line.

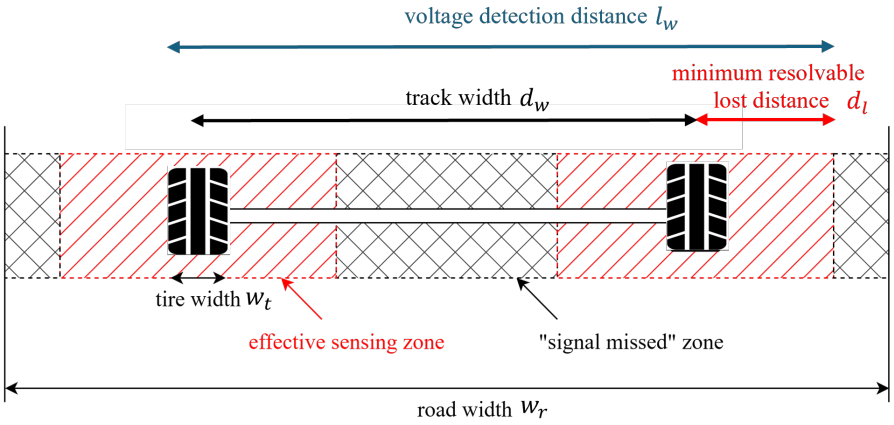


Fig. 5-2: "Signal missed" situation illustration diagram

The minimum required number of sensors must be determined to ensure reliable signal

detection under all traffic scenarios. The derivation is based on the worst case, where a vehicle passes along the road edge. In this case, at least one sensor must lie exactly at the boundary of the effective influence range of the tire to capture a detectable signal. This requirement limits the maximum spacing between adjacent sensors to the effective influence distance. Based on this principle, Eq. (5-2) is proposed to estimate the minimum number of sensors required:

$$l_{\mathrm{w}} = d_w + d_l + \frac{w_t}{2}$$
$$N_{\min} = \left\lfloor \frac{w_r - 2 \cdot l_w}{d_l \times 2} \right\rfloor + 2 \quad \textbf{(5-2)}$$

where d_w is the track width, d_l is the minimum resolvable lost distance (signal resolution limit), w_t is the tire width, w_r is the total road width, l_{w} is the voltage detection distance when a vehicle is passing by the edge of the road, $N_{\min}$ is the minimum number of sensors required.

Based on Eq. (5-2) and considering a single-lane roadway with a width of 3.75 m and adopting the maximum effective output distance of a family car, the calculation indicates that at least two KNN sensors are required under the custom driving path to ensure signal voltages above the minimum threshold. This approach can be extended to any combination of vehicle type and road width. To meet the varying requirements for piezoelectric signal coverage and resolution under different traffic patterns, three representative sensor arrangement strategies were designed and implemented in this research: (1) Uniform Arrangement, (2) Centrally Weighted Arrangement, and (3) Minimum Coverage Arrangement. Each strategy exhibited distinct characteristics in terms of arrangement density, spatial distribution, and coverage of wheel-track response zones. The performance of these arrangements was evaluated and compared in subsequent sections based on simulation results.

In the Uniform Arrangement, all sensors were evenly spaced along the lateral direction of the roadway (perpendicular to the vehicle travel direction). This arrangement is adopted as a baseline case without assuming any preferred vehicle path. The performance of other sensor arrangements is evaluated relative to this reference under different traffic scenarios. The sensor positions in this Uniform Arrangement are given by Eq. (5-3):

$$P_i = \frac{w_r}{N+2} \cdot N_i \tag{5-3}$$

where w_r is the total width of the road, N is the total number of sensors, P_i is the coordinate of the center of ith sensor (the coordinate origin is defined at the leftmost edge of the road), N_i is the index of the ith sensor (starting from 1), $i = 1,2, \dots, N$.

In the Centrally Weighted Arrangement strategy, potential lateral deviations in vehicle paths were addressed by adopting a denser sensor arrangement near the center of the roadway and sparser toward the edges. The arrangement density is controlled using an exponential function in Eq. (5-4):

$$N_i = \left(\frac{i}{N}\right)^{\beta} \tag{5-4}$$

where β is a power-weighting coefficient controlling the distribution density. The parameter β governs the distribution trend of the sensor density: when $\beta > 1$, the sensor placement becomes denser toward the road edges; conversely, when $\beta < 1$, the arrangement is more concentrated around the center of the road.

To prevent excessive sensor density near the center of the roadway, which can result in signal redundancy between adjacent sensors, a spacing constraint is imposed. The minimum distance between any two adjacent sensors in the central region is required to be no smaller than the tire width. Based on this condition, the corresponding value of the exponential distribution parameter β is derived with Eq.(5-5), (5-6), (5-7), and (5-8).

For an even number of sensors ($n = N/2$), the distribution parameter β can be expressed as:

$$\beta = \frac{\log\left(-\frac{w_t}{w_r} + 1\right)}{\log\left(\frac{n}{n+1}\right)} \tag{5-5}$$

The lateral position N_i is then determined by:

$$N_i = \begin{cases} \frac{w_r}{2}\left(\frac{i}{n+1}\right)^{\beta}, & i \le n \\ w_r - \frac{w_r}{2}\left(\frac{i}{n+1}\right)^{\beta}, & i > n \end{cases} \quad \textbf{(5-6)}$$

For an odd number of sensors ($n = (N-1)/2$), the distribution parameter β is obtained using:

$$\beta = \frac{\log\left(-\frac{2w_t}{w_r} + 1\right)}{\log\left(\frac{n}{n+1}\right)} \quad \textbf{(5-7)}$$

The lateral position N_i is then determined by:

$$N_i = \begin{cases} \frac{w_r}{2}\left(\frac{i}{n+1}\right)^{\beta}, & i < n \\ \frac{w_r}{2}, & i = n \\ w_r - \frac{w_r}{2}\left(\frac{i}{n+1}\right)^{\beta}, & i > n \end{cases} \quad \textbf{(5-8)}$$

The objective of the Minimum Coverage Arrangement strategy is to maximize the coverage of potential lateral tire positions with a limited number of sensors. The arrangement is designed to satisfy edge coverage with the minimum required number of KNN sensors. One sensor is placed near each edge of the effective sensing zone, while the remaining sensors are evenly distributed in the central region. The sensor positions in this arrangement are calculated by Eq. (5-9):

$$\begin{aligned} P_1 &= l_{\mathrm{w}} \\ P_n &= w_r - l_{\mathrm{w}} \\ P_i &= P_1 + \frac{P_n - P_1}{n-1} \cdot (N_i - 1) \end{aligned} \quad \textbf{(5-9)}$$

where P_1, P_n are the positions of the leftmost and rightmost sensors. The meaning of other symbols is the same as in the previous equation.

Within the modeling and simulation framework developed, a total of 12 representative test scenarios were defined by systematically combining three sensor arrangement strategies

(Uniform, Centrally Weighted, and Minimum Coverage), two types of lanes, and the presence or absence of wheel-track constraint effects. Because the sensor arrangement on multi-lane roads cannot be a simple linear superposition of single-lane arrangements, sensor arrangements are specifically considered for dual-lane scenarios. For clarity and ease of reference, Table 5-1 assigns a unique identifier to each configuration. The single-lane model corresponds to a typical road width of 3.75 m, while the dual-lane configuration represents a 7.5 m wide roadway, simulating real-world multi-lane traffic conditions.

Table 5-1 Identification of the 12 representative sensor arrangement scenarios

Lane types	Car passage modes	Uniform	Centrally Weighted	Minimum Coverage
Single-lane Road	Random	G1	G2	G3
	Wheel-track constraint	G4	G5	G6
Dual-lane Road	Random	G7	G8	G9
	Wheel-track constraint	G10	G11	G12

5.4.3. Attenuation Function Derivation

For stable signal collections, vehicle classification requires a clear separation in output voltage, where the maximum response of smaller vehicles must be lower than the minimum response of larger vehicles. The measured voltage responses can be further converted into equivalent force ranges, reflecting the vehicle loading effects. Based on a threshold of 0.668 V, only signals exceeding this level were considered to determine the sensor spacing corresponding to the maximum output response. To further characterize the variation of signals with lateral distance, the concept of an attenuation function was introduced. This function reflected the physical process of voltage signals decaying with lateral distance under vehicle loading. Vehicle-specific attenuation functions were then derived through modeling of different vehicle tire-pavement models, providing the basis for optimal sensor arrangement design.

5.4.3.1. Simulation of KNN Sensor Models

Although a myriad of simulation works have been reported for the piezoelectric sensors in pavement engineering (Q. Zhao et al., 2019), unfortunately, most of them were focused on PZT-based sensors (Zhao et al., 2012), which have much higher piezoelectric response at room

temperature compared to KNN-based sensors. As a result, to evaluate the feasibility and practical performance of this environmentally friendly KNN-based sensor, it is imperative to understand the fitting working conditions and find an appropriate installation and arrangement strategy by using this relatively low piezoelectric response material.

A finite element model of the KNN piezoelectric sensing unit was developed to simulate its electromechanical behavior and voltage response at the micro-scale under dynamic mechanical loading. The constitutive relations and geometry of the sensor were defined to preserve material anisotropy in the simulation (Gao et al., 2023). The sensing unit comprises a KNN piezoelectric ceramic element packaged in epoxy resin. The KNN ceramic disk has a diameter of 15 mm and a height of 5 mm, while the complete sensing module measures 19 mm in length and 9 mm in height, as illustrated in Fig. 5-3. To mitigate structural discontinuities within the pavement caused by sensor embedding, a distributed arrangement scheme involving multiple discrete small sensing units in a parallel configuration is adopted. The KNN sensor's durability was studied in a previous study (Zheng et al., 2026b), the sensor signal decreased by only 4.4% after 100,000 loading cycles.

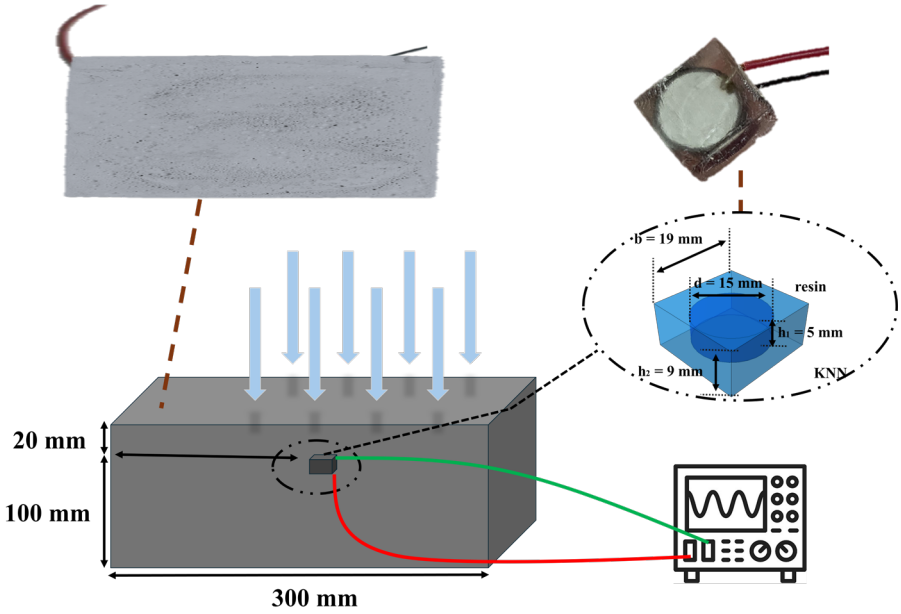


Fig. 5-3: Physical dimensions of the KNN sensor model

The polarization of the KNN sensor was restricted to the vertical direction, and the piezoelectric and mechanical responses along this axis were considered in the model. The material behavior was described using a simplified constitutive relation incorporating the elastic

stiffness, piezoelectric stress constants, and strain of KNN ceramics, as expressed in Eq. (5-10), (5-11), and (5-12). Based on previously measured experiment data (K. Zheng et al., 2025), the corresponding values of each parameter were summarized in Table 5-2.

$$\boldsymbol{C} = \begin{bmatrix} \boldsymbol{c_{11}} & \boldsymbol{c_{12}} & \boldsymbol{c_{13}} & \boldsymbol{0} & \boldsymbol{0} & \boldsymbol{0} \\ \boldsymbol{c_{12}} & \boldsymbol{c_{11}} & \boldsymbol{c_{13}} & \boldsymbol{0} & \boldsymbol{0} & \boldsymbol{0} \\ \boldsymbol{c_{13}} & \boldsymbol{c_{13}} & \boldsymbol{c_{33}} & \boldsymbol{0} & \boldsymbol{0} & \boldsymbol{0} \\ \boldsymbol{0} & \boldsymbol{0} & \boldsymbol{0} & \boldsymbol{c_{66}} & \boldsymbol{0} & \boldsymbol{0} \\ \boldsymbol{0} & \boldsymbol{0} & \boldsymbol{0} & \boldsymbol{0} & \boldsymbol{c_{44}} & \boldsymbol{0} \\ \boldsymbol{0} & \boldsymbol{0} & \boldsymbol{0} & \boldsymbol{0} & \boldsymbol{0} & \boldsymbol{c_{44}} \end{bmatrix} \quad \textbf{(5-10)}$$

$$\boldsymbol{e} = \begin{bmatrix} e_{31} \\ e_{31} \\ e_{33} \\ 0 \\ e_{15} \\ e_{15} \end{bmatrix} \quad \textbf{(5-11)}$$

$$\boldsymbol{\varepsilon} = \begin{bmatrix} \varepsilon_{11} & 0 & 0 \\ 0 & \varepsilon_{22} & 0 \\ 0 & 0 & \varepsilon_{33} \end{bmatrix} \quad \textbf{(5-12)}$$

where $\boldsymbol{C}$ is the elasticity stiffness matrix, $\boldsymbol{e}$ is the piezoelectric stress constant matrix, $\boldsymbol{\varepsilon}$ is the strain matrix.

Table 5-2 Elastic stiffness and piezoelectric stress constants of the material

Elastic stiffness constants	Reference value (N/m^2)	Piezoelectric stress constants	Reference value (C/m^2)
$\boldsymbol{c_{11}}$	15.58	$\boldsymbol{e_{31}}$	-5.7669
$\boldsymbol{c_{12}}$	9.77	$\boldsymbol{e_{33}}$	21.2841
$\boldsymbol{c_{13}}$	10.76	$\boldsymbol{e_{15}}$	14.6888
$\boldsymbol{c_{33}}$	17.29		
$\boldsymbol{c_{44}}$	2.44		
$\boldsymbol{c_{66}}$	2.91		

5.4.3.2. Simulation of Pavement Models

The pavement structure model was defined with dimensions of 7m in the vehicle travel direction and 3.75 m in single-lane width. A six-layer stratified structure was adopted to represent the pavement system, corresponding to the typical configuration of German highway design guidelines (surface, binder, asphalt course, road base course, subgrade, and subbase). Each layer is assumed to be an elastically isotropic material. The tie connection is used between the surface course, binder course, asphalt course, and road base course to simulate no relative

displacement between the upper layers of the pavement. Surface-to-surface contact is employed between the road base course, subgrade, and subbase, and set to allow for relative displacement. Different elastic modules and Poisson's ratios were assigned to reflect the mechanical differences of actual pavement layers (K. Zheng et al., 2025). Detailed parameters of each layer were provided in Table 5-3. The simulation used a time step derived from the time required for a vehicle traveling at 10 m/s to traverse the model length. Vehicle loading was applied as a half-sine wave, discretized into 21 frames to capture the transient stress response.

Table 5-3 Parameter values for multi-layer structures in pavement models in summer and winter

Layer	Thickness (m)	E (Pa)		Poisson's ratio	Density (kg/m$^{3)}$	Min. mesh size (m)
		Summer	Winter			
Surface course	0.04	2.90×10^{9}	1.12×10^{10}	0.35	2377	0.005
Binder course	0.05	6.82×10^{9}	1.04×10^{10}	0.35	2448	0.010
Asphalt course	0.11	4.90×10^{9}	6.89×10^{9}	0.35	2301	0.040
Road base course	0.15	1.00×10^{10}	1.58×10^{8}	0.49	2400	0.080
Sub grade	0.57	1.00×10^{8}	1.26×10^{8}	0.49	2400	0.160
Sub base	2	4.5×10^{7}	9.89×10^{7}	0.49	2400	0.320

Regarding the meshing strategy, a fine mesh was applied in the stress-concentrated region, and a coarser mesh was used in the boundary zones (Vaziri Sereshk and Esmaeili, 2015). In the vertical direction, mesh density decreased layer by layer from top to bottom. The surface course bears the primary load and was assigned a high-density structured mesh to enhance local response accuracy. The subgrade region, located farther from the load, was meshed more coarsely to improve computational efficiency. A more detailed partition was applied to enhance the surface course's mesh quality, and a structured mesh is used (Fig. 5-4), adequately representing its internal stress transmission and piezoelectric response behavior.

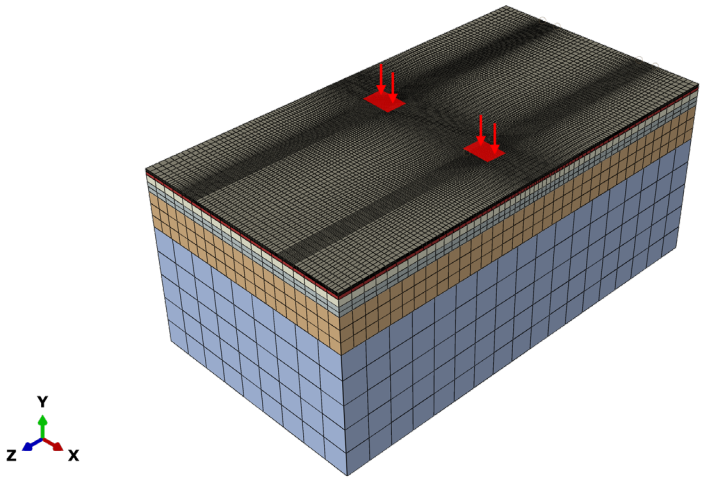


Fig. 5-4: FEM of the pavement-tire-sensor interaction system with embedded sensor arrangement

To guarantee the general applicability of the boundary conditions in the simulation, an encastre constraint was applied along the Y-axis, fully restraining all translational and rotational degrees of freedom. Z-symmetry was imposed on the plane normal to the Z-axis, restricting the displacement and the in-plane rotations. X-symmetry was applied on the plane normal to the X-axis, constraining the corresponding normal displacement and rotational degrees of freedom. Traditional methods add a Y-direction displacement constraint on one side of the model to simulate half-contact locking between the pavement and soil. This study adopted a symmetric boundary constraint, leaving both sides free in the Y-direction. This setup improves scalability for a multi-lane application. It also captures the attenuation and spatial continuity of lateral pressure signals, providing a solid basis for optimizing sensor placement strategies.

5.4.3.3. Simulation of Vehicle and Sensor Signal Collection

Five representative vehicle types were selected as the primary subjects of analysis: family cars, light trucks, buses, heavy trucks, and trailers. A commercially available vehicle model with broad representative characteristics was chosen for each category. During the modeling process, the key structural parameters of each vehicle type were thoroughly considered, including tire specifications, track, individual tire contact area, number of tires, full load, and unladen weight. These parameters were incorporated to ensure the simulation results are realistic and engineering reliable. Detailed specifications of each vehicle type were presented in Table 5-4, based on technical documentation from vehicle manufacturers (“Kraftfahrt-Bundesamt, ‘Traffic flow information.,’” 2025; “Mercedes-benz, Technical parameters for

mercedes-benz bus," 2025; "Mercedes-benz, 'Truck information.,'" 2025; "Organisation Technique Européenne du Pneumatique et de la Jante ADF, "Golf technical specifications," 2025). The loads applied to the various simulated vehicles are subject to a ±10% fluctuation range to account for dynamic effects arising from cargo vibration. To enhance the scalability and reusability of the model, a structured vehicle database was developed to standardize the management and retrieval of the parameters. This database supports read and write operations, providing a flexible and extensible foundation for future development of a comprehensive vehicle load library.

Table 5-4 Representative vehicle types and parameters

Vehicle type	Car model	Tire model	Vehicle mass (kg)	Full load weight (±5%) (kg)	No. of tires
Family car	VW Polo AW Polo 1.0 MPI Volkswagen Transporter T6.1 Kastenwagen	195/55 R16	1090-1300	1600	4
Light truck	VW Transporter T6.1 2.0 TDI (75–150 PS)	215/65 R16 C	1900–2100	3,200	4
Bus	Tourismo RHD M/2	295/80 R22.5	13,500–14,500	18,000	6
Long-haul trailer	Mercedes-Benz Actros 1845 LS	315/70 R22.5	7,500–8,300	40,000	18
Heavy truck	Mercedes-Benz Arocs 4145 8x4	315/80 R22.5	11,000–14,000	40,000	12

The vehicle load on the pavement surface is simplified as a time-varying half-sin function, as given by Eq. (5-13) (Q. Zhao et al., 2019):

$$F = F_0 \sin(2\pi f t)$$
$$f = \frac{1}{T} = \frac{v}{l_1 + l_2} \quad \textbf{(5-13)}$$

where F_0 is the stress peak (Pa), F is the current stress value (Pa), T is the loading period (s), v is the speed of the vehicle (m/s), l_1 is the length of the tire-pavement contact area (m), l_2 is the width of the sensor (m).

Accounting for the differences in total weight, tire number, and tire specifications across

various vehicle types, the tire-pavement contact areas were customized to reflect the mechanical response under loading. For heavy-duty classes (heavy trucks, buses, and trailers), the contact area of a single tire was set within the range of 0.045 m^2-0.055 m^2, whereas for light-duty classes (family cars and light trucks), it was set between 0.018 m^2-0.025 m^2 (Z. Gong et al., 2024b). During the modeling process, the contact width was determined based on the tire specifications corresponding to each category, and the contact length in the driving direction was derived from the mentioned contact area. The contact regions exhibited distinct geometric characteristics across different vehicle groups in this setting. To accurately capture the loading changes, separate FEM models were developed for each vehicle type, ensuring both the specificity and reliability of the analysis.

5.4.3.4. Attenuation Function Fitting from Signal Collection

The attenuation function requires corresponding data points, which were collected in this study through modeling. As reported in earlier studies, the optimal depth of sensor placement was set at 2 cm from the pavement surface. The output voltage of KNN piezoelectric sensors was a function of distance from tire. The baseline model was built with eight sensors to capture specific vehicle attenuation functions (Fig. 5-5). In general, the installation of embedded sensors unavoidably affects the structural continuity and integrity of the pavement. However, due to the small size of individual sensors in this study, their embedment has a negligible impact on the mechanical properties of the pavement. The simulated results of inserting seven sensors 2 cm below the pavement surface showed virtually no difference in the stress response compared to the pavement surface without sensors (Fig. 5-6). Therefore, a continuous attenuation function can be used regardless of the number of sensors. The central sensor was located directly beneath the tire at the center of the tire pavement contact area, and the edge sensor was placed at the outermost boundary of the tire-pavement contact area. On the right side, four sensors were evenly distributed from the contact edge to the roadway's right boundary to capture the spatial attenuation trend. A left boundary sensor was installed on the left side of the tire to evaluate the boundary effects on signal attenuation. Sensors are numbered from the left side of the pavement to the right and denoted as sensor #*i*. The coordinates of sensor #3, listed in Table 5-5, were measured from the left edge of the road (road width is 3.75 m).

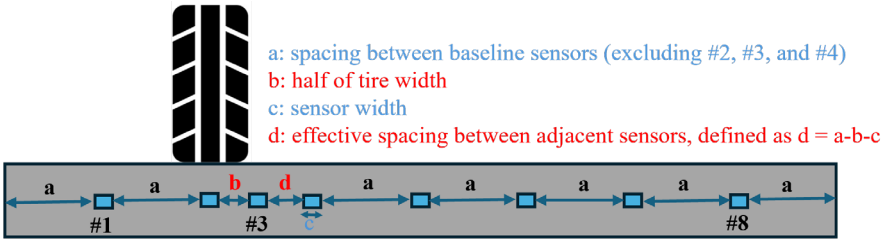


Fig. 5-5: Baseline arrangement of 8 embedded sensors for vehicle attenuation functions

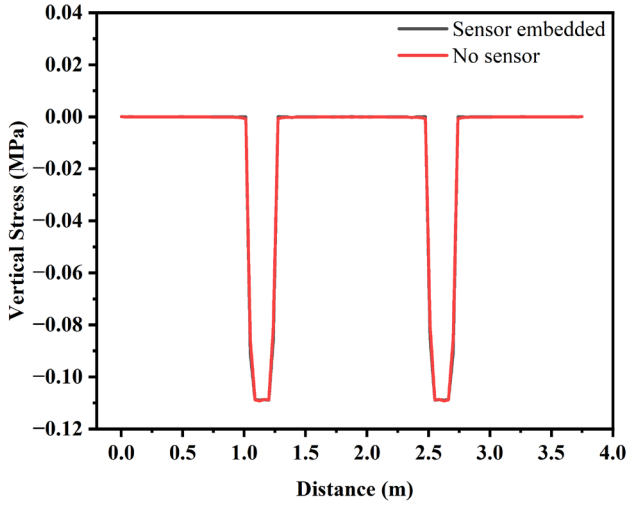


Fig. 5-6: The effect of sensors embedded in pavement stress response

Table 5-5 The specific positions of sensor #3 in the FEM model

Vehicle types	Family car	Light truck	Bus	Trailer	Heavy truck
Sensor #3 (m) (sensor center from left side)	1.0445	1.0545	1.0945	1.1045	1.0945

Due to the relatively small size of the sensor models, a simplification strategy was implemented in a separate model. The stress distribution in the vertical direction within the KNN layer was assumed to be approximately uniform. Under this assumption, the vertical stress component extracted from the top surface of the KNN layer in the pavement model was used as the loading input for the sensor simulation. This stress was applied to the KNN sensor to compute the corresponding voltage output, enabling prediction of the sensor response under pavement loading.

The method used to obtain the open-circuit voltage of a single sensor during vehicle passage is shown in Fig. 5-7. Sensors were embedded 2 cm beneath the pavement surface in the pavement model, and a half sinusoidal load was applied on the pavement surface to simulate the tire-induced dynamic force induced by the passing tire. The mechanical response of the sensor region was obtained, and the vertical stress component on the top surface of each sensor was extracted.

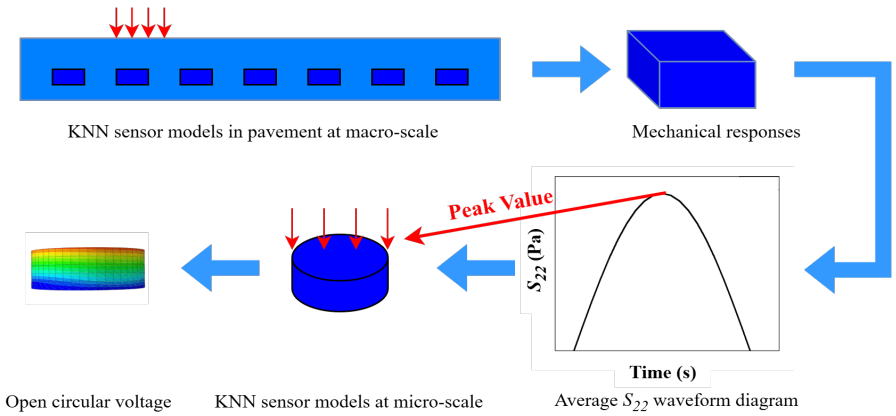


Fig. 5-7: Flowchart for extracting open-circuit voltage of sensors in FEM models

It should be noted that the vehicle passes over the sensor within a very short duration (on the order of milliseconds), and only the peak voltage response is extracted in this study. Under such transient loading conditions, the peak sensor output is primarily governed by instantaneous load transfer, the time-dependent viscoelastic effects of asphalt pavement have a negligible influence on the peak sensor output and are not considered, consistent with previous FEM-based pavement sensing studies (Shi and Cai, 2009). To enable a quantitative interpretation of the measured voltage signals for different sensor arrangements, the sensor output is related to the distance d between the sensor and the tire center. The simulated voltage exhibits a clear attenuation trend with increasing distance across different vehicle types.

The voltage attenuation is decomposed into a geometric attenuation term and a material-related transmission attenuation term, and the voltage response is expressed by Eq. (5-14):

$$V(d,T) = V_{\infty} + V(d)exp(-\alpha(T)d) \quad \textbf{(5-14)}$$

where d is the distance to wheel center, T is the temperature of the surface course, V_{∞} is the far-field background noise, A_0 is the scaling amplitude of voltage in the center of the tire in

room temperature, $V(d)$ is the geometric attenuation term, $exp(-a(T)d)$ is the attenuation in media transmission related to temperature and materials.

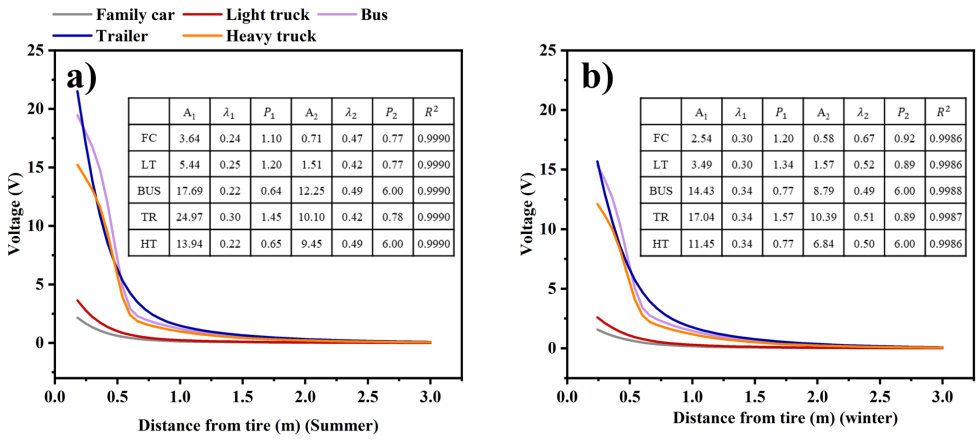
Temperature effects are retained through the attenuation coefficient, as given by Eq. (5-15):

$$\alpha(T) = \alpha(\frac{E(T)}{E_{ref}})^{-\gamma} \quad \textbf{(5-15)}$$

where $E(T)$ is the elastic modulus obtained from laboratory tests, and E_{ref} is the reference modulus at room temperature. The geometric attenuation is described by Eq. (5-16):

$$V(d) = A_1 exp\left[-(\frac{d}{\lambda_1})^{p_1}\right] + A_2 exp\left[-(\frac{d}{\lambda_2})^{p_2}\right] \quad \textbf{(5-16)}$$

where the first exponential term (A_1, λ_1, p_1) catures the near-field rapid attenuation dominated by localized contact stress and surface course of pavement, the second term (A_2, λ_2, p_2) describes the far-field attenuation governed by stress diffusion within the multi-layer pavement, $\lambda_1 < \lambda_2$. The fitted curves for different vehicle types in winter and summer are shown in Fig. 5-8, where similar attenuation trends are observed despite seasonal differences in pavement modulus.



	A_1	λ_1	P_1	A_2	λ_2	P_2	R^2
FC	3.64	0.24	1.10	0.71	0.47	0.77	0.9990
LT	5.44	0.25	1.20	1.51	0.42	0.77	0.9990
BUS	17.69	0.22	0.64	12.25	0.49	6.00	0.9990
TR	24.97	0.30	1.45	10.10	0.42	0.78	0.9990
HT	13.94	0.22	0.65	9.45	0.49	6.00	0.9990

	A_1	λ_1	P_1	A_2	λ_2	P_2	R^2
FC	2.54	0.30	1.20	0.58	0.67	0.92	0.9986
LT	3.49	0.30	1.34	1.57	0.52	0.89	0.9986
BUS	14.43	0.34	0.77	8.79	0.49	6.00	0.9988
TR	17.04	0.34	1.57	10.39	0.51	0.89	0.9987
HT	11.45	0.34	0.77	6.84	0.50	6.00	0.9986

Fig. 5-8: Voltage attenuation curves for different vehicle models in summer and winter (FC: family car, LT: light car, BUS: bus, TR: trailer, HT: heavy truck)

5.4.4. Reliability Assessment and Arrangement Evaluation

In this study, ESAM is proposed as a systematic sensor arrangement evaluation framework, rather than a standalone optimization algorithm. Its primary contribution is to enable reproducible comparison of different sensor layouts based on FEM-derived vehicle voltage

responses and attenuation functions, thereby supporting informed sensor arrangement design under practical constraints.

The reliability of the proposed framework is assessed by examining the consistency between the attenuation-based voltage evaluation employed in ESAM and the corresponding FEM simulation results under identical sensor arrangements and vehicle paths. The attenuation functions and voltage ranges associated with different vehicle types are extracted from FEM simulations and subsequently used within ESAM for arrangement evaluation. Signal separability is evaluated using a confusion matrix, from which a classification accuracy (AC) is derived as a secondary indicator. These steps provide a quantitative basis for comparing sensor arrangements and identifying effective layouts.

5.4.4.1. Reliability Assessment of the ESAM Framework

Five representative vehicle types with dual tires were selected to examine the internal consistency of the ESAM framework. For identical sensor layouts and vehicle trajectories, peak voltage responses predicted by ESAM were compared with results from full FEM simulations. The comparisons under summer and winter conditions are shown in Fig. 5-9. In this study, the summer and winter cases are used to represent different levels of pavement elastic modulus, rather than detailed temperature-dependent or viscoelastic behavior.

Changes in pavement modulus affect the absolute magnitude of the piezoelectric voltage response. For the same vehicle type, this influence mainly appears as a scaling of response amplitude. However, the spatial decay of voltage with tire-sensor distance follows a similar attenuation pattern. The attenuation functions adopted in ESAM describe this dominant distance-dependent decay trend and are not intended to capture local stress irregularities or high-frequency numerical fluctuations. In FEM simulations, the stress of the contact area contains high-frequency fluctuations. These fluctuations introduce uncertainty in the determination of the peak voltage, causing the extracted peak values to vary within a narrow interval rather than collapsing to a single exact value. ESAM represents the voltage response using a smooth attenuation function that captures the dominant distance-dependent trend. Therefore, ESAM provides a single representative peak voltage for a given tire–sensor distance. Because the two approaches treat peak extraction differently, small numerical discrepancies remain under 10% between FEM and ESAM predictions even when the overall trends are

consistent. This agreement indicates that the attenuation-based representation used in ESAM remains applicable under reasonable variations in pavement elastic modulus and is suitable for comparative evaluation of sensor arrangement strategies within the simulated scope.

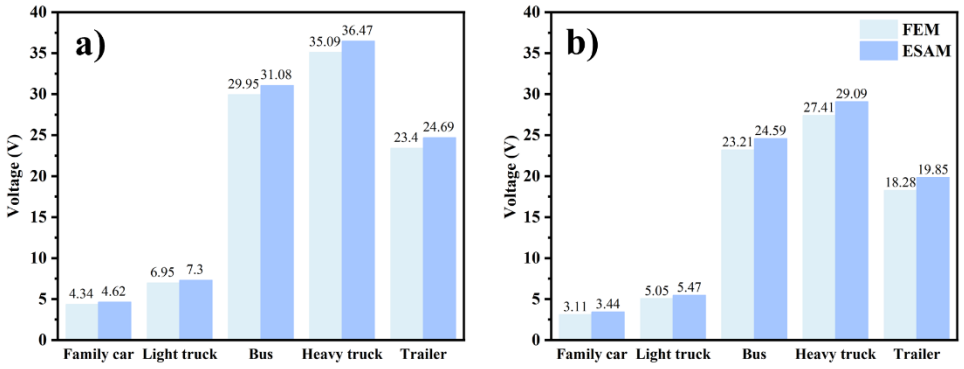


Fig. 5-9: Comparison of FEM results and ESAM prediction results for peak voltage in (a) summer and (b) winter

5.4.4.2. Evaluation for Sensor Arrangement

ESAM is used as an evaluation framework to assess sensor arrangements' ability to separate voltage responses with a limited number of sensors. For a given arrangement, peak voltage responses corresponding to different vehicle types are obtained based on FEM-derived attenuation functions implemented in ESAM. These responses define a voltage range for each vehicle class. Due to differences in vehicle mass and tire-pavement contact stress, partial overlap between the voltage ranges of different vehicle classes may occur (Fig. 5-10). Such overlap limits direct classification using simple voltage thresholds and necessitates a quantitative criterion for evaluating signal separability. A rule-based voltage range decision scheme is adopted, based on which a confusion matrix is constructed to summarize pairwise misclassification tendencies between vehicle classes. The AC is then derived from the confusion matrix as a separability indicator for sensor arrangement evaluation. And the corresponding ESAM software's GUI interface is shown in Fig. 5-11.

For the i^{th} vehicle type, the midpoint of the corresponding voltage range is defined as Eq. (5-17):

$$\mu_i = \frac{V_i{}^{min} + V_i{}^{max}}{2} \tag{5-17}$$

where $V_i{}^{min}$ and $V_i{}^{max}$ are the minimum and maximum peak voltages of the i^{th} vehicle

type from ESAM. For a signal with peak voltage V^{peak}, the corresponding vehicle class ($\hat{c}$) is determined using a nearest-center rule, and is given by Eq. (5-18):

$$\hat{c} = arg^{min}_{i\in\{1,\ k\}} \left|V^{\text{peak}} - \mu_i\right| \tag{5-18}$$

The classification results for each sensor arrangement are summarized in a confusion matrix. Based on this matrix, the AC is defined as Eq. (5-19):

$$AC = \frac{\sum_{i=1}^{K} M_{ij}}{\sum_{i=1}^{K}\sum_{j=1}^{K} M_{ij}} \tag{5-19}$$

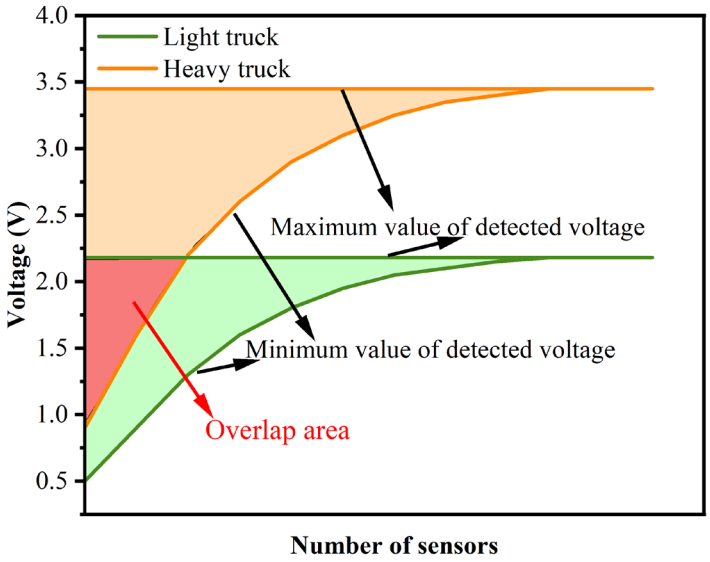


Fig. 5-10: Signal overlap caused by improper sensor arrangement

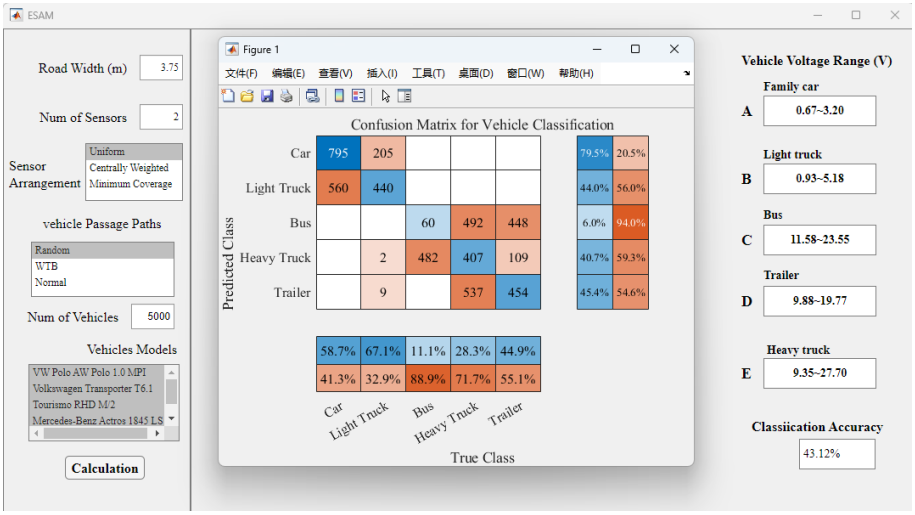


Fig. 5-11: ESAM software GUI

5.5. Results and Discussion

5.5.1. Sensor Response under Different Vehicle Types

The comparison of simulated attenuation functions in Section 5.4.4.1 indicates that seasonal variation mainly affects the response magnitude, while the attenuation pattern with respect to distance remains similar. Therefore, the winter pavement condition is selected as the representative case for the subsequent sensor arrangement evaluation and conclusion.

Given the variability in stress responses induced by different vehicle types, a detailed analysis of the corresponding stress distributions is required to assess their influence on pavement mechanical performance. Fig. 5-12 illustrates the contour distributions of the vertical stress within the surface course layer and at the locations of sensor #2 and #3 under the winter pavement condition. Vertical stress is captured at the moment of peak loading. A unified color scale is applied for light vehicles to facilitate comparison, while a separate, broader scale is used for heavy-duty vehicles to accommodate their larger stress magnitudes. The results show that, with increasing vehicle mass, the effective mechanical influence area within the pavement structure expands, and the lateral attenuation of the vertical stress becomes more gradual. The five vehicle types' peak open-circuit voltage responses at sensor #2 through #8. The open-circuit voltage increases with vehicle weight for the sensor located at sensor #2, which is directly beneath the tire. For sensors positioned farther from the tire, the voltage output decreases progressively. These trends are consistent with the contour results shown in Fig. 5-12.

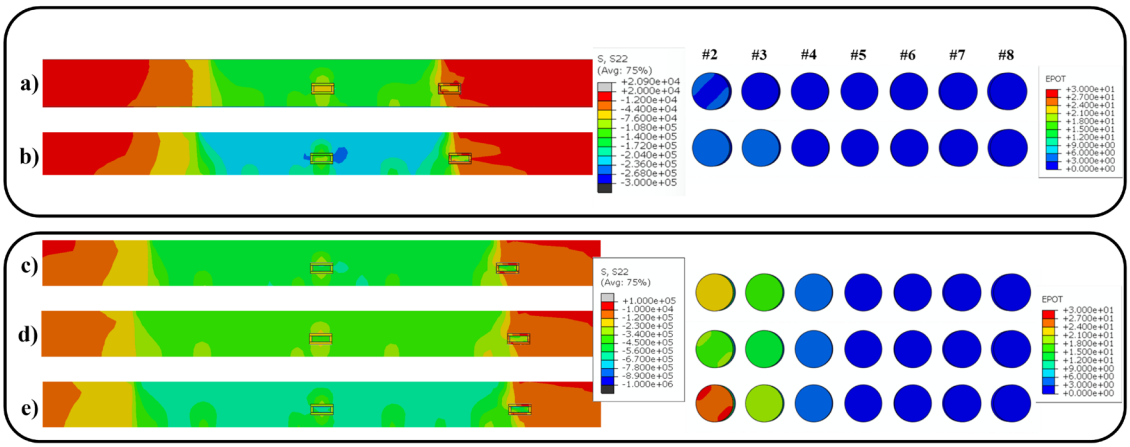


Fig. 5-12: Contour plot of vertical stress and open-circuit voltages distribution with various vehicles, (a) family car, (b) light truck, (c) bus, (d) trailer, and (e) heavy truck

5.5.2. Sensor Arrangement under Random Path

5.5.2.1. Uniform Arrangement

According to Eq. (5-2), the minimum number of KNN sensors required was determined to be two under a road width of 3.75 m and the lightest vehicle type, family car. This number is used as the initial arrangement parameter for the following evaluations of sensor arrangement methods. The comprehensive simulation of various vehicle passage scenarios is achieved by defining the motion pattern as a random path and including all five representative vehicle types in ESAM. For each vehicle type, 1,000 random-path simulations were conducted using a single-row array with two sensors. The family car exhibited the lowest voltage range (0.74-3.24 V), followed by the light truck (1.02-5.21 V). Heavy-duty vehicles produce significantly elevated voltage ranges, with maximum values reaching 27.82 V. Overlaps occurred between family cars and light trucks due to their similar stress profiles and limited signal amplitude margins. The signal overlap was also detected between heavy-duty vehicles.

The earlier case with two sensors demonstrated that the proposed framework could generate valid voltage signals. However, this minimal sensor number is insufficient to distinguish between different vehicle types. Under the random path, simulations considered different vehicle paths, and increasing sensor numbers were analyzed to determine the minimum sensor number required for vehicle distinction. In some cases, a tire passed directly over a sensor, yielding the maximum voltage for that vehicle type. This peak remains nearly constant within each category and is independent of the number of sensors. But the minimum response varied significantly with sensor arrangement and provided a clearer measure of signal classification. As the number of sensors increased, the minimum voltage rose, causing the voltage range of each vehicle type to contract and the differences between vehicle-specific ranges to become more distinct (Fig. 5-13). It should be noted that the minimum voltage has a non-linear relationship with increasing sensor numbers.

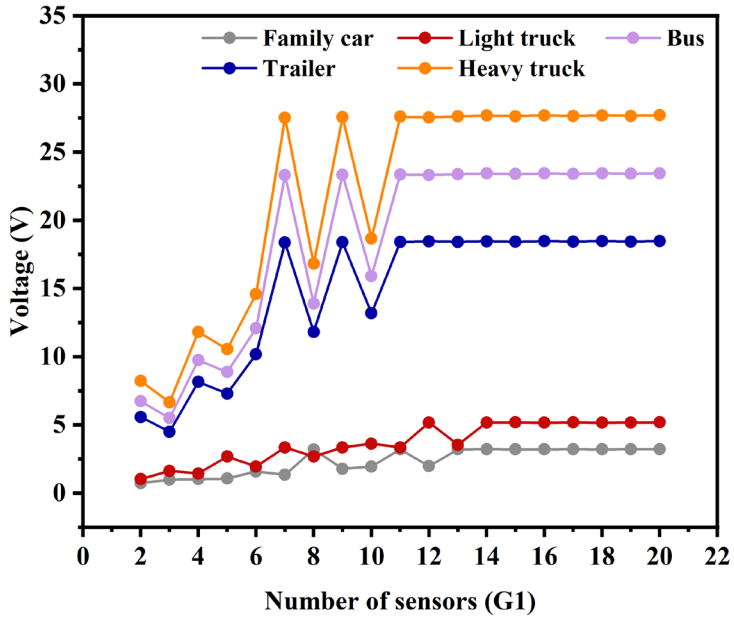


Fig. 5-13: The minimum voltage varies with the number of sensors with Uniform Arrangement in a single-lane road (G1)

For heavy-duty vehicles, the minimum voltage rapidly rises above 20 V after the number of sensors reaches 7, and stabilizes when the sensor numbers exceed 11, indicating that the signal response has converged. For light-duty vehicles, the minimum voltages exhibit a slower increase, and signal convergence occurs when the number of sensors reaches 13 and 14, respectively. Light-duty vehicles have shorter axle spans, leading to smaller "effective sensing zones" and requiring a denser sensor arrangement. When the number reaches 8 to 11, noticeable oscillations appear in the minimum voltage curves. To better illustrate the causes of oscillations, Fig. 5-14a and b illustrate the dynamic variation in the relative positions between tires and sensors as the vehicle traverses laterally from the left to the right side of the road. Under 7 uniformly distributed KNN sensors, at least one sensor is always fully covered by a single tire. Effectively forming a "relay" coverage pattern, the sensors take over the load as the tires move laterally. This arrangement ensures that at least one sensor produces a near maximum voltage, thereby maintaining the minimum voltage at a relatively high value throughout the passage.

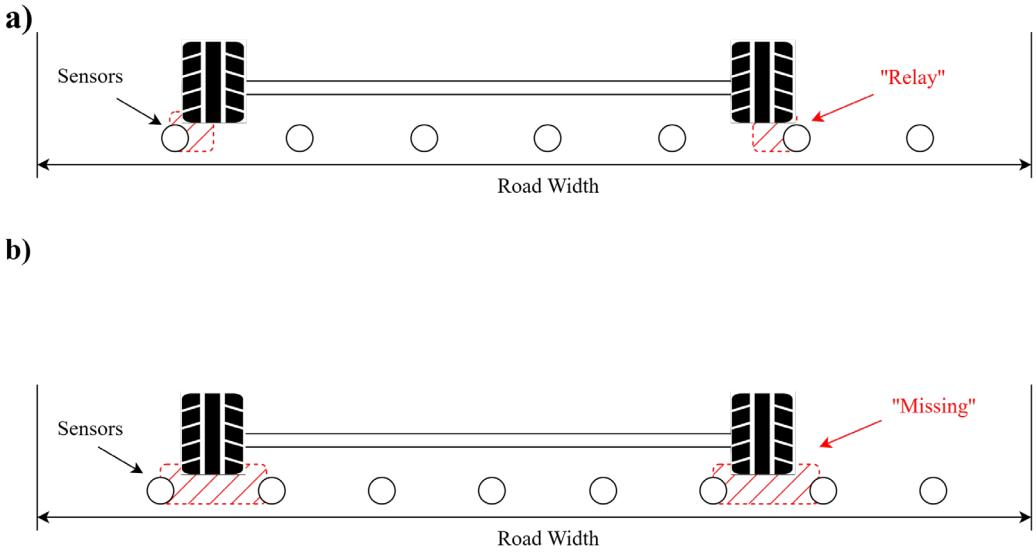


Fig. 5-14: The vehicle type is bus through 7 (a) and 8 (b) sensors on the roadway

When the number of KNN sensors was increased to 8 (as shown in Fig. 5-14b), the reduced sensor spacing introduces new conditions. Both tires may simultaneously fall into the “missing” area between adjacent sensors in certain lateral positions, where no sensor is fully covered. In these cases, the minimum voltage output no longer maintains its peak value and drops significantly, which gives rise to the oscillations observed in the voltage response curves. In other arrangements, signal oscillations are also caused by similar misalignment between the tires and sensors.

In dual-lane road scenarios, heavy-duty vehicle categories produce minimum voltages equal to their peak responses with 15 sensors (Fig. 5-15). This threshold is consistent with the single-lane case with 7 sensors with the same spacing. When the number of sensors increases to 23 or more, the sensor spacing becomes smaller than the tire width. The minimum voltages for heavy-duty vehicles converge. However, light-duty vehicles still display fluctuating values. This observation refers to a nonlinear effect from an arrangement perspective. Once sensor density exceeds a critical threshold, further additions bring little benefit for heavy-vehicle classification. However, higher densities may still be needed for light-duty vehicles.

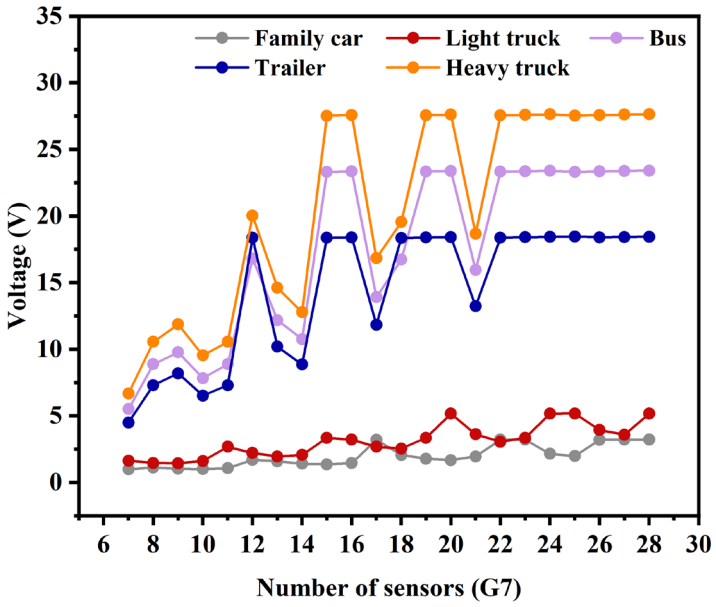


Fig. 5-15: The minimum voltage varies with the number of sensors with Uniform Arrangement in a single lane (G7)

5.5.2.2. Centrally Weighted Arrangement

Unlike the Uniform Arrangement, signal overlap in the Centrally Weighted Arrangement is not limited to vehicles of the same class; even family car signals fall within the voltage range of trailers. The minimum voltage varies with the number of sensors, as shown in Fig. 5-16a. As the number of sensors increases from 2 to 11, the minimum voltages for all vehicle types exhibit an overall upward trend. The voltage converges when the number of sensors reaches 11. In multi-lane conditions, the minimum voltages of heavy-duty vehicles converge with 19 sensors (Fig. 5-16 b). But the minimum voltage outputs of light-duty vehicles show a persistently slow increase accompanied by sustained periodic fluctuations, and the convergence is never reached. This phenomenon can be attributed to the “center-dense, edge-sparse” arrangement adopted in the dual-lane scenario. Under this situation, the wider spacing of sensors near the road edges prevents effective capture of tire loads along certain lateral paths, leading to insufficient signal convergence.

These findings suggest that while Centrally Weighted Arrangement may provide satisfactory performance in narrower, single-lane scenarios, its scalability is constrained in wider road configurations. The degradation in signal resolution and classification separability

with increasing road width underscores a limitation of this arrangement strategy. For multi-lane applications, sensor arrangements with more uniform or well-distributed spatial layouts are better suited to capturing representative voltage responses and supporting vehicle differentiation.

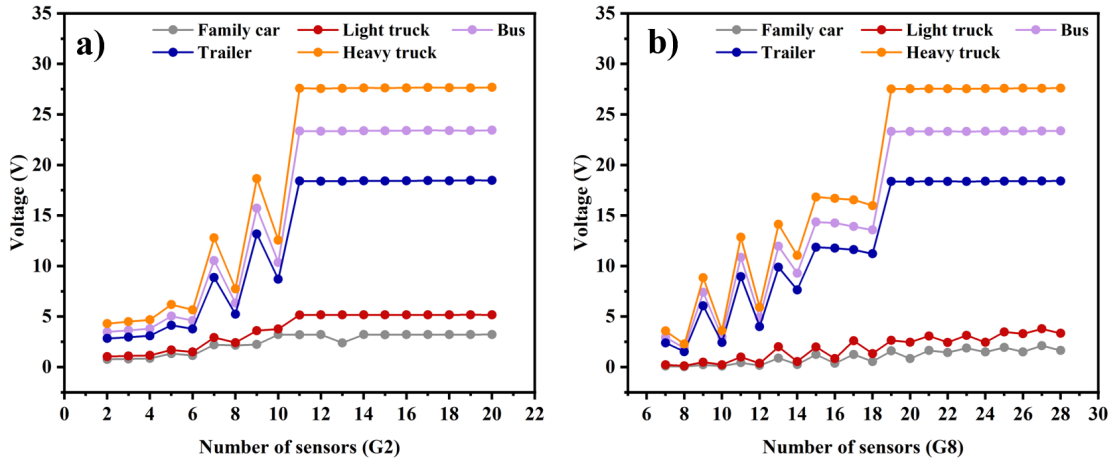


Fig. 5-16: The minimum voltage varies with the number of sensors with the Centrally Weighted Arrangement in a) single-lane (G2) and b) multi-lane (G8)

5.5.2.3. Minimum Coverage Arrangement

Minimum Coverage Arrangement is similar to the Centrally Weighted Arrangement. Except for the family car and light truck, the voltage output ranges of the remaining heavy-duty vehicles do not reach their theoretical maximum values. This phenomenon is primarily attributed to the long axle spans of heavy vehicles and the limited width of the roads. As the vehicle moves laterally across the road, there are 2 sensors embedded in the pavement (Fig. 5-17). When the left tire of a bus is about to load a sensor, its right tire may already be near the outer edge of the road, thus missing the opportunity to contact any sensor. This prevents the voltage range from reaching its maximum value for all vehicle types, resulting in signal overlaps across vehicle types.

The relationship between the minimum voltage outputs of various vehicle types and the number of sensors under the Minimum Coverage Arrangement on a single-lane road is shown in Fig. 5-18a. As the number of sensors increases, the output voltage range for all vehicle types remains nearly constant, resulting in the inability to identify vehicle types. This limitation is primarily attributed to the sensor arrangement design, where the Minimum Coverage

Arrangement places the two sensors at the edge of the “effective sensing zone” to ensure the use of the minimum number of sensors. It results in relatively large distances between the tires and sensors with a wider range of voltages, making the voltage indistinguishable.

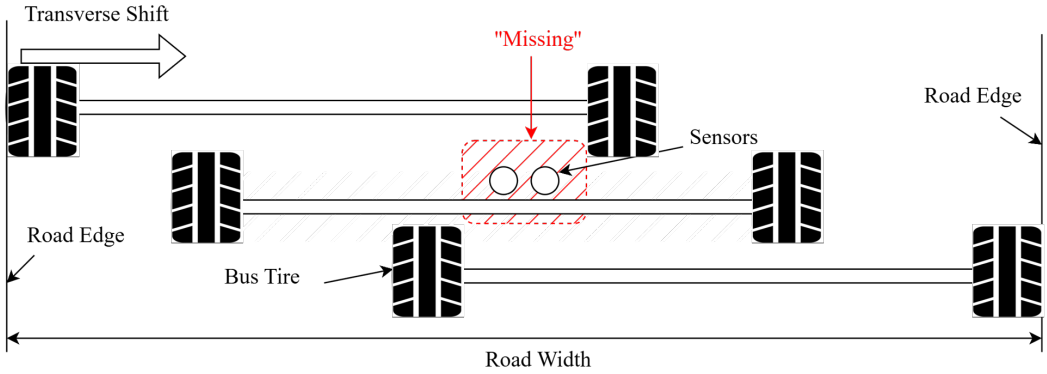


Fig. 5-17: The missing of the bus model when passing over the pavement surface

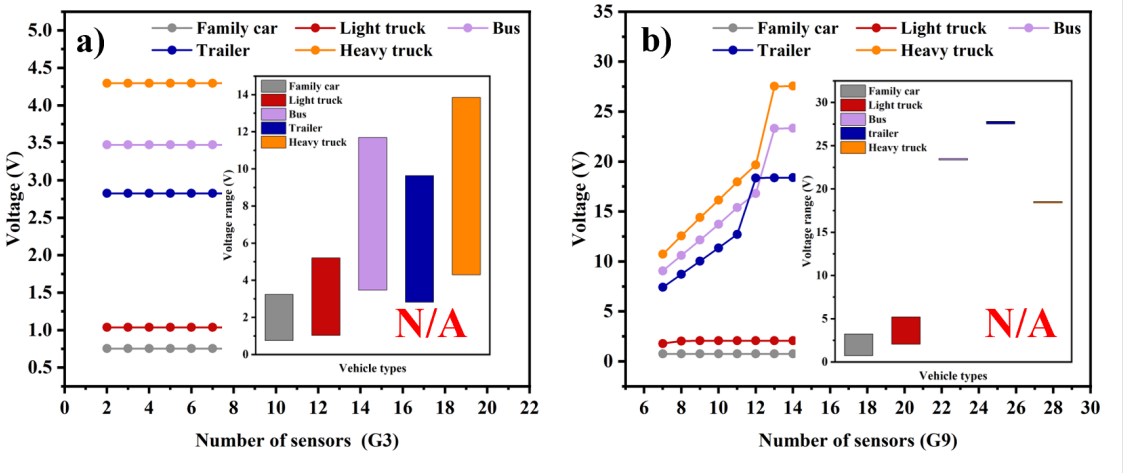


Fig. 5-18: The minimum voltage varies with the number of sensors with the Minimum Coverage Arrangement in a) single-lane (G3) and b) multi-lane (G9)

In the multi-lane case, the maximum voltage output under the Minimum Coverage Arrangement varies with sensor density (Fig. 5-18b). When fewer than 13 sensors are embedded, the voltage of heavy-duty vehicles increases only gradually; once the number exceeds 13, the responses enable reliable differentiation. However, light-duty vehicles maintain relatively stable outputs across all sensors and never achieve effective classification. This is because this arrangement primarily increases sensor density in the central area. Heavy-duty vehicles have longer axles, so when traveling along the edge, tires closer to the road center can press down on the sensors, generating a converging voltage signal. However, light-duty cars

lack sufficiently long axles; under the same conditions, the sensors can only contact the edges of the "effective sensing zone", thus failing to produce a converging voltage, resulting in being unable to achieve effective classification. These results suggest that the strategy is more effective for heavy-duty vehicles, while its ability to capture light-duty vehicle responses remains restricted.

5.5.3. Sensor Arrangement under Wheel-Tack Constraint

In real-world traffic environments, vehicles typically follow fixed wheel-track paths with minor lateral deviations ("Bundesanstalt für Straßenwesen (BASt), 'Lang-Lkw – Bericht über Erfahrungen mit dem verlängerten Lkw (Stand: 2024).' 2024, [Online]," 2025). Wheel-track constraint vehicle passage modes with ± 0.2 m were developed to simulate their lateral positions. The voltage ranges of five vehicle types were compared under different sensor arrangement strategies, as illustrated in Fig. 5-19. For Uniform Arrangement, the maximum output is achieved with only three sensors, since their positions coincide with the tire paths (Fig. 5-19a, G4). As the number of sensors increases from 4 to 11, the minimum output oscillates, but beyond 11 sensors, the responses converge. For the Centrally Weighted Arrangement, the minimum voltage rises gradually with sensor density and reaches its peak only at 11 sensors (Fig. 5-19a, G5). This is because most sensors are clustered near the lane center at low densities, leaving parts of the wheel-track insufficiently covered. Under the Minimum Coverage Arrangement, although each vehicle has a wide voltage output range, they do not overlap. Therefore, vehicles can be accurately classified (Fig. 5-19a, G6).

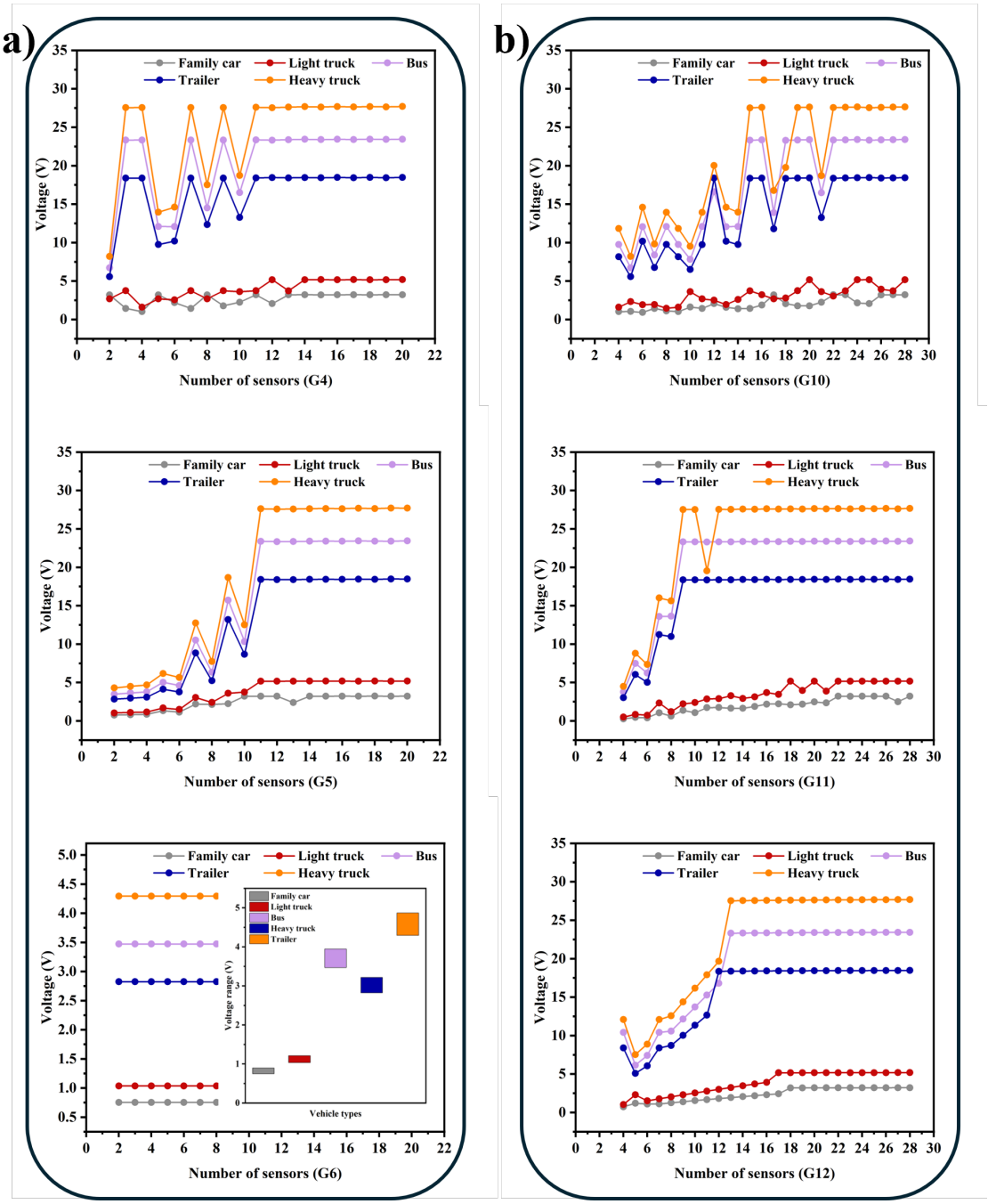


Fig. 5-19: The minimum voltage value varies with the number of sensors in a single-lane with various sensor arrangements: in single-lane, (a) Uniform G4, Centrally Weighted G5, and Minimum Coverage G6; in multi-lane, (b) Uniform G10, Centrally Weighted G11, and Minimum Coverage G12

On multi-lane roads, drivers tend to drift slightly toward the center line. To capture this effect, a 0.2 m lateral offset was introduced in both lanes, producing more realistic driving trajectories. The results for three sensor arrangement strategies under this condition are shown in Fig. 5-19b (G10, G11, and G12). For Uniform Arrangement (G10), at least 15 sensors are required to eliminate signal overlap. With 23 or more sensors, the voltage ranges of all vehicle

types converge, and recognition performance remains stable. In the case of the Centrally Weighted Arrangement (case G11), full signal separability is achieved when the number of sensors reaches 13. When the sensor count exceeds 16, the voltage output ranges associated with different vehicle types can be clearly classified, exhibiting minimal overlap and improved classification clarity. For Minimum Coverage Arrangement (case G12), as the number of sensors increases, their voltage range tends to converge, unlike in single-lane scenarios. This is due to the wider road, where uniformly spaced sensors in the center enhance voltage response. These findings suggest that Centrally Weighted Arrangement and Minimum Coverage Arrangement, when appropriately aligned with expected traffic behavior, can outperform Uniform Arrangement by achieving high-resolution voltage differentiation with fewer sensors.

5.5.4. Comparison of Sensor Arrangement Strategies

The variation of AC with respect to the number of sensors for the three arrangement strategies under single-lane and dual-lane conditions is shown in Fig. 5-20, and the corresponding sensor numbers are summarized in Table 5-6. Based on the acceptability criterion defined in Section 5.4.4.2, an arrangement is regarded as effective when AC exceeds 95%. The sensor number at which this criterion is first satisfied is adopted as the selected sensor arrangement under the simulated conditions.

In the single-lane case, the Uniform Arrangement reaches complete distinction with only 7 sensors (Fig. 5-20a), showing strong classification ability. The Centrally Weighted Arrangement requires 11 sensors for high classification. However, the Minimum Coverage Arrangement remains ineffective in this case. As the AC stays consistently high and each vehicle type exhibits overlapping signal regions, making reliable classification impossible. In the multi-lane roads, signal differentiation is more difficult due to the wider distribution of wheel loads and greater variability in driving paths. Uniform Arrangement requires at least 15 sensors to achieve great classification (Fig. 5-20c). Fluctuations remain until 18 units, beyond which responses stabilize. Although the Minimum Coverage Arrangement improves greatly (achieving 93% classification accuracy with 13 sensors) compared with the single-lane case, it still falls short of the target classification accuracy. Centrally Weighted Arrangement fluctuates at low sensor densities and achieves accurate classification only at 19 sensors.

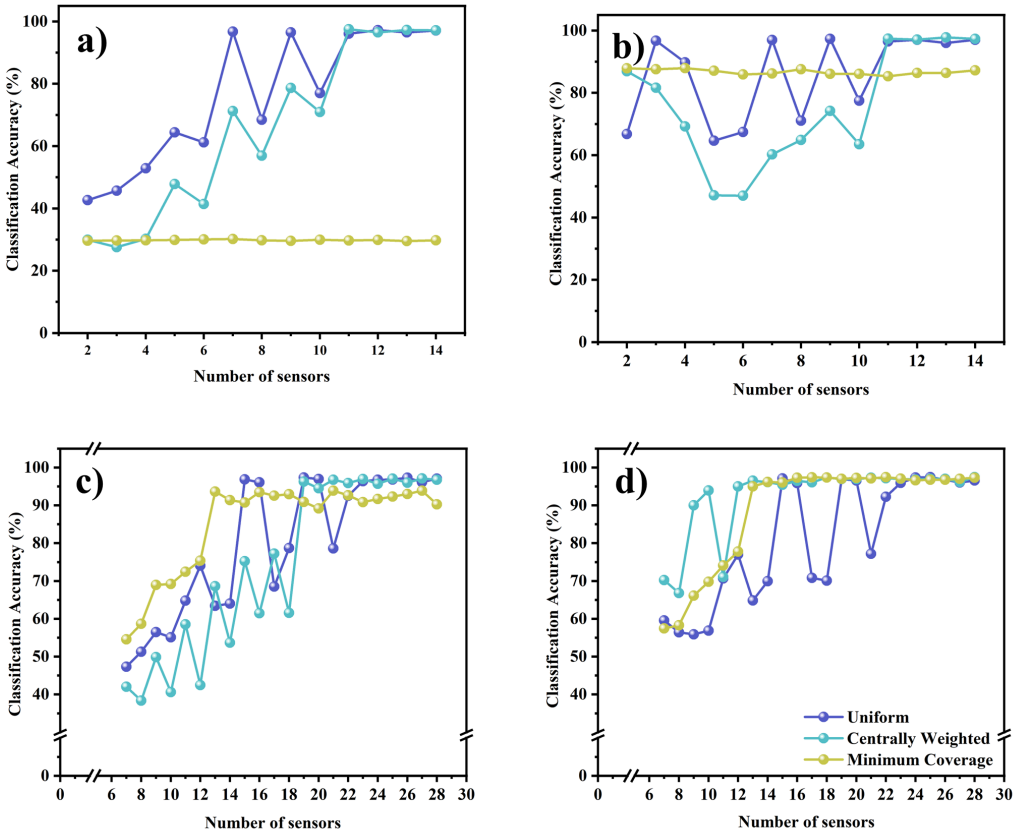


Fig. 5-20: Comparison of AC for three arrangement strategies in single-lane: (a) random path G1, G2, G3, and (b) wheel-track-constraint G4, G5, G6, in multi-lane: (c) random path G7, G8, G9, and (d) wheel-track-constraint G10, G11, G12

Table 5-6 The minimum number of sensors is required to distinguish between five vehicle types

Lane type	Arrangement Constraint	Uniform	Centrally Weighted	Minimum Coverage
Single-lane Road	Random Path	7	11	N/A
	Wheel-Track Constraint	3	11	N/A
Dual-lane Road	Random Path	15	19	N/A
	Wheel-Track Constraint	15	12	13

Under wheel-track-constraint situation, the AC for all arrangements were presented for both single-lane (Fig. 5-20b) and multi-lane (Fig. 5-20d) roads. In the single-lane case, both Centrally Weighted Arrangement and Minimum Coverage Arrangement achieve great signal separation with only two sensors (86.94% and 87.9%, respectively), representing a marked improvement in performance in constrained traffic. Even when the number of sensors is

increased to 14 at Minimum Coverage, the AC remains comparable to the initial 2-sensor arrangement (Fig. 5-20b). This indicates the extreme signal stability of this strategy in traffic scenarios with restricted paths. However, the Centrally Weighted Arrangement exhibits a trend of first decreasing and then increasing when the number of sensors increases from 2 to 11, while the Uniform Arrangement exhibits fluctuations and variations between 3 and 11 sensors. Stable classification becomes possible only after the number of sensors exceeds 11. The arrangement under wheel-track-constraint of the Centrally Weighted Arrangement only needs 12 sensors in the multi-lane roads compared to a random path. In this research, the sensor embedded using the Minimum Coverage Arrangement has an effective impact on vehicle classification for the first time, showing a great ability with the 13 sensors. Compared to a random path, the wheel-track constraint demonstrates superior performance because it enables good signal performance whenever sensors are embedded near the wheel-track bands. Therefore, better signal separation can be achieved with fewer sensors on single-lane and multi-lane roads.

Based on the simulation results, the ESAM framework enables comparative evaluation of sensor arrangement strategies under specified lane functions and traffic assumptions. The results in Table 5-7 illustrate the application of the proposed methodology rather than universal design guidelines. Under the considered pavement structure, vehicle speed, loading representation, and KNN sensor properties, ESAM provides a systematic approach for evaluating and comparing sensor arrangements.

Table 5-7 Recommendation of sensor arrangement for different traffic conditions

Traffic condition	Corresponding cases	Recommended Arrangement
Passenger car lanes of a four-lane highway	G7	Uniform
Truck lanes of a four-lane highway	G4	Uniform
Single-lane highway on-ramps and off-ramps	G4	Uniform
Urban main road	G7/G8	Uniform/ Centrally Weighted
Urban secondary road	G7/G8	Uniform/ Centrally Weighted
Two-way single-lane rural road	G7	Uniform
Tunnel road	G11/G12	Centrally Weighted/ Minimum Coverage

5.6. Conclusions and Outlook

This study proposes a simulation-based framework, ESAM, for determining sensor arrangement design in pavement-embedded vehicle classification systems using lead-free KNN piezoelectric sensors. The framework targets sensing scenarios with relatively low piezoelectric response and focuses on how sensor number and spatial arrangement influence signal separability rather than absolute signal amplitude.

Numerical analyses were performed by coupling pavement-vehicle interaction, piezoelectric response, and signal-based separability evaluation. Several representative arrangement strategies were examined under the modeled traffic and lane configurations. The results indicate that, under the evaluated conditions, a sparse transverse sensor array can achieve high signal separability (with AC exceeding 95%), while substantially reducing the number of embedded sensors compared with conventional dense layouts. Once attenuation-based representations are established, ESAM enables rapid and consistent comparison of alternative sensor arrangements under identical modeling assumptions, avoiding repetitive full-scale finite element simulations. This capability constitutes the main methodological contribution of the proposed framework.

The present study is limited to numerical investigations based on predefined pavement structures, loading models, traffic assumptions, and sensor properties. External validation using field measurements is beyond the scope of this work. The framework nevertheless provides a structured basis for future extensions, including the incorporation of temperature-dependent material behavior, pavement property variability, and more complex traffic scenarios.

6. Conclusions and Outlook

6.1. Conclusions

This dissertation addressed the challenge of integrating lead-free piezoelectric materials into pavement traffic sensing systems. Unlike conventional approaches that focus primarily on improving intrinsic material sensitivity, this work treated pavement sensing as a multi-scale engineering problem. The research demonstrated that reliable sensing performance depends on coordinated design across material properties, device configuration, structural interaction, and system-level deployment. The main conclusions are summarized below.

(1) Lead-free KNN-based piezoelectric ceramics are thermally compatible with pavement service conditions and provide an environmentally favorable alternative to conventional PZT materials. However, their reduced intrinsic piezoelectric response limits signal amplitude and requires system-level engineering rather than direct material substitution.

(2) Sensing performance in pavement structures is strongly influenced by packaging and mechanical confinement. Mechanical strength and peak voltage alone are insufficient indicators of reliability. Stable signal evolution, response linearity, and durability under cyclic loading are critical for practical pavement applications.

(3) A mechanics-based description of signal propagation within layered pavement systems has been established. The derived attenuation functions characterize spatial signal decay under traffic loading and provide a transferable representation that links local sensor behavior to system-level signal interpretation.

(4) A simulation-driven framework for sensor arrangement has been developed. Instead of relying on dense sensor placement, the framework evaluates deployment strategies based on signal distinguishability and information efficiency. The results demonstrate that reliable vehicle classification can be achieved using optimized sensor configurations while minimizing pavement disturbance.

(5) A structured multi-scale engineering methodology has been established, integrating material evaluation, device configuration, numerical modeling, and system-level

deployment within a unified design pathway. This approach shifts the focus from maximizing intrinsic piezoelectric coefficients to optimizing information quality in pavement sensing systems.

6.2. Outlook

Although the present work clarifies the key mechanisms governing lead-free piezoelectric pavement sensing, further development is required for full engineering implementation. Field validation represents the next critical step. Deployment of the proposed framework in real pavement sections will enable calibration of attenuation functions under actual traffic, temperature, and moisture conditions. Long-term monitoring is necessary to evaluate durability and performance stability.

Future research should extend the numerical modeling approach to include multi-axial stress states and environmental coupling effects. Integration of field data into the simulation framework will improve predictive robustness and practical applicability. In addition, combining the mechanics-based deployment strategy with advanced data-driven classification methods may enhance adaptability in complex traffic environments. The proposed multi-scale methodology can also be extended to other sensing materials and smart road infrastructure applications.

This dissertation demonstrates that sustainable pavement sensing can be achieved not by maximizing material performance, but by coordinating material behavior with structural mechanics and system-level design.

Reference

Abdulkarem, M., Samsudin, K., Rokhani, F.Z., A Rasid, M.F., 2020. Wireless sensor network for structural health monitoring: A contemporary review of technologies, challenges, and future direction. Struct. Health Monit. 19, 693–735. https://doi.org/10.1177/1475921719854528

Acosta, M., Novak, N., Rojas, V., Patel, S., Vaish, R., Koruza, J., Rossetti, G.A., Rödel, J., 2017. BaTiO3-based piezoelectrics: Fundamentals, current status, and perspectives. Appl. Phys. Rev. 4, 041305. https://doi.org/10.1063/1.4990046

Aduwenye, P., Chong, B.W., Gujar, P., Shi, X., 2024. Mechanical properties and durability of carbon fiber reinforced cementitious composites: A review. Constr. Build. Mater. 452, 138822. https://doi.org/10.1016/j.conbuildmat.2024.138822

Ait Bassou, A., Figueiras, F.G., Fernandes, J.R., Tavares, P.B., 2024. Photo-ferroelectric oxides for photovoltaic applications: Insights, challenges and opportunities. Appl. Mater. Today 41, 102465. https://doi.org/10.1016/j.apmt.2024.102465

Anbalagan, S., Manojkumar, K., Muthuramalingam, M., Hajra, S., Panda, S., Sahu, R., Joon Kim, H., Sundaramoorthy, A., Nithyavathy, N., Vivekananthan, V., 2024. Progress and recent advances in self-powered gas sensing based on triboelectric and piezoelectric nanogenerators. Chem. Eng. J. 497, 154740. https://doi.org/10.1016/j.cej.2024.154740

Anwer, S., Umair Khan, M., Alazzam, A., Mohammad, B., Abu Nada, E., 2024. 2D Ti3C2Tx-MXene and its superstructures as dual-function electrodes for triboelectric nanogenerators for self-powered electronics. Chem. Eng. J. 502, 157985. https://doi.org/10.1016/j.cej.2024.157985

Ardolino, F., Cardamone, G.F., Arena, U., 2021. How to enhance the environmental sustainability of WEEE plastics management: An LCA study. Waste Manag. 135, 347–359. https://doi.org/10.1016/j.wasman.2021.09.021

ASTM C109/C109M-02：Standard Test Method for Compressive Strength of Hydraulic Cement Mortars (Using 2-in. or [50-mm] Cube Specimens), 2017.

Athira, B.S., George, A., Vaishna Priya, K., Hareesh, U.S., Gowd, E.B., Surendran, K.P., Chandran, A., 2022. High-Performance Flexible Piezoelectric Nanogenerator Based on Electrospun PVDF-$BaTiO_3$ Nanofibers for Self-Powered Vibration Sensing Applications. ACS Appl. Mater. Interfaces 14, 44239–44250. https://doi.org/10.1021/acsami.2c07911

Avanish Babu, T., Madhuri, W., 2022. Microwave synthesis technique for LTCC and colossal dielectric constant in PZT. Chem. Phys. Lett. 799, 139641. https://doi.org/10.1016/j.cplett.2022.139641

Azad, M.M., Kumar, P., Kim, H.S., 2024. Delamination detection in CFRP laminates using deep transfer learning with limited experimental data. J. Mater. Res. Technol. 29, 3024–3035. https://doi.org/10.1016/j.jmrt.2024.02.067

Badaraev, A.D., Koniaeva, A., Krikova, S.A., Shesterikov, E.V., Bolbasov, E.N., Nemoykina, A.L., Bouznik, V.M., Stankevich, K.S., Zhukov, Y.M., Mishin, I.P., Varakuta, E.Y., Tverdokhlebov, S.I., 2020. Piezoelectric polymer membranes with thin antibacterial coating for the regeneration of oral mucosa. Appl. Surf. Sci. 504, 144068. https://doi.org/10.1016/j.apsusc.2019.144068

Bafna, Y., Vashi, J., Bothe, S., 2025. Machine Learning-Driven Prediction of Pavement Sub-Grade Failures Using Vehicle-Mounted Acceleration Sensors. Int. J. Pavement Res. Technol. https://doi.org/10.1007/s42947-025-00613-5

Bairagi, S., Ali, S.W., 2020. Flexible lead-free PVDF/SM-KNN electrospun nanocomposite based piezoelectric materials: Significant enhancement of energy harvesting efficiency of the

nanogenerator. Energy 198, 117385. https://doi.org/10.1016/j.energy.2020.117385

Bairagi, S., Ali, S.W., 2019. Influence of High Aspect Ratio Lead-Free Piezoelectric Fillers in Designing Flexible Fibrous Nanogenerators: Demonstration of Significant High Output Voltage. Energy Technol. 7, 1900538. https://doi.org/10.1002/ente.201900538

Bairagi, S., Khandelwal, G., Karagiorgis, X., Gokhool, S., Kumar, C., Min, G., Mulvihill, D.M., 2022. High-Performance Triboelectric Nanogenerators Based on Commercial Textiles: Electrospun Nylon 66 Nanofibers on Silk and PVDF on Polyester. ACS Appl. Mater. Interfaces 14, 44591–44603. https://doi.org/10.1021/acsami.2c13092

Batra, K., Sinha, N., Kumar, B., 2022. Effect of Nd-doping on 0.95(K0.6Na0.4)NbO3-0.05(Bi0.5Na0.5)ZrO3 ceramics: Enhanced electrical properties and piezoelectric energy harvesting capability. J. Phys. Chem. Solids 170, 110953. https://doi.org/10.1016/j.jpcs.2022.110953

Baumann, H., Arvidsson, R., 2015. Life Cycle Assessment (LCA), in: Kobayashi, S., Müllen, K. (Eds.), Encyclopedia of Polymeric Nanomaterials. Springer Berlin Heidelberg, Berlin, Heidelberg, pp. 1–5. https://doi.org/10.1007/978-3-642-36199-9_386-1

Beigh, N.T., Beigh, F.T., Mallick, D., 2023. Machine learning assisted hybrid transduction nanocomposite based flexible pressure sensor matrix for human gait analysis. Nano Energy 116, 108824. https://doi.org/10.1016/j.nanoen.2023.108824

Beltrán-Mir, H., Vendrell, X., Dos Santos Veiga, E.L., Mestres, L., Cordoncillo, E., 2023. Structural and electrical properties of Zr-doped K0.48Na0.52NbO3 ceramics: “Hard” lead-free piezoelectric. Bol. Soc. Esp. Cerámica Vidr. 62, 468–478. https://doi.org/10.1016/j.bsecv.2022.12.001

Benabdallah, F., Elissalde, C., Seu, U.-C.C., Michau, D., Poulon-Quintin, A., Gayot, M., Garreta, P., Khemakhem, H., Maglione, M., 2015. Structure–microstructure–property relationships in lead-free BCTZ piezoceramics processed by conventional sintering and spark plasma sintering. J. Eur. Ceram. Soc. 35, 4153–4161. https://doi.org/10.1016/j.jeurceramsoc.2015.06.030

Berglund, E.Z., Monroe, J.G., Ahmed, I., Noghabaei, M., Do, J., Pesantez, J.E., Khaksar Fasaee, M.A., Bardaka, E., Han, K., Proestos, G.T., Levis, J., 2020. Smart Infrastructure: A Vision for the Role of the Civil Engineering Profession in Smart Cities. J. Infrastruct. Syst. 26. https://doi.org/10.1061/(asce)is.1943-555x.0000549

Bhatnagar, P., Zaferani, S.H., Rafiefard, N., Baraeinejad, B., Vazifeh, A.R., Mohammadpour, R., Ghomashchi, R., Dillersberger, H., Tham, D., Vashaee, D., 2023. Advancing personalized healthcare and entertainment: Progress in energy harvesting materials and techniques of self-powered wearable devices. Prog. Mater. Sci. 139, 101184. https://doi.org/10.1016/j.pmatsci.2023.101184

Bhatta, T., Faruk, O., Islam, M.R., Kim, H.S., Rana, S.S., Pradhan, G.B., Deo, A., Kwon, D.-S., Yoo, I., Park, J.Y., 2024. Polymeric multilayered planar spring-based hybrid nanogenerator integrated with a self-powered vibration sensor for automotive vehicles IoT applications. Nano Energy 127, 109793. https://doi.org/10.1016/j.nanoen.2024.109793

Bhattacharyya, N., Bhattacharyya, S., Ghosh, K., Pal, S., Jana, A., Mukherjee, S., 2024. Fabrication of sensor technology using thin films for biosensing, agricultural and environmental applications, in: Comprehensive Materials Processing. Elsevier, pp. 88–99. https://doi.org/10.1016/B978-0-323-96020-5.00059-5

Bian, K., Gu, Q., Zhu, K., Zhu, R., Wang, J., Liu, J., Qiu, J., 2016. Improved sintering activity and piezoelectric properties of PZT ceramics from hydrothermally synthesized powders with Pb

excess. J. Mater. Sci. Mater. Electron. 27, 8573–8579. https://doi.org/10.1007/s10854-016-4875-9

Boada-Parra, L.G., Apaza, F., Gulisano, F., Gallego, J., Jurado-Piña, R., 2023. Characterization of interlayer bonding mechanism based on interface morphology between asphalt mix and electronics devices covers materials, in: Schulz, K., Nikolakopoulos, K.G., Michel, U. (Eds.), Earth Resources and Environmental Remote Sensing/GIS Applications XIV. Presented at the Earth Resources and Environmental Remote Sensing/GIS Applications XIV, SPIE, Amsterdam, Netherlands, p. 36. https://doi.org/10.1117/12.2688737

Budinská, Z., Tolde, Z., Horkavcová, D., Vlčák, P., 2025. Effect of addition of CaTiO3 powder to sol-gel coatings prepared by dip coating method on mechanical properties and biocompatibility. Mater. Chem. Phys. 331, 130189. https://doi.org/10.1016/j.matchemphys.2024.130189

Bundesanstalt für Straßenwesen (BASt), "Lang-Lkw – Bericht über Erfahrungen mit dem verlängerten Lkw (Stand: 2024)." 2024, [Online], 2025.

Buonsanti, M., Leonardi, G., 2012. FEM Analysis of Airport Flexible Pavements Reinforced with Geogrids. Adv. Sci. Lett. 13, 392–395. https://doi.org/10.1166/asl.2012.3765

Camargo, J., Osinaga, S., Febbo, M., Machado, S.P., Rubio-Marcos, F., Ramajo, L., Castro, M., 2021. Piezoelectric and structural properties of bismuth sodium potassium titanate lead-free ceramics for energy harvesting. J. Mater. Sci. Mater. Electron. 32, 19117–19125. https://doi.org/10.1007/s10854-021-06430-3

Cao, W., Li, W., Feng, Y., Bai, T., Qiao, Y., Hou, Y., Zhang, T., Yu, Y., Fei, W., 2016. Defect dipole induced large recoverable strain and high energy-storage density in lead-free Na0.5Bi0.5TiO3-based systems. Appl. Phys. Lett. 108, 202902. https://doi.org/10.1063/1.4950974

Chafik, A.A., Gaber, J., Tayane, S., Ennaji, M., Bourgeois, J., Ghazawi, T.E., 2024. From Conventional to Programmable Matter Systems: A Review of Design, Materials, and Technologies. ACM Comput. Surv. 56, 1–26. https://doi.org/10.1145/3653671

Chang, C., Kong, L., Han, L., Li, J., Pan, S., Wei, Y., 2025. Vibration Analysis and Vehicle Detection by MEMS Acceleration Sensors Embedded in PCC Pavement. Sensors 25, 2898. https://doi.org/10.3390/s25092898

Chang, C.-J., Qi, X., 2022. Dielectric relaxation and high recoverable energy density in (1-x)(0.3BiFeO3-0.7SrTiO3)-xK0.5Na0.5NbO3 ceramics. Ceram. Int. 48, 25610–25620. https://doi.org/10.1016/j.ceramint.2022.05.240

Chantima, P., Yarnguy, T., Sarawan, K., Sangmuenmao, R., Sommool, W., Gonwirut, S., 2025. Hybrid Intelligence for Field-Scale Soil Analysis and Crop Advisory Using Embedded Sensors and Machine Learning. IEEE Access 13, 174120–174138. https://doi.org/10.1109/ACCESS.2025.3613848

Chapeleau, X., Blanc, J., Hornych, P., Gautier, J.-L., Carroget, J., 2017. Assessment of cracks detection in pavement by a distributed fiber optic sensing technology. J. Civ. Struct. Health Monit. 7, 459–470. https://doi.org/10.1007/s13349-017-0236-5

Chen, D., Huang, C., Fan, T., Lau, H.C., Yan, X., 2025. Predictive modelling for vessel traffic flow: A comprehensive survey from statistics to AI. Transp. Saf. Environ. 7, tdaf022. https://doi.org/10.1093/tse/tdaf022

Chen, H., Li, Z., Wu, J., Xiong, W., Du, C., 2023. SemiRoadExNet: A semi-supervised network for road extraction from remote sensing imagery via adversarial learning. ISPRS J. Photogramm. Remote Sens. 198, 169–183. https://doi.org/10.1016/j.isprsjprs.2023.03.012

Chen, Kai, Wang, Y., Wu, C., Du, Y., Tang, H., Zheng, S., Zhou, Z., Zheng, H., Wu, G., 2024. ln vitro assessment of immunomodulatory and osteogenic properties in 3D-printed hydroxyapatite/barium titanate piezoelectric ceramic scaffolds. Ceram. Int. 50, 8751–8759. https://doi.org/10.1016/j.ceramint.2023.12.192

Chen, Kairui, Zhuo, J., Liu, W., Huang, Y., Hua, C., Zhu, Q., Yuan, Y., 2024. Self-sensed, self-adapted and self-powered piezoelectric generator architecture by synchronous circuits of autonomous parameter tuning. Energy Convers. Manag. 300, 117919. https://doi.org/10.1016/j.enconman.2023.117919

Chen, W., Wang, F., Yan, K., Zhang, Y., Wu, D., 2019. Micro-stereolithography of KNN-based lead-free piezoceramics. Ceram. Int. 45, 4880–4885. https://doi.org/10.1016/j.ceramint.2018.11.185

Chen, W., Wang, L., Ren, W., Zhao, J., Wang, Z., Quan, Y., Zhuang, J., 2022. Effect of BaZrO3 amounts on the domain structure and electrical properties of lead-free piezoelectric KNN-based films. Mater. Sci. Eng. B 276, 115552. https://doi.org/10.1016/j.mseb.2021.115552

Chen, X., Ma, F., Wu, Y., Han, B., Luo, L., Biancardo, S.A., 2025. MFMDepth: MetaFormer-based monocular metric depth estimation for distance measurement in ports. Comput. Ind. Eng. 207, 111325. https://doi.org/10.1016/j.cie.2025.111325

Chen, Y., Zhang, X., Lu, C., 2024. Flexible piezoelectric materials and strain sensors for wearable electronics and artificial intelligence applications. Chem. Sci. 15, 16436–16466. https://doi.org/10.1039/D4SC05166A

Chowdhury, S., Alam, S., Alam, M.D., Jui, F.S., 2024. Laser lift-off technique for applications in III-N microelectronics: A review. Microelectron. Eng. 290, 112198. https://doi.org/10.1016/j.mee.2024.112198

Cross, E.J., Gibson, S.J., Jones, M.R., Pitchforth, D.J., Zhang, S., Rogers, T.J., 2022. Physics-Informed Machine Learning for Structural Health Monitoring, in: Cury, A., Ribeiro, D., Ubertini, F., Todd, M.D. (Eds.), Structural Health Monitoring Based on Data Science Techniques, Structural Integrity. Springer International Publishing, Cham, pp. 347–367. https://doi.org/10.1007/978-3-030-81716-9_17

Dahiya, P., Hooda, A., 2024. Efficiently high energy storage density in Ba2+ ion modified K0·5Na0·5NbO3 (KNN) ferroelectric ceramics for super capacitors. Mater. Chem. Phys. 323, 129670. https://doi.org/10.1016/j.matchemphys.2024.129670

Dai, N., Lei, I.M., Li, Z., Li, Y., Fang, P., Zhong, J., 2023. Recent advances in wearable electromechanical sensors—Moving towards machine learning-assisted wearable sensing systems. Nano Energy 105, 108041. https://doi.org/10.1016/j.nanoen.2022.108041

Das, R., Sharma, S., Mandal, K., 2016. Aliovalent Ba 2+ doping: A way to reduce oxygen vacancy in multiferroic BiFeO 3. J. Magn. Magn. Mater. 401, 129–137. https://doi.org/10.1016/j.jmmm.2015.10.022

De Fazio, R., Del-Valle-Soto, C., Mastronardi, V.M., De Vittorio, M., Visconti, P., 2025. A smart glove to evaluate Parkinson's disease by flexible piezoelectric and inertial sensors. Sens. Int. 6, 100324. https://doi.org/10.1016/j.sintl.2024.100324

Deng, J., Zhang, G., Yang, Y., Zhu, W., Wu, Z., Wang, Y., 2025. Hydrothermally synthesized KNN NPs boosting P(VDF-TrFE) piezoelectricity for energy harvesting and physiological monitoring. Mater. Res. Bull. 185, 113297. https://doi.org/10.1016/j.materresbull.2025.113297

Deng, J., Zhao, P., Wu, Z., Wang, Y., 2024. Optimized performance of self-driven piezoelectric sensors through KNN/Nb2CTx synergistic effect. Ceram. Int. 50, 31154–31163.

https://doi.org/10.1016/j.ceramint.2024.05.421
Deng, Z., Li, W., Dong, W., Sun, Z., Kodikara, J., Sheng, D., 2023. Multifunctional asphalt concrete pavement toward smart transport infrastructure: Design, performance and perspective. Compos. Part B Eng. 265, 110937. https://doi.org/10.1016/j.compositesb.2023.110937
Di Graziano, A., Marchetta, V., Cafiso, S., 2020. Structural health monitoring of asphalt pavements using smart sensor networks: A comprehensive review. J. Traffic Transp. Eng. Engl. Ed. 7, 639–651. https://doi.org/10.1016/j.jtte.2020.08.001
Di Lorenzo, D., Champaney, V., Marzin, J.Y., Farhat, C., Chinesta, F., 2023. Physics informed and data-based augmented learning in structural health diagnosis. Comput. Methods Appl. Mech. Eng. 414, 116186. https://doi.org/10.1016/j.cma.2023.116186
Díez-Pascual, A.M., 2019. Nanoparticle Reinforced Polymers. Polymers 11, 625. https://doi.org/10.3390/polym11040625
Difeo, M., Osinaga, S., Febbo, M., Machado, S.P., Castro, M., Ramajo, L., 2021. Influence of the (Bi0.5Na0.5)TiO3–BaTiO3 lead-free piezoceramic geometries on the power generation of energy harvesting devices. Ceram. Int. 47, 10696–10704. https://doi.org/10.1016/j.ceramint.2020.12.184
Difeo, M., Pérez, N., Castro, M., Madrigal, J.D., Rubio-Marcos, F., Ramajo, L., Cavalieri, F.J., 2025. Performance evaluation of lead-free potassium sodium niobate-based piezoceramics for ultrasonic motor design. Ceram. Int. S0272884225002366. https://doi.org/10.1016/j.ceramint.2025.01.209
Ding, W., Liu, Y., Shiotani, T., Wang, Q., Han, N., Xing, F., 2021. Cement-Based Piezoelectric Ceramic Composites for Sensing Elements: A Comprehensive State-of-the-Art Review. Sensors 21, 3230. https://doi.org/10.3390/s21093230
Dinh Trung, V., Le, P.-A., Natsuki, J., Zhao, W., Viet Bac Phung, T., Tan, J., Yang, W., Natsuki, T., 2024. Hydrovoltaic–piezoelectric hybridized device for microdroplet-pressure dual energy harvesting and piezo sensing. Chem. Eng. J. 496, 154164. https://doi.org/10.1016/j.cej.2024.154164
Dong, J., Cui, T., Zhang, D., Yang, L., He, X., Xiao, T., Li, C., Xing, S., Jiang, Y., Wang, H., 2025. Design and test of real-time monitoring system for maize entrainment loss based on piezoelectric signal classification. Measurement 242, 116050. https://doi.org/10.1016/j.measurement.2024.116050
Dong, K., Peng, X., Wang, Z.L., 2020. Fiber/Fabric-Based Piezoelectric and Triboelectric Nanogenerators for Flexible/Stretchable and Wearable Electronics and Artificial Intelligence. Adv. Mater. 32, 1902549. https://doi.org/10.1002/adma.201902549
Dong, W., Gao, S., Peng, S., Shi, L., Shah, S.P., Li, W., 2024. Graphene reinforced cement-based triboelectric nanogenerator for efficient energy harvesting in civil infrastructure. Nano Energy 131, 110380. https://doi.org/10.1016/j.nanoen.2024.110380
Du, C., Liu, P., Jin, C., Yang, H., Li, C., Jiang, G., Oeser, M., 2022. Evaluation of the piezoelectric and mechanical behaviors of asphalt pavements embedded with a piezoelectric energy harvester based on multiscale finite element simulations. Constr. Build. Mater. 333, 127438. https://doi.org/10.1016/j.conbuildmat.2022.127438
Du, Q., Diao, H., Niu, Z., Zhang, G., Shu, G., Jiao, K., 2015. Effect of cooling design on the characteristics and performance of thermoelectric generator used for internal combustion engine. Energy Convers. Manag. 101, 9–18. https://doi.org/10.1016/j.enconman.2015.05.036
Dubernet, M., Pitcher, M.J., Zaghrioui, M., Bah, M., Bustillo, J., Giovannelli, F., Monot-Laffez, I., 2022.

Synthesis routes for enhanced piezoelectric properties in spark plasma sintered Ta-doped KNN ceramics. J. Eur. Ceram. Soc. 42, 2188–2194. https://doi.org/10.1016/j.jeurceramsoc.2021.12.030

Duddi, M., Kocherla, A., Subramaniam, K.V.L., 2023. Evaluation of boundary and material influences on the dynamic electromechanical impedance response of the embedded PZT sensor in concrete. Sens. Actuators Phys. 361, 114575. https://doi.org/10.1016/j.sna.2023.114575

Dumoulin, C., Karaiskos, G., Sener, J.-Y., Deraemaeker, A., 2014. Online monitoring of cracking in concrete structures using embedded piezoelectric transducers. Smart Mater. Struct. 23, 115016. https://doi.org/10.1088/0964-1726/23/11/115016

Dwivedi, S., Pareek, T., Kumar, S., 2018. Structure, dielectric, and piezoelectric properties of $K_{0.5}$ $Na_{0.5}$ NbO_3 -based lead-free ceramics. RSC Adv. 8, 24286–24296. https://doi.org/10.1039/C8RA04038A

Eklund, K., Karttunen, A.J., 2025. Pyroelectric Properties of *A* -Site Ordered [$K_{0.5}$ $Na_{0.5}$]NbO_3 Perovskite Studied with Hybrid Density Functional Method. J. Phys. Chem. C 129, 16371–16379. https://doi.org/10.1021/acs.jpcc.5c04089

Elkelany, E.A., Mahmoud, A.E., Abd El-Fattah, Z.M., Farouk, M., Hassan, M.A., 2023. New insights into the effect of glass addition on the piezoelectric and thermal stability properties of (Ba0.85Ca0.15)(Ti0.9Zr0.1)O3 Pb-free ceramic by defect engineering of MPB. Ceram. Int. 49, 38305–38317. https://doi.org/10.1016/j.ceramint.2023.09.163

Emmanuel, M., 2023. 0.98[(Na(1–x)/2Smx/2Nb0.3TiO3)] + 0.02MnO2 Lead-free Ceramic System Design; An antiferroelectrics with Improved Relaxation Behavior. J. Alloys Compd. 960, 170740. https://doi.org/10.1016/j.jallcom.2023.170740

Fadhlina, H., Atiqah, A., Zainuddin, Z., 2022. A review on lithium doped lead-free piezoelectric materials. Mater. Today Commun. 33, 104835. https://doi.org/10.1016/j.mtcomm.2022.104835

Fang, J., Mao, S., Jiang, M., Zhou, C., Yu, H., Rao, G., Zhao, J., Han, J., Hou, L., Sun, K., Cheng, S., 2025. Enhanced piezoelectric properties and thermal stability of BiFeO3-BaTiO3-based ceramics with local structural heterogeneity. Ceram. Int. S0272884225007035. https://doi.org/10.1016/j.ceramint.2025.02.038

Fasquelle, D., Mascot, M., Sama, N., Remiens, D., Carru, J.-C., 2015. Lead-free piezoelectric thin films for RoHS devices. Sens. Actuators Phys. 229, 30–35. https://doi.org/10.1016/j.sna.2015.02.009

Feng, Y., Wu, J., Chi, Q., Li, W., Yu, Y., Fei, W., 2020. Defects and Aliovalent Doping Engineering in Electroceramics. Chem. Rev. 120, 1710–1787. https://doi.org/10.1021/acs.chemrev.9b00507

Firoozi, Ali Akbar, Firoozi, Ali Asghar, Alashker, Y., Ahmad, S., 2024. Advancing civil engineering: The transformative impact of neuromorphic computing on infrastructure resilience and sustainability. Results Eng. 24, 103487. https://doi.org/10.1016/j.rineng.2024.103487

Fu, R., Zhong, X., Xiao, C., Lin, J., Guan, Y., Tian, Y., Zhou, Z., Tan, G., Hu, H., Zhou, L., Ning, C., 2023. A stretchable, biocompatible, and self-powered hydrogel multichannel wireless sensor system based on piezoelectric barium titanate nanoparticles for health monitoring. Nano Energy 114, 108617. https://doi.org/10.1016/j.nanoen.2023.108617

Gao, S., Li, P., Qu, J., Li, W., Zhai, J., Wang, F., Hao, J., Fu, P., Pan, Z., Bai, W., 2023. Crystallographic texture and phase structure induced excellent piezoelectric performance in KNN-based ceramics. J. Am. Ceram. Soc. 106, 3481–3490. https://doi.org/10.1111/jace.19013

Gao, T., Mo, M., Chen, N., Chen, Q., Lang, R., Wang, D., Tan, Z., Xing, J., Zhu, J., 2024. Enhanced comprehensive energy storage properties of lead-free KNN based ceramics through composition

optimization strategy. Chem. Eng. J. 500, 157560. https://doi.org/10.1016/j.cej.2024.157560

Gao, Ziyang, Wang, J., Liu, Z., Song, X., Ding, G., Ye, F., Ye, J., Wu, X., 2024. Encapsulation structure and in-situ embedding test and model study of a new type of road piezoelectric energy collector. Energy Build. 314, 114312. https://doi.org/10.1016/j.enbuild.2024.114312

Gao, Ziyan, Zhou, Y., Zhang, J., Foroughi, J., Peng, S., Baughman, R.H., Wang, Z.L., Wang, C.H., 2024. Advanced Energy Harvesters and Energy Storage for Powering Wearable and Implantable Medical Devices. Adv. Mater. 2404492. https://doi.org/10.1002/adma.202404492

Ge, H., Quezada, J.C., Houerou, V.L., Chazallon, C., 2022. Multiscale analysis of tire and asphalt pavement interaction via coupling FEM–DEM simulation. Eng. Struct. 256, 113925. https://doi.org/10.1016/j.engstruct.2022.113925

Ge, H., Quezada, J.C., Le Houerou, V., Chazallon, C., 2023. Three-dimensional FEM–DEM coupling simulation for analysis of asphalt mixture responses under rolling tire loads. Constr. Build. Mater. 369, 130615. https://doi.org/10.1016/j.conbuildmat.2023.130615

Gonçalves, J.P.C., Ambrósio, J.A.C., 2005. Road Vehicle Modeling Requirements for Optimization of Ride and Handling. Multibody Syst. Dyn. 13, 3–23. https://doi.org/10.1007/s11044-005-2528-5

Gong, S., Lu, Y., Yin, J., Levin, A., Cheng, W., 2024. Materials-Driven Soft Wearable Bioelectronics for Connected Healthcare. Chem. Rev. 124, 455–553. https://doi.org/10.1021/acs.chemrev.3c00502

Gong, Z., Miao, Y., Lantieri, C., 2024a. Review of Research on Tire–Pavement Contact Behavior. Coatings 14, 157. https://doi.org/10.3390/coatings14020157

Gong, Z., Miao, Y., Lantieri, C., 2024b. Review of Research on Tire–Pavement Contact Behavior. Coatings 14, 157. https://doi.org/10.3390/coatings14020157

Graham, S.A., Dudem, B., Mule, A.R., Patnam, H., Yu, J.S., 2019. Engineering squandered cotton into eco-benign microarchitectured triboelectric films for sustainable and highly efficient mechanical energy harvesting. Nano Energy 61, 505–516. https://doi.org/10.1016/j.nanoen.2019.04.081

Gu, L., Poddar, S., Lin, Y., Long, Z., Zhang, D., Zhang, Q., Shu, L., Qiu, X., Kam, M., Javey, A., Fan, Z., 2020. A biomimetic eye with a hemispherical perovskite nanowire array retina. Nature 581, 278–282. https://doi.org/10.1038/s41586-020-2285-x

Gu, W., Yang, B., Li, D., Shang, X., Zhou, Z., Guo, J., 2023. Accelerated design of lead-free high-performance piezoelectric ceramics with high accuracy via machine learning. J. Adv. Ceram. 12, 1389–1405. https://doi.org/10.26599/JAC.2023.9220762

Guan, X., Shi, H., Xu, D., Zhang, B., Wei, J., Chen, J., 2024. The exploration and practice of low-altitude airspace flight service and traffic management in China. Green Energy Intell. Transp. 3, 100149. https://doi.org/10.1016/j.geits.2024.100149

Guan, X., Xu, B., Gong, J., 2020. Hierarchically architected polydopamine modified BaTiO3@P(VDF-TrFE) nanocomposite fiber mats for flexible piezoelectric nanogenerators and self-powered sensors. Nano Energy 70, 104516. https://doi.org/10.1016/j.nanoen.2020.104516

Guo, L., Lu, Q., 2017. Potentials of piezoelectric and thermoelectric technologies for harvesting energy from pavements. Renew. Sustain. Energy Rev. 72, 761–773. https://doi.org/10.1016/j.rser.2017.01.090

Guo, L., Wang, H., Soares, L., Lu, Q., Brito, L., 2022. Multi-physics modelling of piezoelectric pavement system for energy harvesting under traffic loading. Int. J. Pavement Eng. 23, 3647–3661. https://doi.org/10.1080/10298436.2021.1913591

Habib, M., Ahmad, P., Akram, F., Kebaili, I., Rahman, A., Din, I.U., Javid Iqbal, M., Kim, M.-H., Lee, S., Uddin Khandaker, M., Goo Yeo, H., Karoui, A., Song, T.K., 2022. High and temperature-insensitive piezoelectric performance in the lead-free Sm-doped BiFeO3–BaTiO3 ceramics with high Curie temperature. Ceram. Int. 48, 26608–26617. https://doi.org/10.1016/j.ceramint.2022.05.355

Hamza, M., Kanwal, Q., Hussain, M.I., Peng, W., Wang, B., Liu, Z., Liu, C., Chen, Z., 2025. 3D printing of high-performance Ag/BaTiO3 ceramic-polymer piezoelectric sensors for biomedical applications. Chem. Eng. J. 523, 168848. https://doi.org/10.1016/j.cej.2025.168848

He, H., Huang, J., Zhao, Q., Tan, Q., Zang, X., 2025. Self-powered asphalt-based sensors for smart roads. Nano Energy 134, 110525. https://doi.org/10.1016/j.nanoen.2024.110525

He, H., Li, R., Yang, Q., Pei, J., Guo, F., 2021. Analysis of the Tire-Pavement Contact Stress Characteristics during Vehicle Maneuvering. KSCE J. Civ. Eng. 25, 2451–2463. https://doi.org/10.1007/s12205-021-1306-0

He, J., Li, J., Liu, C., Wang, C., Zhang, Y., Wen, C., Xue, D., Cao, J., Su, Y., Qiao, L., Bai, Y., 2021. Machine learning identified materials descriptors for ferroelectricity. Acta Mater. 209, 116815. https://doi.org/10.1016/j.actamat.2021.116815

He, J., Wang, J., Jiao, Y., Wang, B., Mu, Y., Liu, M., Sun, C., Liu, D., Yang, W., Wu, F., 2025. First-principles study of optical band gap modulation in CaTiO3-doped KNN lead-free ceramics. Ceram. Int. S0272884225009381. https://doi.org/10.1016/j.ceramint.2025.02.255

He, M., Du, W., Feng, Y., Li, S., Wang, W., Zhang, X., Yu, A., Wan, L., Zhai, J., 2021. Flexible and stretchable triboelectric nanogenerator fabric for biomechanical energy harvesting and self-powered dual-mode human motion monitoring. Nano Energy 86, 106058. https://doi.org/10.1016/j.nanoen.2021.106058

Herrera-Pérez, G., Solís-Canto, O., Ornelas-Gutiérrez, C., Canche-Tello, J., Hurtado-Macías, A., 2023. The effect of charged defects on the local effective piezo-electric response for the polycrystalline lead-free BCZT bulk ceramic versus thin film. Phys. B Condens. Matter 661, 414946. https://doi.org/10.1016/j.physb.2023.414946

Hirose, B., Imai, T., Ikeda, K., Tsuda, E., Yamauchi, R., Abe, T., Hisahara, S., 2025. A new method to evaluate staircase phenomenon in skeletal muscle using piezoelectric sensor. Clin. Neurophysiol. Pract. 10, 1–9. https://doi.org/10.1016/j.cnp.2024.12.002

Ho, C.K., Robinson, A., Miller, D.R., Davis, M.J., 2005. Overview of Sensors and Needs for Environmental Monitoring. Sensors 5, 4–37. https://doi.org/10.3390/s5010004

Horchidan, N., Ciomaga, C.E., Frunza, R.C., Capiani, C., Galassi, C., Mitoseriu, L., 2016. A comparative study of hard/soft PZT-based ceramic composites. Ceram. Int. 42, 9125–9132. https://doi.org/10.1016/j.ceramint.2016.02.179

Htet, C.S., Manjón-Sanz, A.M., Liu, J., Babori, C., Barati, M., Marlton, F.P., Daniel, L., Jørgensen, M.R.V., Pramanick, A., 2024. Local structural mechanism for enhanced energy storage properties in heterovalent doped NaNbO3 ceramics. J. Eur. Ceram. Soc. 44, 1597–1609. https://doi.org/10.1016/j.jeurceramsoc.2023.10.072

Hu, D., Pan, Z., Zhang, X., Ye, H., He, Z., Wang, M., Xing, S., Zhai, J., Fu, Q., Liu, J., 2020. Greatly enhanced discharge energy density and efficiency of novel relaxation ferroelectric BNT–BKT-based ceramics. J. Mater. Chem. C 8, 591–601. https://doi.org/10.1039/C9TC05528B

Hu, D., Yao, M., Fan, Y., Ma, C., Fan, M., Liu, M., 2019. Strategies to achieve high performance piezoelectric nanogenerators. Nano Energy 55, 288–304.

https://doi.org/10.1016/j.nanoen.2018.10.053
Hu, H., Huang, M., Wang, B., Zhang, D., Tan, T., Yan, K., Wu, D., 2024. Multi-iteration active learning for the composition design of potassium–sodium niobate ceramics with enhanced piezoelectric coefficient. Ceram. Int. 50, 54536–54546. https://doi.org/10.1016/j.ceramint.2024.10.312
Huan, Y., Wang, Xinjian, Yang, W., Hou, L., Zheng, M., Wei, T., Wang, Xiaohui, 2022. Optimizing energy harvesting performance by tailoring ferroelectric/relaxor behavior in KNN-based piezoceramics. J. Adv. Ceram. 11, 935–944. https://doi.org/10.1007/s40145-022-0587-1
Huang, L., Liu, C., Huang, Z., Chen, W., Wang, H., Wang, S., 2023. Simultaneous recovery of valuable metals W, Co, Ta, and Nb from tungsten leaching residue by sodium-based slag refining. Miner. Eng. 203, 108334. https://doi.org/10.1016/j.mineng.2023.108334
Huang, M., Wang, B., Wei, Y., Wang, F., Zhu, K., Yan, K., 2025. Large electrostrain originated from heterogeneous structure in composite piezoelectric ceramics. J. Eur. Ceram. Soc. 45, 117091. https://doi.org/10.1016/j.jeurceramsoc.2024.117091
Huang, Y., Zheng, T., Wu, J., 2024. KNN composite ceramics with superior pyroelectric performance for self-powered thermal detector. Nano Energy 131, 110184. https://doi.org/10.1016/j.nanoen.2024.110184
Hugo, F., Kennedy, T.W., 1985. Surface cracking of asphalt mixtures in Southern Africa (With discussion), in: Association of Asphalt Paving Technologists Proc.
Huo, X., Wang, F., Zhang, T., Zhang, M., Guo, M., 2023. A dispersed polycrystalline phase boundary constructed in CaZrO3 modified KNN based ceramics with both excellent piezoelectric properties and thermal stability. Ceram. Int. 49, 15751–15760. https://doi.org/10.1016/j.ceramint.2023.01.169
Ibn-Mohammed, T., Koh, S.C.L., Reaney, I.M., Acquaye, A., Wang, D., Taylor, S., Genovese, A., 2016. Integrated hybrid life cycle assessment and supply chain environmental profile evaluations of lead-based (lead zirconate titanate) versus lead-free (potassium sodium niobate) piezoelectric ceramics. Energy Environ. Sci. 9, 3495–3520. https://doi.org/10.1039/c6ee02429g
Izadi, N., 2011. Bio-inspired MEMS aquatic flow sensor arrays (PhD). University of Twente, Enschede, The Netherlands. https://doi.org/10.3990/1.9789036531405
Ji, J., Tian, C., Tang, H., Song, H., Zhou, Y., Zhang, S., Sun, J., Tan, H., Zhang, H., Jin, L., Liu, J., Liu, G., Yan, Y., 2025. Achieve high dielectric energy storage efficiency and good temperature stability within a wide range by high-entropy induced relaxor enhancement strategy in NBT-based ceramics. Chem. Eng. J. 522, 167823. https://doi.org/10.1016/j.cej.2025.167823
Ji, W., Fang, B., Zhao, X., Zhang, S., Lu, X., Ding, J., 2019. Enhancing electrical properties of high-Curie temperature piezoelectric ceramics BNT-PZT and their mechanism. Curr. Appl. Phys. 19, 1367–1373. https://doi.org/10.1016/j.cap.2019.09.002
Jiang, X., Lu, D., Yin, B., Leng, Z., 2024. Advancing carbon nanomaterials-engineered self-sensing cement composites for structural health monitoring: A state-of-the-art review. J. Build. Eng. 87, 109129. https://doi.org/10.1016/j.jobe.2024.109129
Jin, R.H., Guo, Y.Q., Jain, A., Shi, L.N., Ren, Z.H., Chen, F.G., Wang, Y.G., 2025. Giant energy storage density, high efficiency and excellent stability achieved in lead-free KNN-based ceramic via a composition optimization strategy. Mater. Res. Bull. 184, 113232. https://doi.org/10.1016/j.materresbull.2024.113232
Julphunthong, P., Wiwatrojanagul, P., Tiantong, P., Bongkarn, T., Rianyoi, R., Potong, R., 2025. Development and evaluation of KNLNTS-cement composites for use as piezoelectric sensors

in structural health monitoring applications. Results Eng. 25, 104526. https://doi.org/10.1016/j.rineng.2025.104526

Jung, Y.H., Pham, T.X., Issa, D., Wang, H.S., Lee, J.H., Chung, M., Lee, B.-Y., Kim, G., Yoo, C.D., Lee, K.J., 2022. Deep learning-based noise robust flexible piezoelectric acoustic sensors for speech processing. Nano Energy 101, 107610. https://doi.org/10.1016/j.nanoen.2022.107610

Kalyani, A.K., Brajesh, K., Senyshyn, A., Ranjan, R., 2014. Orthorhombic-tetragonal phase coexistence and enhanced piezo-response at room temperature in Zr, Sn, and Hf modified BaTiO3. Appl. Phys. Lett. 104, 252906. https://doi.org/10.1063/1.4885516

Kaur, R., Kaur, A., Sharma, V., Singh, A., Singh, L., Singh, M., 2017. An investigation on structural and magnetically induced ferroelectricity in (1−x)Pb(Zr0.45Ti0.55)O3-(x)SmFeO3 solid solutions. J. Alloys Compd. 710, 850–857. https://doi.org/10.1016/j.jallcom.2017.03.271

Kee, S.-H., Zhu, J., 2013. Using piezoelectric sensors for ultrasonic pulse velocity measurements in concrete. Smart Mater. Struct. 22, 115016. https://doi.org/10.1088/0964-1726/22/11/115016

Khan, S., Riaz, S., Arshad, F., Azhar, M., Ahmad, N., Noor, H., Atiq, S., Naseem, S., 2022. Role of Ca doping on oxygen vacancy production in modulating dielectric, ferroelectric and magnetic polarization in BaTiO3 thin films. J. Mater. Res. Technol. 16, 993–1007. https://doi.org/10.1016/j.jmrt.2021.11.148

Khan, S.A., Ahmed, T., Park, H.W., Habib, M., Song, T.K., Wang, C., Mun, S.U., Kim, Y., Kim, M.-H., Lee, S., 2024. Effects of B- and A/B-sites Codoping on lattice distortion and defect concentration for high electromechanical response of lead-free piezoelectrics. Acta Mater. 278, 120262. https://doi.org/10.1016/j.actamat.2024.120262

Khan, Y., Thielens, A., Muin, S., Ting, J., Baumbauer, C., Arias, A.C., 2020. A New Frontier of Printed Electronics: Flexible Hybrid Electronics. Adv. Mater. 32, 1905279. https://doi.org/10.1002/adma.201905279

Khanna, P.K., Hornbostel, B., Grimme, R., Schäfer, W., Dorner, J., 2004. Miniature pressure sensor and micromachined actuator structure based on low-temperature-cofired ceramics and piezoelectric material. Mater. Chem. Phys. 87, 173–178. https://doi.org/10.1016/j.matchemphys.2004.05.021

Kim, S., Azad, M.M., Song, J., Kim, H., 2023. Delamination Detection Framework for the Imbalanced Dataset in Laminated Composite Using Wasserstein Generative Adversarial Network-Based Data Augmentation. Appl. Sci. 13, 11837. https://doi.org/10.3390/app132111837

Kim, S.-B., Shin, J., Kim, H.-S., Lee, D.-G., Park, J.-C., Baik, J.M., Kim, S.Y., Kang, C.-Y., Choi, W., Song, H.-C., Hur, S., 2023. A synergetic effect of piezoelectric energy harvester to enhance thermoelectric Power: An effective hybrid energy harvesting method. Energy Convers. Manag. 298, 117774. https://doi.org/10.1016/j.enconman.2023.117774

Kim, Y., Park, S., Kim, B.-K., Park, W.-J., Kim, H.J., 2021. Laser lift-off of polyimide thin-film from glass carrier using DPSS laser pulses of top-hat square profiles. Opt. Laser Technol. 142, 107245. https://doi.org/10.1016/j.optlastec.2021.107245

Kong, J., Chu, R., Mao, M., Yu, H., Liu, J., Sun, Y., Ge, X., Jin, Z., Huang, W., Hu, N., Wang, Y., 2025. A 3-in-1 wearable and implantable biopatch for integrated in-body energy harvesting, sensing, and self-powered diabetic wound treatments. Nano Energy 136, 110743. https://doi.org/10.1016/j.nanoen.2025.110743

Kraftfahrt-Bundesamt, “Traffic flow information.,” 2025.

Krupska-Klimczak, M., Jankowska-Sumara, I., Sowa, S., 2023. Positive and Negative Electrocaloric Effect in soft- and hard-doped commercial PZT ceramics. Ceram. Int. 49, 36807–36815.

https://doi.org/10.1016/j.ceramint.2023.09.010
Kumar, Amit, Kumari, S., Aditi, Bhawna, Kumar, V., Aggarwal, S., Goyal, P.K., Tomar, A., Kumar, Ashok, Arya, A., 2025. Enhanced T with improved electrical properties by construction of phase boundary in Li+-modified KNN-based piezoelectric ceramics. J. Alloys Compd. 1015, 178831. https://doi.org/10.1016/j.jallcom.2025.178831
Kumari, P., Lal, M., Kumar, S., Rai, R., Singh, A., Karpinsky, D.V., Bdikin, I., 2019. Comprehensive investigation of structural, dielectric and local piezoelectric properties of KNN ceramics. J. Adv. Dielectr. 09, 1950016. https://doi.org/10.1142/s2010135x19500164
Kunimatsu, M., 2001. Measurement of dynamic pressure using piezoelectric sensors at extremely low temperatures. JSAE Rev. 22, 553–558. https://doi.org/10.1016/S0389-4304(01)00133-3
Kuo, C.-C., Yin, Y.-T., 2025. Deposition of binary Cr Zr thin-film metallic glass using Cr/Zr dual-cathode high-power impulse magnetron sputtering. Surf. Coat. Technol. 498, 131867. https://doi.org/10.1016/j.surfcoat.2025.131867
Lam, V.T., Lam, N.H., Van, D.Q., Thoan, N.H., Trung, N.N., Dung, D.D., 2025. Role of substitution Zr-site on the electronic structure and magnetic properties of BaTiO3 materials: A first principles calculation. Comput. Theor. Chem. 1243, 114989. https://doi.org/10.1016/j.comptc.2024.114989
Lang, R., Chen, Qifan, Gao, T., Zhu, J., Xing, J., Chen, Qiang, 2024. BaTiO3-based lead-free relaxor ferroelectric ceramics for high energy storage. J. Eur. Ceram. Soc. 44, 3916–3925. https://doi.org/10.1016/j.jeurceramsoc.2024.01.004
Langat, R.K., Deng, W., De Luycker, E., Cantarel, A., Rakotondrabe, M., 2025. In-situ piezoelectric sensors for structural health monitoring with machine learning integration. Mechatronics 106, 103297. https://doi.org/10.1016/j.mechatronics.2025.103297
Leal-Perez, J.E., Flores-Valenzuela, J., Almaral-Sánchez, J.L., Olive-Méndez, S.F., Cruz, M.P., Auciello, O., Hurtado-Macias, A., 2023. Piezoelectric and nanomechanical properties of lead-free K0.1Na0.9Nb0.97Sb0.03O3 (KNNS) thin films grown by radio frequency sputtering. J. Eur. Ceram. Soc. 43, 7431–7439. https://doi.org/10.1016/j.jeurceramsoc.2023.07.064
Lee, D., Yoon, A., Jang, S.Y., Yoon, J.-G., Chung, J.-S., Kim, M., Scott, J.F., Noh, T.W., 2011. Giant Flexoelectric Effect in Ferroelectric Epitaxial Thin Films. Phys. Rev. Lett. 107, 057602. https://doi.org/10.1103/PhysRevLett.107.057602
Lee, J., Jang, K., 2024. Characterizing driver behavior using naturalistic driving data. Accid. Anal. Prev. 208, 107779. https://doi.org/10.1016/j.aap.2024.107779
Lee, S.-H., Esashi, M., 2004. Characteristics on PZT (Pb(ZrxTi1−x)O3) films for piezoelectric angular rate sensor. Sens. Actuators Phys. 114, 88–92. https://doi.org/10.1016/j.sna.2004.03.010
Leng, W., Liu, Y., Li, S., Geng, X., Liu, L., Du, Y., 2024. Optimizing electromechanical properties of KNN-based piezoelectric ceramics through regulation of lattice distortion. Ceram. Int. 50, 32922–32929. https://doi.org/10.1016/j.ceramint.2024.06.104
Li, C., Lei, S., Xiao, Q., Pan, Y., Han, X., Chen, Q., 2023. An experimental and numerical investigation on the load transfer efficiency of a novel prefabricated cement concrete pavement. Structures 53, 963–972. https://doi.org/10.1016/j.istruc.2023.04.130
Li, D., Wang, Z., Liang, Z., Zhu, F., Xu, T., Cui, X., Zhao, P., 2022. Analyzing Rice Grain Collision Behavior and Monitoring Mathematical Model Development for Grain Loss Sensors. Agriculture 12, 839. https://doi.org/10.3390/agriculture12060839
Li, D.-X., Li, Z., Shen, Z.-Y., Shi, X., Zeng, X., Zhang, Y., Luo, W., Song, F., Wu, C.-F., 2025. Defect

engineering induced phase competition in BNT-based relaxor ferroelectrics for dielectric energy storage. J. Materiomics 11, 100979. https://doi.org/10.1016/j.jmat.2024.100979

Li, G., Chen, X., Guo, H., Liu, L., Li, S., Zhu, Y., Wei, Y., 2025. Insulation properties of polypropylene and silicone rubber modified by barium strontium titanate and interfacial charge accumulation properties. Compos. Sci. Technol. 261, 111037. https://doi.org/10.1016/j.compscitech.2025.111037

Li, J., Li, F., Li, C., Yang, G., Xu, Z., Zhang, S., 2015. Evidences of grain boundary capacitance effect on the colossal dielectric permittivity in (Nb + In) co-doped TiO2 ceramics. Sci. Rep. 5, 8295. https://doi.org/10.1038/srep08295

Li, J., Li, H., Lin, J., Lu, Y., Qin, J., Gao, J., Zhang, X., Zhao, Q., 2025. Multilayer polyimide nanofibrous aerogels for efficient thermal insulation and piezoelectric sensor. Chem. Eng. J. 507, 160807. https://doi.org/10.1016/j.cej.2025.160807

Li, J., Liang, Z., Zhu, F., Liu, C., 2022. Optimum of Grain Loss Sensors by Analyzing Effects of Grain Collision Attitude on Signal Characteristics. Electronics 11, 3187. https://doi.org/10.3390/electronics11193187

Li, P., Zhai, J., Shen, B., Zhang, S., Li, X., Zhu, F., Zhang, X., 2018. Ultrahigh Piezoelectric Properties in Textured (K,Na)NbO_3 -Based Lead-Free Ceramics. Adv. Mater. 30, 1705171. https://doi.org/10.1002/adma.201705171

Li, Q., Zhang, M.-H., Zhu, Z.-X., Wang, K., Zhou, J.-S., Yao, F.-Z., Li, J.-F., 2017. Poling engineering of (K,Na)NbO_3 -based lead-free piezoceramics with orthorhombic–tetragonal coexisting phases. J. Mater. Chem. C 5, 549–556. https://doi.org/10.1039/C6TC04723H

Li, R., Zhao, P., Wang, Y., 2024. Enhanced piezoelectric properties of KNN ceramics through stress bending between KNN and ZnO particles. Ceram. Int. 50, 45557–45565. https://doi.org/10.1016/j.ceramint.2024.08.393

Li, T., Lou, X., Ke, X., Cheng, S., Mi, S., Wang, X., Shi, J., Liu, X., Dong, G., Fan, H., Wang, Y., Tan, X., 2017. Giant strain with low hysteresis in A-site-deficient (Bi0.5Na0.5)TiO3-based lead-free piezoceramics. Acta Mater. 128, 337–344. https://doi.org/10.1016/j.actamat.2017.02.037

Li, Y., Dai, X., Bai, Y., Liu, Y., Wang, Y., Liu, O., Yan, F., Tang, Z., Zhang, X., Deng, X., 2017. Electroactive $BaTiO_3$ nanoparticle-functionalized fibrous scaffolds enhance osteogenic differentiation of mesenchymal stem cells. Int. J. Nanomedicine Volume 12, 4007–4018. https://doi.org/10.2147/IJN.S135605

Li, Y., Hou, Y., Cui, T., Tan, D.S., Xu, Y., Zhang, D., Qiao, M., Xiong, L., 2024. Classifying grain and impurity to assess maize cleaning loss using time–frequency images of vibro-piezoelectric signals coupling machine learning. Comput. Electron. Agric. 227, 109583. https://doi.org/10.1016/j.compag.2024.109583

Li, Y., Pu, Z., Liu, P., Qian, T., Hu, Q., Zhang, J., Wang, Y., 2025. Efficient predictive control strategy for mitigating the overlap of EV charging demand and residential load based on distributed renewable energy. Renew. Energy 240, 122154. https://doi.org/10.1016/j.renene.2024.122154

Li, Z., Lei, N., Long, D., Wang, W., 2024. The structure and electronic properties closely related to piezoelectricity of BaZrO3-modified K0.5Na0.5NbO3 lead-free ceramics: First-principle study. Ceram. Int. 50, 15513–15519. https://doi.org/10.1016/j.ceramint.2024.02.029

Liang, M., Wang, J., Su, L., Xin, X., Chen, Z., Zhang, Y., Jiao, Y., Luan, X., Chen, L., Yao, Z., 2024. Versatile Lamellar Wrap-Structured PVDF/PZT/CNTs Piezoelectric Sensor for Road Traffic Information Sensing, Monitoring, and Energy Harvesting. Chem. Eng. J. 497, 154554.

https://doi.org/10.1016/j.cej.2024.154554
Liang, X., Zhang, X., Hu, Z., Sun, Q., Liu, M., Gu, P., Yang, X., Huang, J., Zu, G., 2024. Broad-Range-Response Battery-Type All-in-one Self-Powered Stretchable Pressure-Sensitive Electronic Skin. Small 20, 2305925. https://doi.org/10.1002/smll.202305925
Lin, L., Zhang, Y.-F., Liu, H.-B., Meng, J.-H., Chen, W.-H., Wang, X.-D., 2019. A new configuration design of thermoelectric cooler driven by thermoelectric generator. Appl. Therm. Eng. 160, 114087. https://doi.org/10.1016/j.applthermaleng.2019.114087
Liu, C., Wei, Y., 2022. Experimental study on interface performance between implantable cement-based sensor and matrix concrete. Constr. Build. Mater. 345, 128316. https://doi.org/10.1016/j.conbuildmat.2022.128316
Liu, H., Zhou, C., Chen, J., Cheng, S., Yuan, C., Xu, J., Li, Q., Zhao, J., Rao, G., 2024. Simultaneously realizing high piezoelectricity and thermal stability in BNT-based ceramics via integrating layered diffusion and thermal treatment. Sens. Actuators Phys. 365, 114874. https://doi.org/10.1016/j.sna.2023.114874
Liu, J., Jiang, X., Huang, W., He, Y., Yang, Z., 2022. A novel approach for navigational safety evaluation of inland waterway ships under uncertain environment. Transp. Saf. Environ. 4, tdab029. https://doi.org/10.1093/tse/tdab029
Liu, P., Ravee, V., Wang, D., Oeser, M., 2018. Study of the influence of pavement unevenness on the mechanical response of asphalt pavement by means of the finite element method. J. Traffic Transp. Eng. Engl. Ed. 5, 169–180. https://doi.org/10.1016/j.jtte.2017.12.001
Liu, P., Zhao, Q., Yang, H., Wang, D., Oeser, M., Wang, L., Tan, Y., 2019. Numerical Study on Influence of Piezoelectric Energy Harvester on Asphalt Pavement Structural Responses. J. Mater. Civ. Eng. 31, 04019008. https://doi.org/10.1061/(ASCE)MT.1943-5533.0002640
Liu, Q., Zhang, Y., Gao, J., Zhou, Z., Wang, H., Wang, K., Zhang, X., Li, L., Li, J.-F., 2018. High-performance lead-free piezoelectrics with local structural heterogeneity. Energy Environ. Sci. 11, 3531–3539. https://doi.org/10.1039/C8EE02758G
Liu, W., Li, N., Wang, Y., Xu, H., Wang, J., Yang, J., 2015. Preparation and properties of 3–1 type PZT ceramics by a self-organization method. J. Eur. Ceram. Soc. 35, 3467–3474. https://doi.org/10.1016/j.jeurceramsoc.2015.06.007
Liu, Y., Wu, C., Qiu, X., Xu, P., Xiang, Y., Xuan, F.-Z., 2024. Air-cavity-free multiphase composite piezoelectrets with high piezoelectric sensitivity for self-powered flexible sensors and energy harvesters. Appl. Mater. Today 37, 102096. https://doi.org/10.1016/j.apmt.2024.102096
Liu, Z., Zhang, Q., Cai, W., Chen, G., Li, X., Gao, R., Deng, X., Fu, C., 2023. Achieving enhanced ferroelectricity and piezoelectric responses in 〈0 0 1〉-textured KNN-BCZT ceramics with BaTiO3 microplates as template. Mater. Lett. 351, 135098. https://doi.org/10.1016/j.matlet.2023.135098
Lone, S.A., Lim, K.C., Kaswan, K., Chatterjee, S., Fan, K.-P., Choi, D., Lee, S., Zhang, H., Cheng, J., Lin, Z.-H., 2022. Recent advancements for improving the performance of triboelectric nanogenerator devices. Nano Energy 99, 107318. https://doi.org/10.1016/j.nanoen.2022.107318
Lu, D., Yang, W., Wu, H., Zhou, T., 2025. Research on simplified tire finite element modeling and simulation method. Proc. Inst. Mech. Eng. Part J. Automob. Eng. 239, 447–463. https://doi.org/10.1177/09544070231207528
Lu, G., Zhao, Y., Zhao, R., Hao, J., Bai, W., Li, P., Li, W., Zhai, J., 2024. High performance (K,Na)NbO3-

based textured ceramics for piezoelectric energy harvesting. Ceram. Int. 50, 54869–54877. https://doi.org/10.1016/j.ceramint.2024.10.279

Lv, Z., Zhao, D., Sun, Q., Liu, C., Cheng, H., Yang, F., Zhang, B., 2023. Simultaneous extraction of uranium and niobium from a low-grade natural betafite ore. High Temp. Mater. Process. 42, 20220260. https://doi.org/10.1515/htmp-2022-0260

Ma, B., Wu, X., Zhao, C., Lin, C., Gao, M., Sa, B., Sun, Z., 2023. An interpretable machine learning strategy for pursuing high piezoelectric coefficients in (K0.5Na0.5)NbO3-based ceramics. Npj Comput. Mater. 9, 229. https://doi.org/10.1038/s41524-023-01187-1

Ma, M., Chen, L., Peng, L., Peng, Y., Bi, J., Gao, D., Wu, J., 2022. Carrier and oxygen vacancy engineering of aliovalent ion modified BiFeO3 and their gas sensing properties. Sens. Actuators B Chem. 370, 132400. https://doi.org/10.1016/j.snb.2022.132400

Ma, X., Dong, Z., Dong, Y., 2022. Toward Asphalt Pavement Health Monitoring With Built-In Sensors: A Novel Application to Real-Time Modulus Evaluation. IEEE Trans. Intell. Transp. Syst. 23, 22040–22052. https://doi.org/10.1109/TITS.2021.3102252

Ma, Y., Jiang, Q., Dai, J., Li, Y., 2022. Influence of PZT volume fraction, composite thickness and cement matrix on the performance of d15 shear mode 1–3 connectivity cement-based piezoelectric composites. Constr. Build. Mater. 329, 127190. https://doi.org/10.1016/j.conbuildmat.2022.127190

Mahanty, B., Kumar Ghosh, S., Lee, D.-W., 2024. Advancements in polymer nanofiber-based piezoelectric nanogenerators: Revolutionizing self-powered wearable electronics and biomedical applications. Chem. Eng. J. 495, 153481. https://doi.org/10.1016/j.cej.2024.153481

Maharjan, P., Bhatta, T., Salauddin, M., Rasel, M.S., Rahman, M.T., Rana, S.M.S., Park, J.Y., 2020. A human skin-inspired self-powered flex sensor with thermally embossed microstructured triboelectric layers for sign language interpretation. Nano Energy 76, 105071. https://doi.org/10.1016/j.nanoen.2020.105071

Maizal Hairi, N.I.I., Md Ralib, A.A., Nordin, A.N., Mohamad Yunos, M.F.A., Ming, L.L., Tung, L.H., Samsudin, Z., 2024. Recent advance in using eco-friendly carbon-based conductive ink for printed strain sensor: A review. Clean. Mater. 12, 100248. https://doi.org/10.1016/j.clema.2024.100248

Malekloo, A., Ozer, E., AlHamaydeh, M., Girolami, M., 2022. Machine learning and structural health monitoring overview with emerging technology and high-dimensional data source highlights. Struct. Health Monit. 21, 1906–1955. https://doi.org/10.1177/14759217211036880

Malič, B., Koruza, J., Hreščak, J., Bernard, J., Wang, K., Fisher, J., Benčan, A., 2015. Sintering of Lead-Free Piezoelectric Sodium Potassium Niobate Ceramics. Materials 8, 8117–8146. https://doi.org/10.3390/ma8125449

Mangi, M.A., Elahi, H., Ali, A., Jabbar, H., Aqeel, A.B., Farrukh, A., Bibi, S., Altabey, W.A., Kouritem, S.A., Noori, M., 2025. Applications of piezoelectric-based sensors, actuators, and energy harvesters. Sens. Actuators Rep. 9, 100302. https://doi.org/10.1016/j.snr.2025.100302

Maria Joseph Raj, N.P., Khandelwal, G., Kim, S.-J., 2021. 0.8BNT–0.2BKT ferroelectric-based multimode energy harvester for self-powered body motion sensors. Nano Energy 83, 105848. https://doi.org/10.1016/j.nanoen.2021.105848

Megdich, A., Habibi, M., Laperrière, L., Li, Z., Abdin, Y., 2024. Advanced 3D-printed PVDF/BT piezoelectric energy harvester with a bio-inspired 3D structure for a self-powered smart mouse. Nano Energy 128, 109876. https://doi.org/10.1016/j.nanoen.2024.109876

Mercedes-benz, Technical parameters for mercedes-benz bus, 2025.

Mercedes-benz, “Truck information.,” 2025.

Mi, Q., Dong, Y., Ge, D., Xie, S., Tian, Y., Zou, F., Yu, H.-Y., Tam, K.C., 2024. Scalable manufacture of efficient, highly stable, and compact 3D imitation skin-based elastic triboelectric nanogenerator for energy harvesting and self-powered sensing. Nano Energy 131, 110283. https://doi.org/10.1016/j.nanoen.2024.110283

Mir, N., Khan, S.A., Kul, A., Sahin, O., Lachemi, M., Sahmaran, M., Koç, M., 2022. Life cycle assessment of binary recycled ceramic tile and recycled brick waste-based geopolymers. Clean. Mater. 5, 100116. https://doi.org/10.1016/j.clema.2022.100116

Mo, C., Xu, W., Xi, K., Zheng, M., Hou, Y., 2025. Robust lead-free capacitor ceramics for harsh electronic service environments with directional phase structure coupled with defect engineering design. Chem. Eng. J. 522, 167853. https://doi.org/10.1016/j.cej.2025.167853

Monazami, M., Sharma, A., Gupta, R., 2022. Evaluating performance of carbon fiber-reinforced pavement with embedded sensors using destructive and non-destructive testing. Case Stud. Constr. Mater. 17, e01460. https://doi.org/10.1016/j.cscm.2022.e01460

Mondal, S., Poddar, S., Bhattacharjee, S., Maiti, S., Banerjee, A., Chattopadhyay, K.K., 2023. Lead free halide perovskite embedded PVDF based efficient mechanical energy harvester: Self-driven respiratory sensor. Nano Energy 115, 108689. https://doi.org/10.1016/j.nanoen.2023.108689

Moriana, A.D., Zhang, S., 2018. Lead-free textured piezoceramics using tape casting: A review. J. Materiomics 4, 277–303. https://doi.org/10.1016/j.jmat.2018.09.006

Mourya, A., Mazumdar, B., Sinha, S.K., 2021. Application of CeO2-MWCNTs nanocomposite for heavy metal ion detection in aqueous solutions by electrochemical technique. Clean. Mater. 2, 100021. https://doi.org/10.1016/j.clema.2021.100021

Mugheri, A.Q., Ali, K., Sangah, A.A., Daudpoto, M.R., Laghari, M.Y., Mugheri, A.A., 2024. Effort in speeding up high-performance, stable, high-rate thin-film electronics based for ultra-long life with enhanced electrochemical performance for next generation technology. J. Energy Storage 77, 109863. https://doi.org/10.1016/j.est.2023.109863

Nallagatla, V.R., Maier, C., Glettler, J., Feteira, A., Reichmann, K., Deluca, M., 2024. Synergistic homovalent and heterovalent substitution effects on piezoelectric and relaxor behavior in lead-free BaTiO3 ceramics. J. Eur. Ceram. Soc. 44, 116689. https://doi.org/10.1016/j.jeurceramsoc.2024.116689

Nanda, A., Fox, J.J., Fanton, M., Yan, Y., Priya, S., Poudel, B., Lanagan, M.T., 2025a. Enhanced Electrical and Thermal Stability in (K,Na)NbO_3 Ceramics via Compositional Engineering. ACS Appl. Eng. Mater. 3, 2933–2942. https://doi.org/10.1021/acsaenm.5c00470

Nanda, A., Karan, S.K., Kunwar, S., Yan, Y., Fanton, M., Priya, S., Lanagan, M., Poudel, B., 2025b. Textured Lead-Free Ceramic with High Thermal Stability and Electrical Quality Factor. Small 21, e05193. https://doi.org/10.1002/smll.202505193

Narayanan, A., Duddi, M., Kocherla, A., Kvl, S., 2024. Smart and autonomous monitoring of cracking in concrete structures with PZT sensor array-based hybrid sensing. Structures 68, 107178. https://doi.org/10.1016/j.istruc.2024.107178

Nath, D., Ankit, Neog, D.R., Gautam, S.S., 2024. Application of Machine Learning and Deep Learning in Finite Element Analysis: A Comprehensive Review. Arch. Comput. Methods Eng. 31, 2945–2984. https://doi.org/10.1007/s11831-024-10063-0

Nie, X., Jing, R., Yang, Y., Chen, F., Meng, M., Yan, Yangxi, Alikin, D., Shur, V., Yan, Yan, Zhang, L.,

Jin, L., 2025. Synergistic enhancement of energy storage performance in BNT-based ceramics through the co-doping of multiple A-site ions. Chem. Eng. J. 507, 160500. https://doi.org/10.1016/j.cej.2025.160500

North Rhine-Westphalia Federal Energy Agency, n.d.

Oh, Y., Kwon, D.-S., Eun, Y., Kim, W., Kim, M.-O., Ko, H.-J., Kang, S.G., Kim, J., 2019. Flexible Energy Harvester with Piezoelectric and Thermoelectric Hybrid Mechanisms for Sustainable Harvesting. Int. J. Precis. Eng. Manuf.-Green Technol. 6, 691–698. https://doi.org/10.1007/s40684-019-00132-2

Organisation Technique Européenne du Pneumatique et de la Jante ADF, "Golf technical specifications, 2025.

Osinaga, S., Difeo, M., Febbo, M., Castro, M., Ramajo, L., Machado, S., 2024. Energy harvesting using lead-free multilayer piezo stacks based on 0.95(Bi0.5Na0.5)TiO3-0.05(BaTiO3) piezoceramics through the addition of ZrO2. Ceram. Int. 50, 19259–19268. https://doi.org/10.1016/j.ceramint.2024.03.025

Oubahdou, Y., Wallace, E.-R., Reynaud, P., Picoux, B., Dopeux, J., Petit, C., Nélias, D., 2021. Effect of the tire – Pavement contact at the surface layer when the tire is tilted in bend. Constr. Build. Mater. 305, 124765. https://doi.org/10.1016/j.conbuildmat.2021.124765

Pan, H.H., Guan, J.-C., 2022. Stress and strain behavior monitoring of concrete through electromechanical impedance using piezoelectric cement sensor and PZT sensor. Constr. Build. Mater. 324, 126685. https://doi.org/10.1016/j.conbuildmat.2022.126685

Pan, X., Wu, Y., Wang, Y., Zhou, G., Cai, H., 2024. Mechanical energy harvesting based on the piezoelectric materials: Recent advances and future perspectives. Chem. Eng. J. 497, 154249. https://doi.org/10.1016/j.cej.2024.154249

Panda, P.K., Sahoo, B., 2015. PZT to Lead Free Piezo Ceramics: A Review. Ferroelectrics 474, 128–143. https://doi.org/10.1080/00150193.2015.997146

Panpho, P., Charoonsuk, T., Vittayakorn, N., Bongkarn, T., Sumang, R., 2024. Flexible hybrid piezo/triboelectric energy harvester based on a lead-free BNT-BT-KNN ceramic-polymer composite film. Ceram. Int. 50, 52041–52050. https://doi.org/10.1016/j.ceramint.2024.03.208

Park, D.-W., Papagiannakis, A.T., Kim, I.T., 2014. Analysis of dynamic vehicle loads using vehicle pavement interaction model. KSCE J. Civ. Eng. 18, 2085–2092. https://doi.org/10.1007/s12205-014-0602-3

Park, J., Lee, Youngoh, Hong, J., Lee, Youngsu, Ha, M., Jung, Y., Lim, H., Kim, S.Y., Ko, H., 2014. Tactile-Direction-Sensitive and Stretchable Electronic Skins Based on Human-Skin-Inspired Interlocked Microstructures. ACS Nano 8, 12020–12029. https://doi.org/10.1021/nn505953t

Pascale, A., Guarnaccia, C., Macedo, E., Fernandes, P., Miranda, A.I., Sargento, S., Coelho, M.C., 2023. Road traffic noise monitoring in a Smart City: Sensor and Model-Based approach. Transp. Res. Part Transp. Environ. 125, 103979. https://doi.org/10.1016/j.trd.2023.103979

Pearson, K., 1895. VII. Note on regression and inheritance in the case of two parents. Proc. R. Soc. Lond. 58, 240–242. https://doi.org/10.1098/rspl.1895.0041

Peng, L., Gao, X., Liu, X., Jiang, M., 2024. Synergism optimization of ferroelectric phase-transition temperature and piezoelectric properties of KNN-based ceramics by chemical composition regulation. Mater. Today Commun. 38, 108214. https://doi.org/10.1016/j.mtcomm.2024.108214

Peng, X., Liu, J., Tan, Y., Mo, R., Zhang, Y., 2022. A CuO thin film type sensor via inkjet printing

technology with high reproducibility for ppb-level formaldehyde detection. Sens. Actuators B Chem. 362, 131775. https://doi.org/10.1016/j.snb.2022.131775

Pinheiro, E., Deivarajan, T., 2019. A Concise Review Encircling Lead Free Porous Piezoelectric Ceramics. Acta Phys. Pol. A 136, 555–565. https://doi.org/10.12693/APhysPolA.136.555

Pirim, F., Atik, A.C., Yüksel, M.B., Yılmaz, A.M., Uğur, M.B., Tunalı, S., Batu, A., Aslan, M.K., Özer, M.B., Külah, H., 2024. Multichannel multimodal piezoelectric middle ear implant concept based on MEMS technology for next-generation fully implantable cochlear implant applications. Biosens. Bioelectron. X 18, 100471. https://doi.org/10.1016/j.biosx.2024.100471

Plati, C., 2019. Sustainability factors in pavement materials, design, and preservation strategies: A literature review. Constr. Build. Mater. 211, 539–555. https://doi.org/10.1016/j.conbuildmat.2019.03.242

Platt, S.R., Farritor, S., Haider, H., 2005. On Low-Frequency Electric Power Generation With PZT Ceramics. IEEEASME Trans. Mechatron. 10, 240–252. https://doi.org/10.1109/TMECH.2005.844704

Pongampai, S., Pakawanit, P., Charoonsuk, T., Vittayakorn, N., 2021. Low-cost fabrication of the highly efficient triboelectric nanogenerator by designing a 3D multi-layer origami structure combined with self-charged pumping module. Nano Energy 90, 106629. https://doi.org/10.1016/j.nanoen.2021.106629

Poompiew, N., Pattananuwat, P., Aumnate, C., Román, A.J., Osswald, T.A., Potiyaraj, P., 2023. 3D printable resin/carbon nanotube composites for wearable strain sensors: Enhancing mechanical and electrical properties. J. Sci. Adv. Mater. Devices 8, 100546. https://doi.org/10.1016/j.jsamd.2023.100546

Qi, X., Ren, P., Wang, F., Tong, X., Wang, X., Wan, Y., 2024. Enhanced temperature stability of piezoelectric properties and electrostrain via a diffused phase transition in LaMnO3-doped (K, Na)NbO3-based ceramics. J. Alloys Compd. 989, 174342. https://doi.org/10.1016/j.jallcom.2024.174342

Qian, K., Xia, H., Xia, Y., 2024. A self-powered interface circuit for piezoelectric and photovoltaic energy extracting. Microelectron. J. 154, 106466. https://doi.org/10.1016/j.mejo.2024.106466

Qiao, Y., Wang, L., Zhang, D., Li, Z., Zhang, M., Jin, L., Zhao, M., Yan, Y., 2024. Effects of heterovalent ions doping-induced oxygen octahedral distortion and defect chemical change on piezoelectric characteristics and thermal stability of PHT-PIN ceramics. Chem. Eng. J. 485, 150145. https://doi.org/10.1016/j.cej.2024.150145

Qiu, J., Liu, S., Guo, Y., Yang, L., Jiang, K., 2025. Anisotropic flexible pressure/strain sensors: Recent advances, fabrication techniques, and future prospects. Chem. Eng. J. 504, 158799. https://doi.org/10.1016/j.cej.2024.158799

Qiu, Q., Xu, Y., Liu, X., Song, H., Zhou, Y., Lv, Z., Zhang, S., Sun, J., Du, H., Liu, G., Yan, Y., 2025. Achieving ultrahigh strain in lead-free piezoelectric ceramics of Bi0.5(Na0.41K0.09)TiO3-(Ba0.5Sr0.5)HfO3 via A/B-site co-doping strategy. Ceram. Int. S027288422503490X. https://doi.org/10.1016/j.ceramint.2025.07.243

Ragni, D., Canestrari, F., Allou, F., Petit, C., Millien, A., 2020. Shear-Torque Fatigue Performance of Geogrid-Reinforced Asphalt Interlayers. Sustainability 12, 4381. https://doi.org/10.3390/su12114381

Rahman, M.A., Hasan, Z., Islam, J., Das, D.K., Chowdhury, F.I., Khandaker, M.U., Zabed, H.M., Bradley, D.A., Osman, H., Ullah, Md.H., 2023. Tailoring the Properties of Bulk $BaTiO_3$ Based

Perovskites by Heteroatom-Doping towards Multifunctional Applications: A Review. ECS J. Solid State Sci. Technol. 12, 103015. https://doi.org/10.1149/2162-8777/ad00da

Rahsepar, H., Hayati, R., Javadpour, S., 2024. Evaluation of the dielectric, and piezoelectric properties and optimizing the figure of merit of the 0–3 KNN-0.8ZnO/PVDF-HFP piezoelectric composite by the Taguchi method. J. Alloys Compd. 1006, 176373. https://doi.org/10.1016/j.jallcom.2024.176373

Rao, J., Hagare, D., Tao, Z., 2024. Upcycling of End-of-Life-Vehicle (ELV) plastics as a replacement for natural fine aggregate in concrete. Resour. Conserv. Recycl. Adv. 21, 200210. https://doi.org/10.1016/j.rcradv.2024.200210

Rathod, V.T., 2019. A Review of Electric Impedance Matching Techniques for Piezoelectric Sensors, Actuators and Transducers. Electronics 8, 169. https://doi.org/10.3390/electronics8020169

Ray, T.R., Choi, J., Bandodkar, A.J., Krishnan, S., Gutruf, P., Tian, L., Ghaffari, R., Rogers, J.A., 2019. Bio-Integrated Wearable Systems: A Comprehensive Review. Chem. Rev. 119, 5461–5533. https://doi.org/10.1021/acs.chemrev.8b00573

Rinke, P., Janotti, A., Scheffler, M., Van De Walle, C.G., 2009. Defect Formation Energies without the Band-Gap Problem: Combining Density-Functional Theory and the G W Approach for the Silicon Self-Interstitial. Phys. Rev. Lett. 102, 026402. https://doi.org/10.1103/PhysRevLett.102.026402

Rocha, H.R.O., Roukos, R., Abou Dargham, S., Romanos, J., Chaumont, D., Silva, J.A.L., Wörtche, H., 2024. Optimizing a machine learning design of dielectric properties in lead-free piezoelectric ceramics. Mater. Des. 243, 113053. https://doi.org/10.1016/j.matdes.2024.113053

Rödel, J., Webber, K.G., Dittmer, R., Jo, W., Kimura, M., Damjanovic, D., 2015. Transferring lead-free piezoelectric ceramics into application. J. Eur. Ceram. Soc. 35, 1659–1681. https://doi.org/10.1016/j.jeurceramsoc.2014.12.013

Rosental, T., Gatani, G., Pirri, C.F., Ricciardi, C., Savraeva, D., Bunin, A., Moshkovitz-Douvdevany, M.Y., Magdassi, S., Stassi, S., 2024. Unlocking enhanced piezoelectric performance through 3D printing of particle-free ceramic piezoelectric complex structures and metamaterials. Chem. Eng. J. 499, 156189. https://doi.org/10.1016/j.cej.2024.156189

Rosental, T., Mizrahi, S., Kamyshny, A., Magdassi, S., 2021. Particle-free compositions for printing dense 3D ceramic structures by digital light processing. Virtual Phys. Prototyp. 16, 255–266. https://doi.org/10.1080/17452759.2021.1922121

Rosso, J.M., Volnistem, E.A., Santos, I.A., Bonadio, T.G.M., Freitas, V.F., 2022. Lead-free NaNbO3-based ferroelectric perovskites and their polar polymer-ceramic composites: Fundamentals and potentials for electronic and biomedical applications. Ceram. Int. 48, 19527–19541. https://doi.org/10.1016/j.ceramint.2022.04.089

Rotan, M., Zhuk, M., Boughton, P., Glaum, J., 2021. The influence of low-temperature sterilization procedures on piezoelectric ceramics for biomedical applications. Open Ceram. 7, 100143. https://doi.org/10.1016/j.oceram.2021.100143

Saber, M., Hosseini-Toudeshky, H., 2024. Interphase elastic modulus characterization in glass/epoxy composite using combined peridynamics and experimental method. J. Reinf. Plast. Compos. 43, 30–53. https://doi.org/10.1177/07316844231155091

Safaei, M., Sodano, H.A., Anton, S.R., 2019. A review of energy harvesting using piezoelectric materials: state-of-the-art a decade later (2008–2018). Smart Mater. Struct. 28, 113001. https://doi.org/10.1088/1361-665X/ab36e4

Sajal, Md.S.R., Ehsan, Md.T., Vaidyanathan, R., Wang, S., Aziz, T., Mamun, K.A.A., 2020. Telemonitoring Parkinson's disease using machine learning by combining tremor and voice analysis. Brain Inform. 7, 12. https://doi.org/10.1186/s40708-020-00113-1

San Emeterio, J.L., Ramos, A., Ruiz, A., 2003. On the Measurement of the Electromechanical Coupling Coefficient k_t Using Different Characteristic Frequencies. Ferroelectrics 293, 331–339. https://doi.org/10.1080/714040583

Sato, T., Takagi, S., Deledda, S., Hauback, B.C., Orimo, S., 2016. Extending the applicability of the Goldschmidt tolerance factor to arbitrary ionic compounds. Sci. Rep. 6, 23592. https://doi.org/10.1038/srep23592

Savakus, H.P., Klicker, K.A., Newnham, R.E., 1981. PZT-epoxy piezoelectric transducers: A simplified fabrication procedure. Mater. Res. Bull. 16, 677–680. https://doi.org/10.1016/0025-5408(81)90267-1

Sayagués, M.J., Otero, A., Santiago-Andrades, L., Poyato, R., Monzón, M., Paz, R., Gotor, F.J., Moriche, R., 2024. Fine-grained BCZT piezoelectric ceramics by combining high-energy mechanochemical synthesis and hot-press sintering. J. Alloys Compd. 1007, 176453. https://doi.org/10.1016/j.jallcom.2024.176453

Sethuraman, B.D., Veluswamy, P., Ikeda, H., Mohandos, S., 2025. Isovalent doping of Cu2+ induced elastic strain on cobalt spinel oxides for enhancing room temperature thermoelectric application. J. Alloys Compd. 1010, 177513. https://doi.org/10.1016/j.jallcom.2024.177513

Sharafi, A., Chen, C., Sun, J.-Q., Fortier, M.-O., 2024. Carbon footprint of piezoelectrics from multi-layer PZT stacks to piezoelectric energy harvesting systems in roads. iScience 27, 110786. https://doi.org/10.1016/j.isci.2024.110786

Sharma, B., Sharma, A., Gupta, R., Chowdhuri, A., Verma, M., Tomar, M., 2024. Flexible sheets of lead free KNN-PVDF composite: A sustainable pyroelectric energy harvester. Ceram. Int. 50, 46982–46992. https://doi.org/10.1016/j.ceramint.2024.09.049

Sharma, J.P., Kumar, D., 2024. Structural, dielectric properties and Raman scattering of Li-modified K0.5Na0.5NbO3 (KNN) lead-free ceramics. Mater. Sci. Eng. B 301, 117182. https://doi.org/10.1016/j.mseb.2024.117182

Sharma, M.K., Lin, Y.-J., Lin, C.-K., Nahak, B.K., Huang, C.-J., Chen, C.C., Wang, Y.-L., Lin, Z.-H., 2025. Self-powered AlGaN/GaN HEMT-based sensor integrated with rotational TENG for comprehensive water quality analysis. Nano Energy 135, 110637. https://doi.org/10.1016/j.nanoen.2024.110637

Shen, Z., Guo, J., Gao, X., Xuan, W., Zhang, J., Wang, D., Cheng, J., Zhang, S., Chen, J., 2025. Advancing piezoelectricity and excellent thermal stability: -textured 0.75BF–0.25BT lead-free ceramics for high temperature applications. J. Materiomics 11, 100946. https://doi.org/10.1016/j.jmat.2024.100946

Shi, C., Ma, J., Wu, J., Wang, X., Miao, F., Huang, Y., Chen, K., Wu, W., Wu, B., 2020. Coexistence of excellent piezoelectric performance and high Curie temperature in KNN-based lead-free piezoelectric ceramics. J. Alloys Compd. 846, 156245. https://doi.org/10.1016/j.jallcom.2020.156245

Shi, N., Jia, H., Zhang, J., Lu, P., Cai, C., Zhang, Y., Zhang, L., He, N., Zhu, W., Cai, Y., Feng, Z., Wang, T., 2024. Accurate expression of neck motion signal by piezoelectric sensor data analysis. Chin. Chem. Lett. 35, 109302. https://doi.org/10.1016/j.cclet.2023.109302

Shi, W., Li, J., Liu, S., Zhou, L., Lai, Y., Zhu, Y., Zhang, H., Qi, T., 2025. Efficient separation and

comprehensive recovery of rare earth, bismuth and iron by one-step extraction and two-step stripping. J. Ind. Eng. Chem. 141, 145–153. https://doi.org/10.1016/j.jiec.2024.06.024

Shi, X.M., Cai, C.S., 2009. Simulation of Dynamic Effects of Vehicles on Pavement Using a 3D Interaction Model. J. Transp. Eng. 135, 736–744. https://doi.org/10.1061/(ASCE)TE.1943-5436.0000045

Shrout, T.R., Zhang, S.J., 2007. Lead-free piezoelectric ceramics: Alternatives for PZT? J. Electroceramics 19, 113–126. https://doi.org/10.1007/s10832-007-9047-0

Shu, X., Kang, M., Zhou, Y., Cui, X., Nie, J., Zhao, Z., Zhang, Y., 2025. Triboelectric nanogenerators based self-powered visualized weight sensor with high accuracy and real time. Nano Energy 135, 110624. https://doi.org/10.1016/j.nanoen.2024.110624

Siddiqui, S., Kim, D.-I., Roh, E., Duy, L.T., Trung, T.Q., Nguyen, M.T., Lee, N.-E., 2016. A durable and stable piezoelectric nanogenerator with nanocomposite nanofibers embedded in an elastomer under high loading for a self-powered sensor system. Nano Energy 30, 434–442. https://doi.org/10.1016/j.nanoen.2016.10.034

Singh, A., Chatterjee, R., Gupta, V., 2021. Proposing a phase diagram for BNT-BKT-KNN and finding a new MPB and large strain region in the system. Ferroelectrics 577, 161–169. https://doi.org/10.1080/00150193.2021.1916359

Singh, N.B., Mahato, D.K. (Eds.), 2025. PIEZOELECTRIC MATERIALS: design and applications. JENNY STANFORD PUB, S.l. https://doi.org/10.1201/9781003598978

Soin, N., Shah, T.H., Anand, S.C., Geng, J., Pornwannachai, W., Mandal, P., Reid, D., Sharma, S., Hadimani, R.L., Bayramol, D.V., Siores, E., 2014. Novel “3-D spacer” all fibre piezoelectric textiles for energy harvesting applications. Energy Env. Sci 7, 1670–1679. https://doi.org/10.1039/C3EE43987A

Sol-Sánchez, M., Castillo-Mingorance, J.M., Moreno-Navarro, F., Mattinzioli, T., Rubio-Gámez, M.C., 2021. Piezoelectric-sensored sustainable pads for smart railway traffic and track state monitoring: Full-scale laboratory tests. Constr. Build. Mater. 301, 124324. https://doi.org/10.1016/j.conbuildmat.2021.124324

Soman, J., O’Neal, C.B., 2011. Fabrication and Testing of a PZT Strain Sensor for Soil Applications. IEEE Sens. J. 11, 78–85. https://doi.org/10.1109/jsen.2010.2050585

Song, G.J., Cho, J.Y., Kim, K.-B., Ahn, J.H., Song, Y., Hwang, W., Hong, S.D., Sung, T.H., 2019. Development of a pavement block piezoelectric energy harvester for self-powered walkway applications. Appl. Energy 256, 113916. https://doi.org/10.1016/j.apenergy.2019.113916

Souza, L.F.B., Teixeira, K.F., Cadore-Rodrigues, A.C., Binotto, F.S., Daudt, N.D.F., Valandro, L.F., Moraes, R.R., Özcan, M., Pereira, G.K.R., 2025. Optimizing adhesion protocols between 3D-printed ceramic-containing composite and resin cement. Int. J. Adhes. Adhes. 140, 104003. https://doi.org/10.1016/j.ijadhadh.2025.104003

Spurling, R.J., Marakovits, M.T., Hossain, A., Almishal, S.S.I., Perini, S.E., Lanagan, M.T., Maria, J.-P., 2024. Temperature-dependent dielectric behavior of A 6 B 2O17 (A = Zr, Hf; B = Nb, Ta) phases. Appl. Phys. Lett. 125, 092901. https://doi.org/10.1063/5.0219964

Srikanth, K.S., Patel, S., Steiner, S., Vaish, R., 2018. Pyroelectric signals in (Ba,Ca)TiO3-xBa(Sn,Ti)O3 ceramics: A viable alternative for lead-based ceramics. Scr. Mater. 146, 146–149. https://doi.org/10.1016/j.scriptamat.2017.11.027

Srikanth, K.S., Singh, V.P., Vaish, R., 2017. Enhanced pyroelectric figure of merits of porous BaSn0.05Ti0.95O3 ceramics. J. Eur. Ceram. Soc. 37, 3943–3950.

https://doi.org/10.1016/j.jeurceramsoc.2017.05.015
Subohi, O., Kumar, G.S., Malik, M.M., Kurchania, R., 2016. Effect of B-site isovalent doping on electrical and ferroelectric properties of lead free bismuth titanate ceramics. J. Phys. Chem. Solids 93, 91–99. https://doi.org/10.1016/j.jpcs.2016.02.019
Sudha, G., Karunagaran, N., 2024. Composition controlled microstructural, photoluminescent, dielectric and ferroelectric properties of Dy3+ and isovalent ion doped NBBT binary electro-optic ceramic systems. Opt. Mater. 150, 115191. https://doi.org/10.1016/j.optmat.2024.115191
Sun, C., Wang, H., Liu, J., Shang, G., 2015. Finite Element Analysis of Vehicle Load Effect on Harvesting Energy Properties of a Piezoelectric Unit. Energy Power Eng. 07, 500–508. https://doi.org/10.4236/epe.2015.710047
Sun, D., Lu, Y., Karaki, T., 2023. Review of the applications of 3D printing technology in the field of piezoelectric ceramics. Resour. Chem. Mater. 2, 128–142. https://doi.org/10.1016/j.recm.2023.02.001
Sun, Y., Du, X., Yao, H., Chen, J., Zeng, Y., 2023. Ultra-high d anti-chiral negative Poisson's ratio BaTiO3 ceramics fabricated by vat photopolymerization 3D printing. J. Alloys Compd. 968, 172054. https://doi.org/10.1016/j.jallcom.2023.172054
Swett, L., Mallick, R.B., Humphrey, D.N., 2008. A study of temperature and traffic load related response in different layers in an instrumented flexible pavement. Int. J. Pavement Eng. 9, 303–316. https://doi.org/10.1080/10298430701576117
Tadaki, D., Ma, T., Yamamiya, S., Matsumoto, S., Imai, Y., Hirano-Iwata, A., Niwano, M., 2020. Piezoelectric PVDF-based sensors with high pressure sensitivity induced by chemical modification of electrode surfaces. Sens. Actuators Phys. 316, 112424. https://doi.org/10.1016/j.sna.2020.112424
Takenaka, T., Nagata, H., 2005. Current status and prospects of lead-free piezoelectric ceramics. J. Eur. Ceram. Soc. 25, 2693–2700. https://doi.org/10.1016/j.jeurceramsoc.2005.03.125
Talbourdet, A., Rault, F., Lemort, G., Cochrane, C., Devaux, E., Campagne, C., 2018. 3D interlock design 100% PVDF piezoelectric to improve energy harvesting. Smart Mater. Struct. 27, 075010. https://doi.org/10.1088/1361-665X/aab865
Taleb, S., Badillo, M., Flores-Ruiz, F.J., Acuautla, M., 2023. From synthesis to application: High-quality flexible piezoelectric sensors fabricated from tetragonal BaTiO3/ P(VDF-TrFE) composites. Sens. Actuators Phys. 361, 114585. https://doi.org/10.1016/j.sna.2023.114585
Tang, X., Xie, J., Xie, H., Zhang, H., 2022. Predictions of three-dimensional contact stresses of a radial truck tire under different driving modes. Adv. Mech. Eng. 14, 168781322210923. https://doi.org/10.1177/16878132221092346
Tao, H., Wu, J., 2016. Giant piezoelectric effect and high strain response in (1−x)(K0.45Na0.55)(Nb1Sb)O3 -xBi0.5Na0.5Zr1−Hf O3 lead-free ceramics. J. Eur. Ceram. Soc. 36, 1605–1612. https://doi.org/10.1016/j.jeurceramsoc.2016.01.043
Teka, A., Bairagi, S., Shahadat, Md., Joshi, M., Ziauddin Ahammad, Sk., Wazed Ali, S., 2018. Poly(vinylidene fluoride) (PVDF)/potassium sodium niobate (KNN)–based nanofibrous web: A unique nanogenerator for renewable energy harvesting and investigating the role of KNN nanostructures. Polym. Adv. Technol. 29, 2537–2544. https://doi.org/10.1002/pat.4365
Tian, Y., Ma, M., Li, S., Ma, X., Wu, H., Ji, X., Wang, J., Jing, Q., 2023. Visualizing sintering process and electrical properties of SnO2 doped K0.48Na0.52NbO3 piezoelectric ceramics. Ceram. Int. 49, 38270–38278. https://doi.org/10.1016/j.ceramint.2023.09.159

Tiantong, P., Bongkarn, T., Rianyoi, R., Julphunthong, P., 2022. Fabrication and characterisation of 0–3 KNLNTS piezoelectric ceramic/alite calcium sulfoaluminate cement composites. J. Mater. Res. Technol. 19, 1563–1577. https://doi.org/10.1016/j.jmrt.2022.05.136

Tielking, J.T., Roberts, F.L., 1987. Tire Contact Pressure and Its Effect on Pavement Strain. J. Transp. Eng. 113, 56–71. https://doi.org/10.1061/(ASCE)0733-947X(1987)113:1(56)

Tong, Y., Li, Y., Song, Q., Xu, Jie, Xu, X., Korzhik, M., Xu, Jun, Lebbou, K., Wu, Y., 2024. Effects of Zr4+ and Hf4+ co-doping on luminescence and scintillation properties of LuYAG:Pr3+ single crystals grown by micro-pulling-down technique. J. Rare Earths S1002072124000577. https://doi.org/10.1016/j.jre.2024.02.012

Trung, V.D., Le, P.-A., Natsuki, J., Zhao, W., Phung, T.V.B., Natsuki, T., 2024. Recent developments in droplet-based devices. Mater. Today Chem. 36, 101943. https://doi.org/10.1016/j.mtchem.2024.101943

Tsai, J.Z., Chen, C.J., Chen, W.Y., Liu, J.T., Liao, C.Y., Hsin, Y.M., 2009. A new PZT piezoelectric sensor for gravimetric applications using the resonance-frequency detection. Sens. Actuators B Chem. 139, 259–264. https://doi.org/10.1016/j.snb.2009.03.055

Van De Loo, M., Poyato, E.C., Díaz, J.A.R., 2025. Using solar energy for irrigation in large water distribution networks: A benchmark study about six irrigation systems in the south of Spain. Energy Nexus 17, 100386. https://doi.org/10.1016/j.nexus.2025.100386

Vaziri Sereshk, M.R., Esmaeili, M.H., 2015. A mesh generation procedure to simulate bimaterials. J. Comput. Appl. Mech. 46. https://doi.org/10.22059/jcamech.2015.55102

Venault, A., Lin, K.-H., Tang, S.-H., Dizon, G.V., Hsu, C.-H., Maggay, I.V.B., Chang, Y., 2020. Zwitterionic electrospun PVDF fibrous membranes with a well-controlled hydration for diabetic wound recovery. J. Membr. Sci. 598, 117648. https://doi.org/10.1016/j.memsci.2019.117648

Vittayakorn, N., Rujijanagul, G., Tan, X., He, H., Marquardt, M.A., Cann, D.P., 2006. Dielectric properties and morphotropic phase boundaries in the xPb(Zn1/3Nb2/3)O3−(1−x)Pb(Zr0.5Ti0.5O3 pseudo-binary system. J. Electroceramics 16, 141–149. https://doi.org/10.1007/s10832-006-4927-2

Wan, T., Ma, S., Liao, F., Fan, L., Chai, Y., 2022. Neuromorphic sensory computing. Sci. China Inf. Sci. 65, 141401. https://doi.org/10.1007/s11432-021-3336-8

Wang, B., Zhou, Z., Huang, M., Chen, X., Wang, F., Zhu, K., Yan, K., 2025. Effects of wide multiphase coexistence on the piezoelectricity of (K, Na)NbO3-based ceramics with superior temperature stability. Ceram. Int. https://doi.org/10.1016/j.ceramint.2025.05.245

Wang, C., Wang, S., Gao, Z., Wang, X., 2019. Applicability evaluation of embedded piezoelectric energy harvester applied in pavement structures. Appl. Energy 251, 113383. https://doi.org/10.1016/j.apenergy.2019.113383

Wang, C., Yu, G., Cao, H., Wang, S., Li, Y., 2020. Structure simulation optimization and test verification of piezoelectric energy harvester device for road. Sens. Actuators Phys. 315, 112322. https://doi.org/10.1016/j.sna.2020.112322

Wang, C., Zhang, R., Jing, Y., Cao, W., 2016. The effect of polymeric filler on poling behavior and thermal stability of 1-3 piezoelectric composites. J. Phys. Appl. Phys. 49, 025301. https://doi.org/10.1088/0022-3727/49/2/025301

Wang, F., Zhang, T., Guo, M., Zhang, M., 2022. Room temperature constructing rhombohedral-tetragonal phase boundary in novel (Bi, Na)(Zr, Ti)O3 modified (K, Na)(Nb, Sb)O3 ceramics: Phase structure, defect and piezoelectric performance. Ceram. Int. 48, 19954–19962.

https://doi.org/10.1016/j.ceramint.2022.03.270

Wang, H., Wang, R., Liu, Y., Gao, Q., Li, L., Cao, H., He, L., Tang, E., 2025. Predicting the impact depolarization behavior of PZT-5H based on machine learning. Measurement 240, 115625. https://doi.org/10.1016/j.measurement.2024.115625

Wang, H., Hu, Z., Guo, W., Zhu, H., Xing, Z., Wang, Haidou, Cai, Z., 2024. Effect of A and B-site ion doping on the structure and properties of KNN-based ceramic coatings. Ceram. Int. 50, 37809–37819. https://doi.org/10.1016/j.ceramint.2024.07.145

Wang, Jiao, Huang, Y., Guo, W., Xing, Z., Wang, H., Lu, Z., Zhang, Z., 2021. First-principles calculations of electronic and optical properties of A and B site substituted BaTiO3. Vacuum 193, 110530. https://doi.org/10.1016/j.vacuum.2021.110530

Wang, J., Xiao, F., Zhao, H., 2021. Thermoelectric, piezoelectric and photovoltaic harvesting technologies for pavement engineering. Renew. Sustain. Energy Rev. 151, 111522. https://doi.org/10.1016/j.rser.2021.111522

Wang, K., Li, J., 2010. Domain Engineering of Lead-Free Li-Modified (K,Na)NbO_3 Polycrystals with Highly Enhanced Piezoelectricity. Adv. Funct. Mater. 20, 1924–1929. https://doi.org/10.1002/adfm.201000284

Wang, P., Chen, X., Xu, Y., Lei, H., Zhao, X., Fang, Q., Shi, P., Lian, H., Liu, P., 2025. Unconventional photo-dielectric effect of Bi0.5Na0.5Ti0.98Nb0.02O3+δ lead-free ceramics: Enhanced dielectric constant with unchanged dielectric loss and low photoconductivity by light irradiation. J. Eur. Ceram. Soc. 45, 117238. https://doi.org/10.1016/j.jeurceramsoc.2025.117238

Wang, P., Pan, J., Wang, J., Shi, L., Wu, J., 2023. Coupled dynamic and piezoelectric response of RPEHs embedded in road under traffic load via multiscale finite element models. Smart Mater. Struct. 32, 105016. https://doi.org/10.1088/1361-665X/acf41f

Wang, P., Zhong, G., Xin, X., Xiao, F., Liang, M., Wang, C., Jiao, Y., Zhu, Y., Liu, S., Wang, H., 2022. Mechanical Response Analysis of Asphalt Pavement Structure with Embedded Sensor. Coatings 12, 1728. https://doi.org/10.3390/coatings12111728

Wang, Qian, Bian, L., He, S., Wang, N., Yang, B., Cao, W., 2024. Morphotropic phase boundary composition PNN-PZT ceramics and their outstanding electromechanical properties. J. Alloys Compd. 1002, 175249. https://doi.org/10.1016/j.jallcom.2024.175249

Wang, Qingping, Li, Z., Bowen, C., Courtney, C., Pan, M., Xu, Q., Chen, W., Fieldhouse, S., Wan, C., 2024. Enhanced buoyancy and propulsion in 3D printed swimming micro-robots based on a hydrophobic nano-fibrillated cellulose aerogel and porous lead-free piezoelectric ceramics. Nano Energy 131, 110254. https://doi.org/10.1016/j.nanoen.2024.110254

Wang, Q., Yang, J., Zhang, W., Khoie, R., Li, Y., Zhu, J., Chen, Z., 2009. Manufacture and Cytotoxicity of a Lead-free Piezoelectric Ceramic as a Bone Substitute—Consolidation of Porous Lithium Sodium Potassium Niobate by Cold Isostatic Pressing. Int. J. Oral Sci. 1, 99–104. https://doi.org/10.4248/ijos.09005

Wang, R., Tang, E., Yang, G., Han, Y., Chen, C., 2020. Electromechanical behaviors of soft and hard PZTs under different compressive stress pulses. Mech. Mater. 149, 103544. https://doi.org/10.1016/j.mechmat.2020.103544

Wang, W., Tang, X.-G., Jiang, Y.-P., Liu, Q.-X., Li, W.-H., Guo, X.-B., Tang, Z.-H., 2022. Phase evolution, dielectric, ferroelectric, and piezoelectric properties of Bi(Mg0.5Hf0.5)O3–modified BiFeO3–BaTiO3. Mater. Today Chem. 24, 100825. https://doi.org/10.1016/j.mtchem.2022.100825

Wang, Xinran, Wu, T., Gao, H., Zhou, D., Qi, H., Song, Y., Ye, S., Tran, N.-M.-A., Tan, H., Zhang, H., 2025. Enhancing the temperature stability of BF-BT-BCZT piezoelectric ceramics for high-temperature acceleration sensors. Ceram. Int. S0272884225013811. https://doi.org/10.1016/j.ceramint.2025.03.251

Wang, X., Yang, X., Huang, F., Yang, H., 2025. Enhanced in-situ piezoelectric properties and thermal stability of lead-free BiFeO3-BaTiO3 ceramics by local structural heterogeneity. Mater. Sci. Semicond. Process. 185, 108948. https://doi.org/10.1016/j.mssp.2024.108948

Wang, Y., Zhu, W., Deng, Y., Zhu, P., Yu, Y., Hu, S., Zhang, R., 2022. High-sensitivity self-powered temperature/pressure sensor based on flexible Bi-Te thermoelectric film and porous microconed elastomer. J. Mater. Sci. Technol. 103, 1–7. https://doi.org/10.1016/j.jmst.2021.07.008

Wang, Z.L., Wang, A.C., 2019. On the origin of contact-electrification. Mater. Today 30, 34–51. https://doi.org/10.1016/j.mattod.2019.05.016

Weber, N., Lee, Y.-S., Shanmugasundaram, S., Jaffe, M., Arinzeh, T.L., 2010. Characterization and in vitro cytocompatibility of piezoelectric electrospun scaffolds. Acta Biomater. 6, 3550–3556. https://doi.org/10.1016/j.actbio.2010.03.035

Wei, J., Hu, X., Li, Y., Bian, Z., Yan, K., Wu, D., 2025. 3D-printed piezoelectric ceramics with auxetic structure for high-performance sensing applications. Ceram. Int. 51, 2509–2517. https://doi.org/10.1016/j.ceramint.2024.11.234

Wei, X., Huang, C., Wei, N., Zhao, H., He, Y., Wu, X., 2019. The impact of freeze–thaw cycles and soil moisture content at freezing on runoff and soil loss. Land Degrad. Dev. 30, 515–523. https://doi.org/10.1002/ldr.3243

Wekalao, J., Baz, A., Patel, S.K., 2025. Design and analysis of high-sensitivity hormone sensor with KNN behavior prediction for healthcare and biomedical applications. Measurement 242, 116172. https://doi.org/10.1016/j.measurement.2024.116172

Wen, F., Zhang, Z., He, T., Lee, C., 2021. AI enabled sign language recognition and VR space bidirectional communication using triboelectric smart glove. Nat. Commun. 12, 5378. https://doi.org/10.1038/s41467-021-25637-w

Wittinanon, T., Rianyoi, R., Potong, R., Chaipanich, A., 2024. Effect of epoxy resin addition on the acoustic impedance, microstructure, dielectric and piezoelectric properties of 1–3 connectivity lead-free barium zirconate titanate ceramic cement-based composites. Ceram. Int. 50, 52144–52151. https://doi.org/10.1016/j.ceramint.2024.10.251

Wittinanon, T., Rianyoi, R., Potong, R., Pan, H.H., Chaipanich, A., 2023. Effect of epoxy resin and barium zirconate titanate contents on the piezoelectric properties of a 0–3 barium zirconate titanate-Portland cement composite with epoxy resin addition. Ceram. Int. 49, 18195–18202. https://doi.org/10.1016/j.ceramint.2023.02.188

Wu, Q., Zhang, F., Wang, B., Cheng, Z., Liu, S., Zhu, R., Huang, Y., Chang, J., Liu, Z., Dong, S., 2025. A lead-free KNN-based, co-fired multilayered piezoceramic energy harvester with a high output current and power. J. Materiomics 11, 100876. https://doi.org/10.1016/j.jmat.2024.04.003

Wu, S., Chen, P., Zhai, J., Shen, B., Li, P., Li, F., 2018. Enhanced piezoelectricity and energy storage performances of Fe-doped BNT–BKT–ST thin films. Ceram. Int. 44, 21289–21294. https://doi.org/10.1016/j.ceramint.2018.08.179

Wu, Y., Ma, Y., Zheng, H., Ramakrishna, S., 2021. Piezoelectric materials for flexible and wearable electronics: A review. Mater. Des. 211, 110164. https://doi.org/10.1016/j.matdes.2021.110164

Xia, X., Spadaccini, C.M., Greer, J.R., 2022. Responsive materials architected in space and time. Nat.

Rev. Mater. 7, 683–701. https://doi.org/10.1038/s41578-022-00450-z

Xiang, Z., Li, L., Lu, Z., Yu, X., Cao, Y., Tahir, M., Yao, Z., Song, Y., 2023. High-performance microcone-array flexible piezoelectric acoustic sensor based on multicomponent lead-free perovskite rods. Matter 6, 554–569. https://doi.org/10.1016/j.matt.2022.11.023

Xie, L., Mo, M., Chen, H., Xie, Y., Cheng, Y., Shu, C., Chen, Q., Xing, J., Tan, Z., Zhu, J., Zhu, H., 2022. Controlling the domain size to enhance the piezoelectricity of $BiFeO_3$ –$BaTiO_3$ *via* heterovalent doping. J. Mater. Chem. A 10, 22540–22550. https://doi.org/10.1039/D2TA06546K

Xin, Y., Tong, J., Hou, T., Liu, H., Cui, M., Song, X., Wang, Y., Lin, T., Wang, L., Wang, G., 2023. BiScO3-PbTiO3 nanofibers piezoelectric sensor for high-temperature pressure and vibration measurements. Measurement 212, 112694. https://doi.org/10.1016/j.measurement.2023.112694

Xing, J., Chen, H., Jiang, L., Zhao, C., Tan, Z., Huang, Y., Wu, B., Chen, Q., Xiao, D., Zhu, J., 2021. High performance BiFe0.9Co0.1O3 doped KNN-based lead-free ceramics for acoustic energy harvesting. Nano Energy 84, 105900. https://doi.org/10.1016/j.nanoen.2021.105900

Xu, D., Huang, S., Cheng, X., 2014. Electromechanical impedance spectra investigation of impedance-based PZT and cement/polymer based piezoelectric composite sensors. Constr. Build. Mater. 65, 543–550. https://doi.org/10.1016/j.conbuildmat.2014.05.035

Xu, H., Bai, G., Afzal, S., He, K., Xiao, Z., Yuan, S., Lu, Z., Zhu, Q., Xu, S., 2023. Multimodal energy harvesting and catalysis of piezoelectric nanosheets for efficient and round-the-clock wastewater treatment. J. Colloid Interface Sci. 651, 705–713. https://doi.org/10.1016/j.jcis.2023.07.173

Xu, L., Wei, C., Liang, Z., Chai, X., Li, Y., Liu, Q., 2019. Development of rapeseed cleaning loss monitoring system and experiments in a combine harvester. Biosyst. Eng. 178, 118–130. https://doi.org/10.1016/j.biosystemseng.2018.11.001

Xue, H., Jiang, L., Lu, G., Wu, J., 2023. Multilevel Structure Engineered Lead-Free Piezoceramics Enabling Breakthrough in Energy Harvesting Performance for Bioelectronics. Adv. Funct. Mater. 33, 2212110. https://doi.org/10.1002/adfm.202212110

Xun, B.-W., Wang, N., Zhang, B.-P., Chen, X.-Y., Zheng, Y.-Q., Jin, W.-S., Mao, R., Liang, K., 2019. Enhanced piezoelectric properties of 0.7BiFeO3-0.3BaTiO3 lead-free piezoceramics with high Curie temperature by optimizing Bi self-compensation. Ceram. Int. 45, 24382–24391. https://doi.org/10.1016/j.ceramint.2019.08.157

Yan, J., Su, Y., Armstrong, J.P.K., Gleadall, A., 2025. Additive Manufacturing of Neuromorphic Systems. Adv. Mater. 2504807. https://doi.org/10.1002/adma.202504807

Yan, M., Liu, S., Liu, Y., Xiao, Z., Yuan, X., Zhai, D., Zhou, K., Wang, Q., Zhang, D., Bowen, C., Zhang, Y., 2022. Flexible PVDF–TrFE Nanocomposites with Ag-decorated BCZT Heterostructures for Piezoelectric Nanogenerator Applications. ACS Appl. Mater. Interfaces 14, 53261–53273. https://doi.org/10.1021/acsami.2c15581

Yang, B., Peng, H., Zhang, Y., Shang, X., Zhou, T., Guo, J., 2023. Enhancing depolarization temperature and thermal stability of KNN-based piezoelectric ceramics through Li substitution and Al2O3 doping. Mater. Res. Bull. 158, 112077. https://doi.org/10.1016/j.materresbull.2022.112077

Yang, C., Chen, F., Sun, J., Chen, N., 2021. Boosted Mechanical Piezoelectric Energy Harvesting of Polyvinylidene Fluoride/Barium Titanate Composite Porous Foam Based on Three-Dimensional Printing and Foaming Technology. ACS Omega 6, 30769–30778. https://doi.org/10.1021/acsomega.1c04998

Yang, H., Guo, M., Wang, L., Hou, Y., Zhao, Q., Cao, D., Zhou, B., Wang, D., 2017. Investigation on the factors influencing the performance of piezoelectric energy harvester. Road Mater. Pavement Des. 18, 180–189. https://doi.org/10.1080/14680629.2017.1329873

Yang, H., Zhao, Q., Guo, X., Zhang, W., Liu, P., Wang, L., 2020. Numerical Analysis of Signal Response Characteristic of Piezoelectric Energy Harvesters Embedded in Pavement. Materials 13, 2770. https://doi.org/10.3390/ma13122770

Yang, H., Zhu, J., Wang, X., Luo, Q., Tan, H., Zhang, H., Xu, J., Chen, Q., 2024. Significantly enhancing high-temperature piezoelectric response and Tdr of BF-BT-based ceramics through multi-component optimization strategy. Chem. Eng. J. 498, 154975. https://doi.org/10.1016/j.cej.2024.154975

Yang, J., Hao, X., 2019. Electrocaloric effect and pyroelectric performance in (K,Na)NbO_3 -based lead-free ceramics. J. Am. Ceram. Soc. 102, 6817–6826. https://doi.org/10.1111/jace.16598

Yang, L., Liu, Qi, Li, M., Liu, Y., Li, X., Liu, Qiongzhen, Zhu, T., Lu, Y., Liu, X., Wang, D., 2025. A high-performance, flexible, and dual-modal humidity-piezoelectric sensor without mutual interference. Sens. Actuators B Chem. 423, 136778. https://doi.org/10.1016/j.snb.2024.136778

Yang, W., Li, P., Wu, S., Li, F., Shen, B., Zhai, J., 2020. Coexistence of excellent piezoelectric performance and thermal stability in KNN-based lead-free piezoelectric ceramics. Ceram. Int. 46, 1390–1395. https://doi.org/10.1016/j.ceramint.2019.09.102

Yang, Z., Zhou, S., Zu, J., Inman, D., 2018. High-Performance Piezoelectric Energy Harvesters and Their Applications. Joule 2, 642–697. https://doi.org/10.1016/j.joule.2018.03.011

Yao, F.-Z., Glaum, J., Wang, K., Jo, W., Rödel, J., Li, J.-F., 2013. Fatigue-free unipolar strain behavior in CaZrO3 and MnO2 co-modified (K,Na)NbO3-based lead-free piezoceramics. Appl. Phys. Lett. 103. https://doi.org/10.1063/1.4829150

Yao, G., Xu, L., Cheng, X., Li, Y., Huang, X., Guo, W., Liu, S., Wang, Z.L., Wu, H., 2020. Bioinspired Triboelectric Nanogenerators as Self-Powered Electronic Skin for Robotic Tactile Sensing. Adv. Funct. Mater. 30, 1907312. https://doi.org/10.1002/adfm.201907312

Ye, F., Ding, X., Ma, T., Ye, Z., Su, Z., Zhang, S., 2025. Application research of epoxy resin mortar composite encapsulated piezoelectric ultrasonic sensors in monitoring dynamic modulus of asphalt concrete. Measurement 246, 116642. https://doi.org/10.1016/j.measurement.2025.116642

Ye, F., Liu, Z., Zhu, X., Zhu, W., Cai, G., Wang, L., 2023. Research on integrated electrical and mechanical response of piezoelectric asphalt pavement material under bidirectional cyclic loads. Constr. Build. Mater. 375, 130957. https://doi.org/10.1016/j.conbuildmat.2023.130957

Ye, Z., Wei, Y., Yang, S., Li, P., Yang, F., Yang, B., Wang, L., 2024. IoT-enhanced smart road infrastructure systems for comprehensive real-time monitoring. Internet Things Cyber-Phys. Syst. 4, 235–249. https://doi.org/10.1016/j.iotcps.2024.01.002

Ye, Z., Wei, Y., Zhang, W., Wang, L., 2022. An Efficient Real-Time Vehicle Monitoring Method. IEEE Trans. Intell. Transp. Syst. 23, 22073–22083. https://doi.org/10.1109/TITS.2022.3150224

Yoo, J., Kim, Y., Cho, H., Jeong, Y.-H., 2017. High piezoelectric d 31 coefficient and high T c in PMW-PNN-PZT ceramics sintered at low temperature. Sens. Actuators Phys. 255, 160–165. https://doi.org/10.1016/j.sna.2016.12.020

Yu, M., You, Z., Wu, G., Kong, L., Liu, C., Gao, J., 2020. Measurement and modeling of skid resistance of asphalt pavement: A review. Constr. Build. Mater. 260, 119878. https://doi.org/10.1016/j.conbuildmat.2020.119878

Yu, Y., Liu, X., Li, J., Wang, Y., Qing, X., 2022. Life-cycle health monitoring of composite structures using piezoelectric sensor network. Smart Mater. Struct. 31, 015033. https://doi.org/10.1088/1361-665x/ac3c09

Yu, Z., Zhu, Z., Zhang, Y., Li, X., Liu, X., Qin, Y., Zheng, Z., Zhang, L., He, H., 2024. Biodegradable and flame-retardant cellulose-based wearable triboelectric nanogenerator for mechanical energy harvesting in firefighting clothing. Carbohydr. Polym. 334, 122040. https://doi.org/10.1016/j.carbpol.2024.122040

Yuan, R., Xue, Deqing, Xue, Dezhen, Zhou, Y., Ding, X., Sun, J., Lookman, T., 2019. The Search for $BaTiO_3$ -Based Piezoelectrics With Large Piezoelectric Coefficient Using Machine Learning. IEEE Trans. Ultrason. Ferroelectr. Freq. Control 66, 394–401. https://doi.org/10.1109/TUFFC.2018.2888800

Zeng, S., Zou, J., Song, M., Liu, S., Zhang, J., Wei, T., Sun, Q., Zhang, Y., Yuan, X., Zhang, D., 2025. The mechanism for the enhanced piezoelectricity, dielectric property and thermal stability in (K,Na)NbO3 ceramics. Acta Mater. 287, 120801. https://doi.org/10.1016/j.actamat.2025.120801

Zhang, B., Guo, C., Cao, X., Yuan, X., Li, X., Huang, H., Dong, S., Wang, Z.L., Ren, K., 2022. Flexoelectricity on the photovoltaic and pyroelectric effect and ferroelectric memory of 3D-printed BaTiO3/PVDF nanocomposite. Nano Energy 104, 107897. https://doi.org/10.1016/j.nanoen.2022.107897

Zhang, Jie, Li, C., Lv, C., Yu, H., Ma, W., Lei, M., Chen, X., Liu, M., Zhang, X., 2025. Ultra-soft, foldable, wearable piezoelectric sensor based on the aligned BaTiO3 nanoparticles. Mater. Today Phys. 50, 101606. https://doi.org/10.1016/j.mtphys.2024.101606

Zhang, Jitao, Yang, H., Filippov, D., Zhang, Q., Zheng, X., Tao, J., Jiang, L., Cao, L., 2025. Multi-channel unequal magnetoelectric power splitter in composite of impedance-gradient piezoelectric ceramics and spinel ferrites. Sens. Actuators Phys. 383, 116232. https://doi.org/10.1016/j.sna.2025.116232

Zhang, M., Duan, Z., Huang, Z., Yu, H., Wang, C., Zhang, H., Li, T., Huang, Q., Yuan, Z., Jiang, Y., Tai, H., 2025. Constructing a high-power self-powered electrochemical pressure sensor for multimode pressure detections. Nano Energy 136, 110747. https://doi.org/10.1016/j.nanoen.2025.110747

Zhang, M., Gao, T., Wang, J., Liao, J., Qiu, Y., Yang, Q., Xue, H., Shi, Z., Zhao, Y., Xiong, Z., Chen, L., 2015. A hybrid fibers based wearable fabric piezoelectric nanogenerator for energy harvesting application. Nano Energy 13, 298–305. https://doi.org/10.1016/j.nanoen.2015.02.034

Zhang, M.-H., Wang, K., Du, Y.-J., Dai, G., Sun, W., Li, G., Hu, D., Thong, H.C., Zhao, C., Xi, X.-Q., Yue, Z.-X., Li, J.-F., 2017. High and Temperature-Insensitive Piezoelectric Strain in Alkali Niobate Lead-free Perovskite. J. Am. Chem. Soc. 139, 3889–3895. https://doi.org/10.1021/jacs.7b00520

Zhang, Q., Cagin, T., Goddard, W.A., 2006. The ferroelectric and cubic phases in $BaTiO_3$ ferroelectrics are also antiferroelectric. Proc. Natl. Acad. Sci. 103, 14695–14700. https://doi.org/10.1073/pnas.0606612103

Zhang, Qixiang, Lei, D., Shi, J., Ren, Z., Yin, J., Jia, P., Lu, W., Gao, Y., Liu, N., 2023. Pressure-Regulated Nanoconfined Channels for Highly Effective Mechanical–Electrical Conversion in Proton Battery-Type Self-Powered Pressure Sensor. Adv. Mater. 35, 2308795. https://doi.org/10.1002/adma.202308795

Zhang, Qingtao, Shangguan, L., Li, T., Ma, X., Yin, Y., Dong, Z., 2023. Tire–Pavement Interaction Simulation Based on Finite Element Model and Response Surface Methodology. Computation 11, 186. https://doi.org/10.3390/computation11090186

Zhang, Qingtong, Zhang, Y., Yu, Z., Fu, J., Zuo, R., 2023. Excellent piezoelectric performance of BiFeO3–BaTiO3– La(Mg2/3Nb1/3)O3 lead-free ceramics via relaxation regulation near the morphotropic phase boundary. Ceram. Int. 49, 20860–20869. https://doi.org/10.1016/j.ceramint.2023.03.219

Zhang, S., Cao, R., Jia, Z., Xiong, Y., Chen, C., Zhang, Y., 2021. Cement/epoxy-based embedded ultrasonic transducers for concrete structure applications. J. Mater. Res. Technol. 14, 242–254. https://doi.org/10.1016/j.jmrt.2021.06.067

Zhang, Shupei, Zhu, H., Zhou, H., Chen, Y., Liu, Y., 2024. Estimation of Road Adhesion Coefficient Based on Camber Brush Model. World Electr. Veh. J. 15, 263. https://doi.org/10.3390/wevj15060263

Zhang, W.L., Yu, Y.C., Luo, W.B., Shuai, Y., Pan, X.Q., Wu, Q.Q., Wu, C.G., 2017. Lead free KNN/P(VDF-TrFE) 0–3 pyroelectric composite films and its infrared sensor. Infrared Phys. Technol. 80, 100–104. https://doi.org/10.1016/j.infrared.2016.09.005

Zhang, Xu, Li, B., Zou, J., Liu, H., Xu, B., Liu, K., 2024. Deep-learning enabled atomic insights into the phase transitions and nanodomain topology of lead-free (K,Na)NbO3 ferroelectrics. Sci. China Mater. 67, 3029–3038. https://doi.org/10.1007/s40843-024-2999-8

Zhang, Xianzhao, Yin, Q., Cheng, H., Zheng, R., Zhang, H., Hu, K., Lin, F., Fang, L., Wang, S., Zhang, Z., 2024. Contribution of (Bi0.45Y0.05)Na0.5ZrO3 to induced multiphase coexistence and enhanced piezoelectric properties of K0.5Na0.5NbO3 lead-free ceramics. Mater. Sci. Eng. B 305, 117416. https://doi.org/10.1016/j.mseb.2024.117416

Zhang, X., Zhang, C., Lin, Y., Hu, P., Shen, Y., Wang, K., Meng, S., Chai, Y., Dai, X., Liu, X., Liu, Y., Mo, X., Cao, C., Li, S., Deng, X., Chen, L., 2016. Nanocomposite Membranes Enhance Bone Regeneration Through Restoring Physiological Electric Microenvironment. ACS Nano 10, 7279–7286. https://doi.org/10.1021/acsnano.6b02247

Zhang, Y., Zhang, H., Lü, C., Chen, Y., Wang, J., 2020. Piezoelectric energy harvesting from roadway deformation under various traffic flow conditions. J. Intell. Mater. Syst. Struct. 31, 1751–1762. https://doi.org/10.1177/1045389X20930089

Zhao, C., Park, J., Root, S.E., Bao, Z., 2024. Skin-inspired soft bioelectronic materials, devices and systems. Nat. Rev. Bioeng. 2, 671–690. https://doi.org/10.1038/s44222-024-00194-1

Zhao, H., Chen, Xiaoming, Xin, C., Zhao, F., Cheng, S., Lei, M., Wang, C., Zhang, Jingyao, Chen, Xiaoliang, Tian, H., Zhang, Jie, Shao, J., 2025. High-sensitivity and self-powered flexible pressure sensor based on multi-scale structured piezoelectric composite. Chem. Eng. J. 519, 164787. https://doi.org/10.1016/j.cej.2025.164787

Zhao, H., Ling, J., Yu, J., 2012. A comparative analysis of piezoelectric transducers for harvesting energy from asphalt pavement. J. Ceram. Soc. Jpn. 120, 317–323. https://doi.org/10.2109/jcersj2.120.317

Zhao, Jinyan, Wang, Z., Dai, L., Chen, C., Zheng, K., An, R., Liu, Z., Zhang, N., Quan, Y., Wang, L., Wang, G., Li, X., Zhao, Y., Niu, G., Ren, W., 2025. Ultra-large strain response in BNT-BT-KNN thin films boosted by electric field-induced inversion of long-range ordered polarization. J. Materiomics 11, 100908. https://doi.org/10.1016/j.jmat.2024.06.005

Zhao, Jiyu, Zhu, M., Li, Y., Zheng, M., Hou, Y., 2025. Simple isovalent substitution route enhancing

energy storage performance of linear dielectric ceramics. J. Alloys Compd. 1016, 178906. https://doi.org/10.1016/j.jallcom.2025.178906

Zhao, K., Zhao, Y., Cao, Y., 2024. Numerical Simulation-Based Investigation of Fatigue Fracture Mechanisms in Hot In-Place Recycling of Asphalt Pavement, in: Feng, G. (Ed.), Proceedings of the 10th International Conference on Civil Engineering, Lecture Notes in Civil Engineering. Springer Nature Singapore, Singapore, pp. 390–407. https://doi.org/10.1007/978-981-97-4355-1_37

Zhao, L., Yuan, X., Zhou, X., Wang, Q., Li, J., Xiong, X., Zhang, Q., Chen, C., Chen, S., Ju, D., Zhang, Y., Zhang, D., 2024. Three-dimensional honeycomb structured BaTiO3-based piezoelectric ceramics via texturing and vat photopolymerization. Addit. Manuf. 95, 104542. https://doi.org/10.1016/j.addma.2024.104542

Zhao, L., Zhang, Y., Yan, M., Li, J., Xiong, X., Roscow, J., Zhang, D., Bowen, C., 2025. Enhanced piezoelectric properties of additively manufactured BCZT with an oriented ceramic lamellar structure formed via vat photopolymerization. J. Eur. Ceram. Soc. 45, 116934. https://doi.org/10.1016/j.jeurceramsoc.2024.116934

Zhao, Q., Wang, L., Zhao, K., Yang, H., 2019. Development of a Novel Piezoelectric Sensing System for Pavement Dynamic Load Identification. Sensors 19, 4668. https://doi.org/10.3390/s19214668

Zhao, Z.-H., Dai, Y., Huang, F., 2019. The formation and effect of defect dipoles in lead-free piezoelectric ceramics: A review. Sustain. Mater. Technol. 20, e00092. https://doi.org/10.1016/j.susmat.2019.e00092

Zheng, K., Xie, N., Deng, Y., Febbo, M., Broeckmann, C., Liu, P., 2026a. A review on lead-free piezoelectric ceramic sensors for sustainable and intelligent applications. Chem. Eng. J. 528, 172363. https://doi.org/10.1016/j.cej.2025.172363

Zheng, K., Xie, N., Jin, J., Liu, P., 2025. Environmentally friendly lead-free piezoelectric ceramics as pavement sensing element: A multi-scale finite element perspective. Case Stud. Constr. Mater. e05174. https://doi.org/10.1016/j.cscm.2025.e05174

Zheng, K., Xie, N., Liu, P., 2026b. Epoxy-cement composite packaging for KNN piezoelectric sensors. Sens. Actuators Phys. 398, 117356. https://doi.org/10.1016/j.sna.2025.117356

Zheng, Q., Hou, Y., Yang, H., Tan, P., Shi, H., Xu, Z., Ye, Z., Chen, N., Qu, X., Han, X., Zou, Y., Cui, X., Yao, H., Chen, Yihan, Yao, W., Zhang, J., Chen, Yanyan, Liang, J., Gu, X., Wang, D., Wei, Y., Xue, J., Jing, B., Zeng, Z., Wang, L., Li, Z., Wang, Z.L., 2022. Towards a sustainable monitoring: A self-powered smart transportation infrastructure skin. Nano Energy 98, 107245. https://doi.org/10.1016/j.nanoen.2022.107245

Zheng, T., Wu, J., 2016. Relationship between Poling Characteristics and Phase Boundaries of Potassium–Sodium Niobate Ceramics. ACS Appl. Mater. Interfaces 8, 9242–9246. https://doi.org/10.1021/acsami.6b01796

Zheng, Y., Wang, S., Jin, W., Li, Z., Yang, G., Li, X., Li, N., Wang, Y., Sheng, F., Song, Z., 2025. An ultrasound-driven PLGA/Zn-KNN hybrid piezoelectric scaffold with direct and immunoregulatory antibacterial activity for bone infection. Bioact. Mater. 47, 295–312. https://doi.org/10.1016/j.bioactmat.2025.01.026

Zhou, F., Chai, Y., 2020. Near-sensor and in-sensor computing. Nat. Electron. 3, 664–671. https://doi.org/10.1038/s41928-020-00501-9

Zhou, H., Liu, Y., Lu, Y., Dong, P., Guo, B., Ding, W., Xing, F., Liu, T., Dong, B., 2016. In-situ crack

propagation monitoring in mortar embedded with cement-based piezoelectric ceramic sensors. Constr. Build. Mater. 126, 361–368. https://doi.org/10.1016/j.conbuildmat.2016.09.050

Zhou, H., Zhang, Y., Qiu, Y., Wu, H., Qin, W., Liao, Y., Yu, Q., Cheng, H., 2020. Stretchable piezoelectric energy harvesters and self-powered sensors for wearable and implantable devices. Biosens. Bioelectron. 168, 112569. https://doi.org/10.1016/j.bios.2020.112569

Zhou, X., Xue, G., Luo, H., Bowen, C.R., Zhang, D., 2021. Phase structure and properties of sodium bismuth titanate lead-free piezoelectric ceramics. Prog. Mater. Sci. 122, 100836. https://doi.org/10.1016/j.pmatsci.2021.100836

Zhou, Y., Zhang, Shuangmeng, Xu, X., Liu, W., Zhang, Shixu, Li, G., He, J., 2020. Dynamic piezo-thermoelectric generator for simultaneously harvesting mechanical and thermal energies. Nano Energy 69, 104397. https://doi.org/10.1016/j.nanoen.2019.104397

Zhou, Z., Chen, K., Li, X., Zhang, S., Wu, Y., Zhou, Y., Meng, K., Sun, C., He, Q., Fan, W., Fan, E., Lin, Z., Tan, X., Deng, W., Yang, J., Chen, J., 2020. Sign-to-speech translation using machine-learning-assisted stretchable sensor arrays. Nat. Electron. 3, 571–578. https://doi.org/10.1038/s41928-020-0428-6

Zhu, T., Jiang, M., Wang, Y.-F., Wang, Y.-S., 2024. Reconfigurable inverse design of phononic crystal sensor based on a deep learning accelerated evolution strategy. Thin-Walled Struct. 204, 112255. https://doi.org/10.1016/j.tws.2024.112255

Zuo, Y., Feng, J., Gao, Y., Li, Y., Qi, L., 2025. A self-powered triboelectric wind detection sensor with adaptive electromagnetic damping adjusting mechanism. Sustain. Energy Technol. Assess. 73, 104132. https://doi.org/10.1016/j.seta.2024.104132

Zygmuntowicz, J., Piotrkiewicz, P., Wachowski, M., Szachogłuchowicz, I., Żurowski, R., Falkowski, P., Korycka, K., Tomaszewska-Krygicz, J., 2024. Ceramic-metal pipes with NiAl2O4 and TiAl2O5 spinel phases with different metallic phase content - Analysis of properties, and microstructure, taking into account LCA. Open Ceram. 18, 100597. https://doi.org/10.1016/j.oceram.2024.100597

Appendix

Declaration by Doctoral Candidate of Own Contribution to Publication-based dissertation with Three or More Authors

I hereby confirm that Kai Zheng contributed to the study as stated below:

Article:

Kai Zheng, Ning Xie, Yuanbin Deng, Mariano Febbo, Christoph Broeckmann, Pengfei Liu. "A review on lead-free piezoelectric ceramic sensors for sustainable and intelligent applications". Chemical Engineering Journal. 2025: 172363.

Author Contributions:

Kai Zheng drafted the original manuscript, reviewed and edited the manuscript, performed formal analysis, developed the conceptual framework, and conducted data visualization. Ning Xie drafted the original manuscript, performed formal analysis, developed the conceptual framework, and conducted data visualization. Yuanbin Deng reviewed and edited the manuscript, contributed to data visualization, and developed the methodology. Mariano Febbo reviewed and edited the manuscript, contributed to data visualization, and developed the methodology. Christoph Broeckmann reviewed and edited the manuscript, contributed to the conceptualization, and performed validation. Pengfei Liu reviewed and edited the manuscript, supervised the study, conducted the investigation, and acquired funding.

Author Confirmation:

Author 1 (Kai Zheng): Kai Zheng

Author 2 (Ning Xie): _____

Author 3 (Yuanbin Deng): _____

Author 4 (Mariano Febbo): _____

Author 5 (Christoph Broeckmann): _____

Author 6 (Pengfei Liu): _____

Date: 04.03.2026

Declaration by Doctoral Candidate of Own Contribution to Publication-based dissertation with Three or More Authors

I hereby confirm that Kai Zheng contributed to the study as stated below:

Article:

Kai Zheng, Ning Xie, Li-Feng Zhu, Jiao Jin, Pengfei Liu. "Enhanced piezoelectric performance and thermal stability in KNN-BNZ ceramics modified by $CaHfO_3$". Journal of Materials Science: Materials in Electronics.37, 379 (2026).

Author Contributions:

Kai Zheng drafted the original manuscript, conducted data visualization, validation, methodology development, investigation, formal analysis, and data curation, and reviewed and edited the manuscript. Ning Xie drafted and reviewed the manuscript and contributed to the investigation and resource provision. Li-Feng Zhu contributed to resource provision, funding acquisition, formal analysis, and validation. Pengfei Liu supervised the study, contributed to resource provision and funding acquisition, and reviewed and edited the manuscript.

Author Confirmation:

Author 1 (Kai Zheng): Kai Zheng

Author 2 (Ning Xie): Xie Ning

Author 3 (Li-Feng Zhu): Lifeng Zhu

Author 4 (Jiao Jin): Jiao Jin

Author 5 (Pengfei Liu): Liu, Pengfei

Date: 04.03.2026

Declaration by Doctoral Candidate of Own Contribution to Publication-based dissertation with Three or More Authors

I hereby confirm that Kai Zheng contributed to the study as stated below:

Article:

Kai Zheng, Ning Xie, Pengfei Liu. "Epoxy-cement composite packaging for KNN piezoelectric sensors". Sensors and Actuators A: Physical. 2025: 117356.

Author Contributions:

Kai Zheng drafted the original manuscript, reviewed and edited the manuscript, developed the methodology, conducted the investigation, acquired funding, performed data curation, and contributed to the conceptualization of the study. Ning Xie reviewed and edited the manuscript, developed the methodology, and conducted the investigation. Pengfei Liu reviewed and edited the manuscript, supervised the study, developed the methodology, and acquired funding.

Author Confirmation:

Author 1 (Kai Zheng): Kai Zheng

Author 2 (Ning Xie): Ning Xie

Author 3 (Pengfei Liu): Liu, Pengfei

Date: 04. 03. 2026.

Declaration by Doctoral Candidate of Own Contribution to Publication-based dissertation with Three or More Authors

I hereby confirm that Kai Zheng contributed to the study as stated below:

Article:

Kai Zheng, Ning Xie, Jiao Jin, Pengfei Liu. "Environmentally friendly lead-free piezoelectric ceramics as pavement sensing element: A multi-scale finite element perspective". Case Studies in Construction Materials. 2025: e05174.

Author Contributions:

Kai Zheng drafted the original manuscript, performed data visualization and validation, developed the software, contributed resources, established the methodology, conducted formal analysis, performed data curation, and contributed to the conceptualization of the study. Ning Xie reviewed and edited the manuscript. Jiao Jin acquired funding. Pengfei Liu reviewed and edited the manuscript, supervised the study, administered the project, and acquired funding.

Author Confirmation:

Author 1 (Kai Zheng): Kai Zheng

Author 2 (Ning Xie): Ning Xie

Author 3 (Jiao Jin): JiaoJin

Author 4 (Pengfei Liu): Liu.Pengfei

Date: 04.03.2026

Declaration by Doctoral Candidate of Own Contribution to Publication-based dissertation with Three or More Authors

I hereby confirm that Kai Zheng contributed to the study as stated below:

Article:

Kai Zheng, Taowei Gao, Pengfei Liu. "A Sensor Arrangement Evaluation Framework for Lead-Free Potassium Sodium Niobate Pavement Sensors in Vehicle Classification". Measurement. 2026: 120999.

Author Contributions:

Kai Zheng drafted the original manuscript, performed visualization and validation, developed the methodology, conducted the investigation and formal analysis, curated the data, and contributed to the review and editing of the manuscript. Taowei Gao drafted the original manuscript, provided resources, conducted formal analysis, and performed validation. Pengfei Liu supervised the study, provided resources, acquired funding, and contributed to the review and editing of the manuscript.

Author Confirmation:

Author 1 (Kai Zheng): Kai Zheng

Author 2 (Taowei Gao): Taowei Gao

Author 3 (Pengfei Liu): Liu. Pengfei

Date: 04.03.2026